Autoselective Regeneration of Gelcast Ceramic Foam Diesel Particulate Filters

By
Andrew M. Williams
MEng (Hons) DIS

A Doctoral thesis submitted in partial fulfilment of the requirements for the award of Doctor of Philosophy of Loughborough University

June 2007

ABSTRACT

This thesis describes the development and application of an electric discharge for regenerating gelcast ceramic foam diesel particulate filters (DPF) for effective and efficient reduction of particulate matter (PM) emissions from diesel fuelled IC engines.

The combustion in diesel compression ignition engines generates a number of unwanted by-products including PM. The PM from diesel engines is believed to be potentially carcinogenic when inhaled into the lungs and, therefore, needs to be controlled. Emission legislation has made it increasingly difficult for engineers to reduce PM emissions whilst meeting NO_x targets by combustion optimisation alone, leading to the requirement for exhaust gas aftertreatment, most notably exhaust gas filtration. Filtration and regeneration (filter cleaning) technology must be robust, filter high amounts of PM, be compact, energy efficient and cost effective. A large number of published solutions do not meet all of these criteria. This research has developed a compact, efficient, robust and cost effective solution: The Autoselective regeneration of gelcast ceramic foam DPFs.

Gelcast ceramic foam geometry can be optimised on a microscopic and macroscopic scale with a large number of material characteristics. This thesis develops and applies new methodology for rapid optimisation of gelcast ceramic foam DPFs. The optimum foam geometry is found to be highly application-dependent. Filters with >95% filtration efficiency and a low filtration volume have been demonstrated, although are limited in their PM mass holding capacity. It was found that filters with higher PM mass holding capacity require larger pore sizes and filtration volume. Design maps were produced to allow rapid optimisation of gelcast ceramic foams with a novel methodology that can be applied to all forms of deep bed filtration, saving both time and cost in future filter development.

Investigation and optimisation of Autoselective regeneration demonstrated that the regeneration system is most effective when the electric discharge is active within the filter volume. Using modelling and novel methods for measuring heat flux from electrical discharges, thermal optimisation of the heat flows in the system were achieved. Rig tests increased the robustness of the regeneration system and developed profiled mesh electrodes to maximise the effective regeneration volume. An engine test programme demonstrated regeneration effectiveness of ~12 g kW^{-1} h^{-1} which is equivalent to ~333 W for a typical 56 kW heavy duty diesel engine. Alternatives such as fuel burners and electrical resistance heaters typically consume between 1 and 5 kW of fuel energy for filter regeneration. Multiple electrode prototypes are presented and evaluated for efficient and effective on-engine and on-vehicle PM control.

Table of Contents

Acknowledgements

The time and effort spent working on this research during the past years has been made possible by the continuous support of Loughborough University, Caterpillar and the EPSRC. Without their financial and technical support the work in this thesis would not have been possible.

In particular, the oustanding support, encouragement and teaching of my supervisor, Professor Colin Garner, has helped guide myself and this work to where it is today. For this I will be ever grateful.

Among the many individuals who contributed their time and expertise to support my work I would like to thank the Powertrain technicians for maintaining the working engine and test cell without fail for the entirety of the research. The expert advice and support from fellow researchers including John Proctor, Karim Ladha, John Harry and Dave Hoare, was invaluable. My thanks go to Colin Garner, Candice Majewski, and John Harry for giving up their own time to read, comment and advise me on my thesis.

Without the support, encouragement and understanding of all my friends and family, as well as those already mentioned, this work would not be what it is now, so I thank everyone who was a part of my life during this work.

List of Figures

List of Tables

Nomenclature

A	area
A_i	quadratic curve fit coefficients
a	incident PM per unit area
C	constant for flow rate calculations
C_{el}	capacitance
c	speed of light
c_i	numerical constant
c_p	specific heat capacity
D_{dist}	deviation of back pressure due to PM loading distribution
D_{corr}	deviation of back pressure due to the correction for PM distribution
d_b	mobility diameter
d_i	electrode seperation
d_r	fractal dimension
E	effect (relative)
E_r	regeneration effectiveness
E_i	electric field strength
f_0	resonant frequency
h	heat transfer coefficient
I	current
I_{BP}	back pressure indicator
I_{flow}	flow indicator
k	Boltzsmann constant
k_i	numerical constant
L	conceptual DPF filtration length
L_{el}	inductance
l	known DPF filtration length
m	mass
m_r	measured mass at reference temperature
m_a	actual measured mass
$\dot{m}$	mass flow rate
$\dot{m}_{inlet}$	engine inlet air mass flow rate
$\dot{m}_{exhaust}$	engine exhaust mass flow rate
$\dot{m}_{PM}$	particulate matter mass flow rate

N	engine speed
N_{FSN}	AVL smoke number
n	integer
P	pressure
P_{inlet}	engine inlet air pressure
P_i	upstream pressure
P_o	downstream pressure
p	pore diameter
$p_{measured}$	measured diameter
p_{MEP}	mean effective pressure
Q	thermal energy flow
q	heat flux
Q_{el}	charge
R	regeneration rate
R_{air}	gas constant of air
R_{el}	resistance
R_1	resistance to fracture initiation
R_2	resistance to fracture propagation
r	radius
r_{vis}	visible radius
S	source term
t	filter thickness
T	temperature
T_{inlet}	engine inlet air temperature
T_r	reference temperature
T_a	ambient temperature
T_{el}	time period
U	internal energy
v	space velocity
V	volume
$\dot{V}$	volumetric flow rate
V_{el}	voltage
V_o	voltage drop
V_b	breakdown voltage
V_f	filter volume
V_{swept}	engine swept volume

w	window diameter
W	power
W_{el}	electrical Power
$W_{thermal}$	thermal heating power
$\overline{W}$	average power
$\overline{W}_{el}$	average electrical power

α	coefficient of thermal expansion
Δ	differential
δ	required resolution
ε	porosity
ε_0	permittivity of free space
ε_r	relative permittivity
$\varnothing$	diameter
η	efficiency
η_h	heating efficiency
η_L	estimated filtration efficiency
η_l	filtration efficiency of the test filter sample
λ	wavelength
ρ	density
ρ_e	effective density
ρ_{FSN}	soot concentration
ρ_{inlet}	engine intake manifold air density
σ	tensile strength
θ	specific PM mass loading
$\overline{\theta}$	average specific PM loading
μ	dynamic viscocity
ν	Poisson ratio

Abbreviations

AC	alternating current
BMEP	brake mean effective pressure
C_2	diatomic carbon
C_nH_m	generalised hydrocarbon fuel

CI	compression ignition
CO	carbon monoxide
CO_2	carbon dioxide
CT	computed tomography
DC	direct current
DISI	direct injection spark ignition
DoE	Design of Experiments
DPF	diesel particulate filter
EPA	Environmental Protection Agency (USA)
EPSRC	Engineering and Physical Sciences Research Council (UK)
HCCI	homogenous charge compression ignition
HFR	hot flow rig
H_2O	water
HV	high voltage
IC	internal combustion
MEP	mean effective pressure
N_2	diatomic nitrogen
NO_x	nitrogen oxides
NTE	not to exceed (emission limits)
NVH	noise, vibration and harshness
O	monatomic oxygen
O_2	oxygen molecule
O_3	ozone
PAH	polycyclic Aromatic Hydrocarbons
PFI	port fuel injection
PM	particulate matter
ppm	parts per million
ppb	parts per billion
PWM	pulse width modulation
rpm	revolutions per minute
SEM	scanning electron microscope
SOF	soluble organic fraction
VOC	volatile organic compound
WFF	wall flow filter

CHAPTER 1

INTRODUCTION

1.1 Internal Combustion Engines

Generation of motive power is of interest to society for commercial, industrial and personal reasons, in particular improving transportation and communication throughout the world. It is essential to have a power source that is compact and efficient. Generally speaking, motive power sources have two main components, normally the energy store and the means of energy conversion. In the case of an electric motor system this could be in the form of a battery and DC motor. Likewise, in the case of internal combustion (IC) engine systems the two components are the fuel and the engine. In this introduction it will become clear as to why the IC engine is one of the most effective solutions for generation of motive power and why compression ignition (CI) internal combustion engines have a significant share of the market. The customer driven and legislatively imposed technological challenges arising with the increased use of diesel CI engines are introduced.

This thesis presents research on a novel technology that allows the use of diesel CI engines with significantly reduced particulate emissions that meet future legislation, while maintaining a compact and adaptable geometry, reliability and low input energy requirement. The following introduces some background to put this research into context.

Table 1.1 shows a selection of energy sources and compares their energy densities, which is a measure of how compact or lightweight the energy source is. This table shows that hydrocarbon based fuels offer >450 times the energy density of electrical energy stores such as batteries. The low energy density in the electrical energy sources mean that for an energy store comparable to a fuel tank on a vehicle they would be unfeasibly large. Interestingly, 71% of the electrical energy production in the UK is derived from burning fossil fuels with average fuel conversion efficiencies of ~39% (calculated from DUKES, 2006). When this is combined with 50% optimum charging efficiency of storage devices such as capacitors, for example, the maximum energy conversion efficiency from fossil fuels to stored electrical energy is approximately 20%. As an alternative, direct conversion of fossil fuel to motive power offers efficiencies of typically 45% (calculated from Heywood, 1988).

Table 1.1 Comparison of the energy density of a range of energy sources

Energy Source	Typical Energy Density kJ kg^{-1}	Reference
Gasoline	44 000	Heywood (1988)
Diesel	42 500	Heywood (1988)
Natural Gas	45 000	Heywood (1988)
Coal (Lignite)	14 800	Forsythe (2003)
Super Capacitors	20	Maxwell Technologies (2007)
Lead Acid Batteries	123	Sonnenschein (2007)
Alkaline Batteries	422	Energizer (2007)

Table 1.2 provides a comparison between alternative methods for converting stored energy into motive power. Power density (in this context) gives a measure of how small and lightweight a motive power source is for a given power output. The example of an IC engine shows the highest power density when compared to external combustion steam engines and electric motors. This means that the smallest and

lightest power source will be the IC engine. Electric motors offer power densities of the same order of magnitude as IC engines, but remain unfeasible due to the additional weight of the energy source.

Table 1.2 Comparison of power density of a range of motive power sources

Power Source	Power Density $W\ kg^{-1}$	$kW\ m^{-3}$	Reference
Diesel Engine	317	291	Perkins Engines (2005)
Steam Engine	40.4	37.2	Wikipedia (2007)
DC Motor	75.9	110	Farnell (2007)
AC Induction Motor	136	167	Electrodrives (2007)

The energy density of the fossil fuel source, combined with the power density of the IC engine explain their widespread use in motive applications. With this interest comes a wide range of technological developments, all offering different advantages and disadvantages. Some of these options will be stated here before discussing the reason why CI diesel engines have a significant share of the IC engine market.

The range of IC engines in use can be grouped broadly into categories based on ignition source, combustion type and fuel-air mixture type. Table 1.3 shows how four commonly known engine types fit into these categories. Due to the variations in ignition, combustion and mixture types these engines all have varying properties such as efficiency, emissions, torque and speed characteristics, which have effects on the target markets.

Table 1.3 Classification of internal combustion engines (Adapted from Robert Bosch GmbH, 2004)

	Internal Combustion Engines			
Combustion	Continuous	Cyclic		
Ignition	External Ignition Source		Auto-ignition	
Type of Mixture	Heterogeneous	Homogenous		Heterogeneous
Type of Engine	Gas Turbine	Spark Ignition	Homogenous Charge Compression Ignition	Compression Ignition

Continuous combustion gas turbines are used commonly for aircraft propulsion since they can be easily designed to generate an exhaust flow with significant momentum to apply a nett forward force to the engine. They are also used for electricity generation offering high power density and direct generation of rotary motion. For land motive applications, their high rotor speed can make the design of the transmission more difficult because of the requirement of reducing from ~30 000 rpm to as little as ~60 rpm that is required for vehicle traction wheel rotation. Cyclic combustion processes, using oscillating pistons and converting the oscillatory motion to rotary motion through a connecting rod and crankshaft assembly, offer slower speeds, higher torques and improved thermal management. Cyclic combustion is most often used for vehicle applications but are also used for electricity generation by direct connection to a generator.

Due to the ease of ignition and combustion control, spark ignition and compression ignition engines are the most widely accepted IC engine technologies. Adequate transient control of homogeneous charge compression ignition (HCCI) engines limits their use currently to research and development. To reduce the load with the spark ignition (SI) engines while maintaining an ignitable air-fuel mixture, it is normally necessary to throttle the intake air, reducing the intake manifold air density in proportion to the reduction in fuel delivery. Since the exhaust pressure is still close to atmospheric pressure, the work done to exchange the gases is larger than if the intake manifold was at atmospheric pressure. This work is referred to as pumping losses. The turbulent nature of the gas flow within the cylinder leads to noticeable variations in cylinder pressures between one cycle and the next, which results in a less pleasurable experience for those using the engine (i.e. noise, harshness and vibration) and also a higher risk of misfire. Thermodynamic analysis of the IC engine shows that increasing the compression ratio leads to increased energy conversion efficiency (and hence fuel economy) (Heywood, 1988). Increasing the compression ratio in the spark ignition engine can lead to the premature auto-ignition of the premixed charge (i.e. knock) setting an upper limit on the compression ratio of ~12:1.

Considering the CI engine where the load is controlled only by the quantity of fuel injected into the cylinder, the air flow does not need to be limited by throttling. This immediately improves the efficiency of the engine by reducing pumping losses,

especially at part loads. The injection of fuel into the cylinder immediately prior to combustion eliminates the risk of knock allowing higher compression ratios and boosting (charge pressurising), therefore, increasing the fuel efficiency and torque capability of the engine respectively. The combustion within a diesel engine is also more repeatable than in spark ignition engines (because of the multiple ignition sites) and the robustness of the diffusion flame combustion process significantly reduces the risk of misfire. Load control is improved with compression ignition direct injection engines (subject to turbocharging characteristics) since the load can be changed within one cycle whereas spark ignition engines have a small delay as the intake manifold pressurises or depressurises.

Despite their advantages over spark ignition combustion, compression ignition engines are traditionally more noisy limiting their use in passenger car applications until recently. Walsh (1999) presents data stating that European new diesel car sales increased from 7.2% of all new car sales in 1980 to 22.1% in 1995. Diesel engines are also heavier than the equivalent spark ignition engine to allow for the higher combustion pressures, related to the higher compression ratio and boosting. The production of smoke when burning with a diffusion flame close to stoichiometric overall mixtures limits the maximum fuel-air ratio that can be used. Typical diesel engines have a richest overall air-fuel ratio of approximately 18:1 by mass, which is equivalent to over 35% excess air (more than the minimum needed to oxidise the fuel). This means that for the same air delivery, a compression ignition engine will have a lower peak mean effective pressure (MEP) than an equivalent swept volume spark ignition engine.

Despite a mix of advantages and disadvantages related to CI diesel engines the improved fuel economy and high torque capability make the CI diesel engine a promising option for industrial and agricultural applications where NVH issues are less important. Compression ignition engines, especially those powered with diesel fuel, are used in tractors, back hoe loaders, trucks, marine applications, diggers, construction machinery and generator sets. Improved noise management, fuel economy and perceived driveability (relating to torque characteristics) is leading to a rapidly expanding diesel engine passenger car market.

1.2 Diesel Engine Emissions

With such widespread use of diesel engines they are considered to be a significant contributor to a number of unwanted pollutants and emissions including carbon dioxide, carbon monoxide, nitrogen oxides, unburnt hydrocarbons and particulate matter. The following sections describe the reasons these major pollutants need to be minimised, the mechanism of their formation and comments more specifically on diesel engine emissions.

1.2.1 Carbon Dioxide (CO_2)

Carbon dioxide (CO_2) is a greenhouse gas, meaning that it acts as insulation in the atmosphere for longwave infrared radiation emitted from the earth. In 1996 anthropogenic (i.e. man made) emissions of CO_2 contributed approximately 3.5% of the worldwide CO_2 emissions (Lenz and Cozzarini, 1999) and are considered to have a significant impact on the thermal equilibrium of the Earth. For this reason they are considered important to minimise.

CO_2 is formed during the burning of any fuel containing carbon. A complete oxidation reaction for a general hydrocarbon fuel in ambient air is

$$C_nH_m + a(O_2 + 3.76N_2) \rightarrow nCO_2 + 0.5mH_2O + 3.76aN_2$$

$$a = n + 0.25m$$

where a, n and m are constants. This reaction shows the production of CO_2 when releasing energy from the fuel. Most of the focus on reducing CO_2 emissions is on improving energy conversion efficiency of IC engines and also reducing the dependence on carbon based fuels in electrical power generation.

1.2.2 Carbon Monoxide (CO)

Carbon monoxide is a colourless, odourless and poisonous gas, and it is considered dangerous in quantities of more than 50 parts per million (ppm) (US Department of Labor, 2007). As well as the risk of local high concentrations of CO in enclosed spaces it is known to react with solar radiation as one of the precursors to

photochemical smog, often affecting densely populated regions such as large cities (Lenz and Cozzarini, 1999). It is, therefore, a regulated emission.

CO is formed during incomplete combustion when there is not enough oxygen present to completely burn the fuel. Figure 1.1 shows the dependence of CO production on oxygen availability. There are low emissions when there is a stoichiometric or lean mixture.

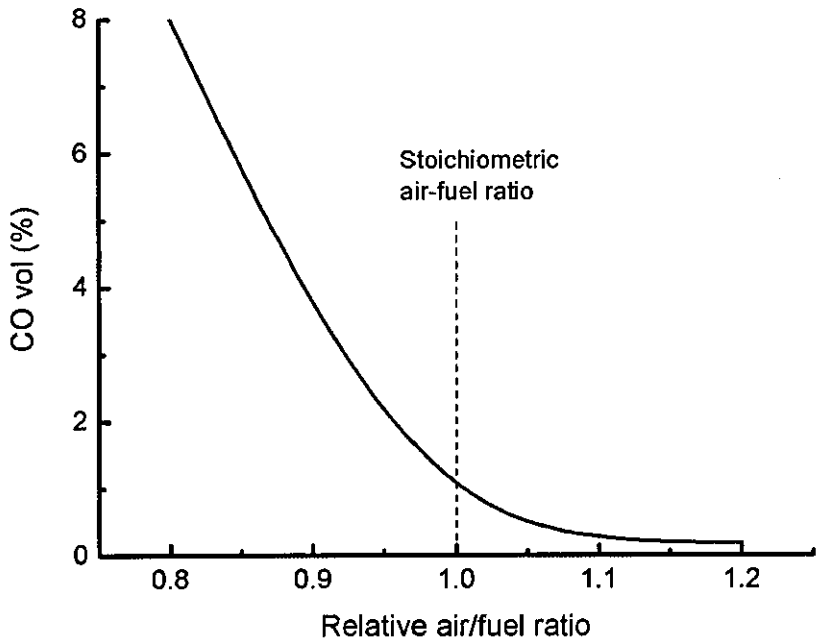

Figure 1.1 Dependence of CO emissions on air/fuel ratio (Adapted from Heywood, 1988)

Diesel engines operate with an overall lean mixture (i.e. excess air) meaning that the exhaust CO emissions are minimal. Within the diffusion flame CO will be formed in the fuel rich region, however, most of this will oxidise in the oxygen rich regions as the flame spreads through the unburned air.

1.2.3 Nitrogen Oxides (NO_x)

Like carbon monoxide, nitrogen oxides (NO, NO_2, N_2O etc hereafter referred to collectively as NO_x) are greenhouse gases. In high concentrations and with exposure to solar radiation they also contribute to photochemical smog. They also affect respiration (e.g. asthma). These are recognised to be of concern and hence are also a regulated emission from IC engines.

Significant nitrogen oxides are formed at temperatures typical of those within the combustion chamber during combustion processes (e.g. Löffler *et al*, 2006). In a diesel engine, the highest local temperatures within the combustion chamber occur between the onset of combustion (when the cylinder pressures are high) and the peak combustion pressure (Heywood, 1988). After the peak combustion pressure the local temperature drops at a sufficiently fast rate such that the NO_x component of the gas is chemically frozen. To reduce NO_x emissions it is, therefore, preferential to limit peak cylinder temperatures. This has a direct influence on the efficiency of the engine and therefore on CO_2 emissions.

1.2.4 Unburnt Hydrocarbons (HC)

The emission of hydrocarbon compounds, especially volatile organic compounds (VOCs) are precursors of photochemical smog (Geiger *et al*, 2002) and, therefore, there is legislative pressure to minimise the exhaust emissions of hydrocarbon compounds.

Hydrocarbon emissions can be generated from a number of sources including the engine lubrication system and the combustion event. During CI combustion in diesel engines there is a small region of the fuel air mixture that has a air fuel ratio beyond the lean limit of combustion. This results in a small amount of the fuel in the cylinder failing to burn and being emitted in the exhaust gases. These emissions can be reduced by increasing combustion pressures and temperatures and by tight control of mixing properties. Post-cylinder control techniques that have proven effective include flow through oxidation catalysts to oxidise unburnt HC.

1.2.5 Particulate Matter (PM)

In diesel engines a small amount of the fuel forms solid particles during combustion that are emitted from the exhaust. These tend to be predominantly elemental carbon with organic compounds and adsorbed water (Kleeman *et al*, 2000). Typical sizes of diesel particulates are 10 to 1000 nm. Further discussion of the formation and properties of particulate matter (PM) follow in Section 1.3. Public concern with the potential health and environmental impacts of inhaled PM emissions have driven a number of detailed biological studies into the effects of PM exposure. Testing by Iwai *et al* (2000) on rodents has shown that diesel particulates are small enough to be

inhaled deep into the lungs and can lead to tumor (or cancer) formation. Other identified effects of diesel particulates are discussed by Ma and Ma (2002) and include localised DNA damage and sensitization of the immune response systems (leading to asthma). Despite recent studies indicating that it is possible for a biological immune system response to limit the effect of inhaled PM (Matschulat *et al*, 2006) it is still important to reduce the quantity of PM emissions from internal combustion engines.

More PM is formed in diffusion flames than with premixed combustion, due to the presence of large fuel rich regions and is, therefore, a major concern with diesel engines. Emission legislators have recognised this concern and are limiting the PM (mass based) emissions from diesel engines (e.g. EPA, 1997). Expectations are that this legislation will be extended to include particle number based as well as mass based limits (Johnsson, 2006) and is resulting in a significant amount of research into reducing PM emissions from IC engines. The area of PM emission reduction is the focus of this research and will be introduced further in the remainder of Chapter 1 and discussed in greater detail in Chapter 2.

1.3 Diesel PM Characteristics

The current understanding of the soot formation process within diesel engines has been summarised by a number of authors (e.g. Heywood, 1988) and the general understanding of the formation process is summarised in this thesis from information published by Setten *et al* (2001). It is illustrated schematically with typical timescales for each formation stage in Figure 1.2.

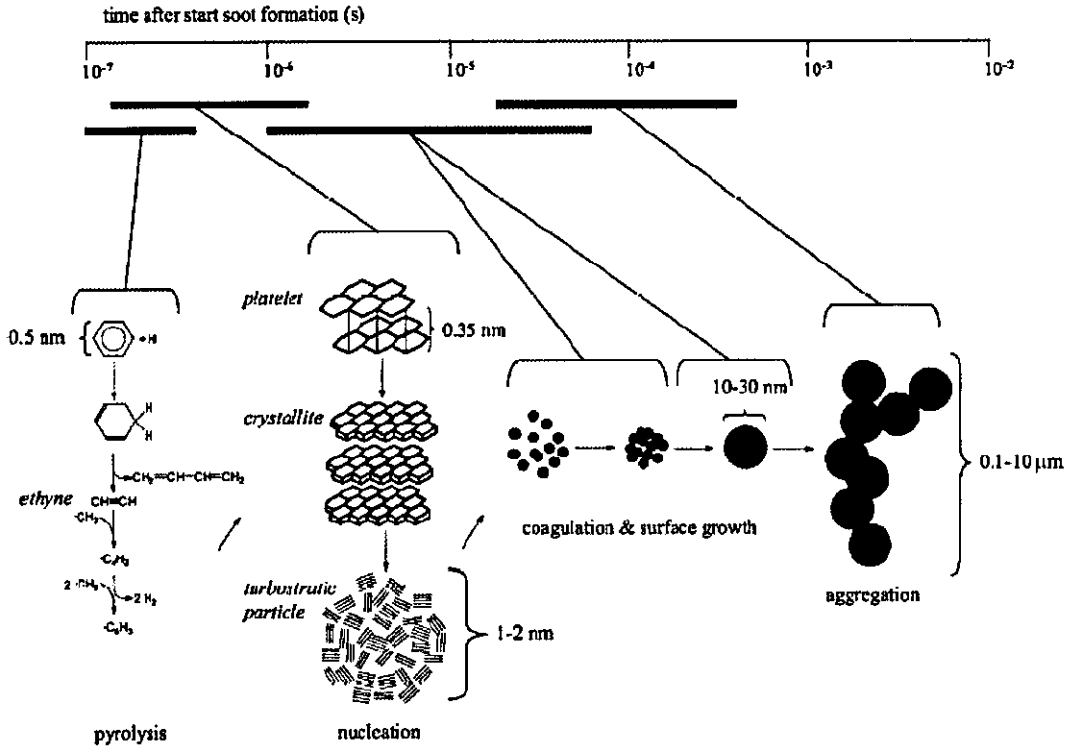

Figure 1.2 Diagram showing the formation process of soot particulates from diesel engines – Setton *et al* (2001)

Within a diffusion flame the air-fuel mixture exists in a range of equivalence ratios from very rich through to beyond the lean combustion limit. Within the fuel rich regions there occurs incomplete combustion (due to lack of available oxygen). The complex hydrocarbon fuel molecules pyrolise to form simpler hydrocarbons such as ethyne, which subsequently polymerize to form polycyclic hydrocarbons. These plate-like structures (known as platelets) coalesce to form crystallites. Crystallites coalesce to form soot nuclei. The nucleated particles grow by a combination of coagulation (joining with other nucleate particles) and surface growth which fills the voids in the soot nucleus. As surrounding conditions change (i.e the engine cycle continues) the surface growth stops and primary soot spherules in the region of 10-30 nm do not grow any further. These spherules, however, combine creating chain like aggregates in the region of 0.1 to 10 μm which can join further to create larger agglomerates.

Micrographs of real soot particles are shown in Figure 1.3. The randomly oriented, turbostratic (random) structure of the crystallites within the individual spherules is almost distinguishable in Figure 1.3 (a). On a larger scale, the irregular and open

shape of the soot aggregate is clearly visible in Figure 1.3 (b), forming a relatively long thin chain of approximately 30 nm diameter soot spherules.

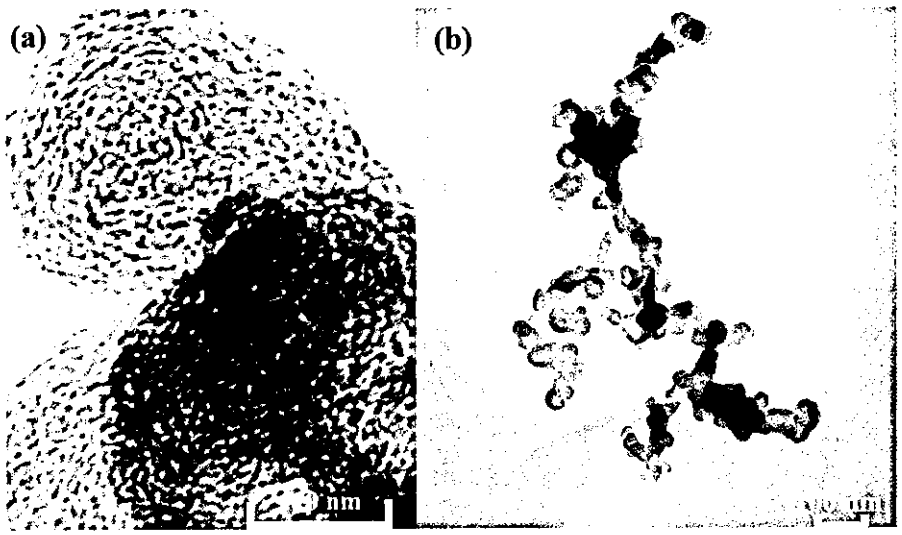

Figure 1.3 (a) Electron micrograph of diesel particulate spherules – Clague *et al* (1999)
(b) Micrograph of a diesel particulate agglomerate – Song *et al* (2004)

Figure 1.4 shows the typical size distribution of diesel particulates based on their overall mass and also the number present. Since legislation currently limits the mass emitted from the engine, the broken line is more commonly seen in published literature concerned with diesel particulate analysis. There are two distinct modes of particulate size corresponding to different stages shown in Figure 1.2. The nucleation mode consists of particles tens of nanometers in size and accounts for most of the particles emitted from the engine. However, since they are small, a large number of these particles have a relatively small mass. The second mode is the agglomeration mode. The agglomerated particles are typically >100 μm size and form most of the mass of PM emitted from diesel engines. This results in a second peak and distribution observable in the broken line in Figure 1.4 at approximately 200 nm diameter. Since this size of particulate contributes the most to the mass emitted in the exhaust, this is the size of particulates most engine developers are focusing on reducing to meet government legislation.

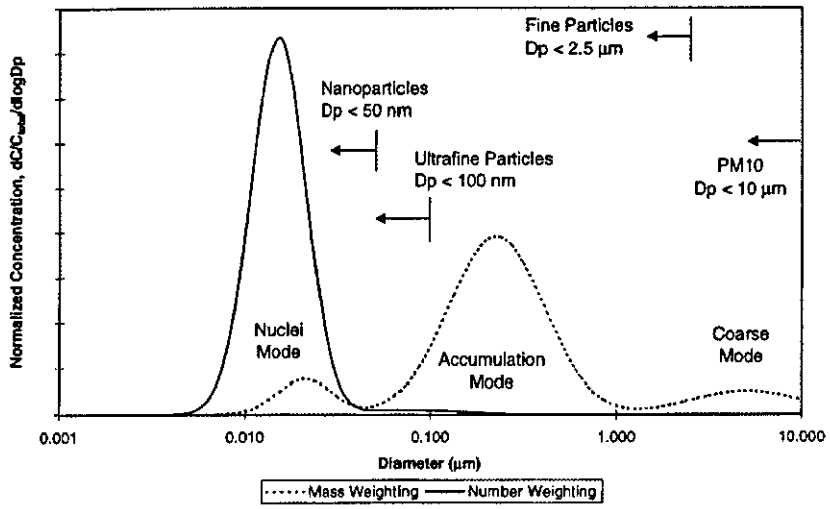

Figure 1.4 Qualitative plot of volume and number distributions of PM emitted from diesel engines - Kittleson (1998)

Experimental studies carried out by Harris and Maricq (2001) yielded results that can be used as a comparison between diesel, port fuel injected (PFI) SI and direct injected spark ignition (DISI) engines. Both DISI and diesel engines showed clear agglomeration peaks with sizes between 50-100 nm and 80-100 nm respectively. PFI engines tested showed no agglomeration peak but a clear nucleation mode peak. The number of particles emitted from the PFI engine was over three orders of magnitude lower than from both the DISI and diesel engines.

In all the samples tested by Kleeman *et al* (2000) the majority of the soot consisted of elemental carbon and organic compounds. Figure 1.5 shows that, in diesel engines, 60-80% of the PM is elemental carbon with a much smaller fraction of organic compounds than seen in the gasoline engines.

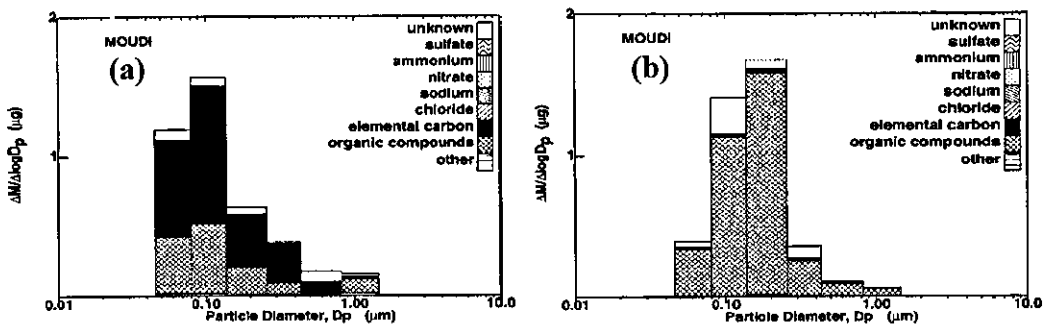

Figure 1.5 Composition distribution of different size particulates from (a) a medium duty diesel and (b) an un-catalysed gasoline engine – Kleeman *et al* (2000)

As particulates cool, volatile components and water condense and adsorb onto the surface of the particulates. Particulates with little or no adsorbed volatile compounds or water are often referred to as 'dry particulates' while those with the adsorbed substances are referred to as 'wet particulates'. Large amounts of the organic components and adsorbed water can be removed from the surface of the particulate by heating. Collura *et al* (2005) observed increases in specific surface area of the soot from 168 $m^2 g^{-1}$ to 229 $m^2 g^{-1}$ during heating of PM in an inert atmosphere.

1.4 Diesel Engine Emission Legislation

Government recognition of the potential health threat of engine-out emissions has led to legislation being put in place in many major countries around the world. Europe has implemented the EURO emission standards, the Environmental Protection Agency (EPA) in USA has implemented its own legislation, often led by the strict limits set in California.

It has long been recognised that diesel engine NO_x or PM emissions can be reduced by optimising the combustion process. Higher in-cylinder temperatures promote oxidation of PM before the exhaust valve opens but increases in gas temperatures significantly increase NO_x formation and hence NO_x emissions. To achieve a noticable reduction in either NO_x or PM emissions often means a significant increase in the other. Legislation of NO_x and PM emissions combined offers a challenge to engine developers that is now leading to the necessity of exhaust aftertreatment methods as well as tight control of combustion processes.

Figure 1.6 shows how the emission legislation has developed through until 2008 in Europe and the USA. Engines with no more than an oxidation catalyst have achieved 2000 European standards and European truck engines have met Euro IV (in 2005) emission standards. Methods for further reducing PM emissions without significant cost are becoming harder to develop and diesel particulate filters offer a promising solution to reduce PM levels if energy efficient and reliable regeneration (i.e. filter cleaning) can be achieved. The effect of some different techniques for treating NO_x and PM that are currently being studied is also shown on Figure 1.6. More details on the advantages and disadvantages of each type of system are discussed later in this

thesis. A large number of the proposed systems, however, do not meet manufacturers' needs in terms of some or all of the following:

1. Cost
2. Reliability
3. Robustness
4. Efficiency
5. Size.

The research presented in this thesis has aimed to develop a novel PM filtration and regeneration technology that is low cost, reliable, robust, compact and energy efficient.

1.5 The Future of PM Emissions from Diesel Engines

Until recent emission legislation, engine developers have been able to achieve acceptable PM and NO_x emissions with in-cylinder controls. Further reductions of legislative limits means exhaust aftertreatment methods are now needed. Filtration technology developed, for example by Corning (e.g. Howitt and Montierth, 1981) and NGK, are known to be capable of achieving > 99% reduction in PM emissions in the exhaust gas (Liu *et al*, 2005). The exhaust gas pressure increases as the filter fills up with PM and without periodic or continuous cleaning, the exhaust pressure would become unacceptable. The difficulty with this filtration technology is maintaining low exhaust pressures by cleaning (regenerating) the filter while being energy efficient, compact, low cost, compact and reliable. New methods that offer benefits in these areas are needed to make diesel exhaust filtration an effective means of reducing particulate emissions. This thesis investigates, applies and evaluates a promising new concept that solves some of the major issues with current filtration and regeneration technology. The remainder of Chapter 1 summarises the structure of the thesis and the contribution to knowledge this research has made.

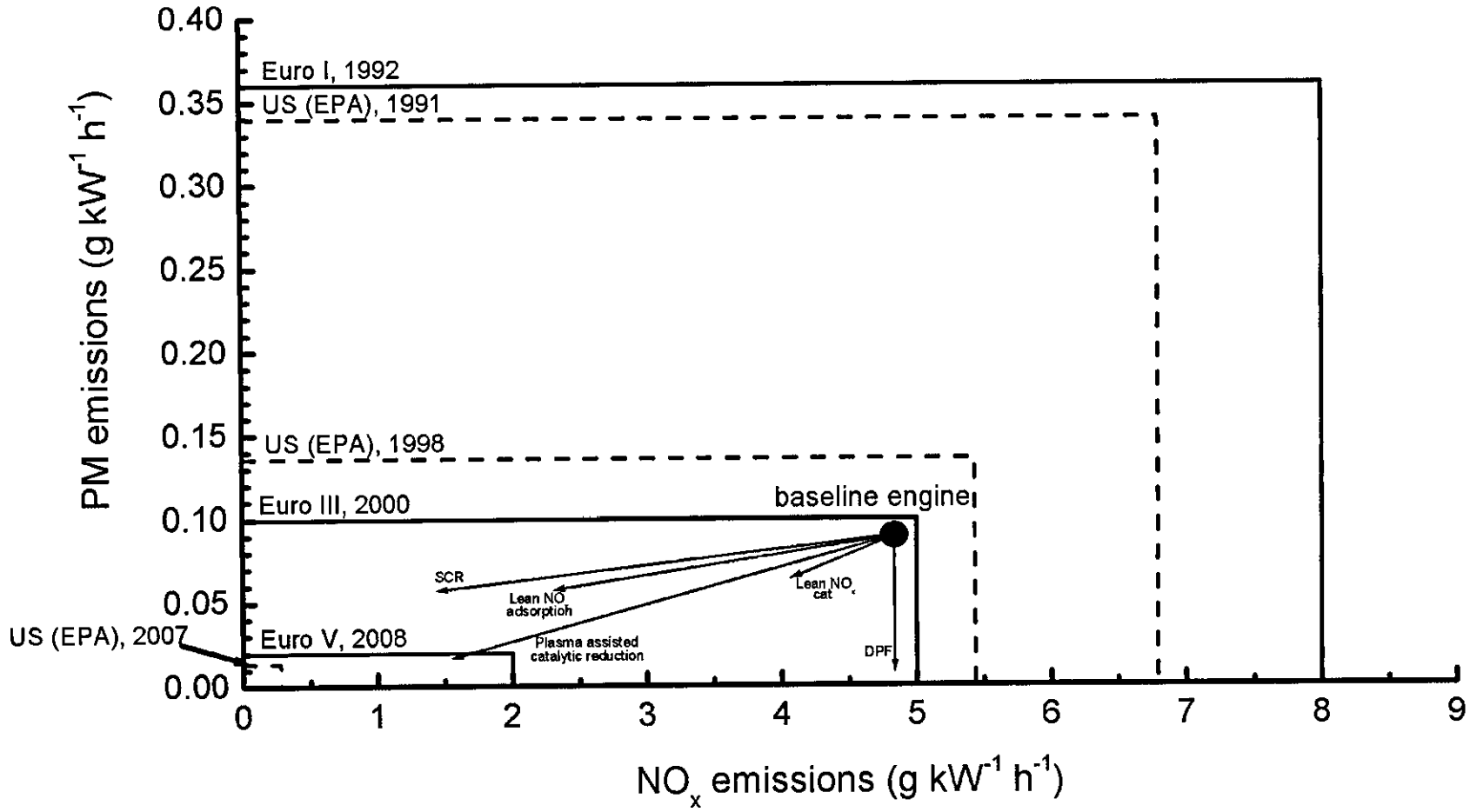

Figure 1.6 Summary of recent legislative changes limiting the NO_x and particulate emissions of truck and bus engines within Europe and North America – DieselNET (2007). Typical effects of a range of aftertreatment methods on NO_x and particulate emissions are also shown – Diesel Emission Evaluation Program (1999)

1.6 Thesis Overview

Chapter 1 of this thesis has discussed the need for internal combustion engines and more specifically diesel fuelled compression ignition engines. The significant emissions that are of concern for current engine development have been introduced and PM emissions from diesel engines have been discussed in more detail. Examples of government legislation were presented to highlight the demand for novel, efficient and effective particulate matter control technologies.

Chapter 2 reviews the current state of the art PM control technologies. It critically evaluates the available filtration and regeneration strategies independently to form a foundation for evaluation of the filtration and regeneration technology developed during the research presented in this thesis. This review of the current literature provides an understanding of the challenges faced during the development of exhaust aftertreatment technologies to reduce PM from diesel engines. This gives enough background to put the new work that is presented in the following chapters into perspective.

Chapter 3 introduces a range of experimental techniques that are used throughout the work in this thesis. It begins by discussing ways of characterising gelcast ceramic foams and follows with methods for evaluating the regeneration performance during testing. Experimental rig and engine test methods are then introduced to provide understanding of the generic methodology used in the subsequent testing.

The research and optimisation of gelcast ceramic foams used as diesel particulate filters (DPFs) is presented in Chapter 4. Investigations into the filtration properties of gelcast ceramic foams leads to models that allow evaluation of conceptual foam DPFs and, in addition, can be applied to any deep bed filtration study. The chapter concludes by discussing and presenting the optimisation process applied to gelcast ceramic foams.

In Chapter 5 the Autoselective regeneration technology is introduced covering previous work in this area before investigating the fundamental mechanism of PM

oxidation with the Autoselective electric discharge. New techniques to measure the heat flux from electrical discharges are developed and used to optimize the regeneration process for the exhaust gas flow environment.

The challenges involved in integrating the gelcast ceramic foam and Autoselective regeneration technology are described in Chapter 6. Equivalent circuit electrical models and experimental investigations are used to understand the effect of a range of variables and to optimize the regeneration for gelcast ceramic foam DPFs.

Chapter 7 examines the thermal energy flows involved with Autoselective regeneration of gelcast ceramic foams, developing understanding and leading to informed design decisions with respect to material choices, durability and energy useage.

Chapter 8 incorporates the proposed technology into a real engine exhaust system and investigates a number of important design factors on the performance of the regeneration system for all the major success criteria.

Chapter 9 discusses the implementation of the Autoselective regeneration of gelcast ceramic foam DPFs. A prototype system is presented before discussing the practicalities of the complete filtration and regeneration technology. Potential limitations of the technology are investigated and found to be tractable.

Chapter 10 summarises the major conclusions of this thesis and outlines potential areas of further work.

1.7 Contributions to Knowledge from the Work Presented in this Thesis

The work presented in this thesis has made novel contributions to both experimental methodology and technological developments. The new methodology includes:

1. A method for accurately measuring the average pore size of a porous structure without the need for complex and expensive three dimensional scanning technologies. This is proven to give a more accurate description of

gelcast ceramic foams than methods that have been previously reported in the published literature on gelcast ceramic foams.

2. A simple and effective method to increase productivity and reduce the time needed for tests that required weighing of porous structures of non-ambient temperatures. This allowed the correction of errors associated with the buoyancy of the air within the filter material when measuring at a temperature different to ambient conditions, that has not been reported in detail in the published literature.
3. A method for understanding the effect of local PM loading on the back-pressure across a depth bed particulate filter. All experimentally based methods discussed in the literature (to the author's knowledge) have presented data or analysis based on average PM loadings and have not considered the effect of PM distribution on the back-pressure across the filter. This new method combined with other physical relationships allows the optimisation of depth bed filters based on a small amount of experimental data, which saves time and money during product development.
4. A novel non-intrusive method for determining the heat flux from an electrical plasma. This method has been used to understand the heat flux from the discharge and offer a tool that can be used in the plasma physics field for optimization of heat flux in a number of technological applications of plasmas.

As well as developing techniques to support research and development work, the research in this thesis contributes significantly towards the engineering solutions and physical understanding of the Autoselective regeneration of gelcast ceramic foam DPFs. The contributions include:

5. Optimisation of 80% porous gelcast ceramic foams used as diesel particulate filters Design maps are proposed and an example of the design maps is demonstrated.
6. Optimisation of Autoselective regeneration of PM from a diesel engine considering system geometries, gas flow rates and direction as well as electrical characteristics of the plasma.
7. Demonstration of the successful integration of gelcast ceramic foam and Autoselective regeneration technologies both on a rig and on a real engine.

The system is evaluated with respect to regeneration rate, energy usage and blow off rates (non-oxidised PM removal from the filter).

1.8 Concluding Remarks

This first chapter has introduced IC engine emissions and highlighted the need for technologies to reduce the harmful emissions, especially carbonaceous PM. The steps taken by legislative bodies to promote investment in developing such technologies have been summarised to highlight some of the difficulties engineers have in meeting suitable emission levels. This demonstrates the need for new technologies that offer compact, efficient, effective and low cost solutions to reduce PM emissions. The novel technologies investigated and presented in this thesis offer such a solution. Following an introduction to diesel engine emissions, the structure of the thesis was outlined and a list stating the contributions of this research to both scientific and engineering methodology, as well as technological developments were presented. The next chapter reviews the published literature on PM reduction strategies before presenting the case for investment in Autoselective regeneration of gelcast ceramic foams.

CHAPTER 2

REVIEW OF PM REDUCTION STRATEGIES

Chapter 1 introduced the pollutant emissions from diesel engines and described the need for reducing PM emissions from diesel engines. Chapter 2 reviews the current literature and summarises PM emission control methods investigated in an attempt to reduce the diesel engine PM emissions. This chapter concludes with a summary and evaluation of the current state of the art technologies, highlighting the need for a compact, low energy usage, efficient filtration system.

2.1 In-Cylinder Strategies

Particulate matter in the exhaust system can be reduced by lowering the PM produced during combustion. The formation of PM within the cylinder is affected by the quality of the burning including, more specifically, the presence of localised fuel

rich regions and gas temperature. A selection of methods that were investigated to reduce the PM produced within the cylinder follows.

2.1.1 Injection Strategies

Fuel injection strategies can have a significant impact on the mixing properties of the fuel and as a result, the combustion and PM formation and oxidation. There are a variety of injection strategies that have been investigated and these include:

1. Fuel heating Heating of fuel lines has been investigated by, for example, Burley and Rosebrock (1979) and Temple-Pediani (1973) to improve fuel vaporisation and hence combustion quality. Promoting the vaporisation of the fuel improves mixing and reduces the amount of fuel rich regions in which the PM platelets form. Burley and Rosebrock's (1979) findings showed an 11% reduction in PM emissions from diesel engines by electrically heating the fuel delivery lines to 127 °C demonstrating that this method can be effective. Issues were experienced with injector reliability as the injector was not designed for fuel delivery at elevated temperatures. The cost and energy consumption associated with maintaining these temperatures was not commented on in the paper.
2. Injection timing Injection timing affects the cylinder temperatures during combustion. Most of the PM that is produced is oxidised as the flame burns the fuel and, therefore, the emitted PM emissions are strongly dependent on the cylinder and flame temperatures during combustion. Late injections burn fuel at lower temperatures and were shown by Dec and Kelly-Zion (2000) to lead to notable increases in PM emissions.
3. Injection pressure Increases in injection pressure from 400 to 1000 bar were found to reduce PM emissions by >80% by Singh *et al* (2003). This was attributed to improved atomisation and turbulent mixing reducing the formation of PM precursors. Benefits of increased injection pressure are already realised on production engines.
4. Injector hole geometry Singh *et al* (2003) demonstrated that reducing the injector hole size generally reduced PM emissions. This was thought to be a result of increased atomisation of the fuel when forced through smaller injector holes.

In summary, Injection strategies with heated fuel, relatively early injection, high injection pressure and small injector holes offer reductions in PM emissions by improving combustion quality.

2.1.2 Oxygenated Fuels

Kitamura *et al* (2002) and Miyamoto *et al* (1998) are two examples of studies of the effect of oxygenated fuels on emissions from diesel engines. Both studies found that increasing the oxygen content of the fuels led to reductions in PM emissions from diesel engines. The oxygen availability aids the reduction of the precursors of soot formation. Miyamoto *et al* (1998) found the reduction of PM to be dependent on the amount of oxygen present in the fuel rather than the type of fuel itself. With ~30% oxygen content by mass they demonstrated negligible Bosch Smoke Units (a measurement of PM emissions).

Increasing the oxygen content of hydrocarbon based fuels reduces the heating value of the fuel. This means that the quantity of fuel needed for each combustion cycle must be increased to achieve an equivalent load to using diesel fuel. This leads to increased injection quantities (and duration, pressure or hole size etc) and also either increased fuel tank size or reduced operating durations. These considerations along with issues with implementation and infrastructure associated with oxygenated fuels need to be overcome for the use of oxygenated fuels to be a viable widespread solution to reduce PM emissions from diesel engines.

2.1.3 Fuel Additives and Blends

Burley and Rosebrock (1979) presented results from using a variety of fuel blends on the emissions from diesel engines. They found that when the aromatic content of the fuel reduced, the PM emissions were also reduced. This is because the aromatic components are a significant precursor to soot formation. Highly volatile (i.e. low boiling point) fuels showed lower PM emissions than fuels with high boiling points. This was related to the improved atomisation and mixing of the fuel during injection.

Burley and Rosebrock (1979) also mentioned the positive effect of a water-fuel emulsion on the PM emissions. Adding water to the fuel led to vaporisation of the water during injection. The rapid expansion of the vaporising water helped to break up the fuel droplets, improving mixing and resulting in reduction of PM emissions. Unfortunately water addition also led to a 100% increase in HC emissions. Methanol within the fuel was found to have a similar effect on PM emissions although no detrimental effects on the HC emissions.

2.1.4 Gas Flow Control

Konno *et al* (2007) utilised a secondary gas injector (7% of the clearance volume) to inject gas into the combustion chamber during the main combustion event. This injection of gas increased the turbulence within the mixing regions and resulted in between 40 and >90% reduction in smoke emissions without increasing NO_x emissions. Increasing the swirl volume in the engine has been shown by Hotta *et al* (1997) to reduce PM emissions at medium loads by improving fuel and gas mixing during combustion. These publications demonstrate the effect gas flow control can have on the PM emissions, although the effect was not repeatable over the entire engine operating range.

2.1.5 Plasma Treatments

A study by Cha *et al* (2005) concerning the interactions between non-thermal electrical plasmas and diffusion flames demonstrated that PM production can be significantly reduced. Optical methods showed that the presence of a non-thermal plasma in the diffusion flame suppressed the formation of polycyclic aromatic hydrocarbons (PAH) and soot precursors without measured changes in bulk gas species or flame temperature. This technology may offer interesting avenues for future in cylinder PM suppression in compression ignition engines.

2.1.6 Summary of In-Cylinder Methods

Positive steps towards reducing PM emissions can be taken by reducing the amount of PM formed in the cylinder by the use of oxygenated fuels, improved mixing, improved fuel atomisation and reduction of aromatic content of the fuels. Maximising the amount of PM oxidised within the cylinder also has a large effect on

the exhaust PM emissions. This can be achieved by increasing cylinder temperatures during combustion, for example by optimising the injection timing.

In cylinder methods that have been dependent on technological advances alone have made it into production and have allowed engine manufacturers to meet early emission legislation without the need for exhaust aftertreatment methods. These include increased injection pressures and injector nozzle geometry design. Techniques that rely on significant changes to the infrastructure relating to fuel supply and delivery (such as oxygenated fuels and fuel blends) have not yet been implemented on a large scale.

2.2 Non-Obstructive Exhaust Strategies

Non-obstructive exhaust strategies for reduction of PM refers to methods that do not lead to significant increases in exhaust back pressure by removing the particulates without significant obstruction of the exhaust flow. This section summarises some basic principles of such methods highlighting some advantages and disadvantages of each.

2.2.1 Electrostatic Precipitators and Agglomerators

Electrostatic precipitators operate by using an electric charge trapped on particulates within an aerosol to apply an electric force which moves the particulates to a trapping surface. Figure 2.1 shows a schematic of an electrostatic precipitator which includes:

1. A particle charger (optional) which is often in the form of a coronal electric discharge. This applies charge to the particles. Without an applied charge the particles will not be affected by the electric field in the precipitator.
2. The electrostatic precipitator with an applied voltage, generating the electric force on the particulates. The precipitator requires a large enough trapping area and long enough particulate residence time for the particles to be able to reach the trapping surface. The residence time (and size of the trap) is greatly affected by the gas flow rate, with higher gas flow rates requiring larger trap volumes.

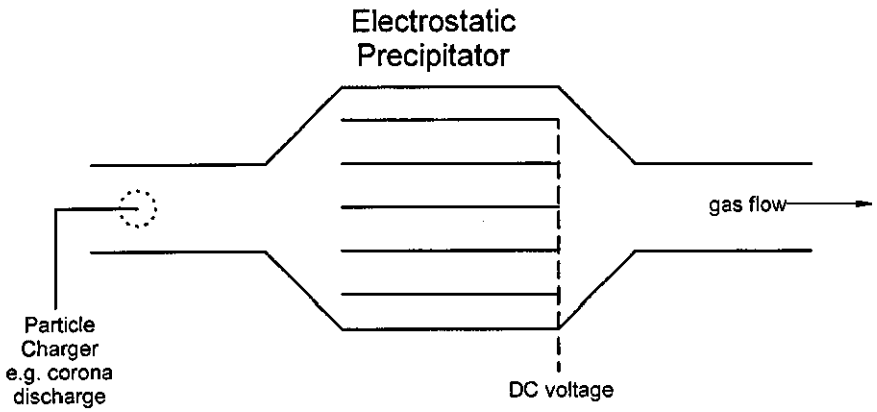

Figure 2.1. Schematic of a generic electrostatic precipitator.

In practice, the PM emitted from diesel engines carries a residual charge meaning that an electrostatic agglomerator can theoretically work without the need of a particle charger. However, Farzaneh *et al* (1994) and Ciach and Sosnowski (1996) showed that pre-charging can increase PM trapping efficiencies from ~20% to >90%.

Figure 2.2 summarises some data presented by Farzaneh *et al* (1994) with estimated power consumptions. Trapping efficiencies of up to 95% were observed, although large amounts of electrical power were required for the pre-charging of the particulates. To achieve this trapping efficiency, residence times needed to be large requiring approximately a 6 litre trap system (excluding power supplies) for a 0.219 litre displacement engine. This compares poorly with filtration trap systems (discussed in Section 2.3) that typically have a trap volume smaller than the engine displacement.

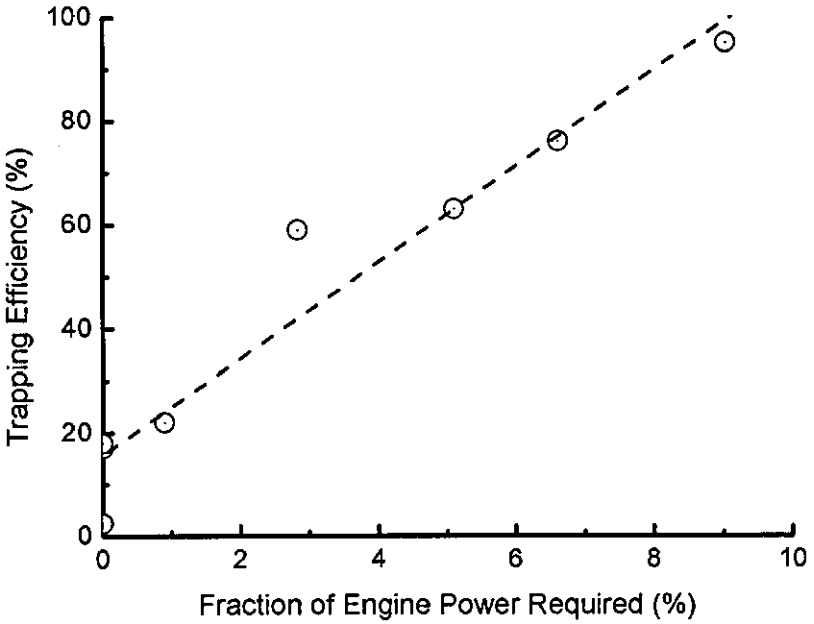

Figure 2.2. Summary of effect of electrical power requirement on the trapping efficiency of an electrostatic precipitator. (Adapted from Farzaneh *et al*, 1994)

Ciach and Sosnowski (1996) also presented promising filtration efficiency results, achieving >90% both with and without particle charging, shown in Figure 2.3. No information was presented that allowed evaluation of power consumption but the system was enhanced greatly by maximising the trapping area by combining the electrostatic precipitator concept with a fibrous filter. However, once a filtering system is being used, issues with filter cleaning (regeneration) must be considered, and are discussed later.

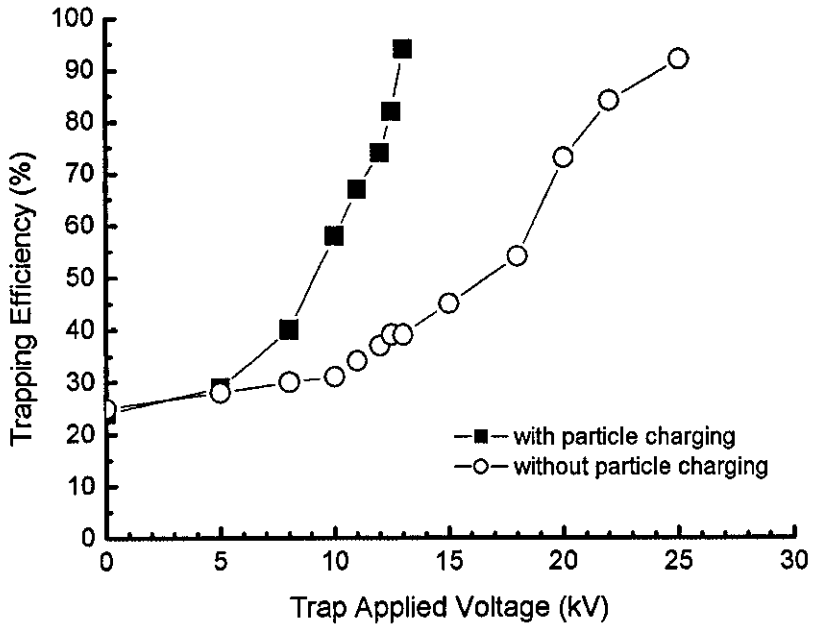

Figure 2.3. Effect of precipitator applied voltage and pre charging on the trapping efficiency of the electrostatic precipitator and fibrous filter combination.

In summary, the use of electrostatic precipitators is unsuitable for diesel engines due to the large trap volume required to achieve large residence times and trapping efficiencies. Use of electrostatic agglomeration to enhance performance of filtration media may offer some advantages if energy requirements and packaging volumes are kept low.

2.2.2 Cyclones

Cyclones are designed to separate aerosol particulates from gas streams using centrifugal forces. Figure 2.4 shows a schematic of a typical cyclone with a tangential gas entry generating a rotating gas flow before the gas exits at the top of the cyclone. During the rotation, the centrifugal forces move the particulates towards the outer edge where they are trapped and fall to the bottom into a hopper. The higher the gas flow the higher the centrifugal force yet the shorter the residence time in the cyclone. The cyclone is also better suited to larger particles where the high inertial–drag force ratio improves the rate of separation. This has implications with diesel engine exhaust flows where future regulations are expected to limit the smaller particle sizes as well as the larger ones.

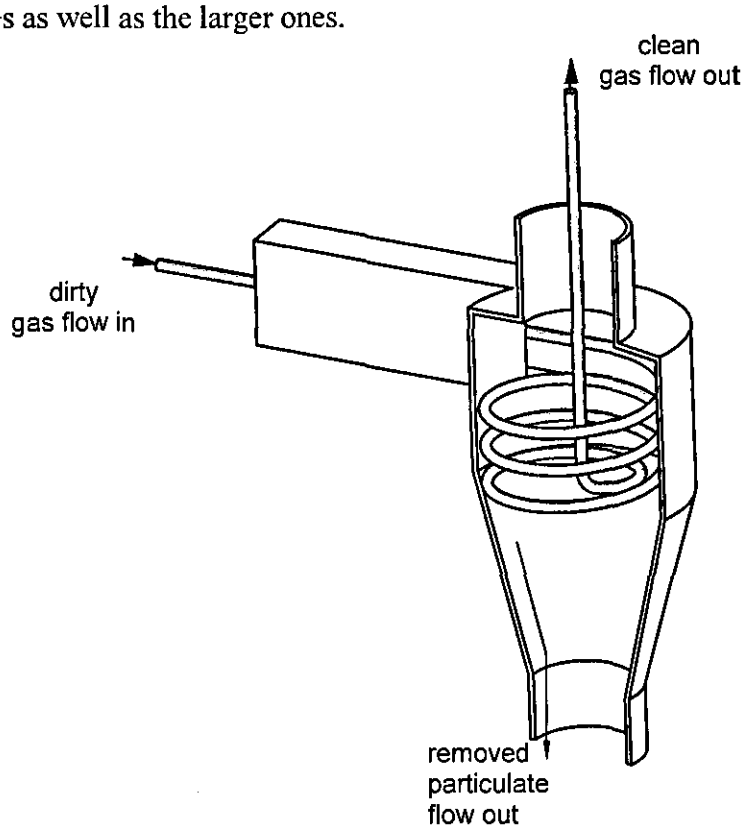

Figure 2.4. Schematic of a typical cyclone particulate separator.

Crane and Wisby (2000) investigated the use of a multicyclone system on diesel engines and found trapping efficiency (by mass) of up to ~60%. To achieve this trapping efficiency the exhaust gas was cooled prior to the cyclones to promote particulate agglomeration (i.e. the production of larger particles). Their modelling showed that the smaller particulates were not trapped which will cause some issues with future emission legislation. If these issues can be overcome, the size and complexity of multiple cyclones and exhaust gas coolers makes this a less attractive option for commercialisation. As with all of the non-obstructive exhaust strategies for reduction of PM the low back pressure in the exhaust system is a major advantage.

2.2.3 Plasma Treatments

The generation of electrical plasmas results in direct conversion of electrical to thermal energy in the gas as well as highly effective oxidants such as ozone (O_3). The use of non-thermal plasmas, with gas temperatures close to the bulk gas temperature utilise the oxidants generated in the plasma to oxidise particulates without having to significantly increase the exhaust gas temperature.

An example of such a system is presented by Dan *et al* (2005) who achieved PM removal rates, by number, of between 25 and 50%. The reduction of particulates was relatively even for all size ranges presented meaning that the mass based removal efficiency would be comparable to the number based efficiency. The peak removal efficiency of close to 50% was achieved with energy densities of 35 J litre^{-1}. A typical 92 kW engine at full load, with an exhaust flow of ~550 kg h^{-1} would require over 10 kW (>10% of engine out power) of energy for a low PM trapping rate. This high power requirement for a low removal rate renders the non-obstructive low temperature plasma treatment of diesel engine exhaust unfeasible.

2.2.4 Summary of Non-Obstructive PM Reduction Strategies.

A selection of non-obstructive methods for PM removal from diesel engine exhaust has been discussed. The main advantage with these systems is the low back pressure

as the exhaust system has no major obstructions. Generally, they suffer from the disadvantage of large size, high energy requirement or low PM removal rates. Large size systems will not be viable on vehicles where there are stringent packaging requirements. A large energy requirement is unfeasible as this will lead to reduced engine out power, potentially increased alternator size and complexity as well as increased fuel consumption and CO_2 emissions. For these reasons non-obstructive exhaust gas PM reduction strategies are unlikely to be commercially realised on most diesel engine applications.

2.3 Diesel Particulate Filtration

Diesel engine exhaust filtration systems use a range of trapping mechanisms to get the particulates to collide with a filtration surface where the inter-surface forces are large enough to overcome forces attempting to remove the particle (for example drag forces). Examples of forces that can lead to trapping of particulates on the filter surface include

1. Impaction The inertia and momentum of a suspended particle under acceleration (e.g. gas flowing around an obstruction) cause the particulate to deviate from the flow streamline. In the case of the gas flowing around an obstruction, the particulate will tend to move closer to the obstruction than the streamline. This can lead to the particle impacting with the trapping surface causing the particle to be filtered from the gas flow. Impaction trapping tends to become more significant with increasing flow velocity, higher particle mass/size ratio and increased flow tortuosity.
2. Interception In the cases where the streamlines take the particle close enough to the surface to make contact, the particles can become trapped. This will tend to occur when there is a very large trapping area and subsequently a restricted gas flow. In reality there will always be some element of impaction with interception for any finite mass particle.
3. Diffusion Random motion of particles in a gas can lead to the particle coming into contact with the trapping surface and hence becoming trapped. The random motion of solid particulates depends on the repeated random collisions with surrounding molecules and particles. To be affected by these

collisions the particle must have a low mass meaning that the particles most affected by collisions tend to be the smaller particles (<0.2 μm diameter).

4. Electrostatic attraction It has already been mentioned in Section 2.2.1 that an electric force can be applied to charged particles. This can be used for filtration to promote the motion of suspended particulates towards a trapping surface. This has the disadvantage of requiring electrical power and complexity of managing high voltages.

Figure 2.5 shows a summary of the predominant trapping mechanism for different size ranges of suspended particulates in air flow. To put the sizes into context, examples of particles of each size range are also shown. This highlights that as the particle size increases, diffusion trapping becomes less significant, with larger amounts of interception. As particle size increases further interception becomes less significant and impaction becomes the predominant trapping mechanism.

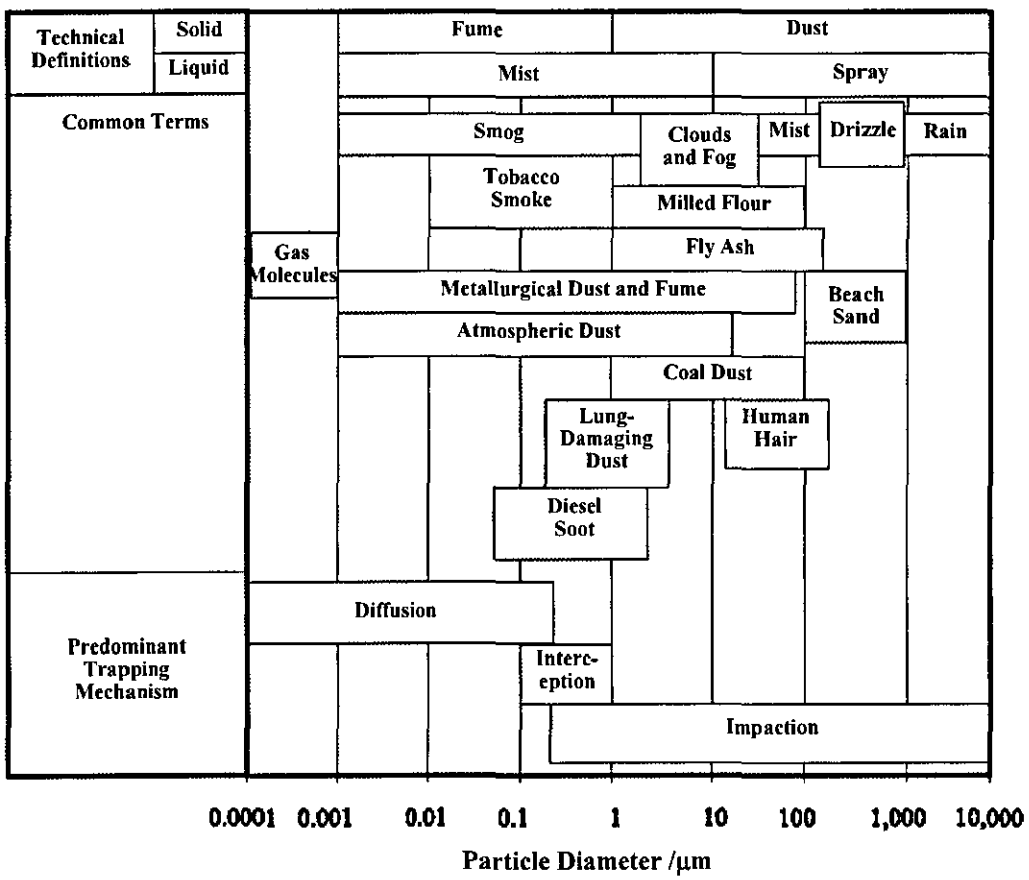

Figure 2.5. Size ranges of different common particles and predominant trapping mechanisms for different particle sizes. (Adapted from Schnell and Brown, 2002)

The theory of filtering the exhaust gas requires obstructions in the exhaust flow that act as trapping surfaces (a filter). The following discussion describes the main types of filters that have been applied to diesel engine exhaust filtration.

2.3.1 Monolithic Wall Flow Filters (WFFs)

Wall flow DPFs consist of an extruded porous ceramic structure that creates a series of channels that the exhaust flows into, shown in Figure 2.6. Alternate ends of the channels are blocked with ceramic plugs that force the gas to flow through the porous ceramic walls of the filter. It is this porous ceramic layer that filters the particulates from the exhaust gases.

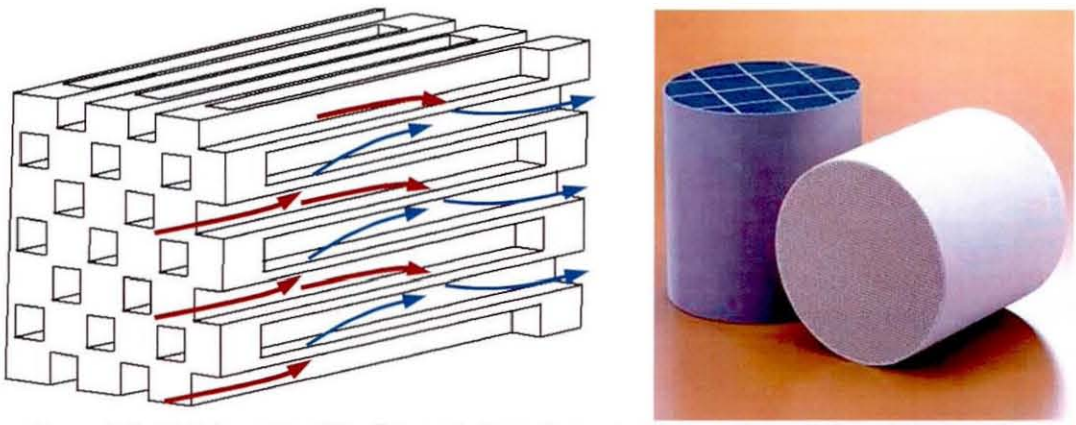

Figure 2.6. (a) Schematic of the flow path through a cross section of a wall flow DPF (based on marketing images by Corning GMBH) and (b) A photograph of a selection of cordierite monolithic wall flow DPF (NGK, 2003).

The pore size and porosity of a wall flow DPF is typically 10-20 μm and 50% respectively (Adler, 2005, Miller *et al*, 1983) which is an order of magnitude larger than the typical particulate size in the gas stream. This leads to a period of depth bed filtration in which the particulates are trapped predominantly by impaction and interception within the porous structure. As the particulates collect on the surface they bridge the gap across the pore and form a finer filtration medium which filter out a large number of particles by cake filtration. The cake is a continuous, highly porous layer of particulates that act as the filtering medium. Cake filtration offers a significantly higher filtration efficiency and is demonstrated in Figure 2.7 and by Liu *et al* (2005). Figure 2.7 shows that within the first five minutes the filtration efficiency can be seen to be close to 100% (by smoke number) compared to

approximately 80% during depth bed filtration. The methodology by which these measurements have been taken is discussed in Chapter 3.

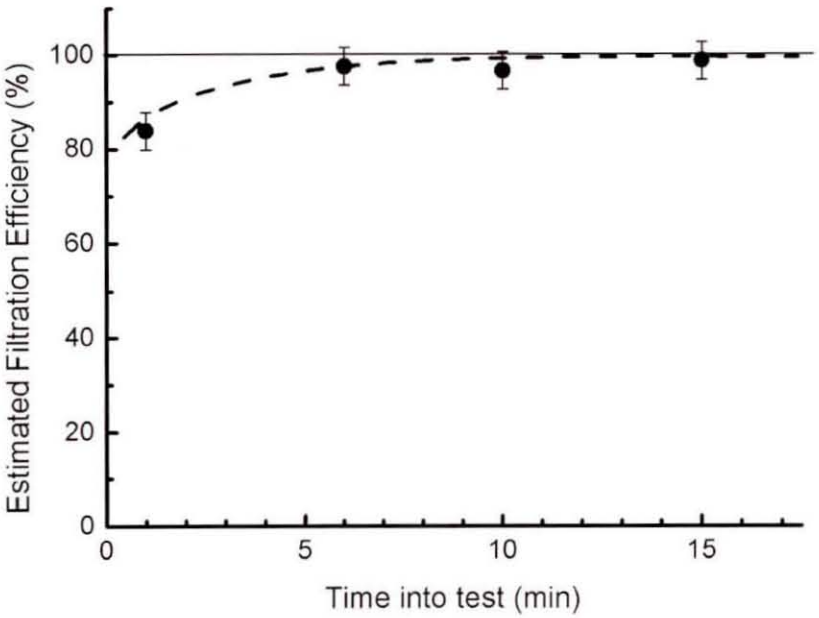

Figure 2.7. Filtration efficiency as a function of time for a 100 cpsi 2.5 litre wall flow diesel particulate filter on the Perkins 1100 series 4 cylinder diesel engine operating at 1000 rpm 130 Nm (methodology described in Chapter 3)

As well as high filtration efficiency, the monolithic structure of the wall flow filter offers a large filtration area that helps to reduce the exhaust back pressure. A 100 cells per square inch (cpsi) (15.5 cells per cm^2) 5.66 inch (144 mm) diameter filter has a filtration area of approximately 1.4 m^2. The back pressure of the clean filter, shown in Figure 2.7, is below 1 kPa for typical flow rates with a filter volume of approximately 2.5 litres.

The effect of PM loading on the backpressure of wall flow filters is shown in Figure 2.8. The change in slope in the plots at approximately 0.5 g $litre^{-1}$ PM loading corresponds to the change of filtration mechanism from depth bed filtration to cake filtration which was found by Konstadopoulos *et al* (2000) to typically occur with PM loadings in the region of 1 g $litre^{-1}$ of filter volume. It can be seen that a smaller cell size filter has a lower back pressure and higher PM holding capacity.

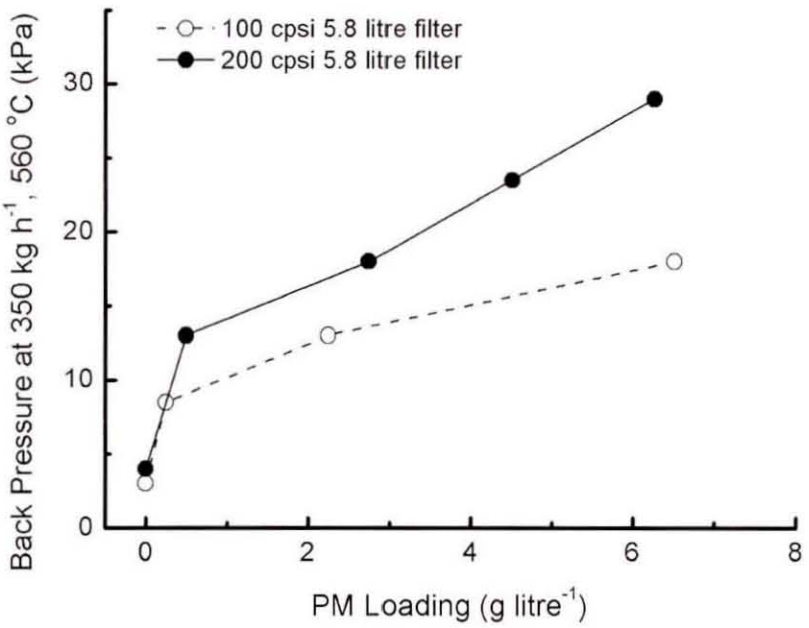

Figure 2.8. Effect of PM loading on the back pressure of the wall flow filters (Corning, 2006).

This combination of high filtration efficiency and low back pressure makes wall flow filters an attractive option for engine manufacturers. Unfortunately, during regeneration the thin structure of the monolithic WFFs makes them prone to failure through melting and thermal shock (Kitagawa *et al*, 1990) In the event of failure of the ceramic filter an open path is created that allows PM to flow directly through the filter significantly reducing the filtration efficiency.

Recent developments published by Li *et al* (2004) and Pyzik and Li (2005) demonstrated further improvements in mechanical strength and filtration properties by growing the monolithic WFF shape from a crystal structure. However, the small scale of the walls and consequences of local material failure still remain.

The wall flow filters offer high filtration efficiency and low back pressures in a compact way making them currently the preferred option for industry, although the implications of filter failure leave potential for more durable filters to offer an improved solution to PM emission reduction.

2.3.2 *Foam Filters*

Foam filters refer quite generally to porous structures that the gas flows through, with the foam, or porous structure filtering out the particulates. In diesel engine applications, the terminology is more commonly used to describe filters that trap the particulates with depth bed filtration, meaning the particles are trapped throughout the filter, or foam volume. The foams have a large number of interconnecting pores to allow the gas to flow through, and a series of struts to maintain the foam structure, and to act as the trapping surface. Figure 2.9 shows an example of a ceramic foam with the struts, pores and windows (holes interconnecting the pores) highlighted.

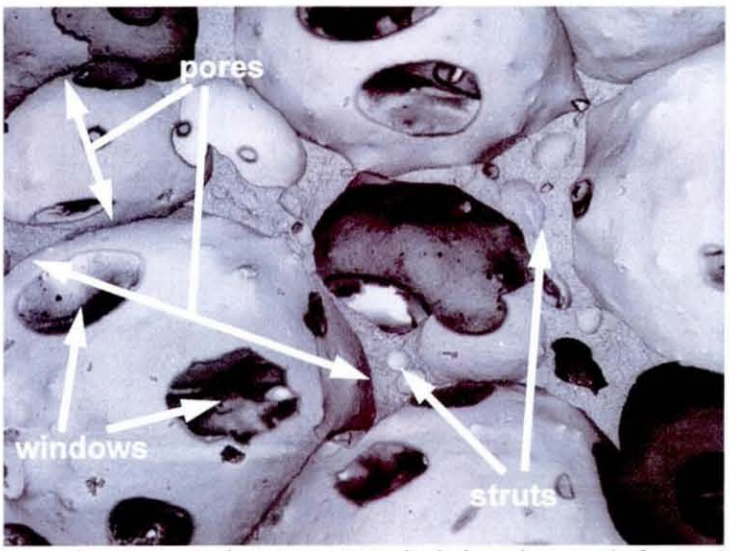

Figure 2.9. Image showing typical struts, pores and windows in ceramic foams. (adapted from Sepulveda and Binner, 1999)

Foam filters capable of high working temperatures for diesel particulate applications have been made predominantly in two ways:

1. Form coating Readily available porous foam structures such as sacrificial packed beds (Thijs *et al*, 2003, Isobe *et al*, 2006) and polymer sponges (Montanaro *et al*, 1998, Jayasinghe and Edirisinghe, 2002) can be coated in a ceramic slurry and sintered. During the sintering process the form that was originally coated is typically burnt out leaving the ceramic foam.
2. Direct foaming Foaming of ceramic slurries by mixing in bubbles from chemical reactions or gas injection (Sepulveda and Binner, 1999, Hughes, 2003, Zhang *et al* 2006, Menchavez *et al*, 2007) can form ceramic foams without the need for sacrificial cores. The same result can be achieved by foaming of a polymer-ceramic mix and subsequent firing (Peng *et al*, 2000)

although the resulting ceramic is less dense. The direct foaming methods have the advantage of producing solid foam struts and result in a stronger foam filter (Sepulveda and Binner, 1999).

Reticulated ceramic foams (form coated) are widely used due to the ease of their manufacture and high porosity and have been tested as diesel particulate filters as far back as the early 1980s (for example, Watabe *et al*, 1983 and Tutko *et al*, 1984). The pore structure, demonstrated in Figure 2.10, is reasonably uniform and well defined by the polymer form structure allowing predictable and repeatable flow properties. Since the foam struts are hollow they tend to be much lighter than gelcast foams and likewise much weaker. The hollow struts also influence electrical and thermal properties due to the lower bulk density.

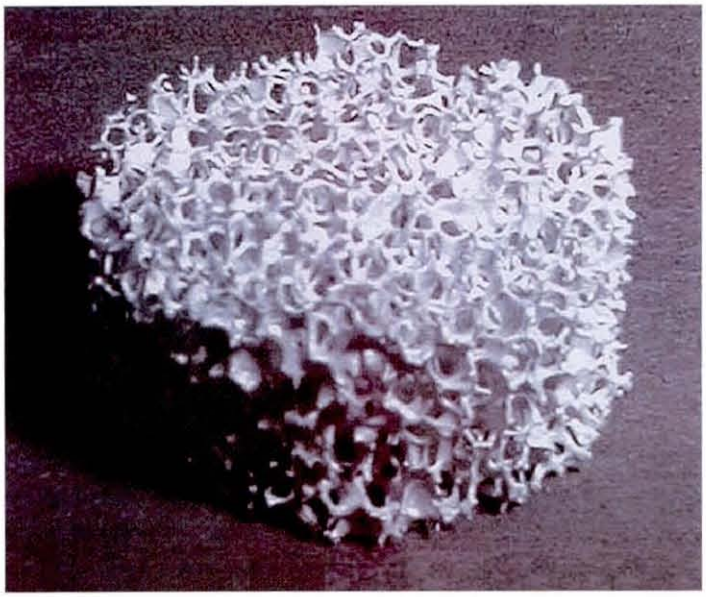

Figure 2.10. Photograph of a typical reticulated ceramic foam structure. (Haugen *et al*, 2004)

A significant advantage of using a form for creating the porous ceramic foam is the ability to optimise the foam geometry. Thijs *et al* (2003) utilised biological forms to produce regular, spherical shaped struts while Isobe *et al* (2006) [a&b] used fibres to generate axially aligned directional pores to optimise the porous structure. Optimisation of the pore structure can generate directional variations in thermal, electrical, mechanical and flow properties that can be beneficial to exhaust gas filtration.

More recent advances in ceramic foam manufacturing allow the direct production of foamed ceramic slurries using the gelcasting process described by Sepulveda and Binner (1999) and presented here in Figure 2.11. The use of surfactants to control bubble growth and decay allow openly porous foam structures to be sintered, generating foam structures like that shown in Figure 2.12.

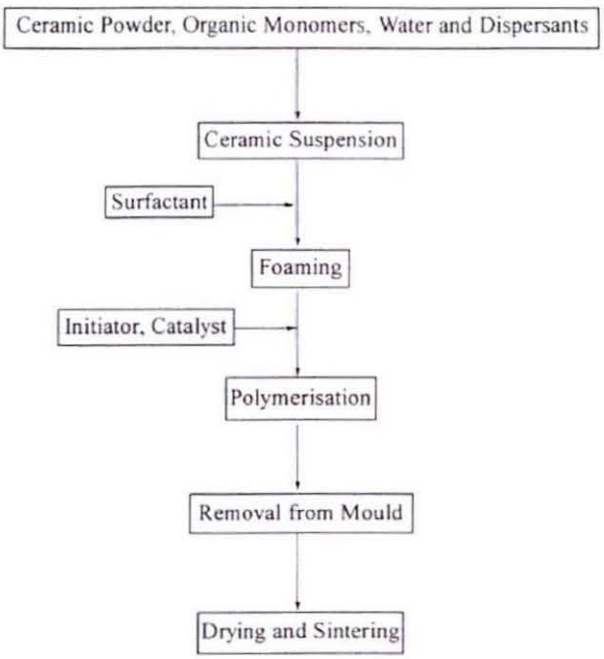

Figure 2.11. Flow chart showing the manufacturing process of a gelcast ceramic foam. (Sepulveda and Binner (1998)

The foam structure of gelcast ceramic foams is less open than the reticulated ceramic foams and they tend to be of a higher density. Developments of the technology and preliminary application of the gelcast ceramic foams to diesel particulate filters is presented by Hughes (2003) considering how the manufacturing process is capable of independently varying the pore size, density and window size allowing more porous structure optimisation than earlier methods.

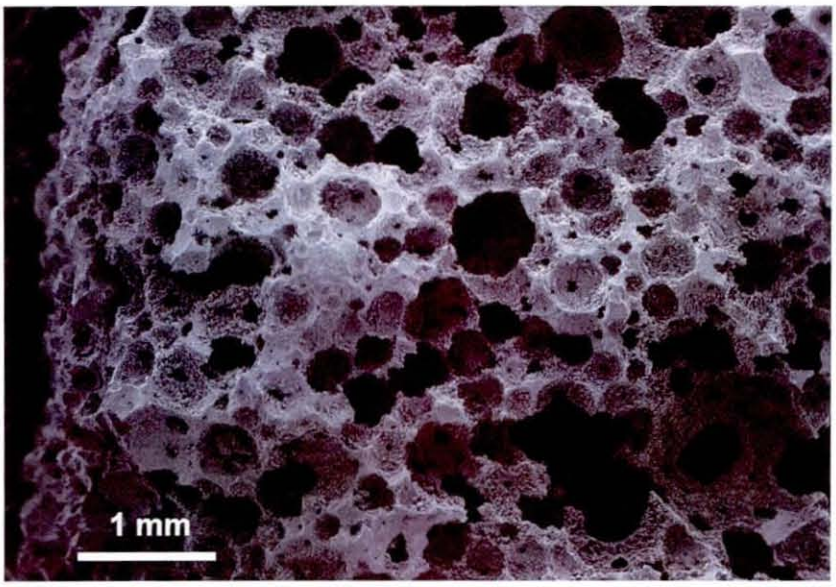

Figure 2.12. SEM image of a gelcast ceramic foam.

Table 2.1 compares typical properties of gelcast and reticulated ceramic foams. It can be seen that both types of foams can be made in a large range of pore sizes and porosity. The strength of gelcast ceramic foams can be seen to be typically notably higher than the reticulated foams, due to the solid struts.

Table 2.1. Comparison of the properties of reticulated (form made) ceramic foams and gelcast ceramic foams.

Property	Reticulated Foams	Gelcast Foams
Pore size	100-1920 μm	50-1150 μm
Open Porosity	64-97%	80-90%
Compressive Strength	1.3-4.44 MPa	2.1-11.2 MPa

Data summarised from: Barris *et al* (1987), Boretto *et al* (1999), Bykowski (1987), Ciambelli *et al* (2002), Gabathuler *et al* (1991), Helferich and Schenck (1989), Matsunuma *et al* (1996), Montanaro *et al* (1998), Sepulveda and Binner (1999)

The flexibility of manufacturing the foams with different pore structures makes the analysis of the current state of the art ceramic foam DPF technology more involved. To compare published data on the filtration efficiency of ceramic foams it is necessary to make some assumptions about the filtration trends. Loading within a depth bed filter follows an exponential relationship which can be explained by considering the filter as a series of comparable elements. This means that a unit length of filter medium will trap a given fraction of the particulates that flow through it. This allows the effect of changing the filtration length on filtration efficiency to be estimated mathematically as

$$\eta_L = 1-(1-\eta_l)^{\left(\frac{L}{l}\right)} \qquad (2.1)$$

where η_L is the estimated filtration efficiency, η_l is the known filtration efficiency, L is the filter length for which the estimate is required and l is the filtration length of the filter with a known filtration efficiency. This relationship does not account for any variation in filtration efficiency with flow rate or loading which are not as commonly published in the literature. Where it has been reported, this effect has been relatively small compared to the effect of varying the pore size (e.g. Pontikakis *et al*, 2001). Applying this equation to available published data provides the results shown in Figure 2.13. The filtration efficiency can be seen to reduce for larger pore sizes as the tortuosity of the flow path and sites for particulate capture are reduced in number.

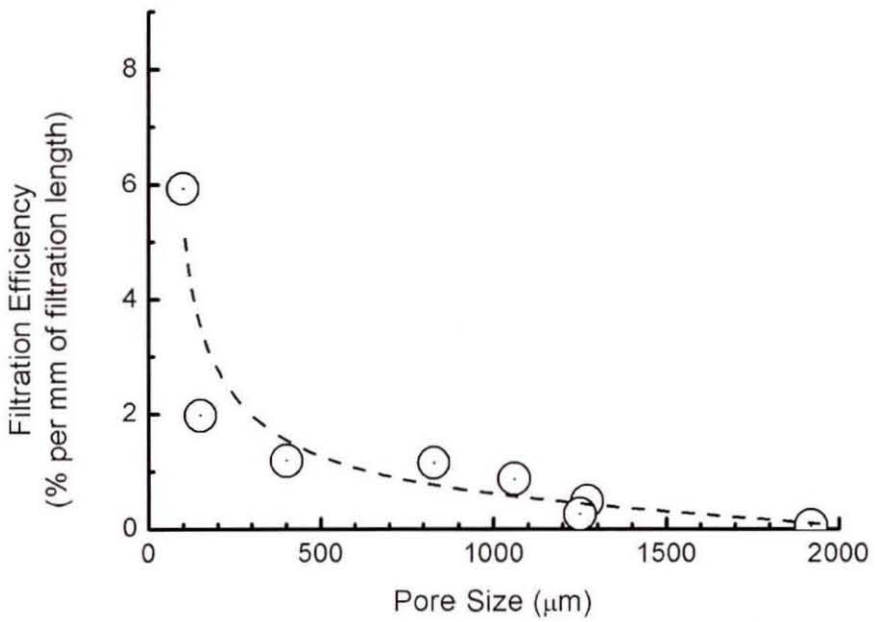

Figure 2.13. Plot of filtration efficiency per unit length as a function of pore size for reticulated ceramic foam published data. References used are: Ambrogio *et al* (2001), Barris *et al* (1987), Mizrah *et al* (1989), Shinozaki *et al* (1990), Tutko *et al* (1984), Watabe *et al* (1983), Xiaoguang *et al* (2001).

A similar analysis can be carried out to compare the back pressure from different publications. The assumptions required to analyse the data are:

1. The back pressure is a linear function of filtration length. This is true if the flow can be approximated as incompressible.

2. The back pressure can be approximated as a linear function of space velocity within the typical flow range. Test results published by Adigio (2005) show a linear fit with $R^2 \sim 0.75$. This allows a general comparison considering the low availability of detailed published data.

Mathematically, these assumptions can be written as

$$\Delta P \propto l \tag{2.2}$$

$$\Delta P \propto v \tag{2.3}$$

where ΔP is the back pressure, l is the filtration length and v is the space velocity. Converting the published data to give an estimate of the back pressure per unit length per unit space velocity gives the results shown in Figure 2.14. There are less data here as the majority of publications on ceramic foam technology lack the information on flow rate to generate these comparisons. As the pore size increases, the back pressure reduces since the obstruction the pores cause to the flow is significantly reduced.

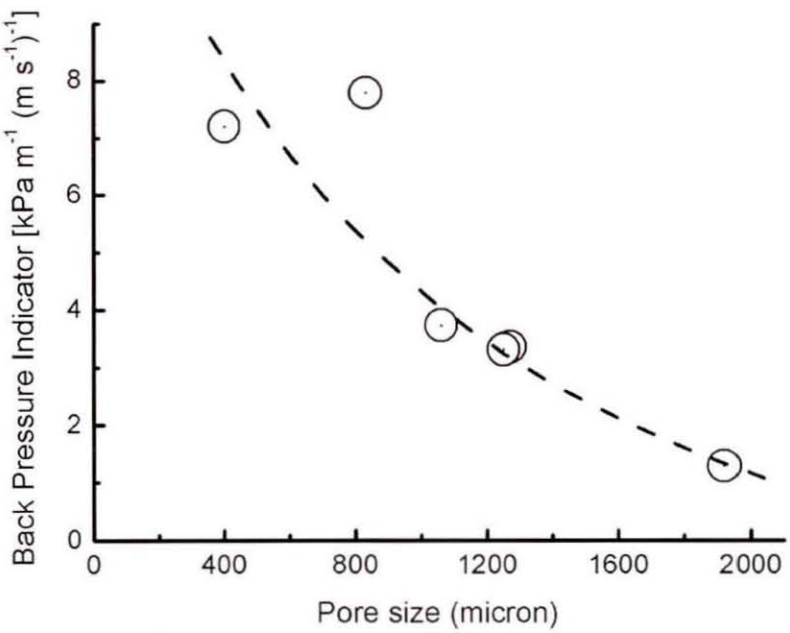

Figure 2.14. Plot of back pressure per unit length per unit space velocity for reticulated ceramic foam published data. References used are: Ciambelli *et al* (2002), Helferich and Schenck (1989), Shinozaki *et al* (1990), Watabe *et al* (1983).

The approximate fit lines for the data shown in Figure 2.13 and Figure 2.14 can be combined to produce a plot that allows evaluation of different ceramic foam filtration technologies. This is shown here in Figure 2.15. The performance of gelcast ceramic foams presented later can be compared to this analysis of published data to evaluate their performance relative to reticulated ceramic foams.

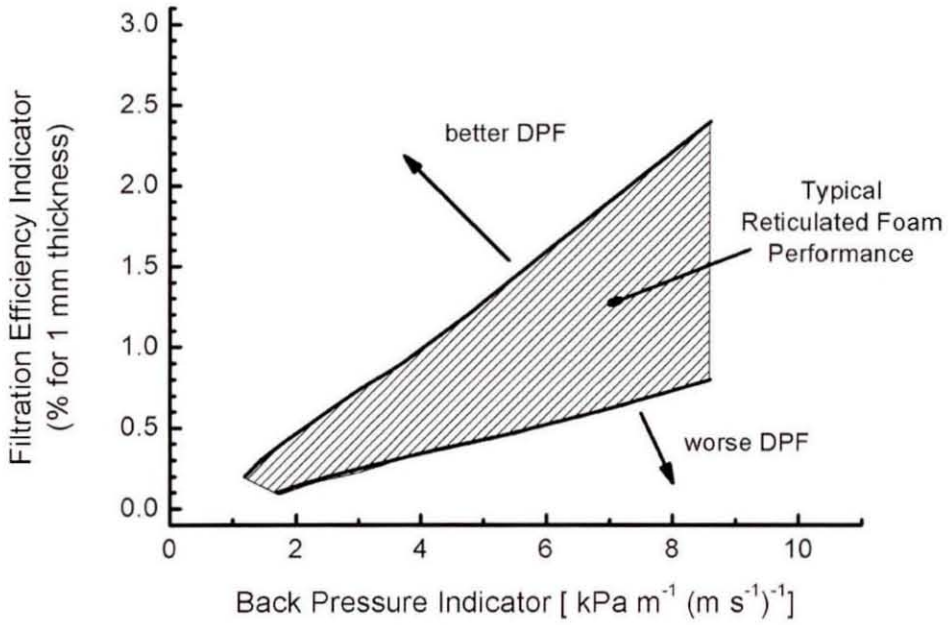

Figure 2.15. Filtration performance plot for reticulated ceramic foams based on available published data.

From the data presented by Hughes (2003) an example data point has been used to calculate a back pressure indicator and filtration efficiency indicator comparable to that used in Figure 2.15. This is shown with the data from Figure 2.15 in Figure 2.16. It can be seen that the gelcast foam properties led to improved filtration efficiency per unit length, with an associated increase in back pressure. The gelcast work of Hughes (2003) showed that the gelcast foam filtration efficiency/back pressure trade-off is comparable to the published data on reticulated ceramic foams.

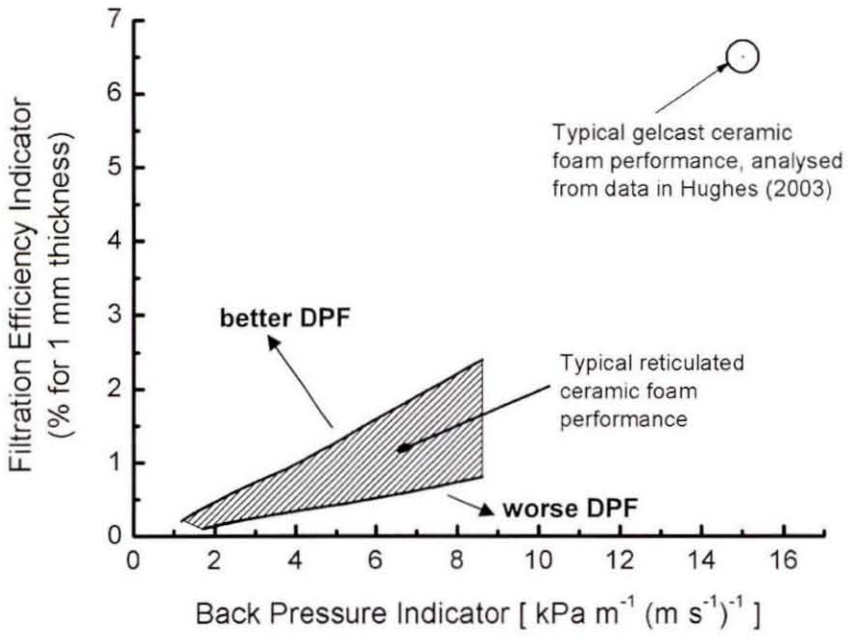

Figure 2.16. Comparison of Hughes (2003) gelcast foam filter performance with published literature on reticulated ceramic foams.

This review of ceramic foam technology has demonstrated that gelcast ceramic foams have significant advantages over reticulated ceramic foams when considering their strength, compactness and ability to independently vary factors such as window size, pore size and density. In comparison to WFF the filtration efficiency/back pressure trade-off is not as good but the filter durability and small impact of minor damage to ceramic foam filters makes them a suitable filter for many applications.

2.3.3 Fibrous Filters

Fibrous filters operate in a similar fashion to foam filters but are made in a different way. Bloom (1995) demonstrated fibrous filters that were formed by winding fibres around a perforated stainless steel tube. Filtration efficiencies of >90% were presented. Due to the flexibility of the fibres excellent thermal durability was achieved. Due to the nature of fibrous filters, high porosities are difficult to achieve. This results in either a high back pressure or large filter volume. In the data published by Bloom (1995) a 26 litre filter was tested on a 14.6 litre turbocharged engine. This compares poorly with the size of ceramic filters such as the WFFs and ceramic foams.

Studies by Xiao and Liu (1994) with significantly larger flow areas achieved with bag filters also demonstrated filtration efficiencies >90%. The regeneration of these filters was effective although required complex mechanical moving parts. Although not highlighted in the paper, the volume of such a filter system makes it unfeasible for mobile applications. A 104 litre filter canister was demonstrated on a 2.27 litre 37 kW engine.

2.3.4 Partial Filtration

Developments of partial filtration of the exhaust gas offer systems that will not clog in the event of excessive amounts of trapped PM. The filter, developed by Johnson Matthey, utilises a composite stamped foil and sintered metal fleece shown in Figure 2.17. A fraction of the flow is directed through the fleece material where the particulates are trapped. As the trapped particulate quantity increases, the fraction of gas filtered will decrease minimising the effect on the exhaust backpressure.

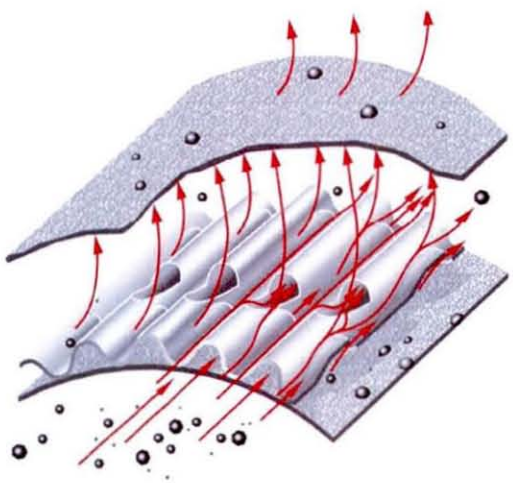

Figure 2.17. Diagram of the partial filter system developed by Johnson Matthey (Jacobs *et al*, 2006).

Tests by Jacobs *et al* (2006) on a Caterpillar 3126 engine demonstrated approximately 42% reductions in PM emissions as a direct result of adding a partial filter into the exhaust system. There is no data showing the effect on the engine back pressure making it difficult to fully evaluate this filtration technology.

2.3.5 Summary of Exhaust Filtration Strategies for PM Control

Filtration of diesel engine exhaust gas offers the advantage of reliable and repeatable filtration properties over a wide range of engine conditions with a high trapping

efficiency. This is at the expense of engine exhaust back pressure which acts to reduce the fuel conversion efficiency of the engine by increasing pumping losses.

One significant issue with all filtration systems is the need for filter cleaning (regeneration) to maintain acceptable exhaust back pressures. Without cleaning the filters the back pressure would continue to rise as the amount of trapped particulates increases. In many ways, effective, efficient and reliable regeneration of particulate filters has offered a greater challenge to engineers than the filtration itself. The following section therefore reviews the literature relating to filter cleaning strategies and highlights that there is a strong need for regeneration methods that are efficient, compact and effective.

2.4 Filter Regeneration Strategies

A large fraction of particulate matter is carbon based. This allows oxidation of particulate matter into carbon dioxide in an environment with high enough temperature and oxygen concentrations. Filter regeneration strategies can be classified into passive and active systems. Passive systems are those which continuously oxidise PM trapped on the filter under normal engine conditions. Active regeneration systems are those which periodically initiate a regeneration event during which a majority of the trapped PM is oxidised. As well as increasing the PM temperature, to promote oxidation, there are methods to reduce the temperature at which PM rapidly oxidises, typically using catalysts. The following text reviews the literature and current state of the art DPF regeneration methods.

2.4.1 Catalytically Assisted Regeneration

Catalysts act to increase reaction rates without changing the overall reaction, although they are usually involved in producing short lived intermediate species. Active catalysts do this by reducing the energy barrier needed for a reaction to occur, with species adsorbed onto the surface of the catalytic material (in the case of a solid catalyst). Solid catalysts have a direct influence on molecules within about 1 atomic distance from the solid surface (Twigg, 1989), giving a small volume of influence,

however, coupled with diffusion and convection can lead to significant improvements in reaction rates.

Tao *et al* (2003) demonstrated catalytic coatings on monolithic wall flow filters that promoted hydrocarbon and coluble organicfraction (SOF) oxidation, using the heat released from these reactions to initiate the main PM combustion. Regeneration of the filter was evident but required engine conditions giving exhaust temperatures above 400 °C, which is only over a small region of the engine operation. The catalyst on the filter also produced limited amounts of NO_2 from engine out NO which promoted low temperature oxidation of soot.

Gieshoff *et al* (2001) investigated a number of different oxidising catalysts to evaluate their effect and found promising reductions in soot ignition temperatures using vanadia based salts. A large contact region was achieved as the salts tested became molten at temperatures lower than the normal soot ignition temperatures. Ignition temperatures of diesel soot were reduced by approximately 100 °C, which would still require active means of regeneration. During soot oxidation the vanadia salts were observed to decompose, limiting the catalyst life in a real engine.

An alternative to solid or coated catalysts are fuel borne catalysts. Fuel borne catalysts consist of one or more metals (for example iron) which are chemically reacted with hydrocarbons to produce fuel soluble organo-metallic compounds. These are then added to the fuel before being injected into the cylinder. During combustion, the hydrocarbon portion of the organo-metallic compounds is burnt off leaving the metal based compound predominantly intact (e.g iron oxide). This then forms an integral part of the PM, resulting in the distinct advantage of an evenly dispersed catalyst regardless of how the soot is trapped. In comparison with catalyzed soot filters the catalyst contact region is significantly larger. The result of adding the catalyst is a reduction in the ignition temperature of the soot to approximately 400 °C from the uncatalyzed 550 °C. Issues and complexities of fuel dosing systems can discourage implementing such a system although 250,000 km tests (performed by Richards and Kalischewski, 2004) on heavy duty truck engines have shown some success.

To the author's knowledge, there are no diesel PM oxidation catalysts available that reduce the oxidation temperature of PM enough to allow passive regeneration under all engine conditions. This leads to some requirements on the user for speed and load cycles to achieve successful regeneration, that many manufacturers do not wish to impart on their customers. The catalyst coating, therefore, offers a means to reduce the energy requirement during regeneration but not a means of regeneration in itself.

2.4.2 Electrical Heating

The heat flux from the porous filters to the air flow through the filter under typical exhaust conditions is high enough that the trapped PM will be kept at a temperature close to the exit air temperature (e.g. Law, 2006). This means that with full exhaust flow through the filter during regeneration, enough energy must be input to the filter, PM and exhaust gas to raise them to typical regeneration temperatures of 550 °C (Heywood, 1988) for non-catalysed systems. A calculation of the energy requirement for a 300 kg h^{-1} gas flow at 250 °C shows that 26 kW of energy is needed. For a typical ~100 kW diesel engine this power demand is not feasible, therefore, electrical heating systems typically require the gas flow to be reduced (the filter bypassed). The electrical heater can be used to heat the PM to a temperature where the energy released from the PM is enough to sustain the regeneration event. The gas flow can then be controlled to manage the burning rate and filter temperatures.

Arai *et al* (1987) applied a 1.5 kW electrical heater regeneration system to a monolithic WFF on a 3.9 litre DI turbocharged engine. The arrangement is shown schematically in Figure 2.18. They stopped the air flow through the filter during the heating stage and once the front face of the filter was above the PM ignition temperature, the airflow was increased to begin self-sustained combustion of the PM. To minimise the electrical demand on the engine during the heating, the filter was bypassed and the PM ignition temperature reduced to between 350 and 450 °C by applying a catalyst coating. Similar systems using fuel borne catalysts instead of filter coatings have been investigated by Zikoridse *et al* (2000), relying on the catalyst to reduce the ignition temperature of the PM. Non-contact methods such as infrared heating have also been proposed (Xiaoguang *et al*, 2001) which used infrared radiation to couple thermal energy to the PM on the front face of the filter.

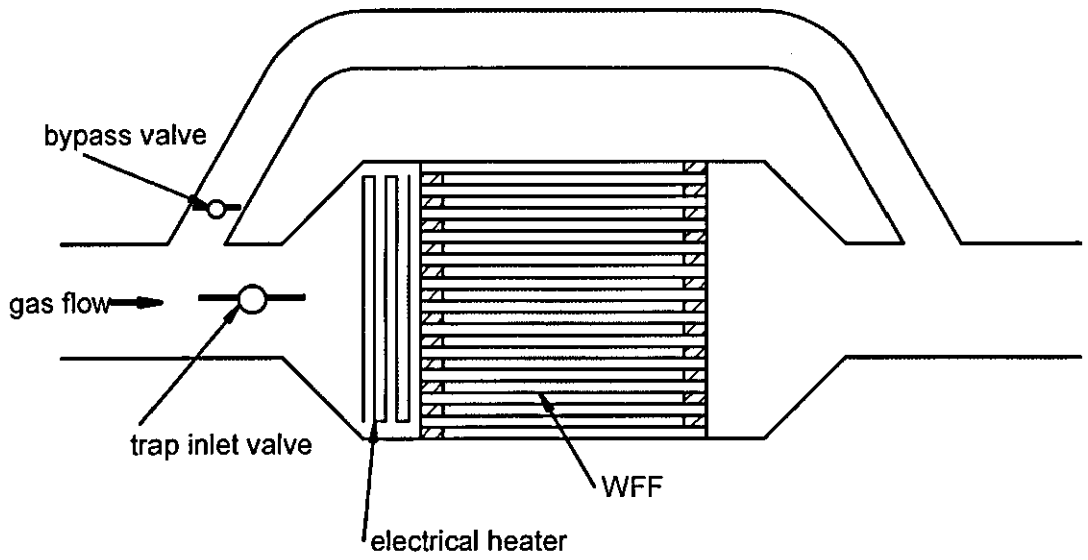

Figure 2.18. Schematic of a typical electrical heater regeneration system.

Further energy savings can be made by spot heating of the filter (heating localised regions) and relied further on self-sustained burning of the trapped PM. Zelenka *et al* (2001) fixed four 100 W spot heaters to the front face of a 5.66 inch diameter WFF, filter to initiate self-sustained combustion. For regeneration of a large volume of the filter, PM mass loadings of >10 g litre^{-1} were required. Such loadings would lead to excessive exhaust back pressure or large filter volume.

Typical electrical regeneration strategies successfully ignited the PM but often struggled to regenerate the entire filter volume. Self-sustained regeneration, such as electrical heating methods, are highly dependent on the amount of trapped PM, oxygen concentration and gas flow rate through the filter. Trapped PM rates are difficult to measure on-engine and with the dynamic nature of the engine operation, oxygen concentration and gas flow rates can be difficult to accurately control. Failed regeneration events therefore occur with only part of the filter being regenerated or with filter damage due to excessive temperatures or thermal gradients.

2.4.3 Microwave Heating

Microwave heating is known to preferentially heat up certain materials, including PM (e.g. Garner, 1989). This allows the direct application of energy to the PM within the filter volume, heating up the PM more evenly than electrical heaters. Early application of microwave regeneration of diesel particulate filters by Garner and Dent (1989) used a conventional magnetron to direct microwave radiation at the front face of a loaded particulate filter, heating the PM to self-ignition temperatures and controlled the gas flow using a bypass to manage the PM combustion process. Such a setup is shown schematically in Figure 2.19.

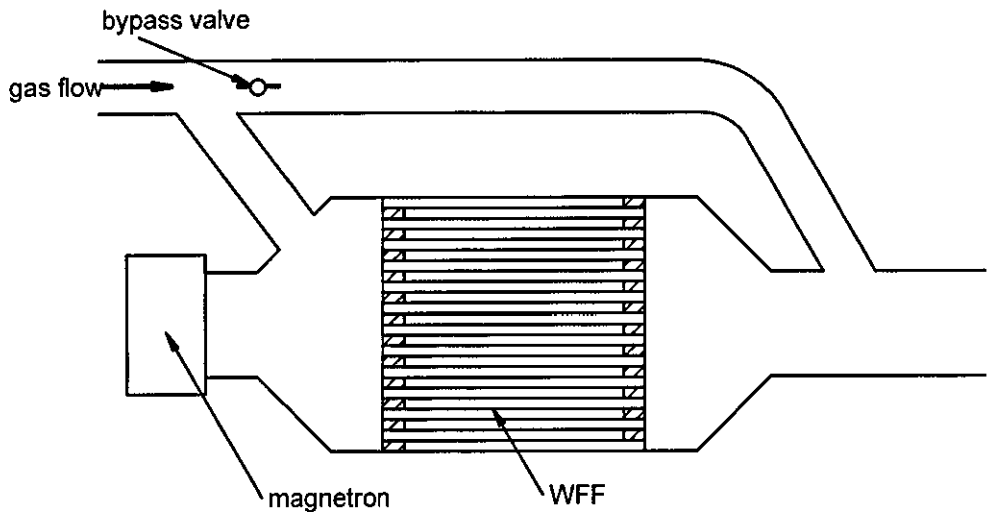

Figure 2.19. Schematic showing a typical microwave regeneration system.

Nixdorf *et al* (2001) made use of the microwave absorption of silicon carbide to increase the coupling of energy. They demonstrated heating of the filter to 800 °C in 3 minutes, but still relied on a bypass system for successful regeneration. The more even distribution of the energy was shown by Xiaoguang *et al* (2001) to cause difficulty in regenerating the front face of a ceramic foam DPF, attributed to the cooler temperatures of the gas flow during regeneration. Issues with failure to regenerate the periphery of the filter were observed by Palma *et al* (2002). The success of the regeneration was shown to be strongly dependent on the flow properties (e.g. Ning and He, 1999) in a similar way to the electrical heating methods

discussed earlier. Without tight control of the PM loading, uncontrolled regeneration and filter damage were observed by, for example, Gautam *et al* (1999).

Instantaneous energy input requirements for microwave systems are typically 1 to 3 kW with regeneration times and frequency typically estimated between 2 minutes every 6 hours (by Nixdorf *et al,* 2001) and 10 minutes every several hours (by Ning and He, 1999). The fuel consumption penalty will be small due to the low duty cycle however instantaneous power requirements can lead to issues with alternator size and capability. Further reduction of energy requirements can be achieved with the use of a catalyst (Ma *et al*, 1997) although the issue of bypassing and precious metal dependence remain.

2.4.4 Fuel Based Heating

It is clear that raising the temperature of the PM requires energy. With internal combustion engines the main energy store on the vehicle is the hydrocarbon fuel. Conversion of fuel to electrical energy with an alternator results in ~40% of the fuel energy being lost due to alternator inefficiencies (Robert Bosch GmbH, 2004). Burning of the fuel to generate the required heat, therefore, offers a potentially more efficient regeneration from a readily available energy source with high instantaneous power capabilities. The fuel is oxidised upstream of the filter to raise the air temperature to the required PM oxidation temperature. The air then heats up the filter and oxidises the PM.

Zelenka *et al* (2001) demonstrated trap regeneration with PM loadings as low as 2.5 g litre^{-1} with such a fuel burner system, as the heat is evenly distributed throughout the filter, and self sustained combustion is not a requirement. Running on a 3 litre diesel engine required (fuel) power inputs between 10 and 35 kW, much larger than that which can be achieved from on vehicle electrical supplies.

Issues with fuel burners include the quality of combustion and, in the event of a misfire, the unacceptable hydrocarbon emissions that would result. There is also a need for a secondary air supply to ensure the oxygen availability for fuel and PM oxidation. More energy is needed for heating using fuel burners as the air quantity that is heated is more than with bypassed systems although this can be improved by

partial bypassing of the filter during regeneration, demonstrated by Ludecke and Dimick (1983).

Ignition problems can be overcome by oxidising the fuel using an oxidation catalyst instead of burning the fuel. This is shown schematically in Figure 2.20. Late injection can increase the hydrocarbon content of the exhaust or, alternatively, a secondary injector can be used. Further air supplies are still required under certain engine conditions.

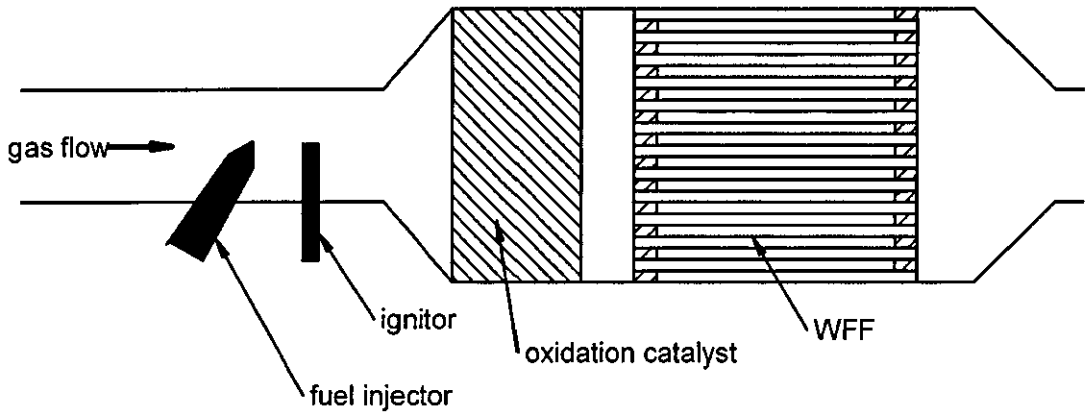

Figure 2.20. Schematic of an oxidation catalyst and fuel injection regeneration strategy.

Singh *et al* (2006) presented such a system that utilised an oxidation catalyst upstream of a catalysed diesel particulate filter. They successfully demonstrated regeneration of a loaded filter with upstream temperatures of ~300 °C. Hydrocarbon slip through the oxidation catalyst would make such a system unfeasible without further catalyst on the DPF. Potential issues with catalyst oxidation also occur at low temperatures when only a small amount of fuel oxidises as if flows through the catalyst leading to inefficient heating. This may lead to demands on the engine cycles that must be imposed on the consumer.

2.4.5 Other Regeneration Methods

Lakkireddy *et al* (2006) presented work that used an oxidation catalyst, in a configuration similar to Figure 2.20, to oxidise the engine out NO to NO_2. The NO_2 oxidised diesel PM between 250 and 380 °C, significantly lower than that for PM

oxidation with molecular oxygen (O_2). The presented regeneration system is limited in the range of working temperatures. At low temperatures the PM oxidation is slow and at temperatures of above 400 °C, the NO_2 formation is thermodynamically limited. In addition to a narrow operating window, the amount of NO_x required (~8 times the PM) may necessitate further NO_x controls downstream of the DPF.

The use of electrical plasmas or discharge systems has received increasing interest in a variety of forms including low temperature plasmas (close to room temperature) and non-thermal plasmas. A summary of typical features of such systems follows. Further discussion of plasma properties and definitions are in Chapter 5.

Okubo *et al* (2004)[a] presented the benefits of generating pulsed dielectric (low temperature) discharges in the exhaust flow to increase the quantity of PM oxidants, most notably NO_2 and applied it both directly and indirectly to the exhaust gas (Okubo *et al*, 2004[b]). The NO_2 promoted the oxidation of the PM while still, however, requiring appropriate exhaust temperatures which are not achieved over the entire engine operating range. Similar work by Levendis and Larsen (1999) considered the effect of other species such as Ozone (O_3) and found their effect to be small relative to NO_2 and potentially monatomic oxygen (O). A significant issue highlighted by Okubo *et al* (2004)[b] is the energy consumption associated with treating the exhaust gas, indicated ~12% fuel consumption penalty.

Studies by Yang (1981), Garner *et al* (2006) and Proctor (2006) have shown that the application of non-thermal plasmas to diesel PM leads to rapid PM oxidation. Yang (1981) considered oxidising PM within the gas flow, and determined that agglomeration is required for efficient PM oxidation with non-thermal plasmas. Application of non-thermal plasmas directly to DPFs was proposed by Garner and Harry (2003) who demonstrated the feasibility and potential low energy requirement of such a system. Further work by Proctor (2006) showed that stable, non-thermal plasmas can be used to automatically and selectively oxidise PM trapped on a cordierite wall flow filter while being insensitive to temperature, oxygen concentration and water concentration typical of diesel engine exhaust. The possibility of a regeneration system capable of working over the entire engine

operating range warranted further investigation and forms part of the research presented in this thesis.

2.5 Summary of PM Control Strategies

A selection of PM control strategies have been presented, highlighting the need for future diesel exhaust PM filtration. Filtration technology has been summarised and shows the need for regeneration (filter cleaning) methods to maintain acceptable exhaust pressure. Most of the regeneration strategies discussed require energy input to raise the exhaust temperature. This is manifested as a fuel consumption penalty and must be minimised to be competitive. Figure 2.21 shows data from a selection of published literature that has been summarised for the case of a 5 g h^{-1} average PM output with 300 kg h^{-1} flow rate. The data is presented in the form of the fuel energy which, in the case of electrical systems, is calculated based on 60% alternator efficiency. Most notably, bypassing the gas flow during regeneration has a significant effect on reducing the energy requirement of most systems due to the lower mass of air being heated. The exception is the work by Proctor (2006) which applied a non-thermal plasma to PM trapped on a wall flow diesel particulate filter. The ability to regenerate without bypassing is important since emission legislators are introducing 'not to exceed' (NTE) limits (Johnson, 2006). This means that at any test condition, the emissions from the engine should not exceed a legislated limit. The result is that any regeneration system requiring a bypass will need a dual filter system, with added cost, complexity and size.

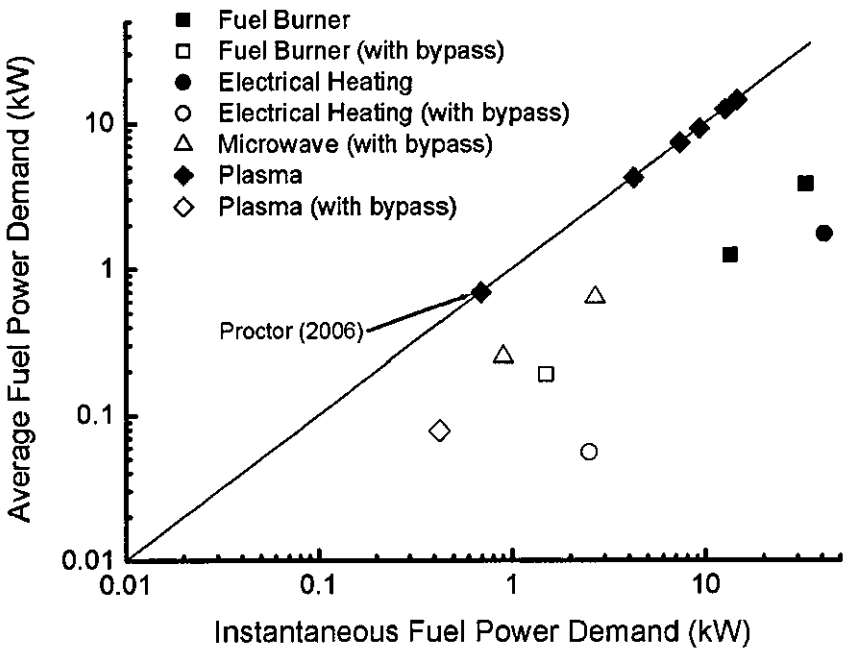

Figure 2.21. Comparison of published data on energy requirements of typical regeneration methods. Sources:- Arai et al (1987), Gautam et al (1999), Levendis and Larsen (1999), Ludecke and Dimick (1983), Matsui et al (2001), Okubo et al (2004), Palma et al (2002), Proctor (2006), Yang (1981), Yao et al (2004).

Table 2.2 compares the main regeneration strategies, highlighting their advantages and disadvantages. In summary:

1. Bypassing the airflow during regeneration leads to lower energy requirement, with the added size of a dual filtration system
2. Catalytic systems are limited in their working temperatures and, therefore, limited in the engine speeds and loads they are effective
3. Regeneration that relies on self-sustained oxidation of trapped PM is difficult to control and can often result in incomplete regeneration or filter damage.

Table 2.2. Summary of the main advantages and disadvantages of typical DPF regeneration strategies.

Regeneration Strategy	Advantages	Disadvantages
Catalyst	No moving parts No energy requirement	Limited working temperature Precious metal dependence
Electrical heating without bypass	No moving parts Additional air requirement	High energy requirement Difficult to control
Electrical heating with bypass	Low energy consumption Additional air requirement	Moving parts Difficult to control
Microwave heating with bypass	Low energy consumption Additional air requirement	Moving parts Difficult to control
Fuel burners without bypass	No moving parts Compact Additional air requirement	High energy requirement Robustness
Fuel burners with bypass	Low energy consumption Additional air requirement	Moving parts Robustness
Catalytic fuel oxidation	No moving parts Compact Additional air requirement	High energy requirement Limited working temperature Precious metal dependence
Dielectric barrier discharges	No moving parts	High energy requirement Limited working temperature
Non-thermal stable plasmas	No moving parts Low energy consumption Effective over all speeds/loads	

2.6 Concluding Remarks

This chapter has reviewed the current literature discussing current state of the art filtration and DPF regeneration strategies for the reduction of diesel engine PM emissions. It has shown that the potential of a regeneration system based on non-thermal stable plasmas developed by Garner and Harry (2003), Garner *et al* (2006) and Proctor (2006), combined with the robustness and configurability of gelcast ceramic foam diesel particulate filters offers a promising technological solution for a complete and effective diesel particulate filtration system.

The remainder of this thesis presents the original research carried out in developing the Autoselective electric discharge regeneration of gelcast ceramic foam DPF system. Chapter 3 introduces the experimental methodology used throughout the following chapters before Chapter 4 discusses the development and optimisation of gelcast ceramic foam DPFs.

CHAPTER 3

DESIGN OF EQUIPMENT AND MEASUREMENT PROCEDURES

Throughout the work presented in this thesis there were numerous experimental methods used. A number of techniques and considerations that were applicable to the work throughout the subsequent chapters are presented in this chapter. Techniques relevant to specific parts of the thesis are discussed in the appropriate chapters. Methodology used throughout the thesis includes:

1. improved methods for characterising the gelcast ceramic foams
2. methods for evaluating the regeneration system performance
3. an introduction to the experimental rig used for prototype testing
4. an introduction to the on-engine test setup

3.1 Characterising Gelcast Ceramic Foams

The spherical nature of the pores of gelcast ceramic foams has been shown in Chapter 2. Where neighbouring spherical pores overlap, open windows are formed that allow gas to flow through the porous structure. There have been a number of descriptions of gelcast ceramic foams including face centred cubic lattices (Peng *et al*, 2000) with 12 windows for each pore and multiple orifice flow models based on two windows per pore (Adigio, 2005). The scanning electron microscopy (SEM) image of a loaded gelcast ceramic foam in Figure 3.1 shows that there is a more random nature to the pore size distribution than considered in these models.

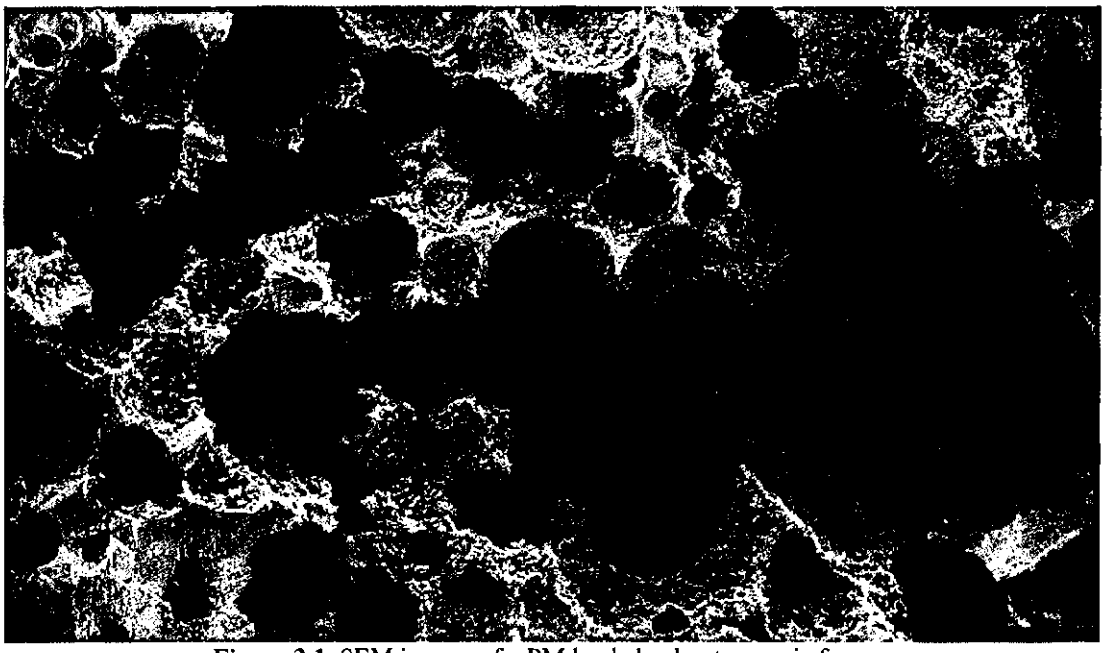

Figure 3.1. SEM images of a PM loaded gelcast ceramic foam.

Individual pores are often characterised by their window size and pore diameter. The window size is defined as the diameter of the openings between the cells, and the pore size is defined as the diameter of the spherical shape of the pore. This is illustrated in Figure 3.2 for an ideal spherical pore with six windows. These descriptors, along with knowledge of the porosity of the ceramic foam can give an indication of how the foam will behave with respect to gas flow through the pores, and its bulk mechanical behaviour. The open porosity (defined as the ratio of the interconnected volume to the overall volume) of gelcast ceramic foams is typically close to the overall porosity (defined as the ratio of open volume to overall volume). When this is not the case, the open porosity is used most appropriately for flow

discussions while the overall porosity is most appropriate for discussions of mechanical strength.

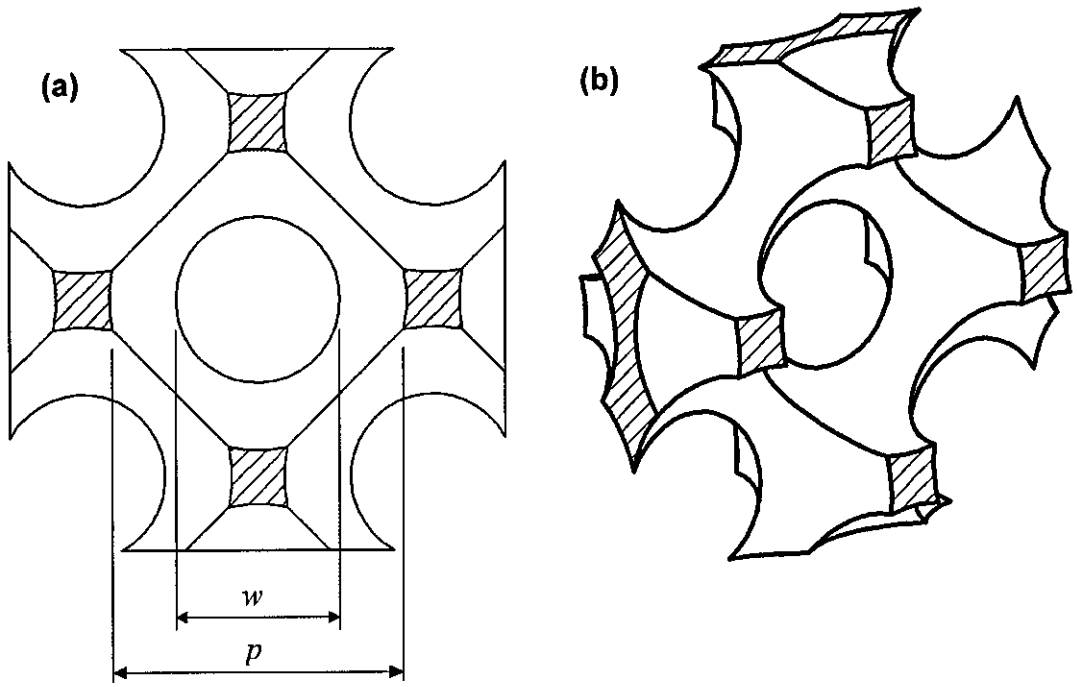

Figure 3.2. (a) Cross section of the ideal pore showing the pore diameter (p) and window size (w). (b) Pictorial representation of the ideal pore.

Due to the random nature of the foams it is necessary to take a large number of measurements of pore size and window size to find suitable averages. The large spread of pore size is demonstrated by measurements taken on a reconstructed micro-CT (computed tomography) scan of a sample of gelcast ceramic foam that was supplied by Dytech Corporation as a 400-500 μm pore diameter foam. This data is shown as a histogram in Figure 3.3 from a CT scan using a Skyscan 1172 system.

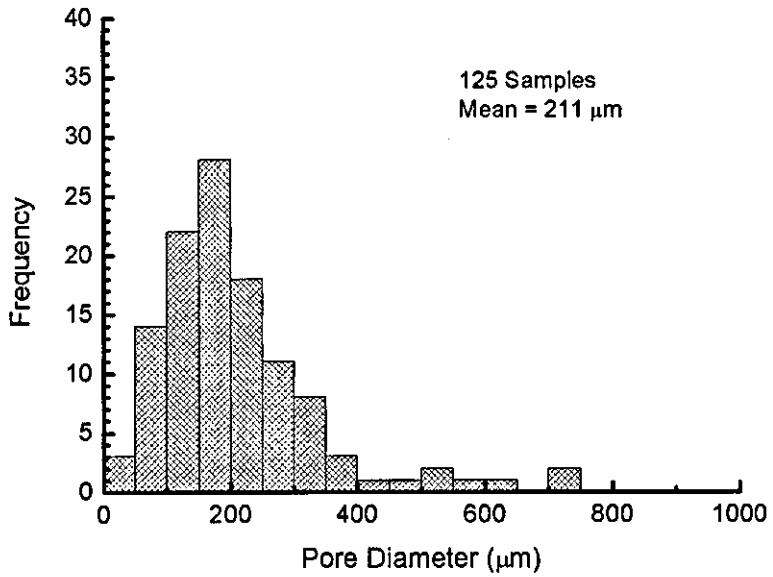

Figure 3.3. Histogram of the range of pore diameters measured from a reconstructed micro-CT scan of a sample of gelcast ceramic foam.

To allow an accurate description of the foam samples used in this project it was necessary to define a suitable methodology for estimating rapidly the average pore size. Pore diameters can be measured from images of filter cross sections using various forms of microscopy, or in three dimensions from CT scanning data. The cost and time involved in collecting CT scan data was not suitable for day to day measurements where up to 20 or 30 samples need to be measured, since reconstruction of a single series of images takes a number of hours. For this work, optical microscopy using a Nikon SMZ-2T microscope and JVC colour digital camera was used to measure visible diameters of filter cross sections.

Measurements of the visible pore diameter from a two dimensional (2D) cross section of the same sample that was used for the CT scanning data in Figure 3.3 is shown in the form of a histogram in Figure 3.4. A comparison of Figures 3.3 and 3.4 showing data from the same sample indicates that measuring the average visible diameter from a two dimensional cross section leads to an underestimate of the actual average pore diameter. This can be explained by considering the effect of a randomly placed cutting plane on the visible diameter of a single pore. Figure 3.5 shows three example cutting planes on an ideal pore of the same form as Figure 3.2 and demonstrate how they affect the visible diameter. It is clear that the further the cutting plane is from the centre of the pore, the smaller the visible diameter is relative to the actual pore diameter. By assuming that the cutting plane position is

random it is possible to correct the mean measured visible pore diameter to give an estimate of the actual mean pore diameter. The determination of the value of this correction factor follows.

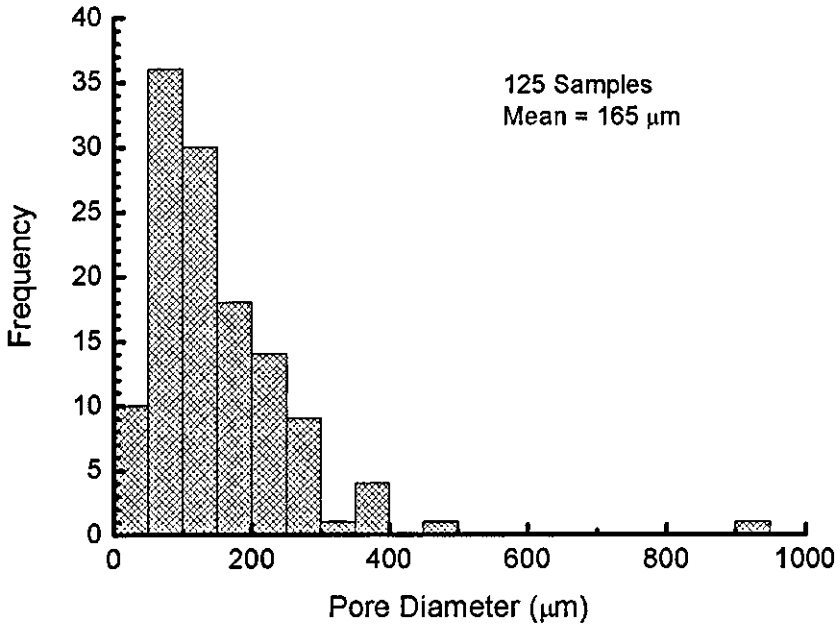

Figure 3.4. Histogram of the average visible pore diameter measured from a two dimensional cross section of a sample gelcast ceramic foam.

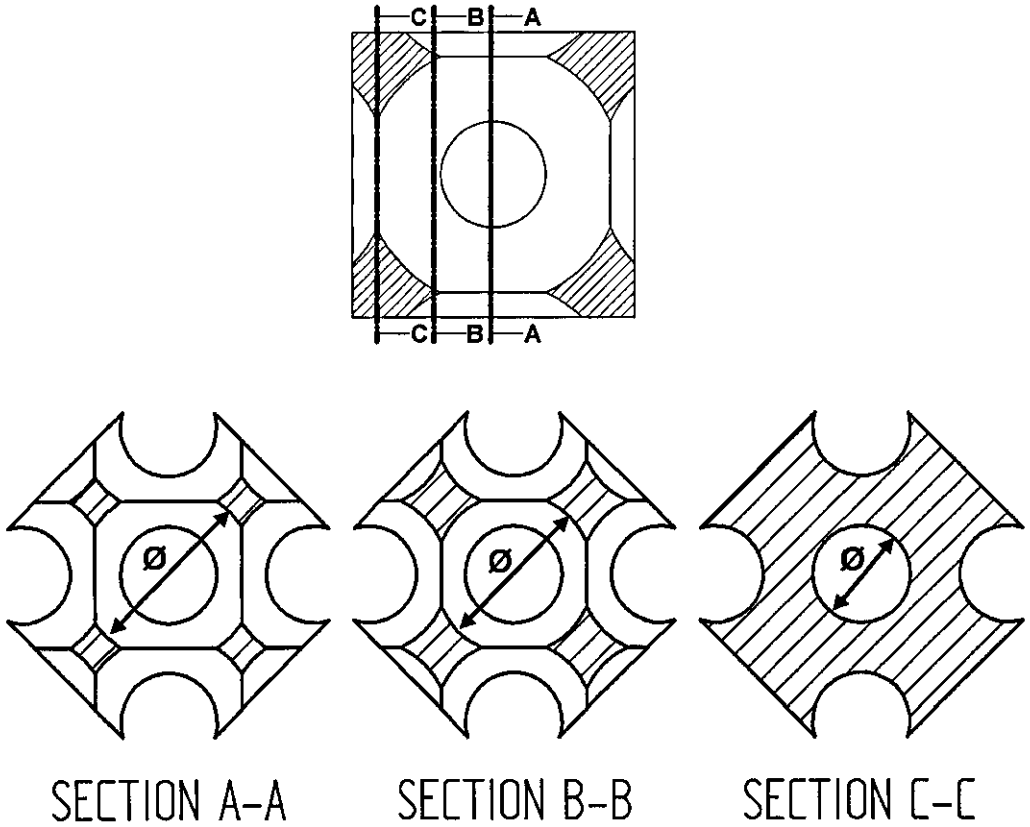

Figure 3.5. Schematic showing the effect of the randomly placed cutting plane on the measured visible pore diameter.

To carry out the analysis, the geometry was simplified and considered as a single spherical pore. This can be represented graphically in two dimensions as shown in Figure 3.6. The cutting plane in this image is considered to be vertical (i.e. constant x). If the cutting plane is located at a random value of x there is an equal probability that it will be at any given value of x. Therefore, the probability of measuring a given radius can be calculated.

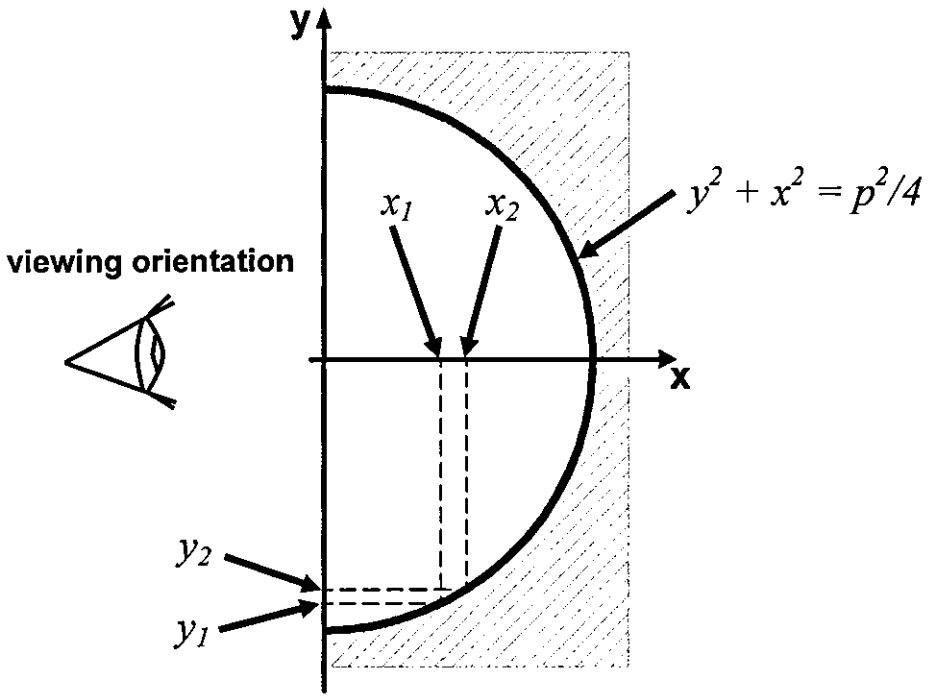

Figure 3.6. Graphical representation of the model of the random cutting plane for understanding the effect of the cutting plane position on the measurement of pore diameter.

The probability of the cutting plane lying between the coordinates x_1 and x_2 is defined as

$$P(x_1 < x < x_2) = \frac{2(x_2 - x_1)}{p} \qquad (3.1)$$

where p is the actual pore diameter and x, x_1 and x_2 have the same meanings as in Figure 3.6. Since the relationship between x and y is known from the geometry of the pore, the probability of the visible radius being between y_2 and y_1 is the same as the probability of the cutting plane lying between x_1 and x_2. This gives

$$P(y_2 < y < y_1) = \frac{2\left[\left(\frac{p^2}{4} - y_2^{\,2}\right)^{0.5} - \left(\frac{p^2}{4} - y_1^{\,2}\right)^{0.5}\right]}{p} \qquad (3.2)$$

The average visible pore size can be found by finding the probability for constant size intervals of y between 0 and $p/2$. This was converted into a probability distribution as shown in Figure 3.7. As the interval size is reduced the validity of this approximation increases. The ratio of the average measured pore size to the actual pore size can be found from

$$\frac{p_{measured}}{p} = \frac{\sum_{i=1}^{(n-1)}\left[P(y_{i+1} < y < y_i)\left(\frac{y_i + y_{i+1}}{2}\right)\right]}{p} \qquad (3.3)$$

where n is the number of discreet intervals. The effect of interval size on the average measured pore diameter relative to the actual pore diameter is shown in Table 3.1. This demonstrates that as the interval size reduces, the mean visible pore diameter tends towards 79% (2 s.f.) of the actual pore diameter.

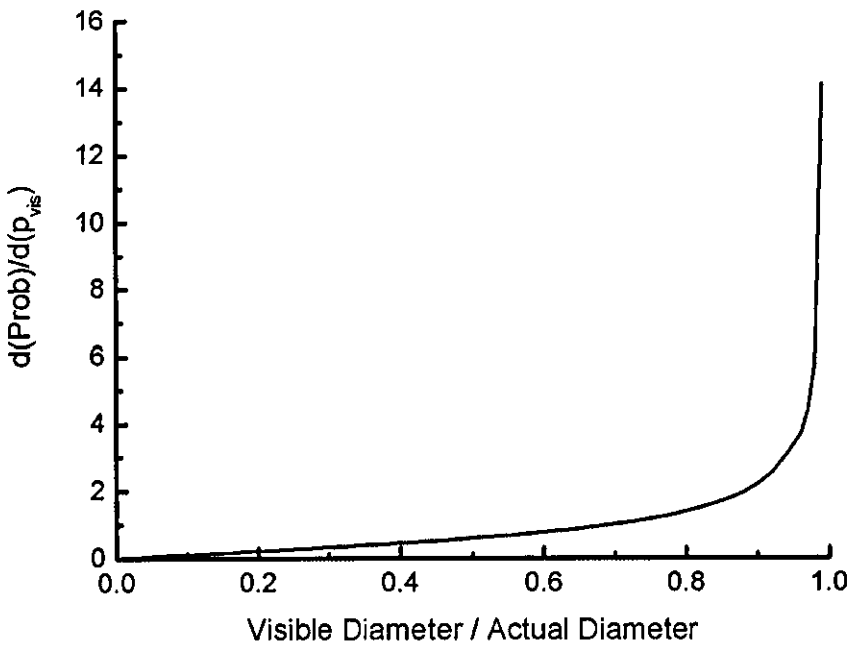

Figure 3.7. Probability distribution of measuring a given pore diameter.

Table 3.1. Effect of interval size on the calculation of the correction factor for the measured pore size.

Interval Size	Mean Measured Diameter/Actual Diameter
p/10	0.759
p/20	0.776
p/40	0.782
p/100	0.785
p/1000	0.785

If this result is used to correct the mean from Figure 3.4, the corrected diameter (208 μm) is very close to the measurement of 211 μm taken from the 3 dimensional (3D) reconstructed image. This shows that the visible mean pore diameter can be corrected to give an approximation of the actual pore diameter by dividing it by a factor of 0.79.

When considering previous work (e.g. Hughes, 2003) where no correction was made to visible pore diameter, the actual pore size will be larger than quoted. This therefore offers a methodology that can be used for future research involving measurements of gelcast (or similar) porous structures.

3.2 Methods for Evaluating Regeneration Performance

When developing an integrated filtration and regeneration system for diesel engine exhaust aftertreatment the system must be evaluated. Methods for evaluating regeneration performance are:

1. Regeneration Rate

   The aim of a regeneration system is to remove PM from the DPF to maintain acceptable exhaust flow back pressures. The regeneration system, therefore, needs to be capable of regenerating the proposed filter at a rate at least equal to the average engine PM production rate and preferably at the maximum engine production rate to prevent risk of filter clogging. Details of the typical magnitude of the PM output from an example engine will be given later in Section 3.4. The regeneration rate needs to be measured in a repeatable and reliable way in order to evaluate the system performance. A summary of the advantages and

disadvantages of the available techniques for measuring the regeneration rate are discussed later in this chapter.

2. Regeneration Effectiveness

The power supplied to a regeneration system is derived from the fuel on board a vehicle and has a direct impact on engine fuel economy and CO_2 emissions. Regeneration effectiveness considers the energy consumption required and is defined as the amount of PM burnt off per unit electrical energy input to the regeneration system, given by

$$E_R = \frac{R}{W} \tag{3.5}$$

where E_R is the regeneration effectiveness (g kW^{-1} h^{-1}), R is the regeneration rate (g h^{-1}) and W is the electrical power used (kW).

The following sub-sections describe the range of techniques that are available for measuring regeneration rate and power consumption, leading to calculation of regeneration effectiveness.

3.2.1 Pre- and Post-Filter Weighing

Using analytical balances, the change of weight over a short period of time can be measured by weighing the sample before and after a known regeneration period. This will give an average regeneration rate during that test period. Factors that can lead to errors in the regeneration rate measurement using this method include:

1. weighing scale errors
2. handling effects
3. environmental conditions
4. damage during filter mounting and dismounting
5. filter temperature.

Each of these error sources need to be considered to identify how much they affect the measured mass, and as a result, the measured regeneration rate.

Weighing Scale and Handling Errors

The general handling and measurement errors were evaluated using a KERN ARJ 220-4NM (0-220 g +/- 0.2 mg) analytical balance by repetitive weighing of a single sample, removing the sample from the balance enclosure prior to each weighing. This therefore includes errors originating from balance repeatability, positioning of the sample on the balance and sample contamination during handling.

Figure 3.8 shows a histogram of 300 measurements of a ceramic filter sample that was typical of those used during this work. The weight of the ceramic filter sample was found to approximate a normal distribution with a 95% confidence interval of 1.6 mg.

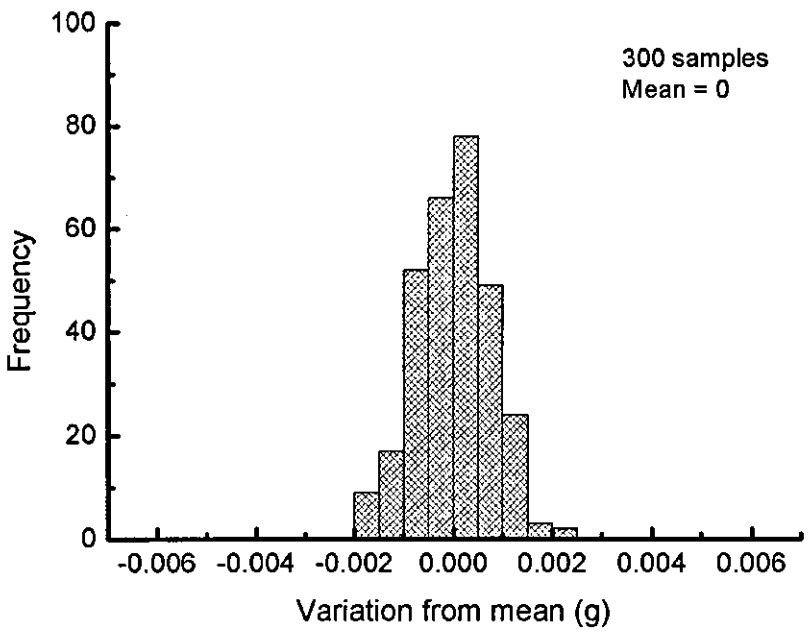

Figure 3.8. Histogram showing results of repetitive weighing of a ceramic filter sample.

Environmental Conditions

To determine the environmental effects on the weighing of PM and filter samples, clean and loaded ceramic foam DPF samples were stored in a desiccator for a period of one month prior to being weighed. Supporting research work carried out by R. Bull (2006) showed that for typical PM used for this work, the water and volatile component of the PM was ~5% of the PM mass. This means that oven preparation of the samples is not essential.

Figure 3.9 shows the weight of the samples after being removed from the dessicator. It can be seen that both the ceramic foam DPF and the trapped PM are insensitive to the desiccation and exposure to atmospheric conditions on a short timescale. This means that environmental effects will not affect the weight measurements of samples that have been stored in a controlled humidity environment.

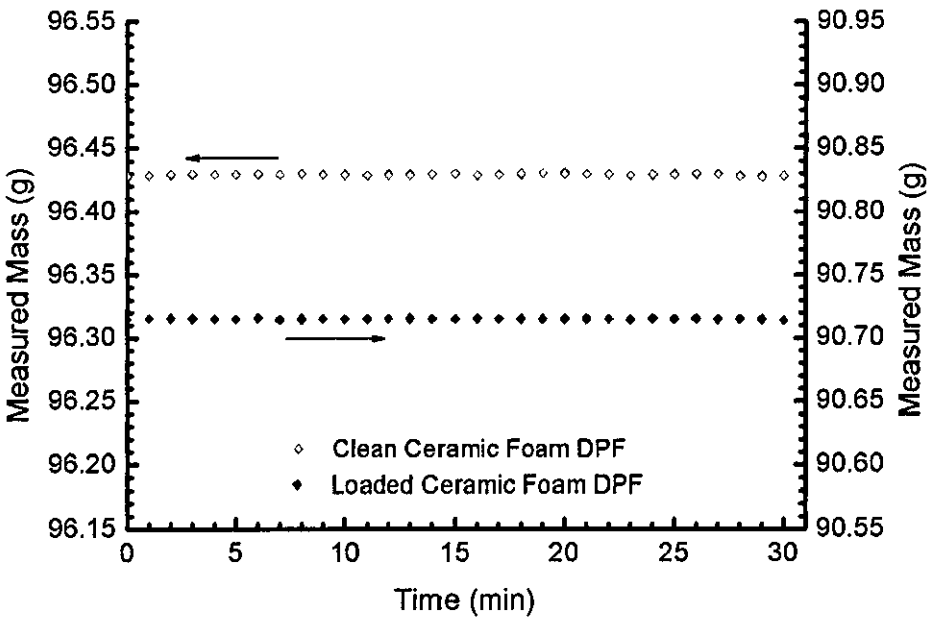

Figure 3.9. Transient mass measurements of clean and loaded ceramic foam DPFs.

Mounting and Dismounting Effects

Errors originating from mounting and dismounting the filter in the rig can be caused by filter damage or material addition (for example gasket material adhering to the filter). To evaluate these errors, 9 ceramic filters were pre-weighed, mounted and dismounted in the rig and then post-weighed to identify any trends. The measurements are shown in Table 3.2. Samples 1 to 4 are control samples that were not mounted on the rig.

Table 3.2. Effect of mounting and dismounting of filters on filter mass.

Ceramic Filter Number	Pre mounting mass (g)	Post mounting mass (g)	Difference (mg)
1	98.3164	98.3178	1.2
2	89.1488	89.1446	-4.2
3	89.9729	89.9734	0.5
4	91.1317	91.1299	-1.8
5	101.1436	101.1413	-2.3
6	92.3303	92.3276	-2.7
7	93.9422	93.9400	-2.2
8	92.6382	92.6386	0.3
9	102.8650	102.8604	-4.6

The mean variations were compared statistically using a T-test and, within a 95% confidence interval, there was found to be no effect of mounting and dismounting.

Filter Temperature

Variations in temperature of the ceramic foam sample were observed during this research, to affect the mass reading from an analytical balance. An error of >0.1 g was observed when measuring PM loadings of 0.2 g. To explain this temperature dependence it is necessary to consider the open pore ceramic foam as a porous structure for which gas flow through the pores is restricted enough that the gas heats up (or cools down) relative to the ambient temperature, depending on the temperature of the ceramic. If the structure is openly porous the time taken for the pressure to equalize when the gas is heated or cooled is negligible, resulting in the air within the foam being less dense than the surrounding air, in the case of a hot filter. The less dense air is buoyant in the ambient air and acts to reduce the mass reading observed on the analytical balance.

There are two possible methods for overcoming this problem:

1. Allow the sample to cool to ambient temperatures before taking any mass measurements. Experience has shown that this can take up to several hours, which limits the amount of testing that can be completed in any given time.

2. Develop a mathematical relationship that allows the correction of the mass measurement for temperature variations assuming ambient and filter temperatures are known.

The latter approach was developed and adopted here to enable significantly higher data rates and good knowledge of potential errors. Applying the ideal gas law to the gas within the ceramic foam allows the mass, m, of air in a known volume to be calculated from

$$m = \frac{PV}{R_{air}T} \tag{3.6}$$

where P is atmospheric pressure, V is the volume of air, R_{air} is the gas constant for air and T is the absolute temperature of the air.

Applying this to the reference temperature and actual temperature cases respectively, and noting that the pressure and volume in each case can be considered to be equal, Equation 3.7 can be derived. This allows the prediction of the error in mass measurement reading from analytical scales resulting from non-ambient filter temperatures.

$$m_r - m_a = \Delta m = \frac{PV}{R_{air}}\left(\frac{1}{T_r} - \frac{1}{T_a}\right) = \frac{\varepsilon P V_f}{R_{air}}\left(\frac{1}{T_r} - \frac{1}{T_a}\right) \tag{3.7}$$

where ε is the porosity of the ceramic foam, V_f is the filter volume, T_r is the reference temperature (normally ambient) and T_a is the actual filter temperature. This relationship does not account for temperature variations throughout the ceramic or the flow of the gas through the ceramic.

To validate this relationship, sample filters were heated up to a known temperature (measured with a 0.5 mm diameter K-type thermocouple) and weighed using analytical balances with a resolution of 0.01 g. Each filter sample was tested three times across a range of temperatures.

The results are shown in Figure 3.10 and Figure 3.11 along with a predicted variation based on Equation 3.7. The relationship shows good agreement with experimental data. The level of agreement shows that such a relationship could be used in future testing to correct for buoyancy errors in mass measurement resulting from ceramic temperature variations, the temperature is known. This saved a significant amount of testing time during parts of this research and is of longer term value.

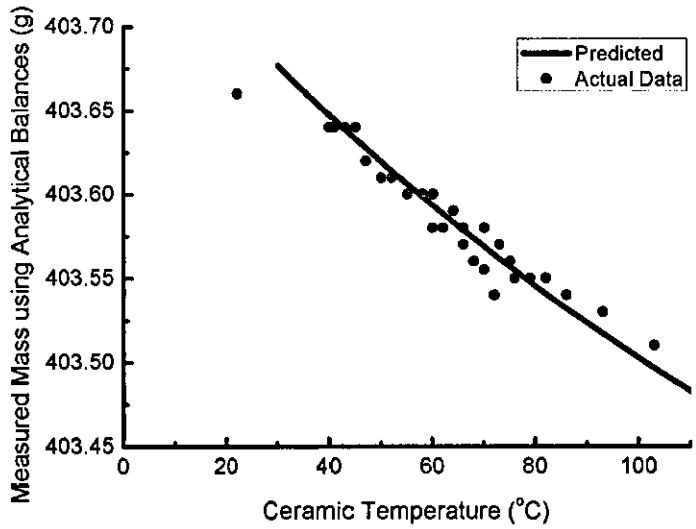

Figure 3.10. Variation in analytical balance reading resulting from changes in filter substrate temperature. 143 x 50 mm sample, 80% porous.

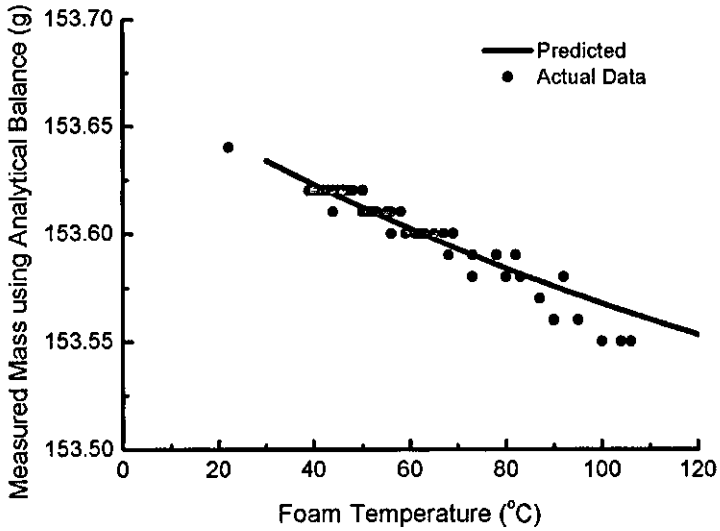

Figure 3.11. Variation in analytical balance reading resulting from changes in filter substrate temperature. 143 x 20 mm sample, 80% porous.

Summary

To summarise and complete the mass measurement methodology, the following guidelines were followed during the testing presented in this thesis:

1. Samples were handled with tweezers or disposable gloves (as guidelines in EPA Testing Procedure §86.1312-2007, 2006).
2. Where the filter temperature is non-ambient, corrections for temperature effects were made using Equation 3.7.

It has been shown that mounting effects are negligible and that using the previously described methods, variations in mass of 10 mg could be confidently measured (based on the results from the mounting effect tests).

3.2.2 Visual Observations

Visual observations of filter surfaces are a simple and effective qualitative method to evaluate regeneration performance. The more common DPF materials such as cordierite, aluminium titanate and alumina are pale in colour which means that as the PM loading increases the filter surface becomes darker. An example of this is shown in Figure 3.12 showing scanned filter surfaces of different PM mass loading. This is a qualitative evaluation but is useful as a simple method to compare different tests and was, therefore, used throughout this work to support analysis and conclusions.

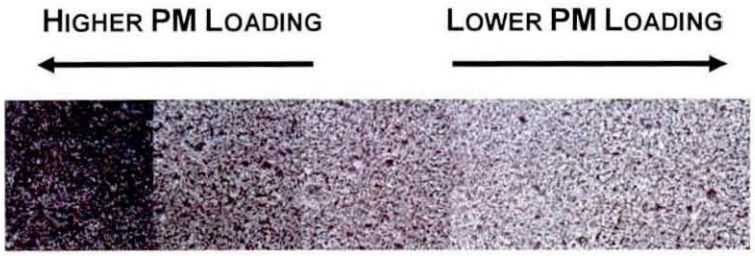

Figure 3.12. Scanned images of filters of varying loading.

3.2.3 Back Pressure Measurements

As the amount of PM trapped on a DPF increases, the flow pressure drop across the DPF increases. Increasing back pressure in the exhaust system leads to increases in pumping losses which, in turn, results in loss of power output and fuel efficiency of the engine. To maintain acceptable exhaust flow back pressure the PM must be continuously or periodically removed from the filter. Measuring the pressure drop across a DPF is the most appropriate method for evaluating regeneration systems on-

engine and can be carried out using readily available equipment such as digital manometers.

The pressure drop cannot easily be related to regeneration rate but supplements other performance measures to understand phenomena relating to the regeneration system.

3.2.4 Power Consumption

Power measurements between the electrodes of the Autoselective regeneration system are made difficult by the presence of high voltages. The electric potential was measured using a high voltage 1000:1 ratio probe (Tektronix P6015) and the current was measured using a 1:1 ratio current probe (Pearson 2877) on the grounded side of the transformer. This type of current probe cannot be used effectively on the high voltage (HV) side of the transformer since the electric field becomes concentrated within the probe volume leading to corona discharges which can affect the Autoselective discharge. The voltage and current probe can then be monitored using an oscilloscope.

Figure 3.13 shows a typical high voltage current and voltage trace. This case is for a predominantly capacitive current but the technique for measuring the power consumption is applicable to any waveform.

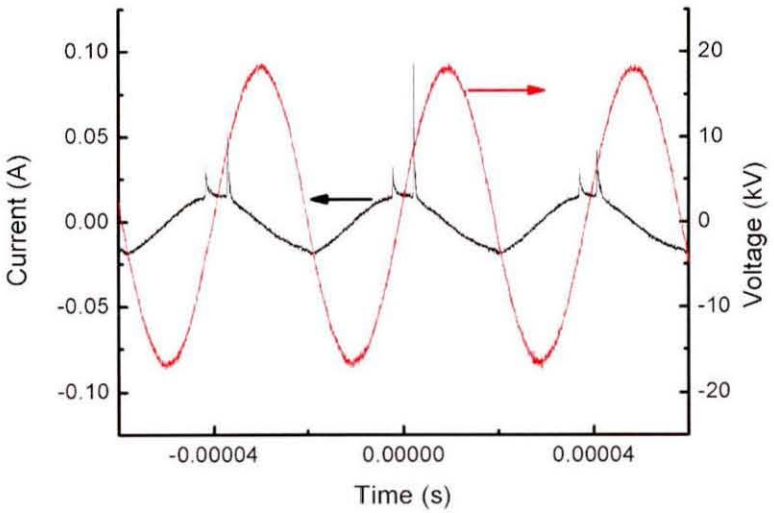

Figure 3.13. Example high voltage capacitive voltage and current waveform.

At any given time the instantaneous power being dissipated between two points in a circuit can be calculated as

$$W_{el} = IV_{el} \tag{3.9}$$

where W_{el} is the instantaneous electrical power, I is the instantaneous current and V_{el} is the instantaneous voltage. The resulting calculation based on the data in Figure 3.13 is shown in Figure 3.14. It can be seen in this case that some energy is cycling backwards and forwards through the electrodes.

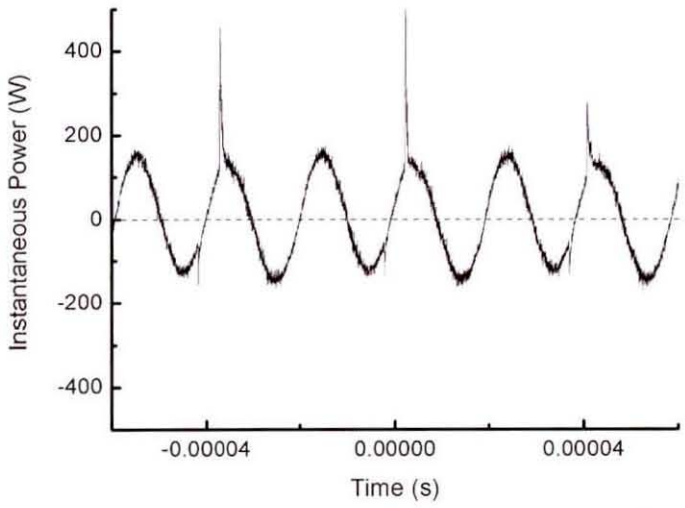

Figure 3.14. Plot of calculated instantaneous power.

The calculation of average power dissipated between the electrodes is then

$$\overline{W_{el}} = \frac{1}{nT_{el}} \int^{(t+nT_{el})} IV_{el}\,dt \tag{3.10}$$

where T_{el} is the time period of the signal and n is an integer describing the number of cycles the average is taken over. Integrating with a non integer value of n gives misleading results as the cycling energy will not be adequately considered.

3.3 Controlled Hot Flow Rig (HFR) Test Methods

A large part of the initial development work on the Autoselective system by Proctor (2006) used a purpose built hot flow rig (HFR) that was capable of generating a hot gas flow to simulate a diesel engine exhaust in a controlled manner. This concept formed the basis of the new rig development for the investigation of ceramic foam properties that allows reliable, repeatable and controlled conditions for prototype testing. The use of ceramic foams introduced a number of additional requirements relating to the adaptability, temperature and pressure capability of the HFR.

The design requirements relating to the second generation hot flow rig are discussed before highlighting the important details and key features of the design.

3.3.1 Hot Flow Rig Design

The most important requirements of the hot flow rig for this work were:

1. Visual Access When investigating electrical discharges a lot of information could be obtained by observing the light emitted from the discharge. It is therefore essential to have visual access to the electrodes and filter surfaces wherever possible.
2. Mass Flow Rate Peak flow rates in diesel engine exhausts that are appropriately sized for 5.66 inch diameter wall flow filters are typically 150 kg h^{-1} (based on data presented by Corning, 2006). With high pressure centrifugal blower systems the peak flow rate that can be achieved is a function of back pressure. The back pressure is a combination of the pressure drop across the filter and the pressure drop across the pipework and heater (initially estimated at around 15 kPa). To allow investigation with higher flow rates, the centrifugal blower on the hot flow rig should be capable of achieving flow rates of 225 kg h^{-1} (150% of the required flow rate) with back pressures in excess of approximately 30 kPa (the sum of the pipework and typical maximum filter back pressure).
3. Gas Temperature Although exhaust temperatures of diesel engines are commonly below temperatures needed for the PM to oxidise without external stimuli, they can operate with exhaust gas temperatures up to ~550 °C. The hot flow rig should, therefore, be capable of generating exhaust gas temperatures between ambient temperatures and ~550 °C.

4. Gas Addition Diesel engine exhaust gas contains higher levels of carbon dioxide (CO_2) and water (H_2O) and lower levels of oxygen (O_2) than the ambient environment. The hot flow rig should be capable of simulating these conditions.
5. Adaptability The ceramic foam DPFs can be produced in a configurable geometry and size. The rig should be capable of investigating a range of filter geometries and easily adaptable should an unusual geometry filter need testing.
6. Electrical Feedthrough The behaviour of the Autoselective system can vary depending on the side (upstream or downstream) of the filter the electrodes are placed. The hot flow rig should, therefore, be capable of achieving a high voltage electrical feedthrough without compromising the flow rate through the filter.

Any such rig should also consider:

7. Measurements Flow rate, back pressure and temperature are essential measurements during the majority of testing with the hot flow rig.
8. Mobility If the rig is self contained and mobile it can be more easily transported and located for a specific series of tests.
9. Safety Any non-essential metallic parts need to be grounded to reduce the risk of electric shocks from high voltage equipment.

Figure 3.15 shows the key components of the HFR. A high pressure centrifugal blower was used to generate the required mass flow rate. A series of valves were used to control the flow rate while minimising the pressure on the blower outlet. This maintained the blower outlet air temperature closer to ambient conditions. The air flowed through an electrical air heater that raised the air temperature. The power input to the heater was 100% PWM modulated to control the temperature. The hot air flowed into the test chamber section of the rig where gas species such as water or nitrogen could be added prior to flowing through the filter and regeneration system. The net result was a hot gas flow potentially with reduced oxygen and high humidity representative of a diesel engine exhaust gas flow.

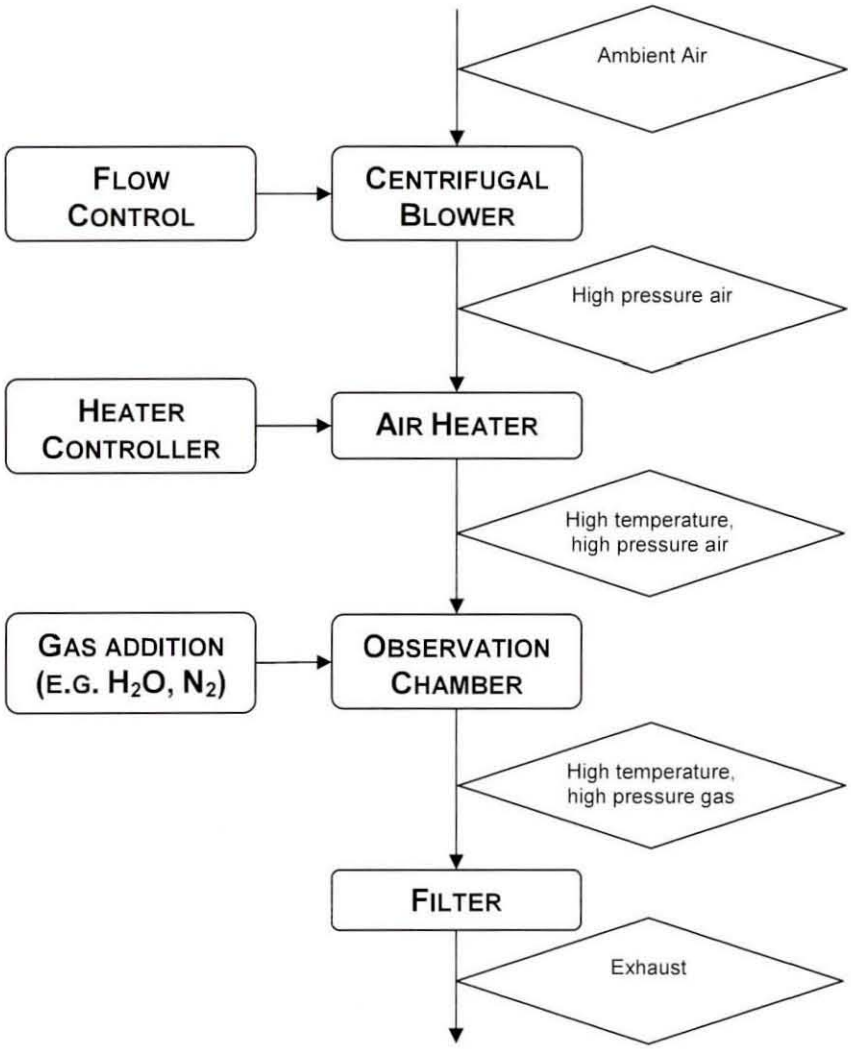

Figure 3.15. Flow chart showing the key parts of the hot flow rig.

It was estimated initially that the pressure at the outlet of the blower would be ~30 kPa with a peak flowrate of 225 kg h^{-1} when using the ceramic foam filters. This is higher than the pressure drop across the filter alone due to the additional losses through the pipework and heater. The maximum flow rate and back pressure test point is shown as a circle in Figure 3.16 (b). The lines plotted on Figure 3.16 (b) are the flowrate performance characteristics of a series of centrifugal blowers of the type shown in Figure 3.16 (a) of varying power and size. It can be seen that the 7.5 kW blower is the only one of the three shown that can achieve the target flow rate and is therefore the one chosen as part of the hot flow rig.

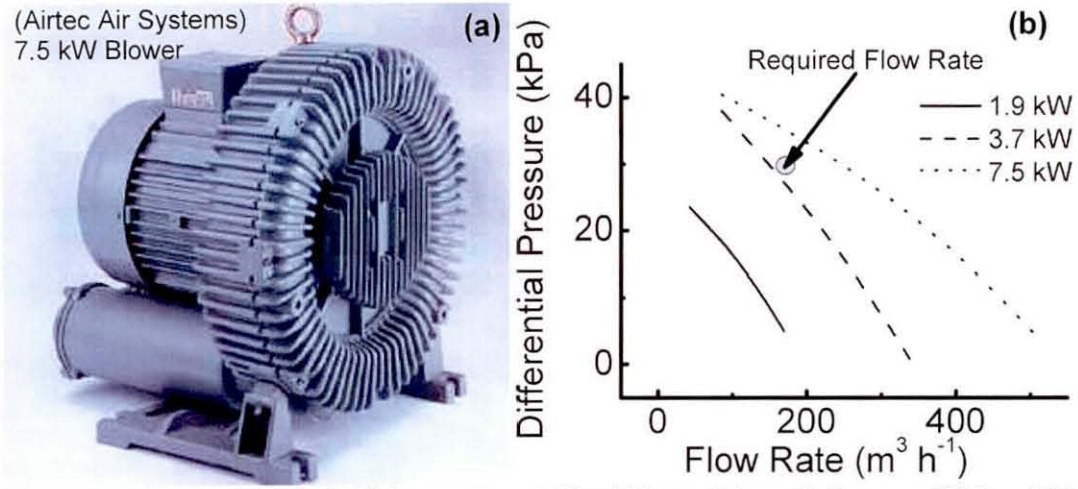

Figure 3.16. (a) Photograph of a high pressure centrifugal blower (Airtec Air Systems, 2001) and (b) plot of flow rate as a function of differential pressure for different size blowers.

A similar analysis was performed for a range of air process heaters as shown in Figure 3.17 (a). The curves in Figure 3.17 (b) show the peak temperature as a function of flow rate that can be achieved with different size air process heaters from Osram Sylvania. The hatched region is the specified operating region required to simulate a diesel engine exhaust. The 36 kW heater can achieve temperatures corresponding to the majority of the required test area, missing only the maximum temperatures at the highest flow rate. If required, this test condition could be simulated by reducing the area of the filter to reduce the flow rate through the heater, therefore the 36 kW heater was chosen.

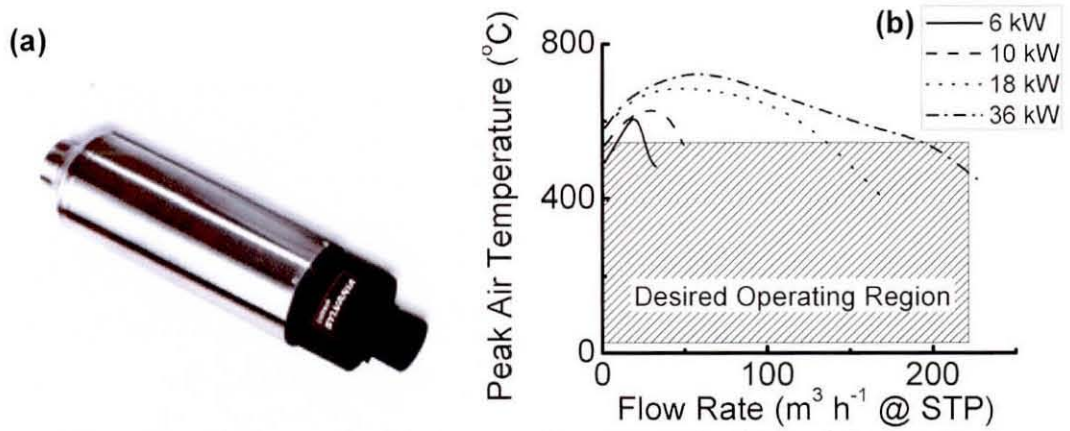

Figure 3.17. (a) Photograph of the air heater (Osram Sylvania, 2001) and (b) plot of peak temperatures as a function of flow rate.

The control of the flow temperature was achieved using feedback control to modulate the input power to the heating elements. The feedback control unit was designed and assembled in-house.

Figure 3.18 shows an exploded view of the observation chamber and modular enclosure. The individual parts that form the rig are listed in Table 3.3. The observation chamber was based around a cubic frame with a series of panels that could be fitted to any side of the cubic shape. There were three different length filter holders (25 mm, 50 mm and 100 mm) that could be combined together to make 7 different length cylindrical filter holders. Visual access was provided with a fused silica window mounted in one of the side panels. The electrical feed through was achieved with a Macor plate fitted to one of the side panels. Macor is a high temperature electrically insulating ceramic that has the advantage of being machineable, therefore allowing complex geometries to be manufactured. The inlet and outlet conical sections had fittings matching the filter holder to increase the flexibility of configurations. This modular design allowed the rig to be assembled with or without the window, electrical feed through or observation chamber.

Sealing of the joins was achieved using a 1 mm Supergraf™ graphite based gasket material that could be cut to any shape and withstand operating temperatures of 500 ^{o}C (James Walker, 1997).

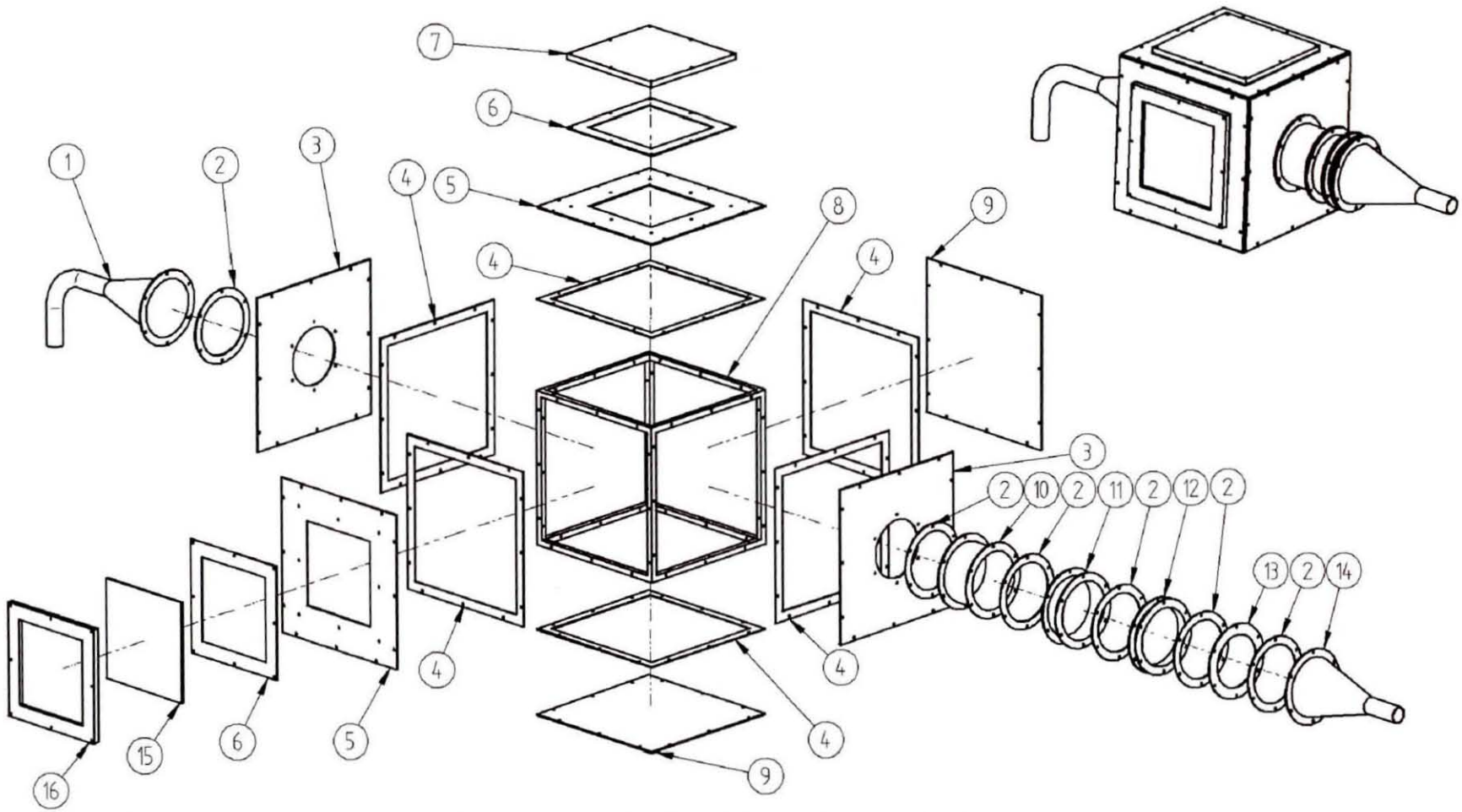

Figure 3.18. Exploded view of the modular structure of the observation chamber assembly. The numbers refer to components listed in Table 3.2

Table 3.3. List of modular enclosure parts shown in Figure 3.18

Part Number	Description	Quantity
1	Heater Outlet/Observation Chamber Inlet	1
2	Circular Gasket	6
3	Coverplate (Circular Hole)	2
4	Coverplate Gasket	6
5	Coverplate (Square Hole)	2
6	Square Gasket	2
7	Macor Feedthrough Plate	1
8	Observation Chamber Frame	1
9	Coverplate (Plain)	2
10	Filter Holder (Large)	1
11	Filter Holder (Medium)	1
12	Filter Holder (Small)	1
13	Retaining Plate	1
14	Observation Chamber Outlet	1
15	Window	1
16	Window Frame	1

The observation chamber was surrounded by an interlocked polycarbonate enclosure that cut off the electrical supply to any high voltage equipment within the enclosure if the door was opened. During high temperature tests the polycarbonate was protected from the heat of the metal parts using glass fibre insulation matting wrapped around the heater outlet and laid across the upper panel of the observation chamber. The rig was assembled on a purpose built castor mounted steel table that included an empty shelf for equipment used during testing. The assembled hot flow rig is shown in Figure 3.19. The rig was set up in this photograph for low to mid temperature tests so the glass fibre matting insulation was not present.

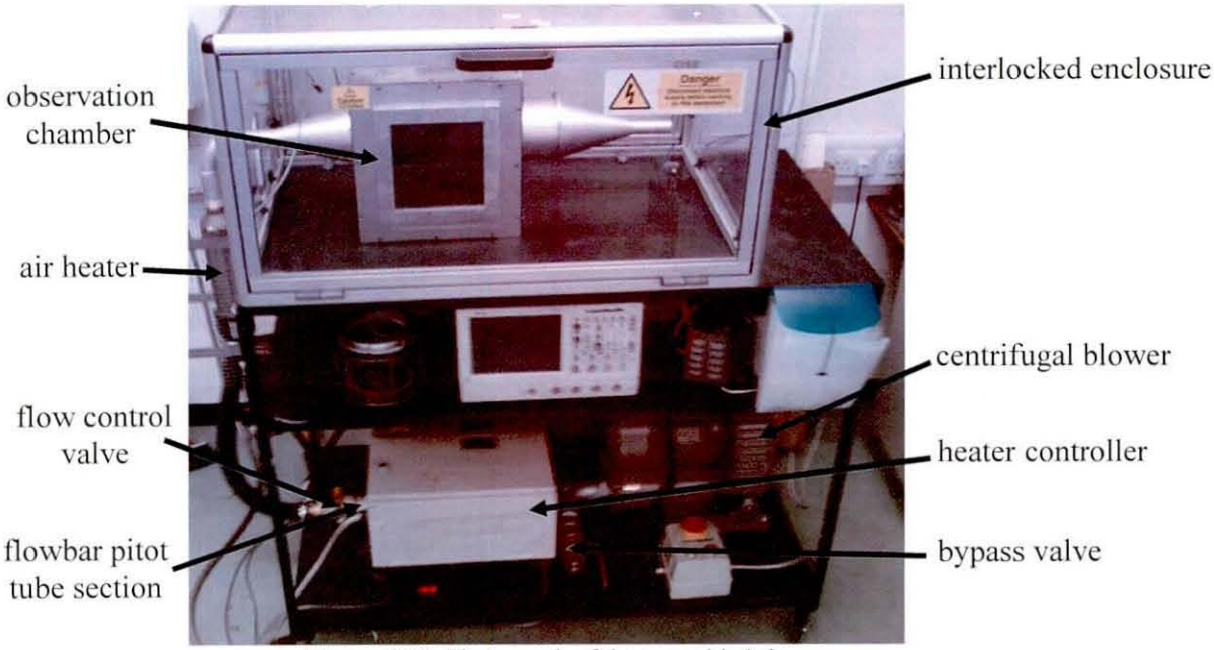

Figure 3.19. Photograph of the assembled rig

Post commissioning tests evaluated the performance of the rig in comparison to the design specifications. The blower performance and heater performance were found to match the manufacturer's specifications shown in Figure 3.16 and 3.17 respectively. Figure 3.20 shows the pressure drop across the pipe work which was the main unknown quantity. The back pressure of the pipe work and heater was in line with early estimations. The sum of this pressure drop and the pressure drop across the filter was the pressure differential the blower experienced and hence determined the maximum possible flow rate which was found to be adequete.

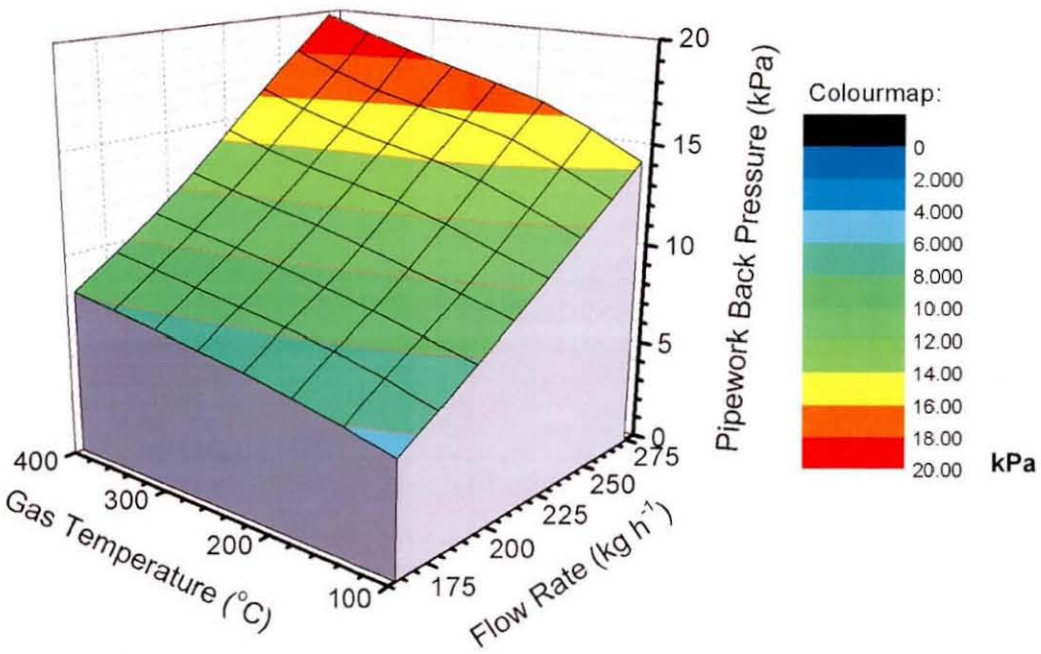

Figure 3.20. Contour plot of pressure drop through the pipe work and heater as a function of flow rate and temperature.

3.3.2 Measurements with the Hot Flow Rig

Measurements required during rig testing include gas flow rate, temperature and pressure. The flow rate was measured using a calibrated in-line pitot "Flo-bar" pipe section (manufactured by RM&C, UK) that used a digital manometer with 1 Pa resolution to measure the dynamic pressure. The flow rate was then calculated from

$$\dot{m} = C\sqrt{\frac{P\Delta P}{T}} \qquad (3.11)$$

where $\dot{m}$ is the mass flow rate (kg s^{-1}), C is a constant that is a function of the gas constant and pitot tube calibration, P is the absolute pressure (Pa), ΔP is the dynamic pressure (Pa) and T is the gas temperature (K). For the measurement setup used in this testing the calibrated constant, supplied by the manufacturer, C = 0.0001252 (s^2 $K^{0.5}$ m^{-1}).

Locations of temperature and pressure measurements in the modular enclosure are shown in Figure 3.21. T1 is a fast response K-type thermocouple that formed part of

the feedback control for the heater. It was located close to the heater outlet to minimise thermal delay between variations in temperature and control action from the heater controller. T2 and T3 were mineral insulated semi-flexible k-type thermocouples that measure the filter inlet air temperature. The relevance of measurement locations depended on the setup of the modular enclosure. P1 and P2 were pressure tappings that were connected to a U-tube digital manometer to measure the pressure drop across the filter. Without the conical section P2 was considered to be ambient pressure.

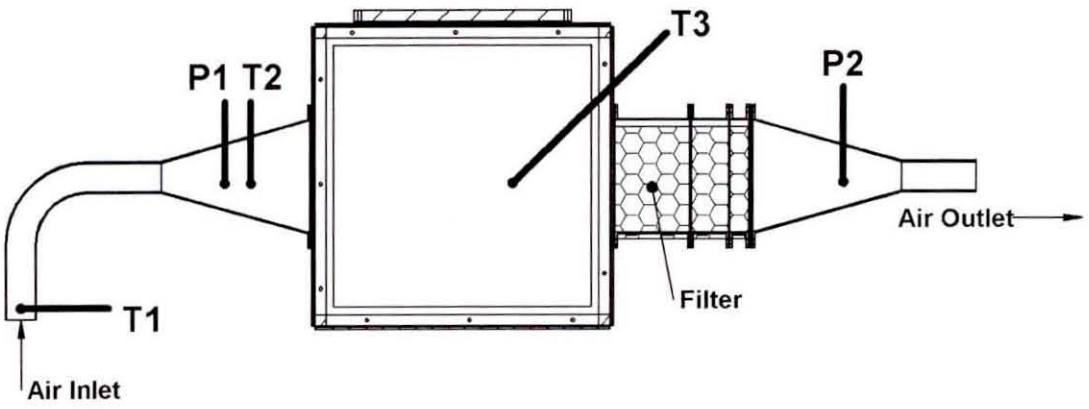

Figure 3.21. Schematic cross section of the rig showing the location of key measurements.

3.3.3 Pre-Loading of Test Filters

Testing on a rig required pre-loading of a DPF on an engine before mounting in the rig. PM composition and density are known to change as a function of engine condition and, therefore, to achieve typical PM properties it was necessary to evaluate and understand the effects of engine use. Typical engine cycle data from a Caterpillar C7 engine were supplied by Caterpillar Inc for a concrete mixer, fuel hauler, garbage truck and line hauler. To protect confidentiality, these are not presented in this thesis. The cycle data was used together with available literature to determine suitable steady-state loading conditions for pre-loading of DPFs and are discussed in the following text.

The first factor that was considered was the PM density. The mass fractal dimension of PM is a term that describes the effective density of the PM produced from diesel engines. It was defined by Schmidt-Ott (1988) as

$$\rho_e \propto d_b^{\,d_r-3} \tag{3.12}$$

where ρ_e is the effective density of the PM, d_b is the mobility diameter of the particles and d_r is the fractal dimension. d_r can take values between 1 and 3. A value for d_r of 1 represents a simple chain of nuclei mode particles. A value for d_r of 3 represents a solid, compact particle. Figure 3.22 shows results, presented by Virtanen *et al* (2004), that show how the fractal dimension was affected by engine load for a range of diesel engines.

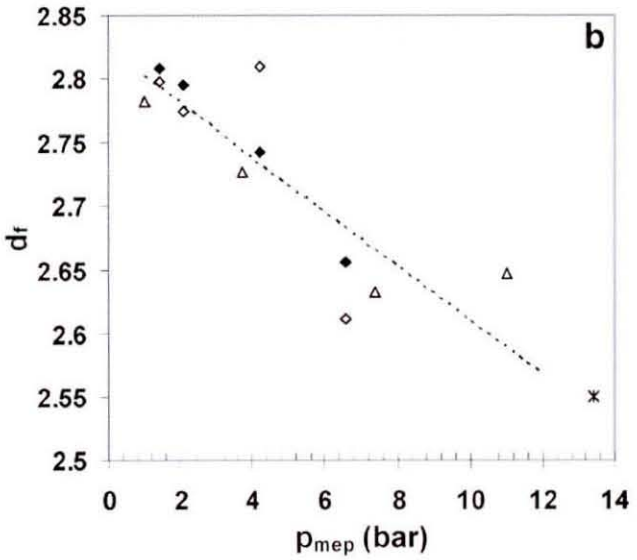

Figure 3.22. Effect of engine load on the fractal dimension of diesel engine soot (Virtanen *et al*, 2004)

Approximating the PM as carbon, the effective density with a fractal dimension of 3 (i.e. solid) will be, 2270 kg m^{-3} (Shackelford and Alexander, 2001). This means that the density of the PM is

$$\rho_e = 2270 d_b^{\,d_r-3} \tag{3.13}$$

The linear approximation of fractal dimension with load was estimated by the author from the broken line in Figure 3.22 as approximately

$$d_f = 2.815 - 0.0201 p_{MEP} \tag{3.14}$$

where p_{MEP} is the mean effective pressure (BMEP) of the combustion cycle. The majority of particulates are anticipated to be ~0.3 μm in diameter (Virtanen *et al*, 2004). This means that the effective density can be calculated as a function of engine load as

$$\rho_e = 2270(300)^{-(0.185+0.0201 p_{MEP})} \tag{3.15}$$

This gives an engine load to PM relationship shown in Figure 3.24. These numbers are of the order of magnitude often reported for PM densities (e.g. Park *et al*, 2003).

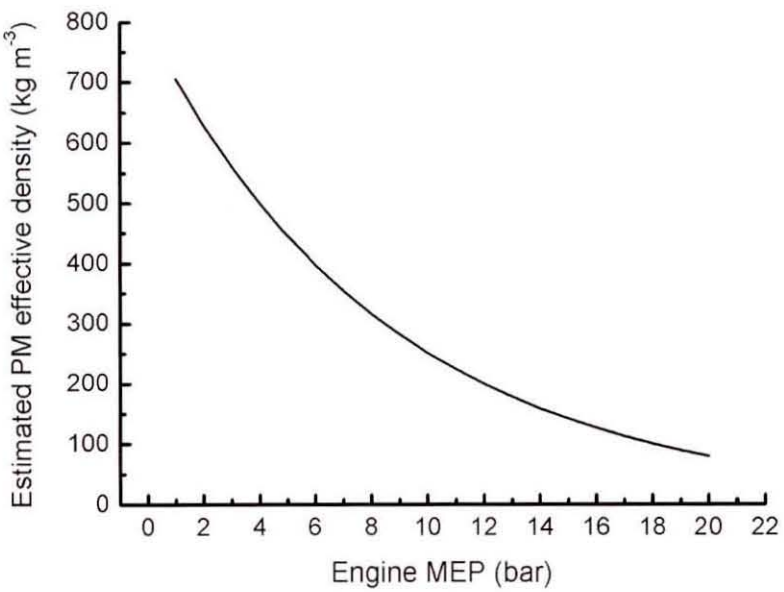

Figure 3.23. Predicted effect of engine load on effective PM density using Equation 3.15.

The average PM densities calculated from the available cycle data are shown in Table 3.4. They vary between 116 and 177 kg m^{-3}, corresponding to a BMEP of between approximately 13 and 16 bar (58 and 74% load). This indicates that to

achieve a representative PM layer density, the filter should be loaded at approximately 2/3 engine load.

Table 3.4. Calculated average PM densities for a range of load cycles supplied by Caterpillar Inc.

Vehicle	Calculated average PM density kg m^{-3}	Equivalent Steady State Engine Load %
Concrete Mixer	133	70
Fuel Hauler	177	58
Garbage Truck	130	70
Line Haul	116	74

PM composition can also vary depending on the engine and fuel used. To try to understand the possible effects of engine load on pre-loading filters, data has been taken from Sharma *et al* (2005) and reproduced here in Figure 3.24. Their work suggested that the engine load has a large affect on elemental carbon and soluble organic fraction (SOF) of the PM, and a small affect on the metal components of the PM. The SOF and elemental carbon are evaluated here for the load cycles supplied by Caterpillar. The trends are shown in Figure 3.24. Elemental carbon increases with increasing engine load and SOF tends to reduce.

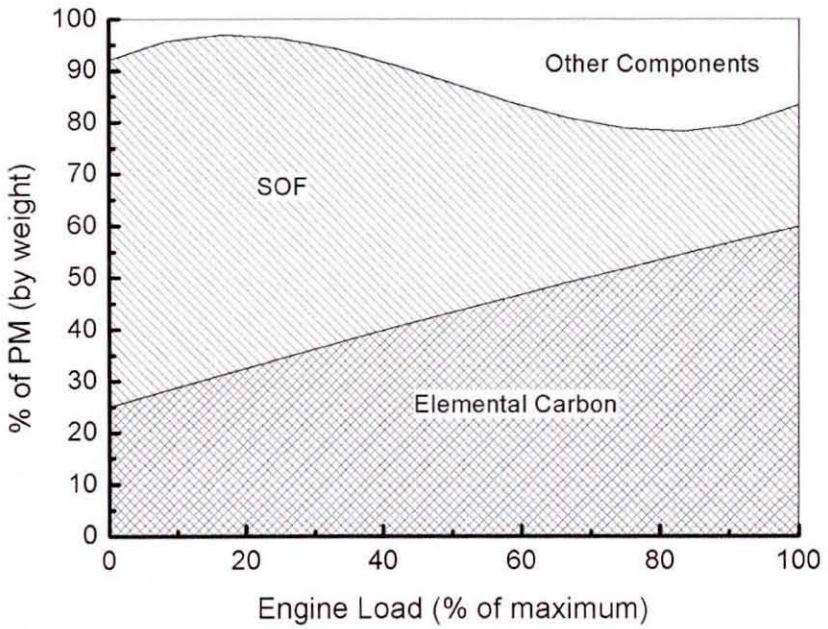

Figure 3.25. Effect of engine load on SOF and elemental carbon (adapted from Sharma *et al*, 2005)

The cycle data for the carbon and SOF allows calculation of average values similar to the density. Like the data on density, the average composition is close to the high load case due to the larger amount of PM produced under high load conditions. The summary of the equivalent load is shown in Table 3.5. This shows that to get representative SOF and elemental carbon content in a pre-loaded DPF loaded at a constant load, the engine should be between 59-74% load.

Table 3.5. Average SOF and elemental carbon compositions of PM over cycles supplied by Caterpillar.

Vehicle	Average SOF % weight	Equivalent Engine Load % full load	Average Elemental Carbon % weight	Equivalent Engine Load % full load
Concrete Mixer	37.9	58	47.5	62
Fuel Hauler	38.7	57	46.3	59
Garbage Truck	32.1	66	50.0	69
Line Haul	31.0	68	51.6	74

We can therefore say:

1. To achieve representative average PM layer densities, SOF and elemental carbon fraction the pre-loaded filters should be loaded at between 60 and 74% engine load.
2. Local PM distribution trends cannot be achieved for this work as a transient dynamometer is not available.

3.3.4 Summary

The design and implementation of a controlled diesel exhaust flow simulator capable of achieving 225 kg h^{-1} air flow with up to 15 kPa filter back pressure has been presented. Its use and typical measurements were shown. Analysis determining appropriate methods of pre-loading filter samples for rig testing has indicated that the engine should be operated at between 60 and 74% engine load.

3.4 On-Engine Test Methods

Although rig testing offered a fast, efficient and reliable method for developing diesel particulate filtration systems, the technology should ultimately be demonstrated in the environment it will be used. There are also a number of differences remaining between the rig and the engine, most notably that the rig does not continuously produce soot to be trapped by the filter. For these reasons the latter series of tests were carried out in an engine test cell with a heavy duty diesel engine and purpose built filter canister. The engine and its characteristics are introduced before describing the filter canister and basic measurement techniques used during on-engine testing.

3.4.1 Test Engine

The test engine was a Perkins 1100 series, heavy duty 4.4 litre diesel engine (shown in Figure 3.25), with specifications shown in Table 3.6. It was connected to a Froude AG400-HS steady state eddy current dynamometer. The engine was used to produce PM and real diesel engine exhaust which was forced through a purpose built filter canister where the regeneration tests were carried out.

Table 3.6. Test engine specifications. (Perkins, 2005)

Model Number	1104C-44TA
Peak Power (at engine speed)	92 kW (2200 rpm)
Peak Torque (at engine speed)	475 Nm (1400 rpm)
Number of Cylinders	4
Swept Volume	4.4 litres
Aspiration	Turbo charged
Charge cooling	Simulated air to air
Compression Ratio	18.2:1
Bore x Stroke	105 x 127 mm

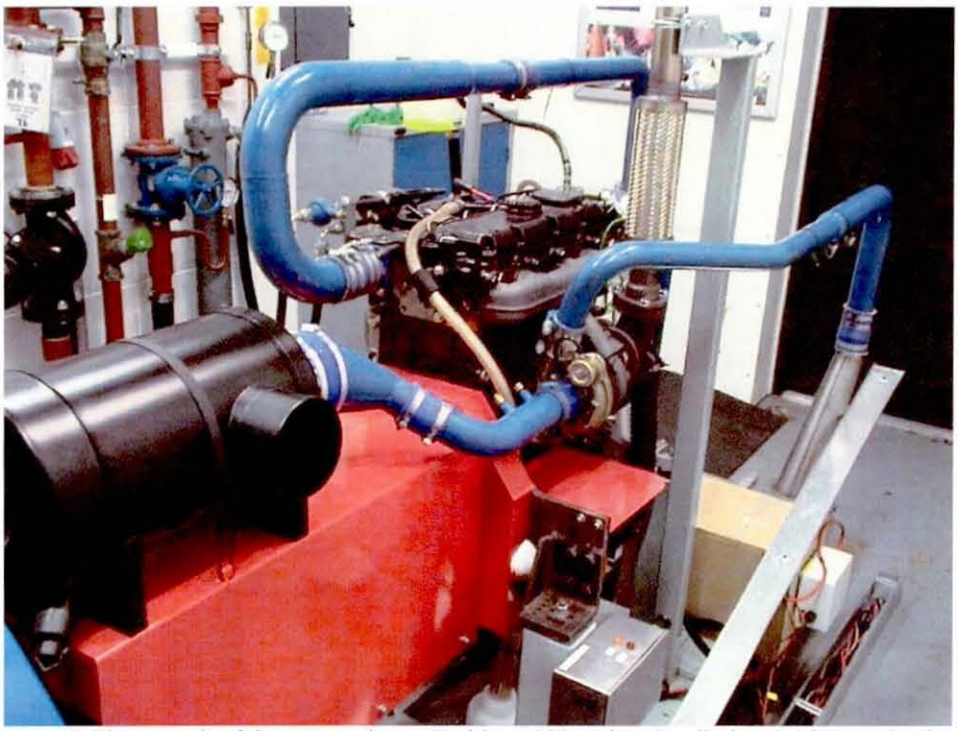

Figure 3.25. Photograph of the test engine; a Perkins 1100 series, 4 cylinder, 4.4 litre turbocharged, charge-cooled diesel engine.

The flow rate of the engine over the majority of its speed load range has been calculated based on test bed data from the engine cell at Loughborough University. The intake manifold pressure (P_{inlet}) and temperature (T_{inlet}) were used to estimate the inlet air density. Assuming a volumetric efficiency of 90% the flow rate can be estimated as

$$\dot{m}_{inlet} = 0.9 \times \frac{N}{2} \times 60 \times \frac{V_{swept}}{1000} \times \rho_{inlet} = \frac{0.027 N V_{swept} P_{inlet}}{R_{inlet} T_{inlet}} \quad (3.16)$$

where $\dot{m}$ is the air mass flow rate (kg h^{-1}), N is the engine speed (rpm), V_{swept} is the swept volume of the engine (litres), ρ_{inlet} is the intake manifold air density (kg m^{-3}) and R_{inlet} is the gas constant for the intake air. The fuel mass flow rate was measured by timing the consumption of 150 ml of fuel, and multiplying by an estimated fuel density of 0.86 kg m^{-3}. This was then added to the air flow rate to give the exhaust mass flow rate. A contour plot of the estimated exhaust gas mass flow rate is shown in Figure 3.26. The flow rate can be seen to increase with engine speed as the volume

swept by the engine per unit time increases. It also increases with engine load as the intake air density increases.

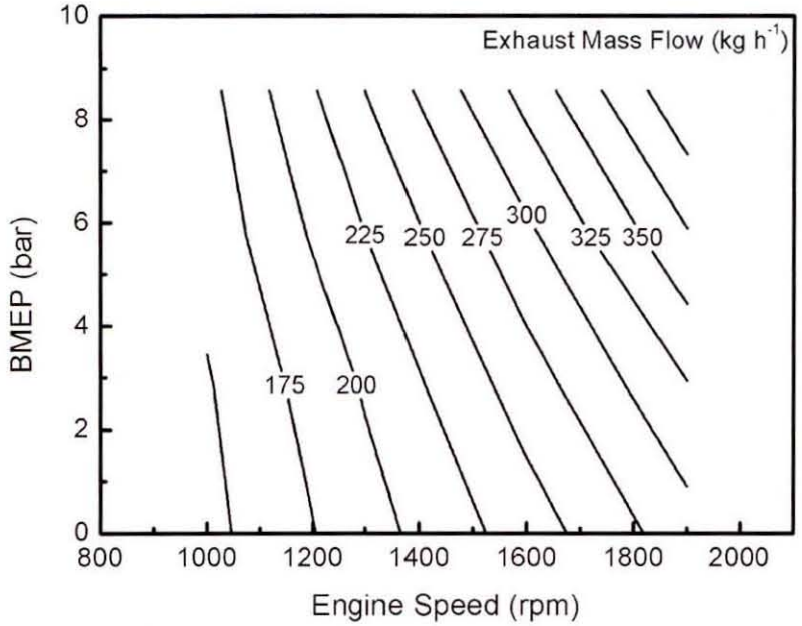

Figure 3.26. Contour plot of estimated exhaust gas mass flow rate as a function of engine speed and load.

Exhaust gas temperature was measured using a K-type thermocouple mounted upstream of the DPF canister. Figure 3.27 shows the temperature measurements, which increase with engine speed and load. The temperature is low due to the filter being mounted ~6 m from the turbine outlet.

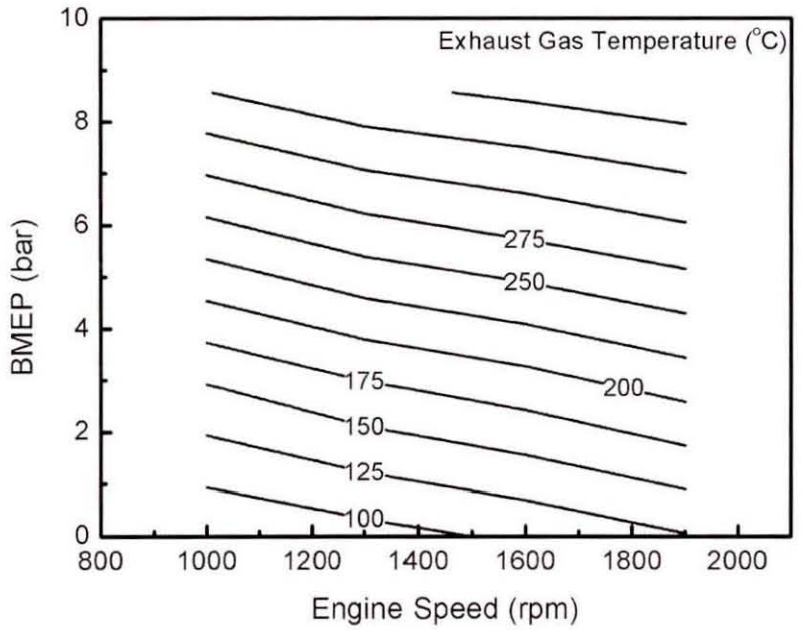

Figure 3.27. Contour plot of exhaust gas temperatures as a function of engine speed and load.

PM content in the exhaust gas was measured using an AVL 415 Smokemeter which allowed estimation of the PM concentration in a sample of exhaust gas. The smoke meter measurement (AVL smoke number) was converted to a soot concentration using the manufacturer supplied correlation (AVL, 2002)

$$\rho_{FSN} = \left(12.22 \times 10^{-3}\right) N_{FSN} \exp\left(0.38 N_{FSN}\right) \tag{3.17}$$

where ρ_{FSN} is the soot concentration in the exhaust gas (kg m^{-3}) and N_{FSN} is the AVL smoke number from the smoke meter. The soot concentration was used with the exhaust mass flow rate data to calculate the engine out PM production rate from

$$\dot{m}_{PM} = \dot{m}_{ex} \rho_{FSN} \left(\frac{R_{air} T}{P} \right) \tag{3.18}$$

where $\dot{m}_{PM}$ is the PM mass flow rate (g h^{-1}), $\dot{m}_{ex}$ is the exhaust mass flow rate (kg h^{-1}) and R, T and P are the gas constant, temperature and pressure respectively, at the smoke meter inlet. The estimated PM flow rate in the exhaust gas calculated from Equation 3.18 is plotted in Figure 3.28.

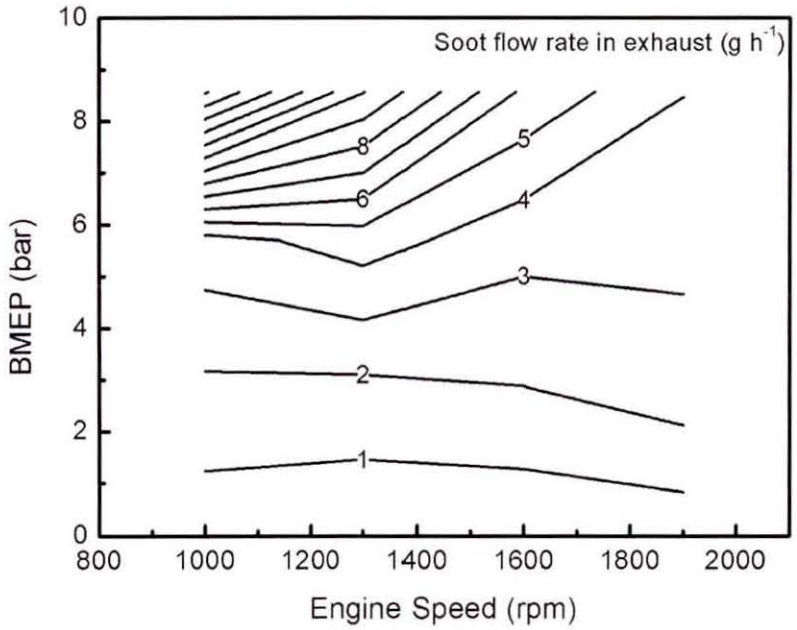

Figure 3.28. Contour plot of estimated smoke production rates as a function of engine speed and load.

This key information has been used to identify test points with suitable soot flow rates, exhaust temperatures and exhaust gas mass flow rates for a given test.

3.4.2 Engine Canister Design and Capability

The engine rig was designed to have similar capabilities to the hot flow rig discussed in Section 3.3, and an exploded view is shown here in Figure 3.29. The individual parts are listed in Table 3.7. Where a number of optional parts could be fitted, they are differentiated by an additional letter. There was scope for optical access both upstream and downstream of the filter by using fused silica windows (parts 1 or 8 on the exploded view). The filter was housed in a cylindrical section fixed with quick release clamps and sealed with Supergraf gaskets. The inlet consisted of a conical section to maintain relatively even flow distribution. The outlet was at 90 degrees to the filter exit flow to allow electrical feedthroughs on the clean side of the filter. Two conical inlet and cylindrical filter holders were designed and manufactured to fit 5.66 inch and 7.5 inch diameter wall flow filters respectively and could be interchanged by removing and replacing four bolts.

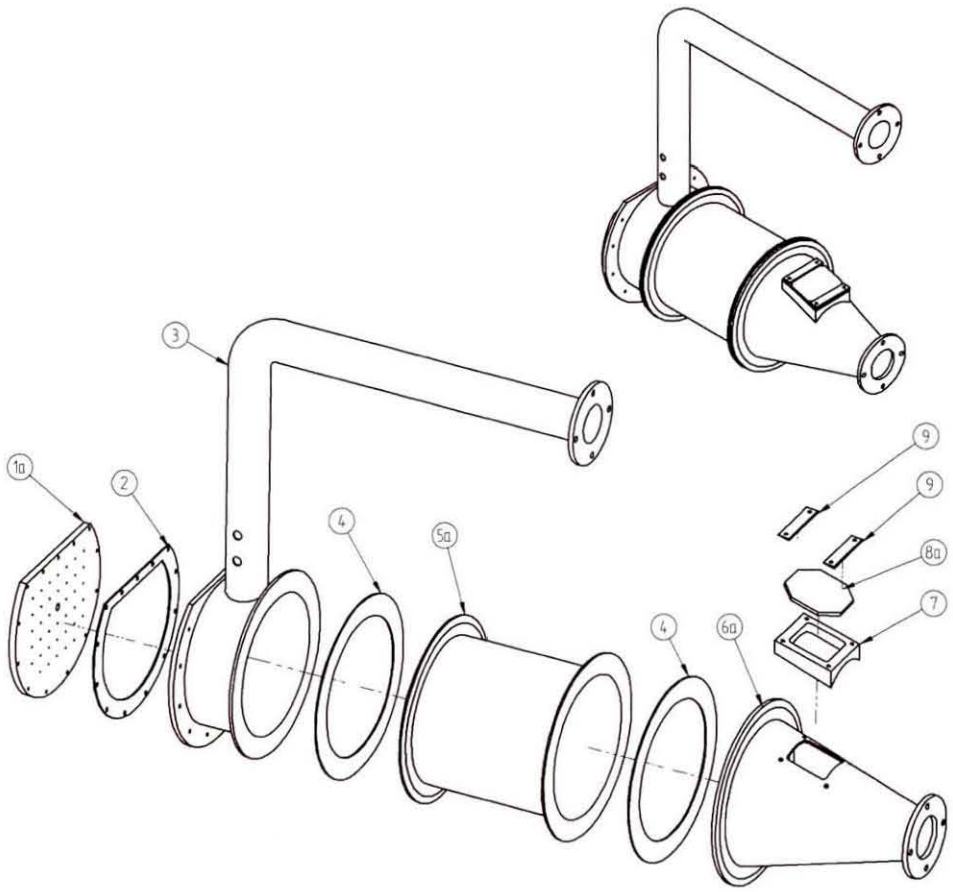

Figure 3.29. Exploded and assembled view of the engine test canister.

Table 3.7. List of test engine filter canister parts shown in Figure 3.29

Part Number	Description	Quantity
1a	downstream electrical feedthrough	1
1b	downstream optical window	1
1c	downstream coverplate	1
2	downstream coverplate gasket	1
3	canister outlet	1
4	gasket	1
5a	7.5 inch diameter filter holder	1
5b	5.66 inch diameter filter holder	1
6a	7.5 inch diameter canister inlet	1
6b	5.66 inch canister inlet	1
7	upstream access adaptor	1
8a	upstream electrical feedthrough	1
8b	upstream optical window	1
8c	upstream coverplate	1
9	upstream access securing plates	2

The filter canister assembly was made from 316 stainless steel to avoid corrosion. A flexible section was included in the outlet pipe to assist assembly, although it is not

shown in Figure 3.29. The 5.66 inch canister assembly is shown in situ in Figure 3.30.

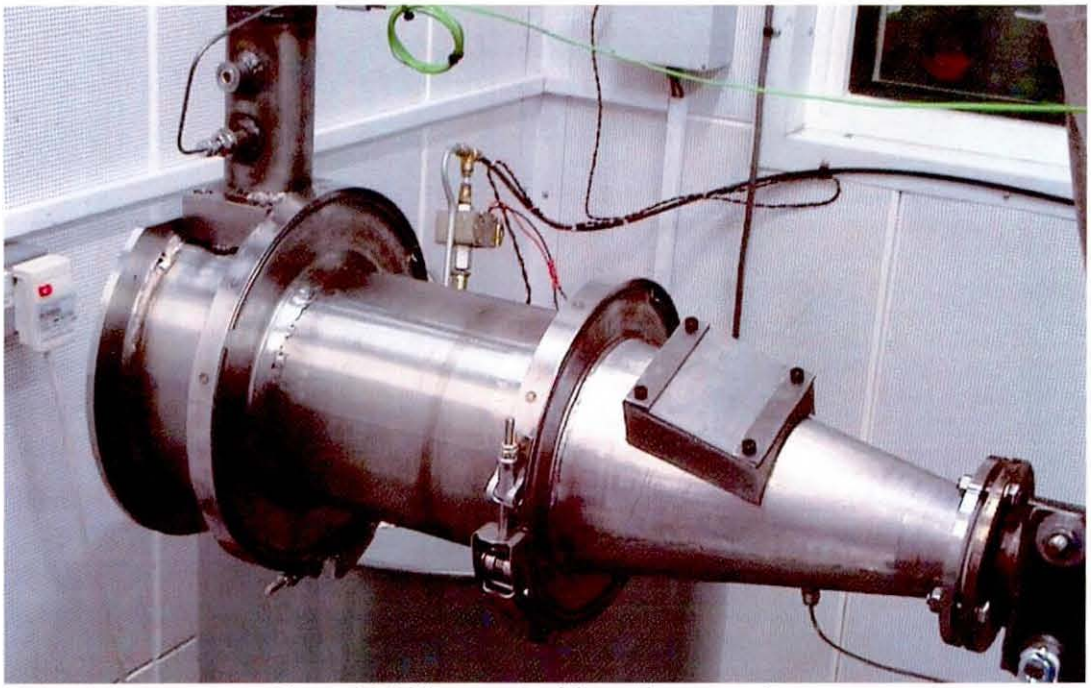

Figure 3.30. Photograph of the engine test canister.

3.4.3 Measurements During Engine Tests

When testing on the engine electrical measurements were carried out using the same methods described in Section 3.2.5. Figure 3.31 shows a cross section of the filter canister on the engine with the pressure and temperature measurements that were taken before and after the filter. The back pressure and absolute pressure were measured using calibrated pressure transducers (Transinstruments Series 2000 1.6 bar absolute pressure transducer) and the temperatures were measured using semi-flexible K-type thermocouples.

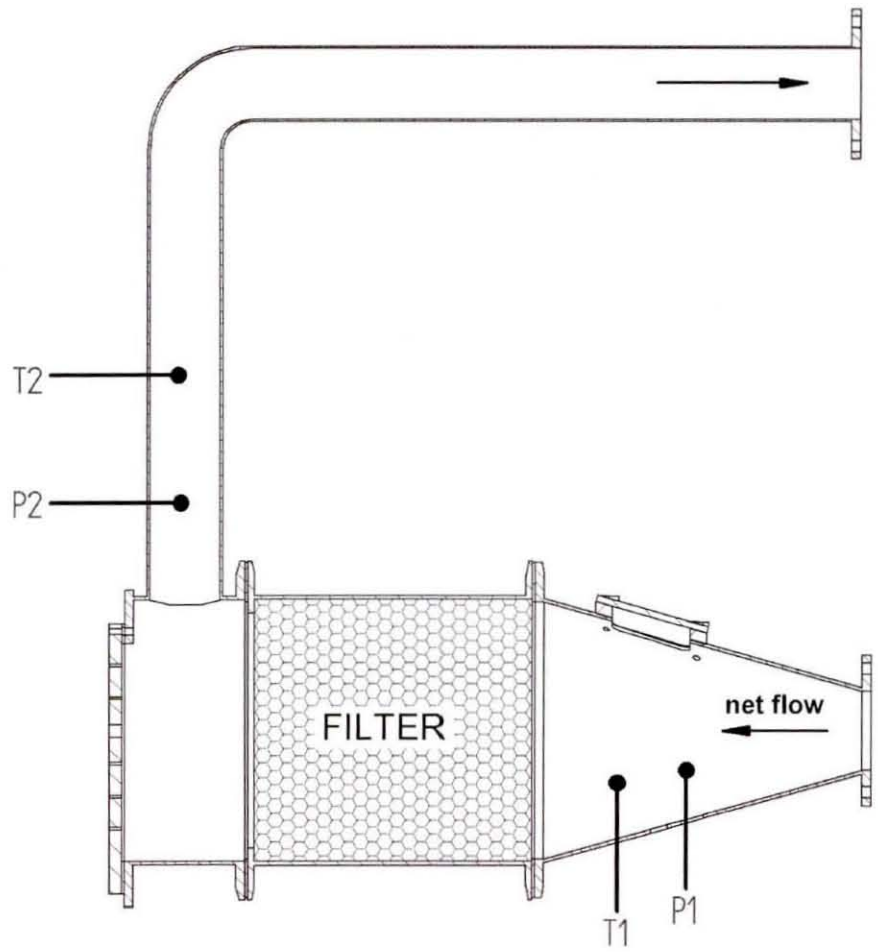

Figure 3.31. Cross section of the engine canister showing the location of pressure and temperature measurements.

Filtration Efficiency Measurements

Experimental setups that are capable of measuring filtration efficiency include:

1. AVL 415 smoke meter
2. Series filter arrangements.

AVL smokemeters are robust and widely used pieces of equipment that offer quick and repeatable results. With the smokemeter, the filtration efficiency is calculated as

$$\eta = \left(1 - \frac{\dot{m}_{downstream}}{\dot{m}}\right) \times 100\% \qquad (3.19)$$

where η is the filtration efficiency, $\dot{m}_{downstream}$ is the PM mass flow rate downstream of the filter and $\dot{m}$ is the PM mass flow rate from the engine. With a series filter

arrangements, if a filter with known filtration efficiency is available, pre- and post-mass measurements can allow calculation of the unknown filtration efficiency. The gas flow is forced through the unknown filter and then through the filter with the known filtration efficiency. The mass trapped on the unknown filter is

$$m_{unknown} = \dot{m}\Delta t\,\eta_{unknown} \tag{3.20}$$

where $m_{unknown}$ is the unknown filter's trapped PM mass (measured by pre and post weighing), $\dot{m}$ is the PM mass flow rate from the engine, Δt is the duration of the test and $\eta_{unknown}$ is the unknown filtration efficiency. The PM trapped on the downstream filter can then be calculated from

$$m_{known} = \dot{m}\Delta t(1-\eta_{unknown})\eta_{known} \tag{3.21}$$

where m_{known} is the known filter's trapped mass and η_{known} is the known filters filtration efficiency. Solving these two equations to find the unknown filtration efficiency gives

$$\eta_{unknown} = \frac{m_{unknown}\eta_{known}}{m_{known} + m_{unknown}\eta_{known}} \tag{3.22}$$

Evaluation of Filtration Efficiency Measurement Methods

During this work an AVL 415 smokemeter was used to determine filtration efficiency using Equation 3.19. A typical spread of smokemeter data is +/- 10%. Analysis of example data shows that the error is a function of the filtration efficiency of the sample. This is shown in Figure 3.32. As the sample filtration efficiency increases the accuracy of the measurement increases. At anticipated filtration efficiencies of >70% the error is <10%. The smoke meter has the advantage that it can take many readings in a short space of time, especially in comparison to weighing methods.

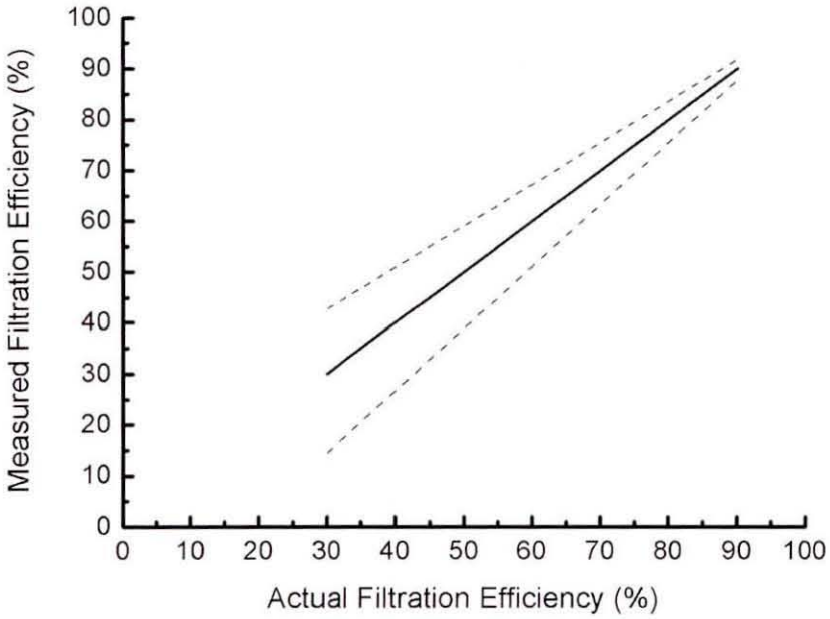

Figure 3.32. Effect of sample filtration efficiency on smoke meter method of estimating filtration efficiency. Broken lines indicate error bands.

A wall flow filter was mounted downstream of the foam filter sample to determine filtration efficiency using Equation 3.22, with the mass being measured to +/- 2 mg. Analysis of example data showed that the accuracy of the pre- and post-weight measurement method (Equation 3.22) was independent of filtration efficiency of the sample but dependent on the test duration. This is shown in Figure 3.33. For short duration tests the error is large meaning that transient filtration efficiency measurements using this method were very difficult. Also testing large number of samples would not be possible due to the amount of time required.

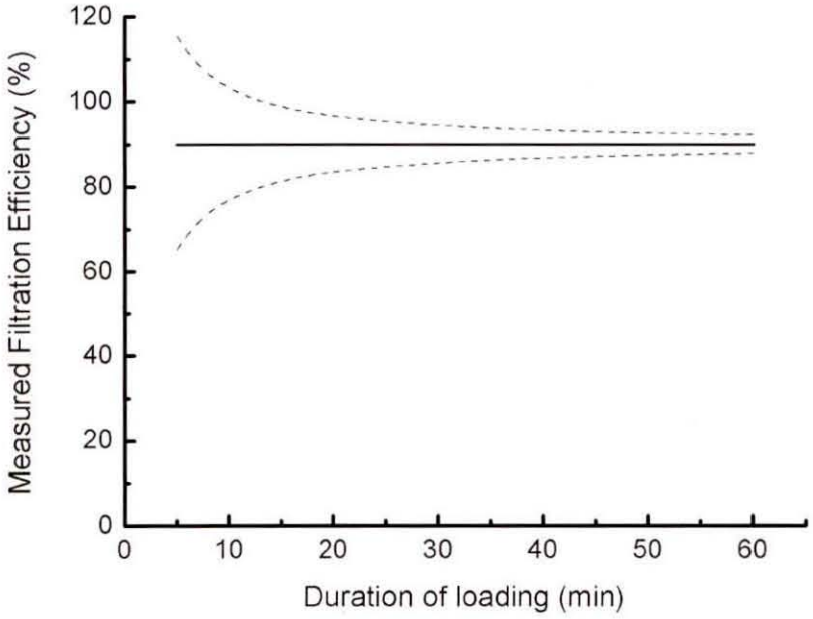

Figure 3.33. Effect of test duration on the accuracy of the pre- and post-weighing method of estimating filtration efficiency. Broken lines indicate error bands.

3.4.4 Summary of On-engine Test Methods

The test engine has been introduced, followed by descriptions of the filter canister used for regeneration testing. Methods for measuring filtration efficiency of a sample have been described with the error analysis indicating that, of the available methods, the use of an AVL 415 Smokemeter offers low errors and high data capture rates.

3.5 Concluding Remarks

Experimental methodology that has been used throughout this work has been described in this chapter. The following chapters discuss the development of the combined regeneration and filtration system using experimental methods presented in this chapter. Experimental methodology that is used for specific tests only is presented in the appropriate part of the following chapters. Chapter 4 now discusses the use of gelcast ceramic foams as DPFs, including new optimisation methodology, evaluation and example optimisation of gelcast foam DPFs.

CHAPTER 4
STUDY AND OPTIMISATION OF GELCAST CERAMIC FOAM DPFS

Gelcast ceramic foam used as a particulate filter has been demonstrated previously on a rig by Hughes (2003) using Printex U as a diesel particulate substitute. Gelcast foams have the advantage over reticulated ceramic foams and monolithic WFFs of geometric optimisation both on a macroscopic (through machining of the 'green' form ceramic substrate) and microscopic scale (by optimising the pore sizes and window sizes). The work presented here describes the behaviour of gelcast ceramic foam DPFs with new experimentally based methodology. Based on previous work (e.g. Hughes, 2003), an initial porosity of 80% was chosen to form the basis of these studies to achieve suitable filter strength. The effect of the choice of pore size and filter topology (i.e. filtration thickness and filtration area) was investigated and evaluated to optimise an 80% porous gelcast ceramic foam DPF. The evaluation and optimisation is presented in this chapter.

The evaluation of gelcast ceramic foam DPFs considers:

1. Filtration Efficiency The reduction of PM required depends on specific engine technology, although Johnson (2006) suggests that a minimum filtration efficiency of ~60% will be needed for typical engines to meet US 2010 emission standards with 2007 and 2010 projected engine technology.
2. Back Pressure Exhaust back pressure leads to increased pumping losses and reduced fuel conversion efficiency and, therefore, should be minimised. Back pressure refers generally to the pressure drop across the entire exhaust system, although here is used to evaluate the pressure drop across the filter section only.
3. Filtration Volume Packaging requirements and cost push for reductions in filtration volume. Canister volume is not considered separately in this work due to the range of geometries a filter can be manufactured.

The optimisation of filtration efficiency, back pressure, filtration volume and canister volume cannot be achieved independently because:

1. increasing the filtration efficiency leads to higher back pressure or larger filtration volume.
2. reducing the back pressure requires lowering the filtration efficiency or increasing the filtration volume.
3. reducing the filtration volume leads to lower filtration efficiency or higher back pressure.

These conflicting requirements create a complex system to optimise when considering variable foam parameters such as pore size. This optimisation process is the main subject of this chapter, which ends with an evaluation of ceramic foam DPFs in comparison with current state of the art filtration technology.

4.1 Filtration of the Exhaust Gas with Gelcast Ceramic Foams

An imaging study of PM loaded gelcast ceramic foams has been carried out to understand the trapping characteristics of the DPFs. An SEM image showing typical PM distribution around a number of pores is shown in Figure 4.1. The PM distribution covers a large area of the pore wall, mainly around the windows. This

agrees with earlier observations by Adigio (2005) and Hughes (2003). The PM appears to be in the form of large agglomerates ~10 μm in diameter. The lack of colour on the SEM image makes it difficult to clearly identify the continuity of the PM layer and it was, therefore, also observed using optical microscopy techniques.

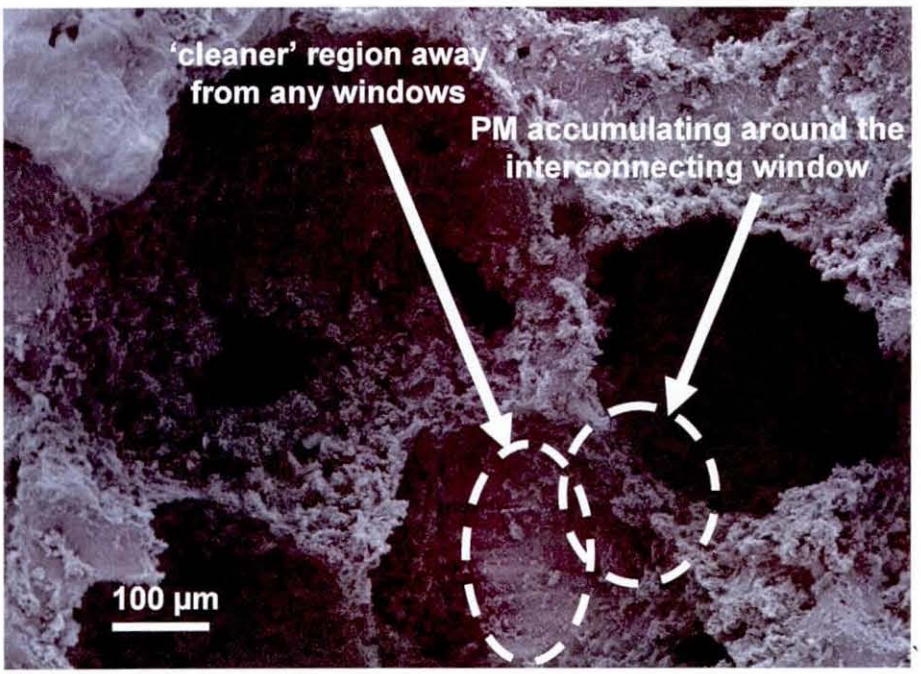

Figure 4.1. SEM image showing typical PM distribution within the pores.

Figure 4.2 shows microscopy images of gelcast ceramic foams with varying PM loadings. A typical microscope image of a gelcast DPF only allows a small part of the image to be in focus as the depth of the image is comparable to the planar distances, which is beyond the capability of conventional microscope arrangements. The images in Figure 4.2 are, therefore, reconstructed images using z-stepping techniques (e.g. Automontage by Synchroscopy). It can be seen that with PM loadings of between 1 and 2 g litre^{-1} the PM is captured in discrete locations on the filter surface. The discrete locations begin to merge at around 3 g litre^{-1} and can be seen to form a continuous layer in extreme loadings of around 12 g litre^{-1}. The pale surfaces visible in the extreme loading case are the cutting planes through the ceramic generated when preparing the sample. The change at higher loadings implies that there will be a change in electrical behaviour of the PM layer as the interconnecting discrete PM clusters create a continuous conducting layer. This may have significant effects on the interaction of the PM and regeneration system at high loadings.

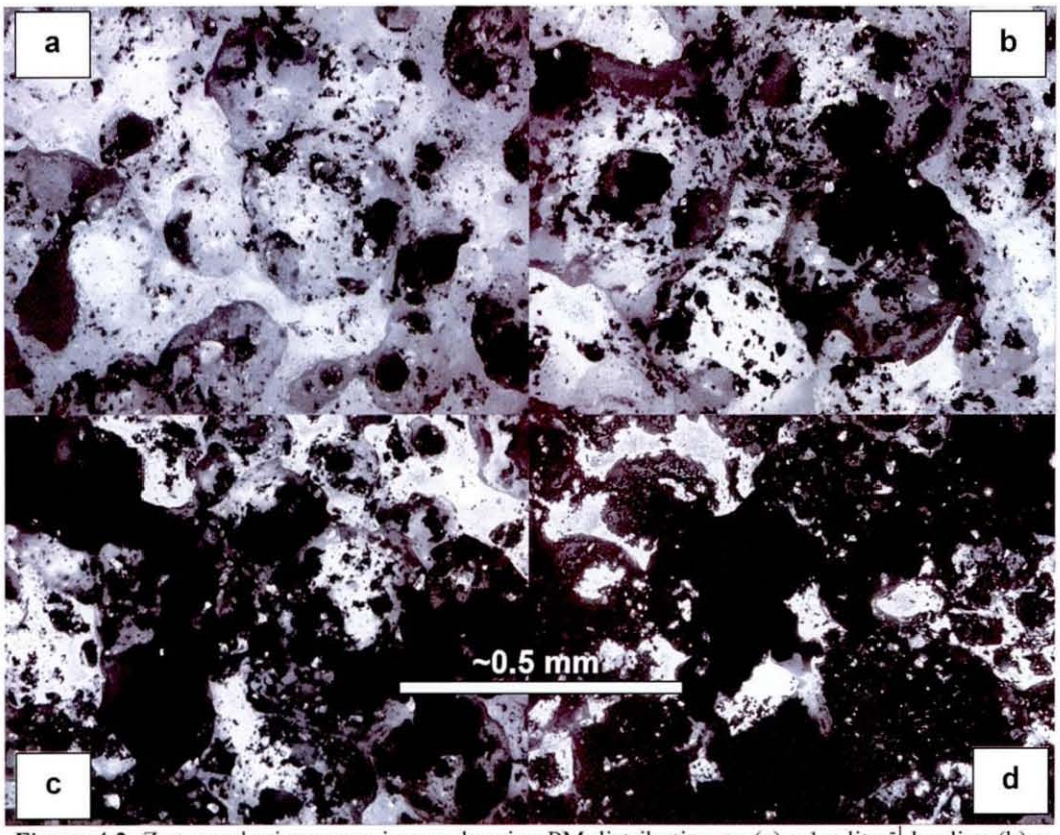

Figure 4.2. Z-stepped microscope image showing PM distribution on (a) a 1 g litre^{-1} loading (b) a 2 g litre^{-1} loading (c) a 3 g litre^{-1} loading and (d) a 12 g litre^{-1} loading.

4.2 Determining Filtration Efficiency of Gelcast Ceramic Foams

The filtration efficiency of the filter is a description of how much of the PM is filtered from the exhaust, and can be measured with respect to particle number or mass. Current legislation is defined on a mass basis (e.g. EPA, 1997) and, therefore, filtration efficiency in this work is described relative to the mass of PM removed from the exhaust gas.

On-engine tests using an AVL smoke meter to measure filtration efficiency for a range of pore size foams provided data such as that shown in Figure 4.3. Reducing the pore size increased the filtration efficiency, with the 30 mm thick 250 μm pore size foam achieving >95% filtration efficiency. The filtration efficiency increased with time, corresponding to the increase in PM loading, surface area for trapping and reduction in window size, as previously reported by authors such as Callé *et al* (2002). To characterise the filters for this study, the average filtration efficiency from the last 15 minutes of the test was used.

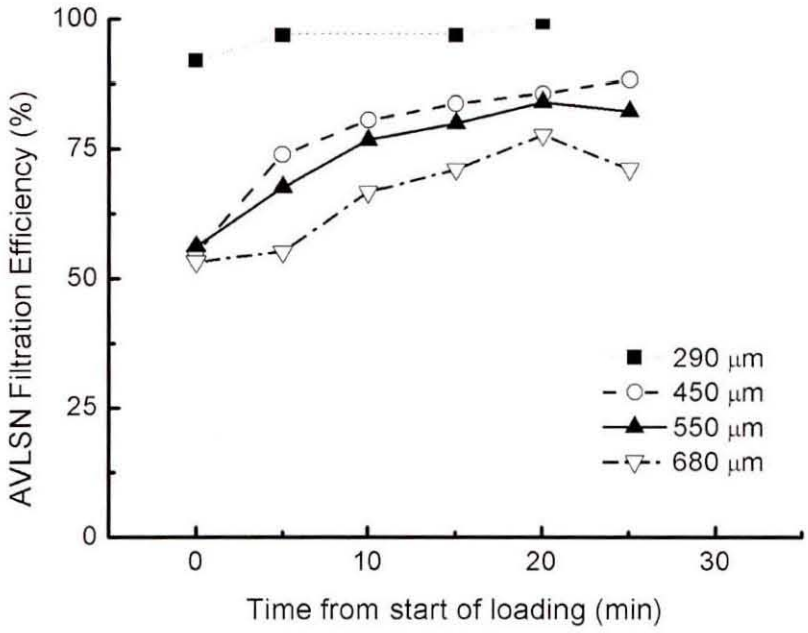

Figure 4.3. Filtration efficiency as a function of time for a range of pore sizes at 1300 rpm, 120 Nm.

The filtration efficiency can be predicted for a different length of filter, from test data using Equation 2.1. The filtration efficiency is compared typically with the equivalent filtration efficiency for a 1 mm filtration thickness. Table 4.1 shows the filtration efficiency calculated from the data in Figure 4.3. This will be used directly in the foam DPF optimisation presented later.

Table 4.1. Filter data showing filtration efficiency for test filters.

Pore diameter	Filtration Efficiency	
μm	η_{test}, %	η_{1mm}, %
290	98.0	12.2
450	84.6	6.04
550	80.8	5.34
680	71.6	4.11

4.3 Determining Back Pressure of Gelcast Ceramic Foams

The effect of flow rate, gas temperature, pore size, filtration length and PM loading on the back pressure of gelcast ceramic foam DPFs is reviewed and expanded here to

develop a model to predict back pressures for various filter geometries with a range of PM loading.

Figure 4.4 shows the effect of flow rate on the pressure drop across clean, 30 mm thick, 5.66 inch diameter gelcast ceramic foam filters of different pore sizes with a gas temperature of ~50 °C. Increasing the pore size led to reductions in back pressure for a given flow rate, as previously demonstrated by Hughes (2003) and Adigio (2006). The back pressure follows the Forcheimer relationship,

$$\frac{dP}{dx} = \frac{\mu}{k_1} v + \frac{\rho}{k_2} v^2 \qquad (4.1)$$

where x is the position through the filter, μ is the dynamic viscosity, v is the gas space velocity, ρ is the gas density and k_1 and k_2 are constants. The linear term is due to the viscous losses and the quadratic term is due to the kinetic losses within the filter (Ergun, 1952).

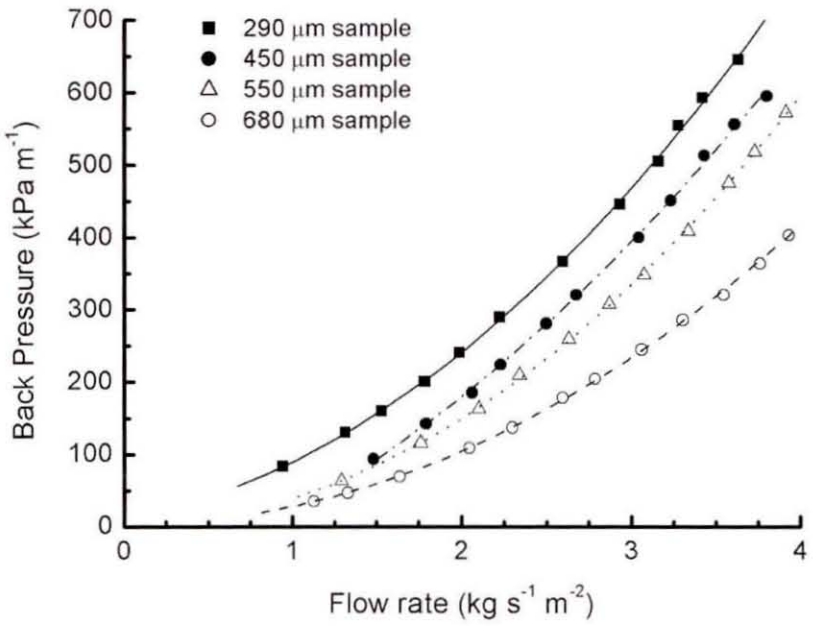

Figure 4.4. Plot of back pressure as a function of flow rate for a range of pore size gelcast ceramic foams at ~50 °C

Gas temperature has a noticeable effect on the back pressure of the gelcast ceramic foams (Figure 4.5) by affecting the space velocity, gas density and gas viscosity.

Increasing temperature leads to increasing back pressure. This can be accounted for in the Forcheimer equation by considering the velocity and density relationships,

$$v = \frac{\dot{V}}{A} = \frac{\dot{m}}{\rho A} = \frac{RT\dot{m}}{PA} \tag{4.2}$$

where v is the gas velocity, $\dot{V}$ is the volumetric flow rate, A is the flow area, $\dot{m}$ is the mass flow rate, ρ is the gas density, R is the gas constant, T is the gas temperature and P is the gas pressure. The dynamic viscosity is also a function of gas temperature which can be described between 296 and 1023 K (Forsythe, 2003) as

$$\mu = k_3 T^{0.754} \tag{4.3}$$

Where μ is the dynamic viscosity and k_3 is a function of the fluid properties. The Forchiemer Equation (4.1) can hence be rewritten in terms of mass flow rate and temperature as

$$\frac{dP}{dx} = \frac{k_3 RT^{1.754}\dot{m}}{k_1 PA} + \frac{RT\dot{m}^2}{PA^2 k_2} = \frac{1}{P}\left(k_4 T^{1.754}\frac{\dot{m}}{A} + k_5 T\frac{\dot{m}^2}{A^2}\right) \tag{4.4}$$

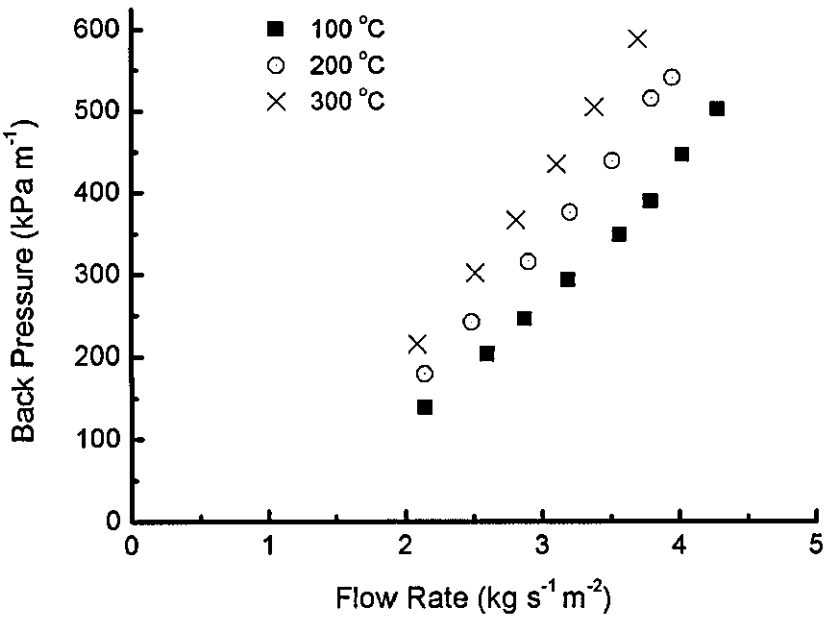

Figure 4.5. Plot of filter back pressure for a sample 680 μm clean filter at gas different temperatures.

Data showing k_4 and k_5 for the data in Figure 4.5 is shown in Figure 4.6. It shows that Equation 4.4 accounts for the temperature effects on the back pressure.

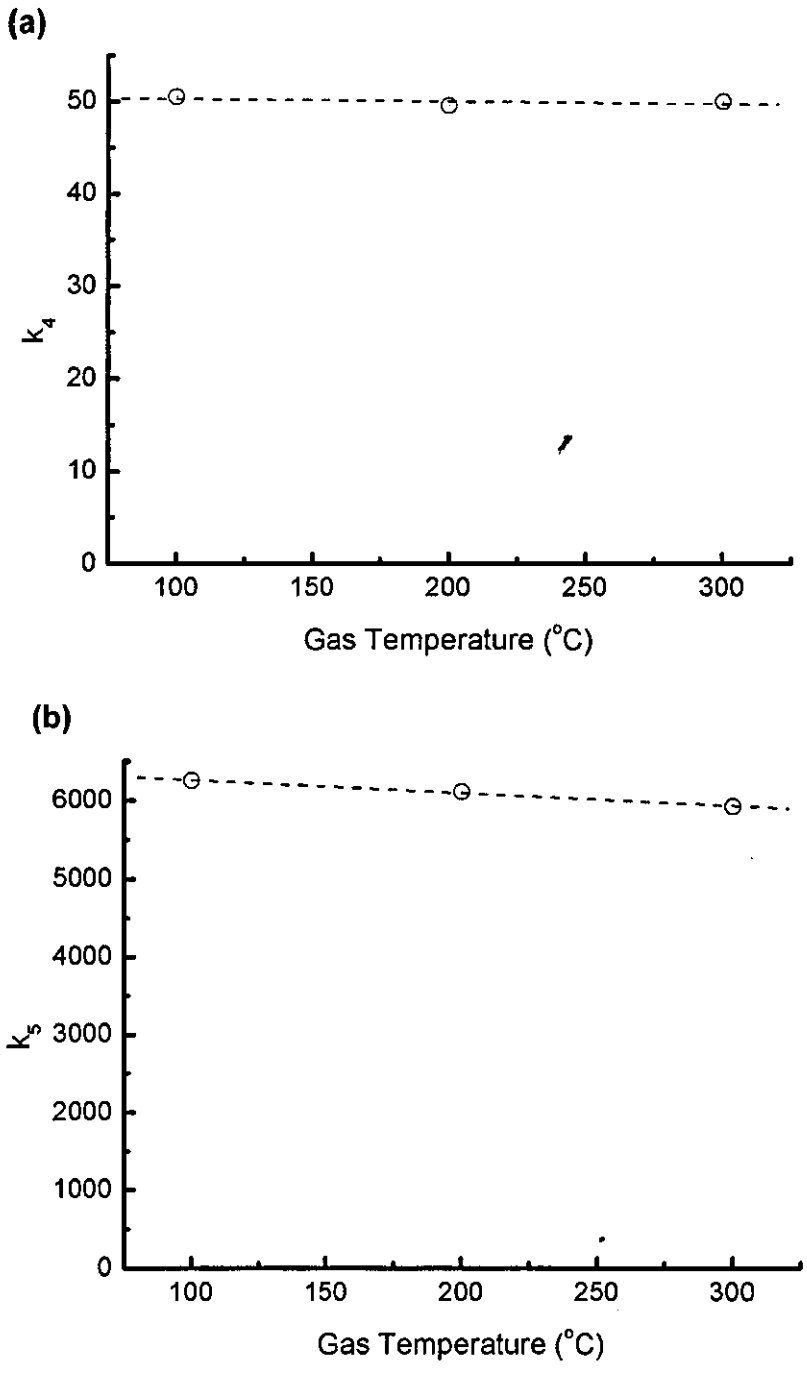

Figure 4.6. Plot showing the dependence of (a) $1/k_1$ and (b) $1/k_2$ on gas temperature and showing the independence of k_4 and k_5 on gas temperature.

The effect of PM loading on the back pressure is more difficult to describe from fundamentals and is hence evaluated using a polynomial expansion such that

$$k_4 = c_{1v} + c_{2v}\theta + c_{3v}\theta^2 + ... + c_{mv}\theta^{m-1} \quad (4.5)$$

and

$$k_5 = c_{1k} + c_{2k}\theta + c_{3k}\theta^2 + ... + c_{mk}\theta^{m-1} \quad (4.6)$$

where c_i are constants and θ is the specific local filter loading (g litre^{-1}).

This study considers the final form of the Forcheimer equation when considering a quadratic approximation for the effect of PM loading. The derivation of the final equations follows.

4.3.1 Quadratic Loading Relationships

Considering the constants to be a quadratic function of PM loading means

$$k_4 = c_{1v} + c_{2v}\theta + c_{3v}\theta^2 \quad (4.7)$$

$$k_5 = c_{1k} + c_{2k}\theta + c_{3k}\theta^2 \quad (4.8)$$

The filtration efficiency can be calculated from Equation 2.1. Given that a filter of length x has a filtration efficiency of

$$\eta_1 = 1 - (1 - \eta_t)^{\left(\frac{x}{t}\right)} \quad (4.9)$$

and the filtration efficiency of a filter of length $(x+L)$ is

$$\eta_2 = 1 - (1 - \eta_t)^{\left(\frac{x+L}{t}\right)} \quad (4.10)$$

the mass of PM trapped in the section between x and L is

$$PM = a(\eta_2 - \eta_1) = a\left[(1-\eta_t)^{\left(\frac{x}{t}\right)} - (1-\eta_t)^{\left(\frac{x+L}{t}\right)}\right]$$
$$= a(1-\eta_t)^{\left(\frac{x}{t}\right)}\left[1-(1-\eta_t)^{\left(\frac{L}{t}\right)}\right] \quad (4.11)$$

where a is the mass of PM that was incident through the front face of the filter per unit area (g m^{-2}). The specific loading between x and L is therefore

$$\theta = \frac{a}{L}(1-\eta_t)^{\left(\frac{x}{t}\right)}\left[1-(1-\eta_t)^{\left(\frac{L}{t}\right)}\right] \quad (4.12)$$

where L is the filter thickness (mm). As L approaches zero, this becomes

$$\theta = -\frac{a}{t}\ln(1-\eta_t)(1-\eta_t)^{\left(\frac{x}{t}\right)} \quad (4.13)$$

where t is the thickness (mm) of the test filter (used to find the filtration properties), η_t is the filtration efficiency of the tested sample and x is the position in the filter (mm) measured from the dirty side. This means the Forcheimer equation becomes

$$P\frac{dP}{dx} = \left(c_{1v} - c_{2v}\frac{a}{t}\ln(1-\eta_t)(1-\eta_t)^{\left(\frac{x}{t}\right)} + c_{3v}\frac{a^2}{t^2}[\ln(1-\eta_t)]^2(1-\eta_t)^{\left(\frac{2x}{t}\right)}\right)T^{1.754}\frac{\dot{m}}{A}$$
$$+\left(c_{1k} - c_{2k}\frac{a}{t}\ln(1-\eta_t)(1-\eta_t)^{\left(\frac{x}{t}\right)} + c_{3k}\frac{a^2}{t^2}[\ln(1-\eta_t)]^2(1-\eta_t)^{\left(\frac{2x}{t}\right)}\right)T\frac{\dot{m}^2}{A^2} \quad (4.14)$$

Rearranging gives

$$\int PdP = \int\left[\left(c_{1v} - c_{2v}\frac{a}{t}\ln(1-\eta_t)(1-\eta_t)^{\left(\frac{x}{t}\right)} + c_{3v}\frac{a^2}{t^2}[\ln(1-\eta_t)]^2(1-\eta_t)^{\left(\frac{2x}{t}\right)}\right)T^{1.754}\frac{\dot{m}}{A}\right.$$
$$\left.+\left(c_{1k} - c_{2k}\frac{a}{t}\ln(1-\eta_t)(1-\eta_t)^{\left(\frac{x}{t}\right)} + c_{3k}\frac{a^2}{t^2}[\ln(1-\eta_t)]^2(1-\eta_t)^{\left(\frac{2x}{t}\right)}\right)T\frac{\dot{m}^2}{A^2}\right]dx \quad (4.15)$$

Which, following integration becomes

$$\frac{1}{2}P^2 + k_6 = \left(c_{1v}x - c_{2v}a(1-\eta_t)^{\left(\frac{x}{t}\right)} + c_{3v}\frac{a^2}{2t}\ln(1-\eta_t)(1-\eta_t)^{\left(\frac{2x}{t}\right)} \right) T^{1.754}\frac{\dot{m}}{A} + \left(c_{1k}x - c_{2k}a(1-\eta_t)^{\left(\frac{x}{t}\right)} + c_{3k}\frac{a^2}{2t}\ln(1-\eta_t)(1-\eta_t)^{\left(\frac{2x}{t}\right)} \right) T\frac{\dot{m}^2}{A^2} \quad (4.16)$$

k_6 can be found by considering the case where $x = 0$, i.e. $P = P_i$ giving

$$k_6 = \left(-c_{2v}a + c_{3v}\frac{a^2}{2t}\ln(1-\eta_t) \right) T^{1.754}\frac{\dot{m}}{A} + \left(-c_{2k}a + c_{3k}\frac{a^2}{2t}\ln(1-\eta_t) \right) T\frac{\dot{m}^2}{A^2} - \frac{1}{2}P_i^2 \quad (4.17)$$

giving the Forchiemer equation as

$$\frac{P^2 - P_i^2}{2} = \left[c_{1v}x + c_{2v}a\left(1-(1-\eta_t)^{\left(\frac{x}{t}\right)}\right) + c_{3v}\frac{a^2}{2t}\ln(1-\eta_t)\left((1-\eta_t)^{\left(\frac{2x}{t}\right)} - 1\right) \right] T^{1.754}\frac{\dot{m}}{A} + \left[c_{1k}x + c_{2k}a\left(1-(1-\eta_t)^{\left(\frac{x}{t}\right)}\right) + c_{3k}\frac{a^2}{2t}\ln(1-\eta_t)\left((1-\eta_t)^{\left(\frac{2x}{t}\right)} - 1\right) \right] T\frac{\dot{m}^2}{A^2} \quad (4.18)$$

For a complete filter where $x = t$, the average PM loading is

$$\bar{\theta} = \frac{a\eta_t}{t} \quad (4.19)$$

which can be rearranged to give

$$a = \frac{\bar{\theta} t}{\eta_t} \tag{4.20}$$

Replacing a in Equation 4.18 and letting $x = t$ gives a final form of the quadratic version of the Forcheimer equation as

$$\frac{P_o^{\,2} - P_i^{\,2}}{2t} = \left[c_{1v} + c_{2v}\bar{\theta} + c_{3v} \frac{\bar{\theta}^2}{2\eta_t} \ln(1-\eta_t)(\eta_t - 2) \right] T^{1.754} \frac{\dot{m}}{A}$$

$$+ \left[c_{1k} + c_{2k}\bar{\theta} + c_{3k} \frac{\bar{\theta}^2}{2\eta_t} \ln(1-\eta_t)(\eta_t - 2) \right] T \frac{\dot{m}^2}{A^2} \tag{4.21}$$

If the quadratic term is significant, the pressure drop is not a direct function of the average PM loading but it also depends on the distribution of PM within the filter, included in the equations using the t and η_t terms. The constants can be found obtaining base data from a foam sample at different flow rates and PM mass loadings.

4.3.2 Back Pressure Data Analysis

Figure 4.7 shows the linear curve fits to the 550 μm pore size foam where the gradient is equal to the kinetic coefficient for that loading. The back pressure indicator, I_{BP}, is calculated as

$$I_{BP} = \frac{P_o^{\,2} - P_i^{\,2}}{2t} \tag{4.22}$$

and the flow rate indicator, I_{flow}, (the x-axis) is calculated as

$$I_{flow} = T\left(\frac{\dot{m}}{A}\right)^2 \tag{4.23}$$

The viscous loss term was found to be negligible over the flow rates and filter properties tested. The back pressure increased with loading. Similar linear fits were made for five loadings of each pore size sample.

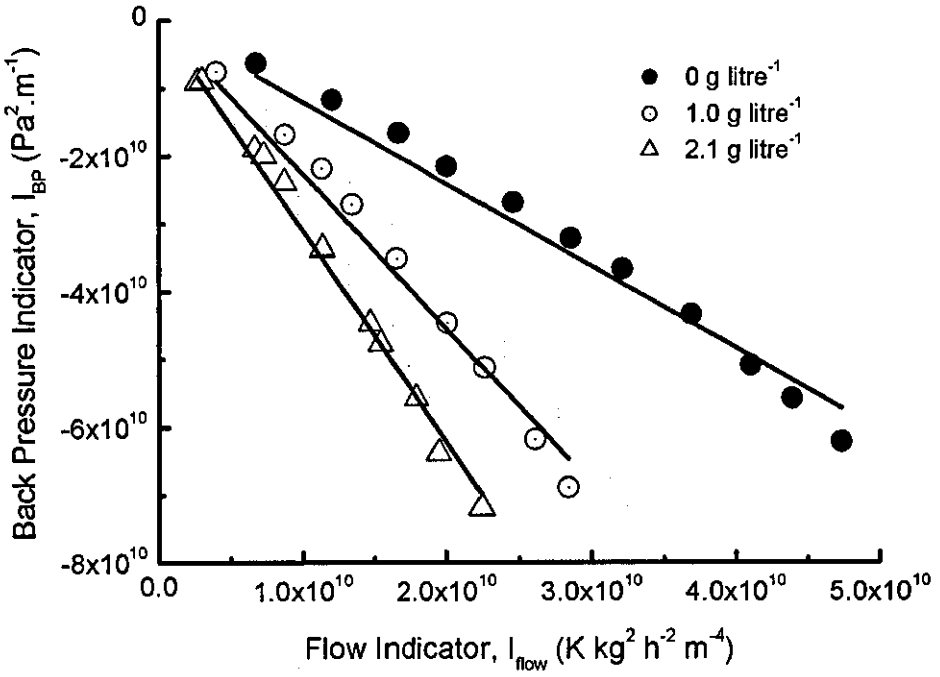

Figure 4.7. Example graph showing the calculation of the kinetic flow loss coefficients.

Plotting the kinetic coefficients, k_5, against the average specific loading allows a curve fit to find the constants c_i. The quadratic curve fits and kinetic coefficients for all the tested samples are shown in Figure 4.8. The constants of the quadratic curve fit are shown in Table 4.2, where A_1, A_2 and A_3 are the constant, linear coefficient and quadratic coefficient of the curve fit respectively. Using Equation 4.21, the constant c_3 has been calculated and is also shown.

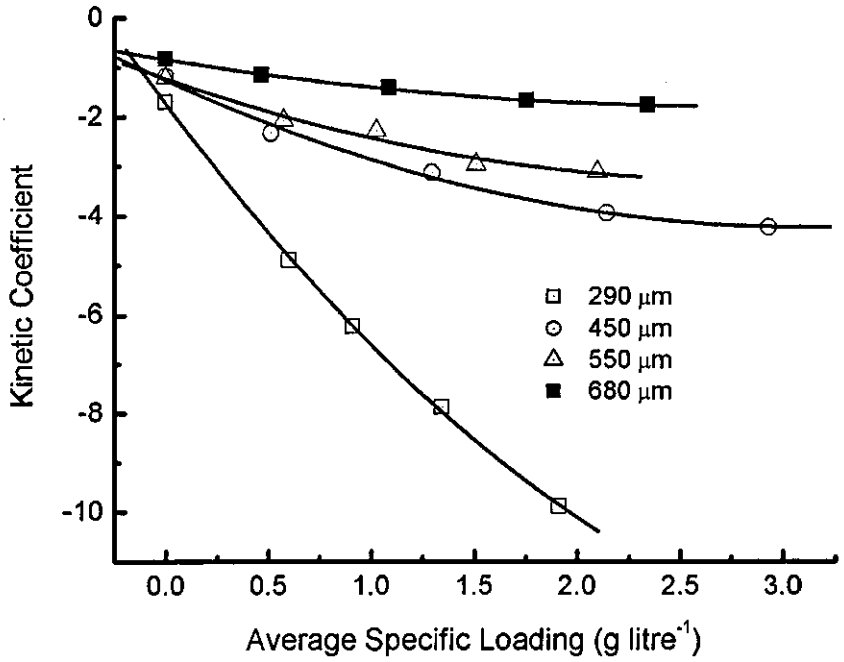

Figure 4.8. Effect of average specific loading on the bulk kinetic flow loss coefficient.

Table 4.2. Coefficients for describing the back pressure of loaded gelcast ceramic foams.

Pore Size µm	A_1, c_{1k}	A_2, c_{2k}	A_3	c_{3k}
290	-1.734	-5.557	0.683	0.336
450	-1.260	-1.912	0.308	0.241
550	-1.224	-1.468	0.264	0.217
680	-0.836	-0.698	0.129	0.113

4.3.3 Validation

To validate the use of this empirical model a 10 mm thick 5.66 inch diameter filter section with a measured pore size of 356 µm was loaded and the back pressure measured for a range of flow rates and PM mass loading. The filter properties shown in Table 4.1 and Table 4.2 were used to predict the filter properties of the validation sample by curve fitting. The curve fits and associated filter properties are shown in Figure 4.9 and Table 4.3 respectively.

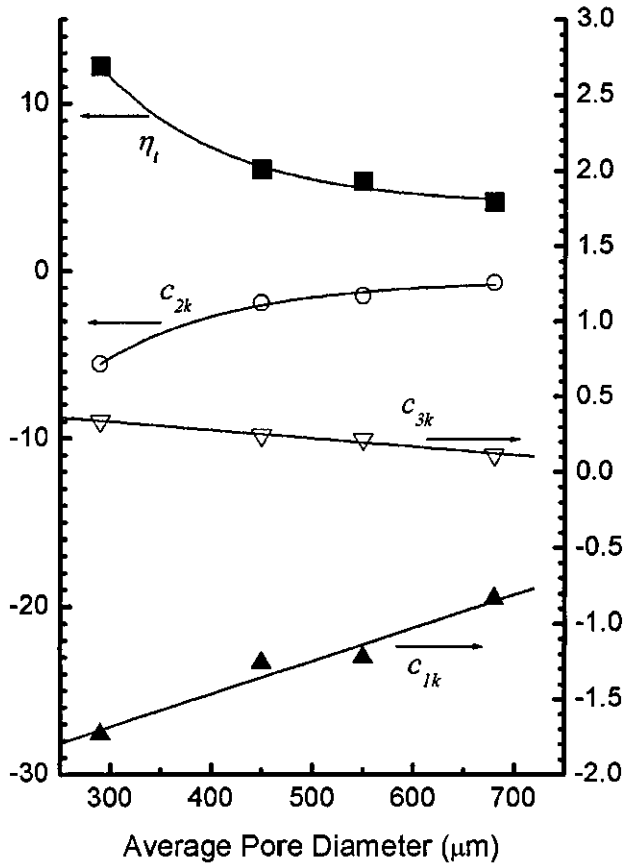

Figure 4.9. Curve fits to foam data from Table 4.1 and 4.2, used for predicting foam properties.

Table 4.3. Predicted foam properties for an 80% porous 356 μm pore size foam.

Property	Value
η_{1mm}	8.81
c_{1k}	-1.56
c_{2k}	-3.58
c_{3k}	0.50

The predicted filter properties were used with Equation 4.21 to predict the back pressure characteristics of the foam sample. The experimental data and model predictions are shown in Figure 4.10. The agreement with the experimental data can be seen to be acceptable, improving as the PM loading increases.

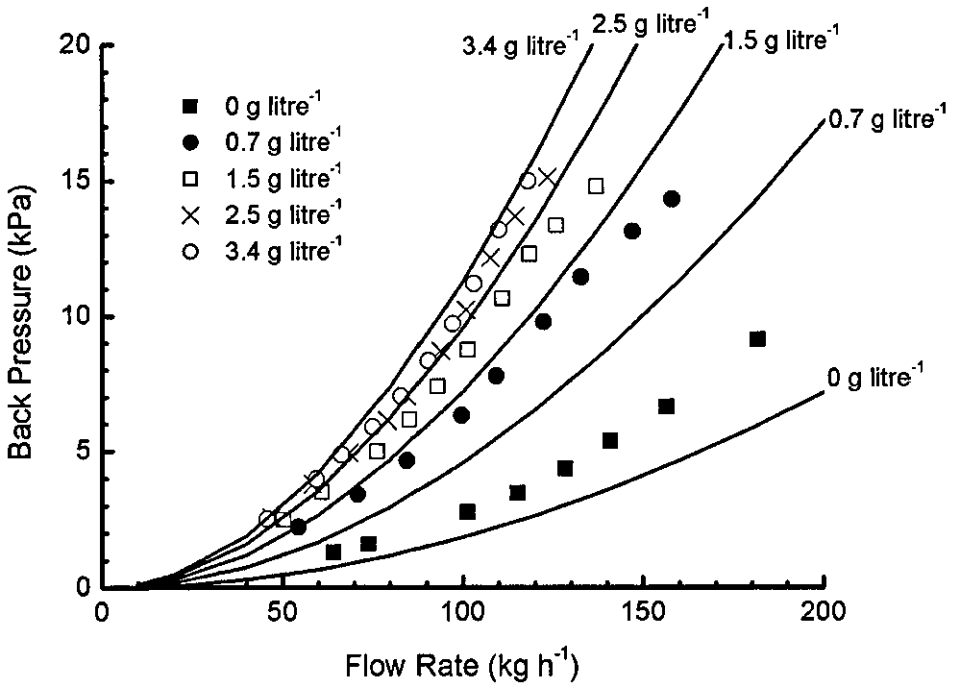

Figure 4.10. Comparison of predicted foam back pressure and actual foam back pressure.

Figure 4.11 compares the predictions from Equation 4.21 with the case when the assumption is made that the back pressure is independent of PM distribution and is only a function of the average PM loading, i.e.

$$\frac{P_o^2 - P_i^2}{2t} = \left[c_{1v} + c_{2v}\bar{\theta} + c_{3v}'\bar{\theta}^2\right]T^{1.754}\frac{\dot{m}}{A} + \left[c_{1k} + c_{2k}\bar{\theta} + c_{3k}'\bar{\theta}^2\right]T\frac{\dot{m}^2}{A^2} \quad (4.24)$$

Including the effect of the PM distribution in the analysis leads to a higher predicted back pressure. This is a result of the more even PM loading with the thinner filter, as will be discussed later.

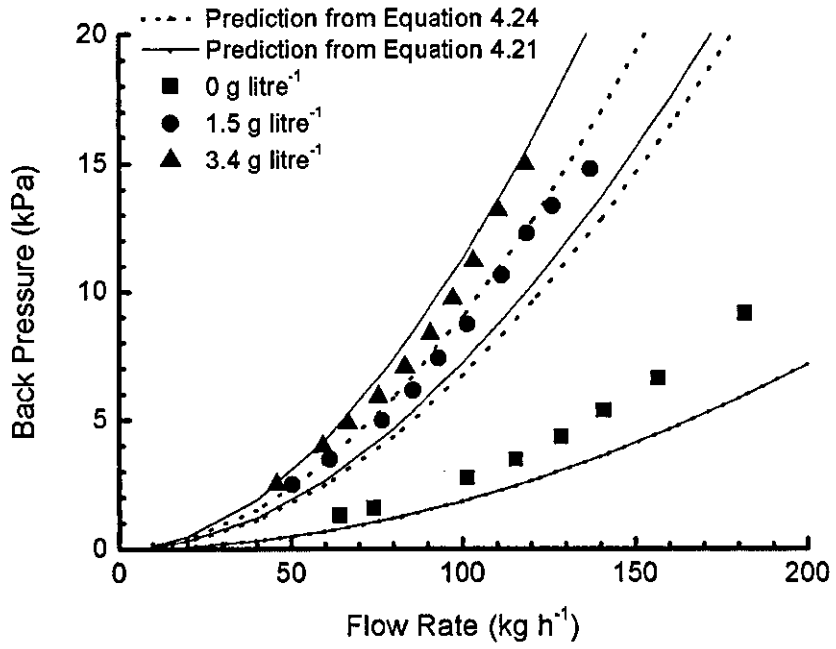

Figure 4.11. Graph showing the effect of accounting for the PM distribution in the back pressure predictions.

This comparison of the modelling prediction with experimental data shows that the empirical model is adequate for investigating conceptual foam designs. Where improved accuracy of the model predictions is needed, it is expected to be achievable by increasing the number of test points used for the foam property predictions.

4.3.4 Effect of PM Distribution

With the calculation of the effects of local PM loading, the effect of the PM distribution on the back pressure can be seen. Figure 4.12 shows the effect of the PM loading on the deviation in back pressure due to the PM distribution, calculated as

$$D_{dist} = \left(\frac{\Delta P_{\exp}}{\Delta P_{even}} - 1 \right) \times 100 \qquad (4.25)$$

where D_{dist} is the deviation due to distribution (%), $\Delta P_{\exp}$ is the projected back pressure of an exponentially loaded foam, ΔP_{even} is the projected back pressure of an evenly loaded foam. Figure 4.12 shows that with no loading, there is no effect. The deviation becoming increasingly large in magnitude as the loading increases, up to

>5% with 2 g litre^{-1} loading. The maldistribution of PM loading tends to reduce the back pressure for a given average specific loading. This results from the first stages of loading having a greater effect on back pressure than the later stages, meaning that the more localised the PM concentration is, the lower the overall back pressure for a given filter.

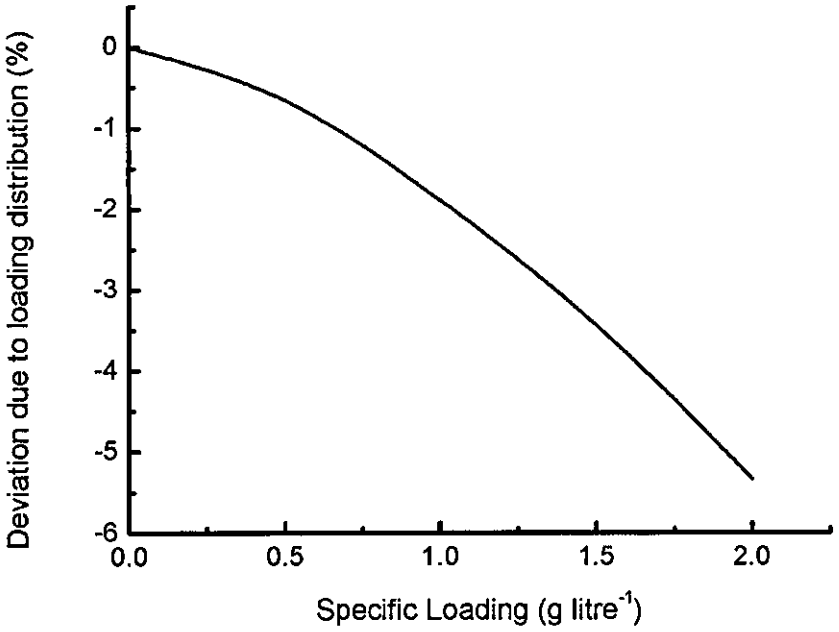

Figure 4.12. Predicted effect of maldistribution of loading on the back pressure of a 20 mm thick, ~400 µm pore size foam.

Figure 4.13 shows the deviation resulting from considering the changes in PM distribution (i.e. the effect of using the corrected kinetic coefficient from Equation 4.21) as the conceptual foam filter thickness is varied, calculated as

$$D_{corr} = \left(\frac{\Delta P_{corr}}{\Delta P_{uncorr}} - 1 \right) \times 100 \qquad (4.26)$$

where D_{corr} is the deviation due to the correction (%), ΔP_{corr} is the projected back pressure with the correction and ΔP_{uncorr} is the projected back pressure without the correction for changes in PM distribution. Figure 4.13 shows that projections for filtration thickness equal to the tested sample are independent of the correction, as the kinetic coefficient remains valid. For smaller filtration thickness the correction results in increased back pressure which is explained by considering the PM

distribution. With smaller filtration thickness, the variation of PM loading from upstream face to downstream face of the filter is lower than with higher filtration thickness, shown in Figure 4.14. Due to the higher sensitivity of the back pressure to low PM loadings, this increases the overall back pressure, an effect which is not considered without the correction used in Equation 4.21. Similarly, with higher filtration thickness than the tested sample, consideration of the changes in PM distribution result in reduced overall back pressure. By a similar argument, this is a result of the increased variation in PM loading.

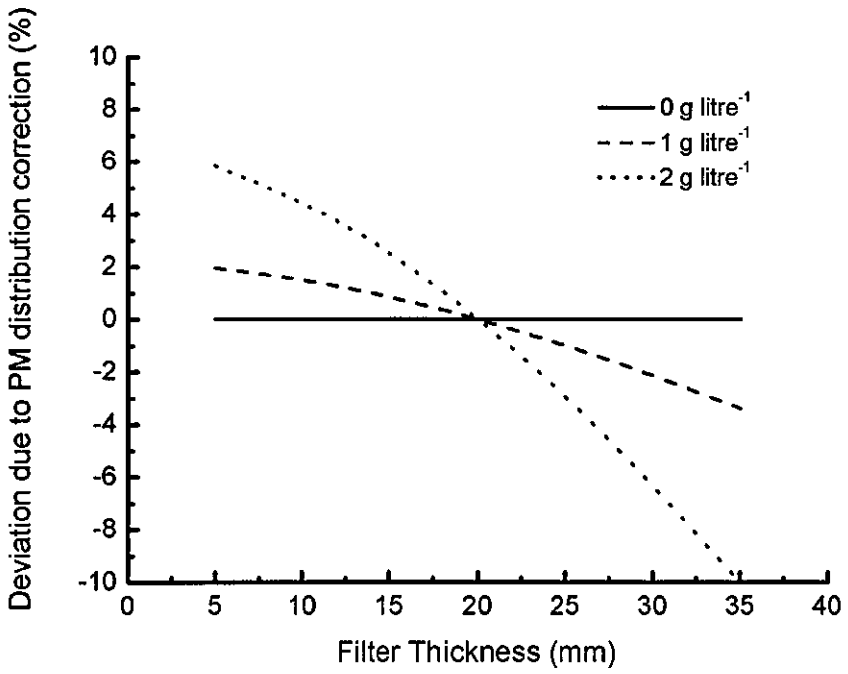

Figure 4.13. Predicted effect of considering changes in PM distribution with filtration thickness.

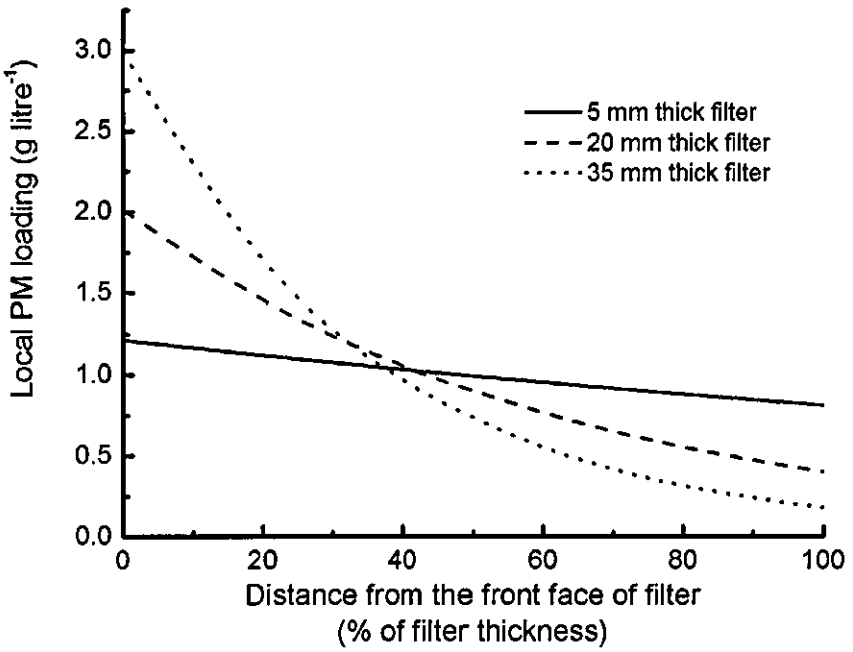

Figure 4.14. Graph showing the effect of filtration thickness on PM distribution.

4.4 Optimising the Gelcast Ceramic Foam DPF

There are three significant factors that are evaluated for optimisation of the Gelcast foam DPFs:

1. Back pressure
2. Filtration Efficiency
3. Filter Size

Optimising any one of these parameters tends to have a detrimental effect on the others. Minimising back pressure can easily be done by making a large filter with large pores. This leads to an undesirable filter with respect to filter size and filtration efficiency. Maximising filtration efficiency can be achieved by minimising pore size or making the filter thicker, leading to higher back pressure and larger filters respectively. Filter size can be minimised by making the filter thinner or reducing its diameter, reducing filtration efficiency or increasing back pressure respectively. These relationships can be summarised graphically by the triangle, shown in Figure 4.15. Design solutions can be found within this triangle, requiring a trade-off between all three of the parameters, but not optimum in more than one.

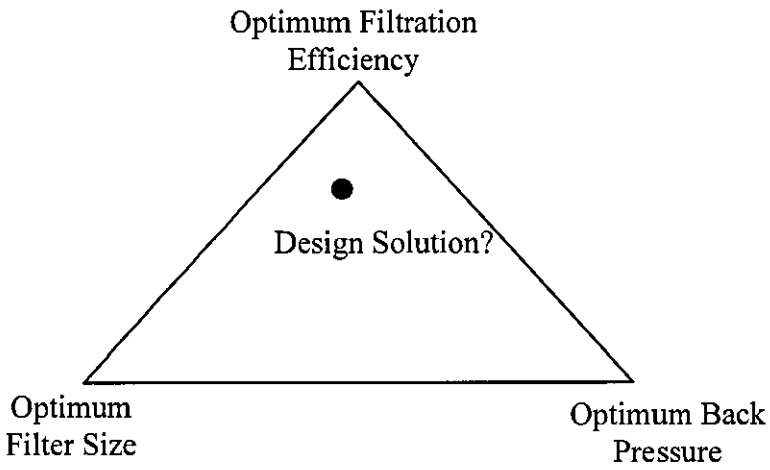

Figure 4.15. Design space relating to compromising between filtration efficiency, back pressure and filter size when designing a ceramic foam diesel particulate filter.

The compromise depends on design parameters such as pore size. Using the filtration efficiency and back pressure models discussed earlier in this chapter, a design space can be defined to make predictions of the performance that is achievable.

4.4.1 Design Limitations

There are a number of external factors that limit the macroscopic and microscopic geometry of gelcast ceramic foam diesel particulate filters. A thin filter is more likely to fracture under the high exhaust gas back pressures anticipated. Dytech Corporation (the gelcast ceramic sample manufacturer) recommended a minimum thickness of 10 mm based on a combination of their predictions of manufacturing losses and vibrational mechanical strength.

A reasonable upper limit for the back pressure in the exhaust system of a heavy duty engine is approximately 15 kPa (Heaton, 2007). To account for other losses in the exhaust system, the target upper limit of the back pressure across the filter at rated speed and load of the engine (i.e. maximum flow space velocity) is considered to be 10 kPa.

4.4.2 The Design Space

The back pressure and filtration efficiency relationships have been used to generate design spaces for conceptual foam filter designs. The design spaces for a 0.03 m^2 and 0.06 m^2 area filter are shown in Figure 4.16. The 0.03 m^2 design space can be seen to be significantly smaller than the 0.06 m^2 design space due to the increased back pressure and consequently the reduced PM holding capacity at peak allowable back pressure. The 0.06 m^2 plot shows that:

1. For a given filtration efficiency, the larger pore size foams require a larger filtration volume (i.e. filtration thickness).
2. For a given filtration efficiency the larger pore size foams offer a higher specific PM holding capacity than smaller pore sizes.
3. For a given pore size foam, reducing the required filtration efficiency reduces the filtration volume and increases the specific PM holding capacity.

With any two design requirements (out of filtration efficiency, filtration volume, pore size and specific loading capacity) the design space can be used to determine the other two design parameters. For example, if a filter must have an 80% filtration efficiency and be able to hold up to 3 g $litre^{-1}$ PM then the design space can be used to establish that with a 0.06 m^2 filter, the filter would need ~550 μm average pore size, giving a filtration volume of approximately 1.8 litres.

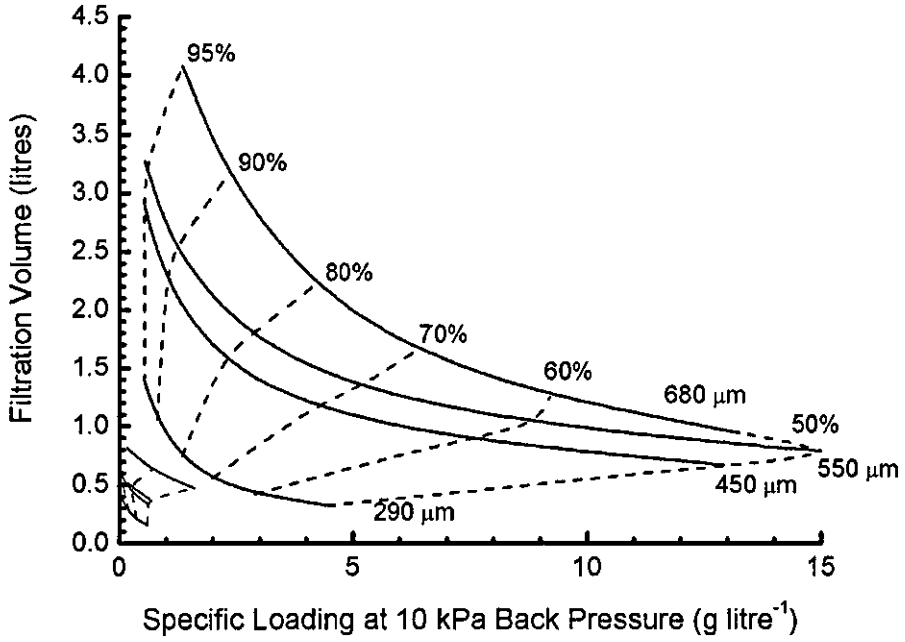

Figure 4.16. Design space for 0.06 m^2 (black) and 0.03 m^2 (red) flow area filters.

As with many engineering applications, the optimum design is application dependent. The new design space and methodology presented, however, offers a comprehensive tool to support the design process of a gelcast ceramic foam filter.

4.5 Comparison of Gelcast DPFs with Current State of the Art

The data in Figure 4.16 can be used to compare the performance of a number of conceptual foams to current DPF state of the art. Table 4.4 shows a comparison of a gelcast ceramic foam filter with a comparable size and PM holding capacity to a monolithic WFF. The gelcast foam clean filter back pressure can be seen to be 175% that of the WFF, although the PM loading capacity (an indication of the effect of PM on the absolute back pressure) is comparable. The 80% filtration efficiency of the gelcast ceramic foam concept is considered sufficient for 2007 and 2010 engine technology to meet 2010 US emission standards (based on Johnson, 2006) with the advantage of geometric optimisation of the filters to suit consumer packaging requirements.

Table 4.4. Comparison of an example gelcast ceramic foam with monolithic WFF.

Comparator	Monolithic WFF	Comparable Gelcast Foam
Clean Filter Back Pressure (kPa)	~2	~3.5
Loading Capacity (g litre^{-1})	~6	~6
Filtration Size (litres)	~2.5	~2.5
Filtration Efficiency (%)	>95	~80

The design space in Figure 4.16 also shows the capability of thin filter sections to achieve high filtration efficiency, for example 90% filtration efficiency can be achieved with a 17.5 mm filtration thickness and 290 μm foam. This is a 1.05 litre filtration volume reducing filter cost and filter canister volume when compared to the equivalent WFF.

The two conceptual foams discussed in this section have been compared to previous foam technology in Figure 4.17. This shows that the gelcast ceramic foams do offer comparable performance to alternative foams with the advantage of reduced filtration thickness and increased strength. The previous gelcast work presented by Hughes (2003) shows better performance than the current projections. This is attributed to the porosity of the foam samples since this research has optimised 80% porous gelcast ceramic foams while Hughes considered foams samples of up to 94%. The methodology developed in this research can be applied effectively to other foam porosities in the future.

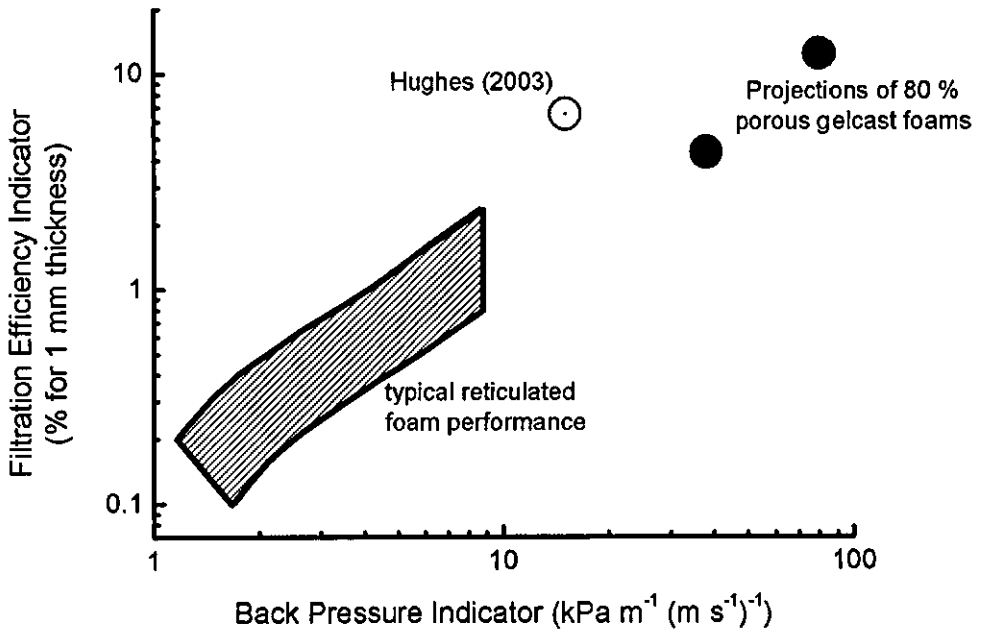

Figure 4.17. Comparison of gelcast foam projections to state of the art foam DPF performance.

4.6 Concluding Remarks

Chapter 4 has investigated the performance of gelcast ceramic foams. A new method for predicting the performance of PM loaded gelcast ceramic foams has been developed and applied to create a design space for future gelcast foam DPF design. The methodology can also be applied to any depth bed type filters. Chapter 5 now discusses and develops the fundamentals of the electric discharge regeneration technique which aimed to increase regeneration effectiveness and improve understanding.

CHAPTER 5

FUNDAMENTALS OF AUTOSELECTIVE REGENERATION OF PM

5.1 Previous Work

The use of atmospheric pressure electric discharges by Garner and Harry (1998) demonstrated that electrical discharges could effectively remove PM from a filter surface and led to an EPSRC grant to further investigate the potential of the Autoselective technology. Subsequent work by Proctor (2006) demonstrated that atmospheric pressure glow discharges have the potential for regenerating a filter with a regeneration efficiency of up to ~40 $g\,kW^{-1}\,h^{-1}$, which is more competitive than most systems reported in the literature discussed in Chapter 2. This compared to

efficiencies of up to 0.1 g kW^{-1} h^{-1} and 9 g kW^{-1} h^{-1} when using atmospheric pressure dielectric barrier discharges and corona discharges respectively.

Proctor (2006) developed a prototype regeneration system for regenerating monolithic wall flow diesel particulate filters. Rig tests demonstrated that the Autoselective regeneration was tolerant to the flow rates, gas temperatures, oxygen concentration and moisture concentration typical in diesel engine exhaust allowing the regeneration to be effective at all engine operating conditions. Monolithic WFFs were found to be sensitive to damage and required tight control of thermal flux into the ceramic material to achieve damage free regeneration.

The work presented in this chapter develops further the Autoselective regeneration technology with the aim of improving fundamental understanding and achieving gains in energy efficiency. An introduction to electric plasmas is followed by a description and investigation of the plasma characteristics pertinent to the Autoselective regeneration system. New methods for measuring heat flux from atmospheric pressure electric discharges are developed and used to determine the effect of gas flow, electrode spacing and electrode current on the heat flux characteristics of the Autoselective discharge.

5.2 Introduction to Plasmas

For efficient PM oxidation by heating, without the need for bypassing the flow through the filter, rapid heating is needed. Due to high instantaneous power demands, it is not suitable to heat up the entire filter in a fraction of a second, instead, small areas of the filter can be regenerated at a time. An electric discharge or plasma is often very hot, and focused in a localised region (e.g. lightning) and can be generated on a small scale with commonly available electronic components. This makes it an interesting solution for achieving efficient regeneration of DPFs without the need for by-passing the exhaust gas around the filter.

Solids, liquids and gases are considered the three most common states of matter, with plasmas as the fourth. In most solids, liquids and stable gases, the matter can normally be considered to be electrically neutral. Gas in plasmas are ionised,

meaning that a significant fraction of the atoms have less electrons than their neutral state, i.e. a plasma consists of neutral atoms, ions (positively charged atoms) and free electrons. The electrons can be freed from the orbit of an atom if they possess enough energy, often referred to as a temperature which can be achieved by heating or by applied electric fields. Figure 5.1 shows the gas temperatures needed to achieve varying degrees of ionisation from heating alone. When the entirety of the gas is at the same temperature the plasma is considered to be in thermal equilibrium and is called a thermal plasma. Temperatures of thermal plasmas limit their direct use on common DPF materials.

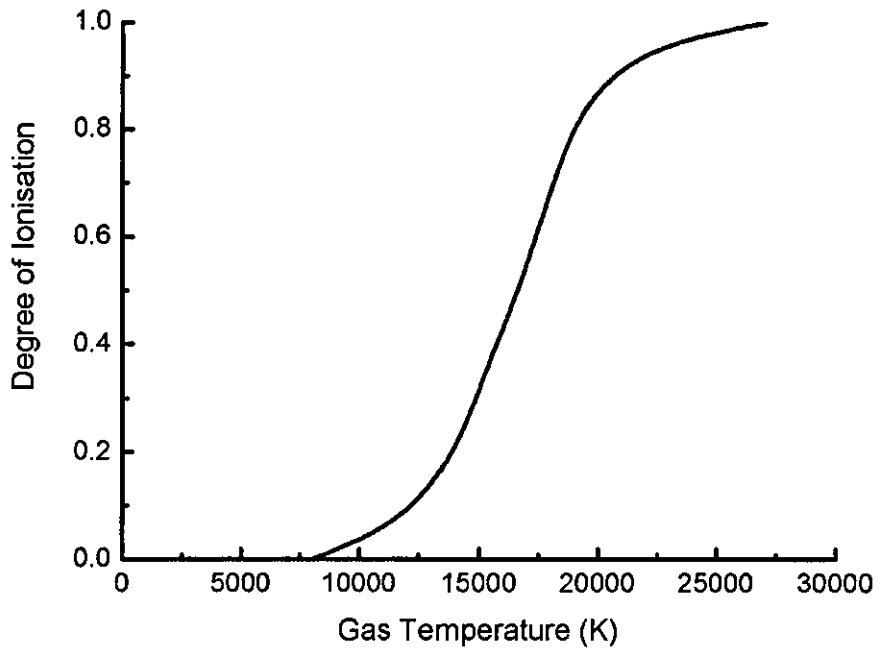

Figure 5.1. Degree of ionisation of Nitrogen as a function of temperature of thermal plasmas (adapted from Gross, 1968)

Applying an electric field to a non-ionised gas can accelerate the small number of free electrons in the gas to temperatures (or kinetic energies) high enough to free other electrons during electron-atom collisions. In this way gases can be ionised by creating large numbers of energetic electrons with only a small amount of energy input into the ions. In such electrical plasmas the average gas temperature (and ion temperature) can be close to room temperature, as observed in common technology such as fluorescent lighting. Due to the imbalance in energy between the electrons, ions and neutral gases these plasmas are called non-thermal plasmas, cold plasmas or non-equilibrium plasmas. Electrically generated plasmas can be in thermal

equilibrium if enough energy is coupled into the gas, for example with arc discharges. The generation of electrical plasmas allows direct conversion of electrical energy to concentrated thermal energy in a gas which cannot be achieved with other methods.

The range of energies and density of typical plasmas are shown in Figure 5.2. Most of the electrically generated plasmas can be seen to occur with electron energies between approximately 1 and 20 eV, since this is the range of energy required to free electrons in electron-ion collisions, causing a cascade of ionisation events, known as an electron avalanche. The electron density varies over a wide range corresponding to varying average gas temperatures.

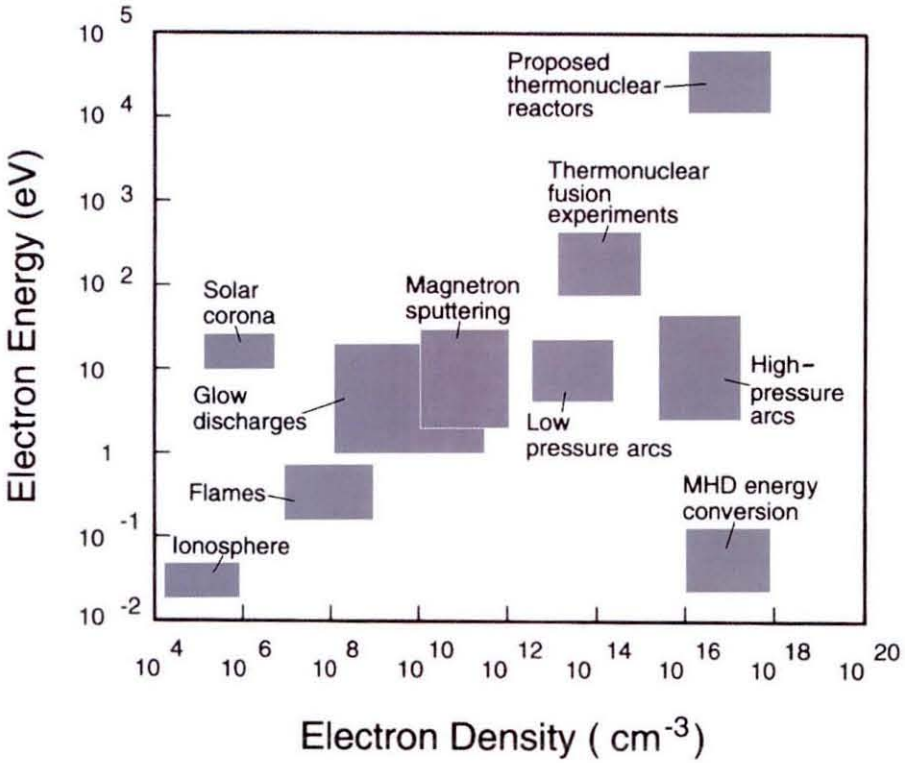

Figure 5.2. Different types of plasmas as a function of electron density and energy (Grill, 1994)

To create a stable glow discharge in a controlled manner an alternating electric field is used (i.e. an AC power supply). The discharge itself is not continuous although there is enough ionised gas in the discharge space to reduce the break down voltage of subsequent discharges. How the discharge is generated and typical current voltage characteristics are discussed in Section 5.3.

There is a vast amount of information in the literature regarding detailed plasma theory which is not reproduced in this work. General texts on electrical plasmas such as Grill, 1994 offer a more complete background and theory relating to this complex field. Here the focus will be on specific properties of plasmas pertinent to the Autoselective regeneration process.

5.3 Oxidation of PM with Plasmas

The electrical plasma is initiated at an electrode where the electric field is focused by the electrode geometry. The discharge then travels through the air to local conductive sites, the trapped PM, shown in Figure 5.3. At this contact point the environment is suitable to oxidise rapidly the local PM.

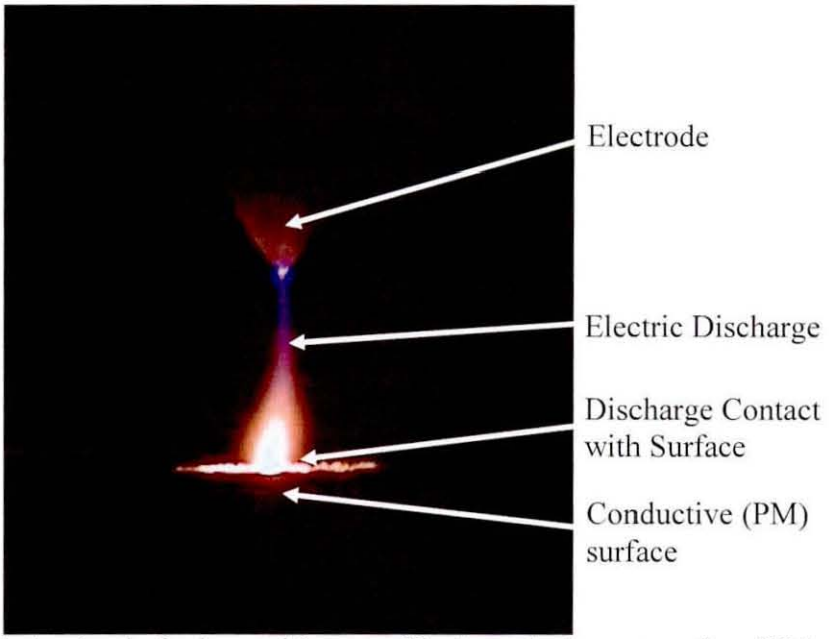

Figure 5.3. Photograph showing the fundamental features of the Autoselective regeneration of PM with plasmas.

There are a number of features of atmospheric pressure electrical discharges that can contribute to the regeneration of a DPF. These can be grouped into three main areas:

1. Thermal effects Heating of the filtered PM leads to high reaction rates with oxygen in the exhaust gas.
2. Chemical effects Generation of reactive gas species and ions within the discharge column can increase oxidation rates, for example, generation of

monatomic oxygen which has been shown by Rosner and Allendorf (1965) to be up to 80 times more reactive with carbon than diatomic oxygen.

3. Physical effects Diesel particles can accumulate charge and experience a force due to the electric fields generated by the high voltage on the electrodes. If the electrostatic forces are large enough, trapped PM can be released back into the gas stream. Electron and ion bombardment can also erode the surface of the PM.

It is likely that the PM experiences a combination of these effects. For example, the physical removal of trapped PM from the filter surface into the hot discharge column increases the PM temperature and leads to oxidation through thermal effects. Identifying the relative importance of these effects is necessary to direct the optimisation of the regeneration system. The following sections investigate the characteristics of the Autoselective discharge and, using new methods for measuring heat flux from electric discharges, shows that the thermal effects are a major cause of regeneration using the Autoselective system.

5.3.1 Plasma Characteristics

The electrical discharge is created between a high voltage and ground electrode using a resonating power supply designed and manufactured by Ladha (2007). The main components are shown in Figure 5.4. A typical high voltage circuit that relies only on the turns ratio of the transformer to reach electrode voltages up to 10 kV can be downsized significantly by using a resonating electrical circuit where the output voltage (or gain) is a strong function of frequency. For a typical electrode arrangement the effect of frequency for the transformers (shown in Figure 5.4) driven by a square wave is shown in Figure 5.5, achieving voltage gains of up to 10 times more than from the turns ratio alone. The magnification due to resonance is a strong function of the electrical load on the circuit and changes for different electrode arrangements.

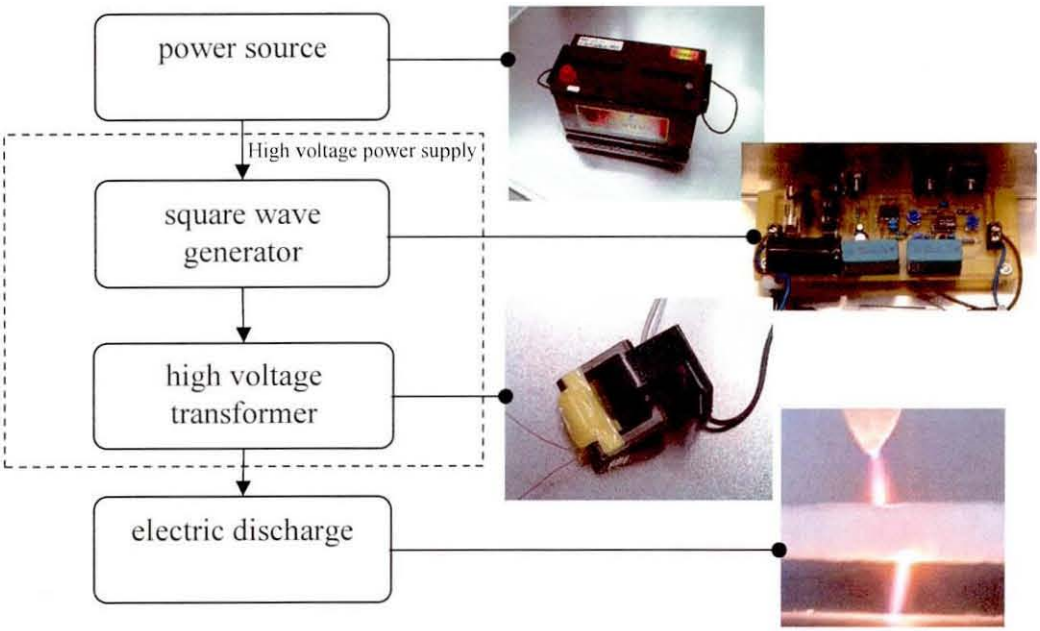

Figure 5.4. Schematic showing the electrical system used to generate the plasma.

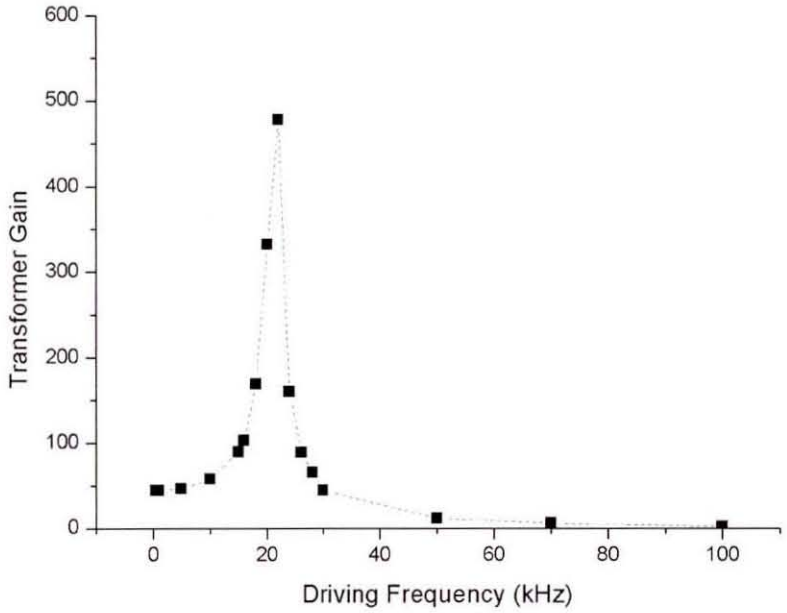

Figure 5.5. Power supply gain (proportional to voltage) as a function of frequency for a typical electrode arrangement.

This type of power supply creates a glow discharge comprising of an ionised column of gas that varies in diameter depending on the current flowing through the discharge. Close to the electrode the diameter of the discharge column reduces significantly increasing the current density and gas temperature in these regions.

Operating at frequencies ~20 kHz leads to the discharge operating semi-intermittently. This means that each time the voltage rises the discharge strikes and every time the voltage falls the discharge extinguishes, although it may leave ionised or excited particles that reduce the break down voltage for the next cycle. A typical voltage and current waveform are shown in Figure 5.6. The current shows a number of features:

1. With rising and falling voltage there is a minimum voltage required before any significant current flows. This is the voltage required to break down the gas after the previous discharge was extinguished.
2. The current is not directly proportional to the voltage. This is a result of the effective resistance of the discharge changing throughout the cycle.

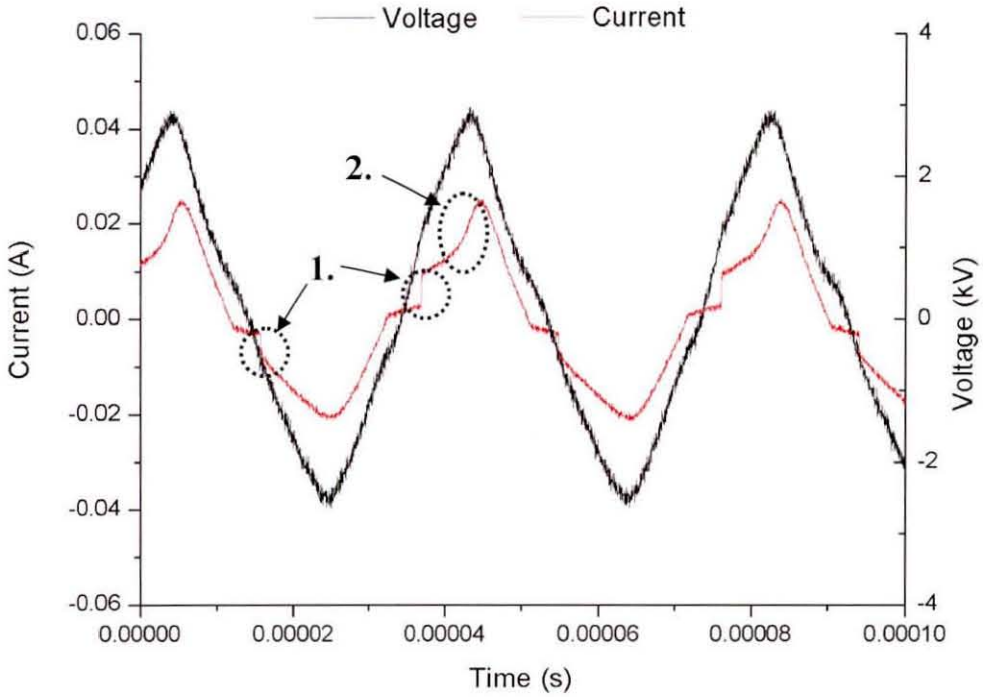

Figure 5.6. Typical voltage and current waveforms for atmospheric pressure glow discharges generated using a resonating circuit. '1.' and '2.' refer to the numbered points in the text.

An improved understanding of the interactions of the discharge with the electrodes was achieved by analysing the light emitted from the system using a calibrated optical emission spectrometer. The details of the equipment and calibration procedure is given in Appendix A. Figure 5.7 (a) shows the typical wavelength composition of the light emitted from the discharge contact regions showing the broadband light with a number of spectral lines generated by the plasma. Figure 5.7

(b) shows the light from the plasma column as mostly spectral peaks, with a major peak in the yellow wavelengths and a series of peaks in the blue and violet wavelengths. This shows that the surface temperatures are high, and can be quantified by comparing the curve with predicted spectral emission from black body radiation.

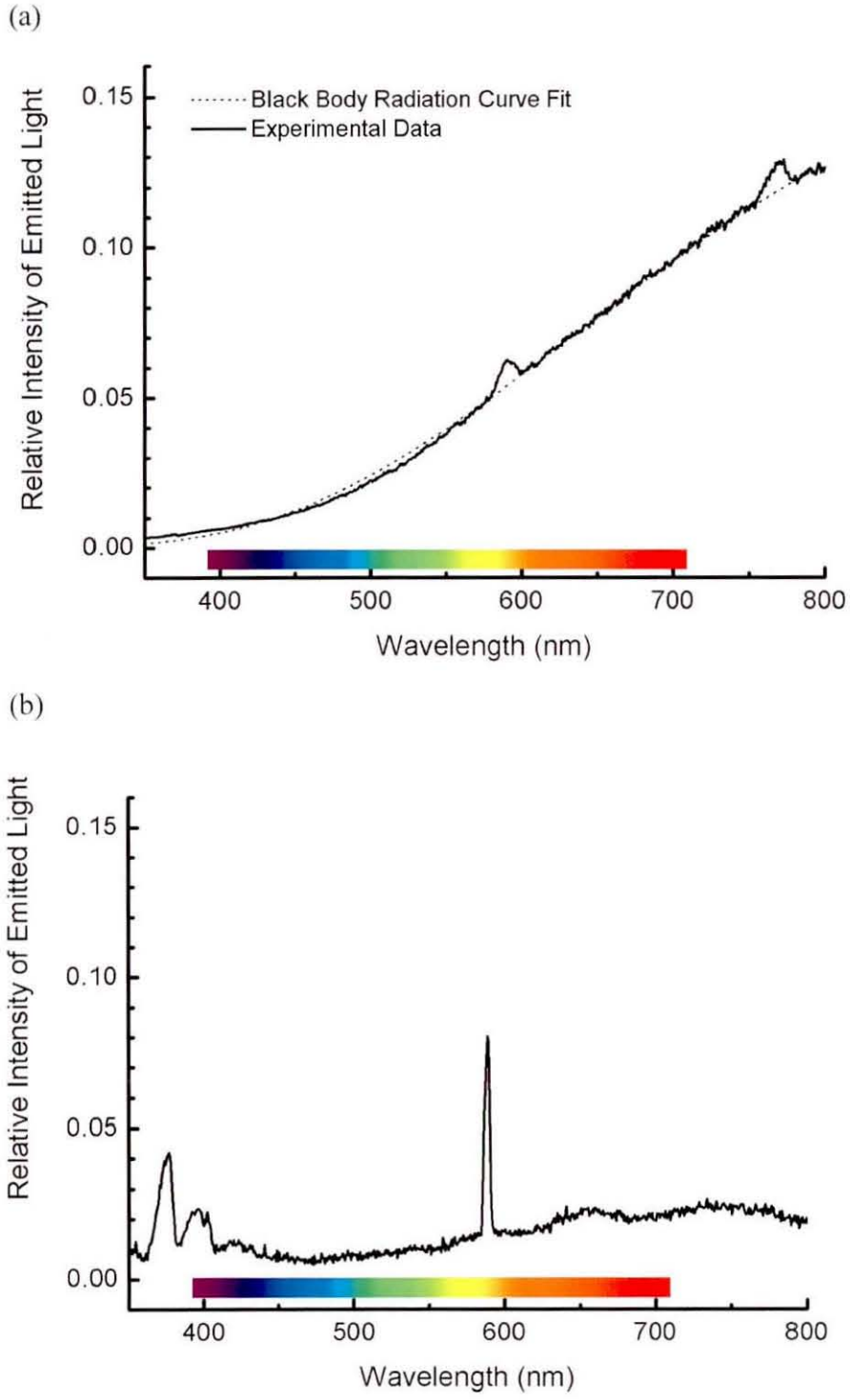

Figure 5.7. Plot of light intensity as a function of wavelength for (a) the discharge root (b) the plasma column close to the surface contact.

Black body radiation can be predicted by the Planck Radiation Formula:

$$Energy \propto \frac{2hc^2}{\lambda^5}\left(\frac{1}{e^{\frac{hc}{\lambda kT}}-1}\right) \qquad (5.1)$$

where h is the Planck constant (6.626×10^{-34} m^2 kg s^{-1}), c is the speed of light (2.998×10^{8} m s^{-1}), λ is the wavelength of the electromagnetic radiation, k is the Boltzsmann constant (1.381×10^{-23} J K^{-1}) and T is the temperature of the black body. Adjusting the magnitude to suit the units of the experimental data and the temperature to achieve a best fit gives the dashed line shown in Figure 5.8 (a). This corresponds to a surface temperature of approximately 2600 K which is enough to rapidly oxidise the local PM in atmospheric gas or diesel exhaust gas. This suggests that thermal effects on oxidation of the PM will be significant although this temperature would be strongly dependent on a number of factors such as material, contact duration and discharge power and current.

To confirm this theory it was necessary to quantify the amount of thermal energy applied to the soot and confirm whether this alone could oxidise the PM at the observed rates. A new method for measuring the heat flux from the electric discharge to solid surfaces was developed and the knowledge used to compare the discharge system with a comparable system that applies thermal energy without the chemical or physical effects associated with electrical plasmas. This method is now described.

5.3.2 Methodology for Measuring Heat Flux from Electric Discharges

Common techniques for measuring heat flux include energy balances, thin and thick film sensors and circular foil gauges. Electronic sensor technology has been developed that allows measurements on scales down to <10 mm^2 with thin film gauges (Rencz *et al*, 2004), which depend on measurement of thermal gradients across the sensor. A discussion of errors with this technique by Trethowen (1986) highlighted the importance of maximising the surface area and minimising the thickness of the sensor to minimise errors. To apply this to an electric discharge with

a surface area of less than 1 mm^2 will lead to significant errors in the measurement. A major problem with surface mounted sensors, circular foil gauges and thermocouple based measurements applied to electric discharges is the necessity to measure μV magnitude signals in an environment with high oscillating electric fields and potentials. This leads to a large amount of signal interference that prevents reliable measurements.

Use of non-contact thermal imaging techniques with thin and thick film surface sensor approximations has been discussed by Astarita *et al* (2005) who describe steady state and transient heat flow theory to derive heat flux from temperature measurements. Applying this technique to a specific geometry in the discharge environment allowed measurement of plasma to surface heat flux without the need for approximations of conduction, convection or radiation from the surface.

A control volume can be defined anywhere within the solid electrode, with a surface that coincides with the discharge-electrode contact area. The internal energy of the control volume is

$$U = \int \rho c_v T dV \qquad (5.2)$$

where U is the internal energy of the control volume, ρ is the material density, c_v is the specific heat capacity, T is the material temperature and V is the volume. When this system is in thermal equilibrium the net heat flux into the control volume is zero. If the system is in thermal equilibrium when the discharge is in contact with it, at the instant the discharge is switched off the convective, radiative and conductive heat flux away from the control volume will remain the same as during the previous thermal equilibrium. This is because all the heat flux to and from the system, with the exception of that from the discharge is a function of the material temperatures which are constant until just after the instant the discharge is extinguished.

This interruption to one of the modes of heat flux into the control volume leads to an imbalance where the control volume is losing internal energy at a rate equal to the imbalance in heat flux. The heat flux from the discharge can now be described as

$$\Delta Q = \left.\frac{dU}{dt}\right|_{t=0} \tag{5.3}$$

where ΔQ is the step change in power, equal to the heat flux from the discharge and t is the time after extinguishing the discharge. This can be represented graphically as the gradient of the transient plot of internal energy at the instant the discharge is extinguished, shown schematically in Figure 5.8.

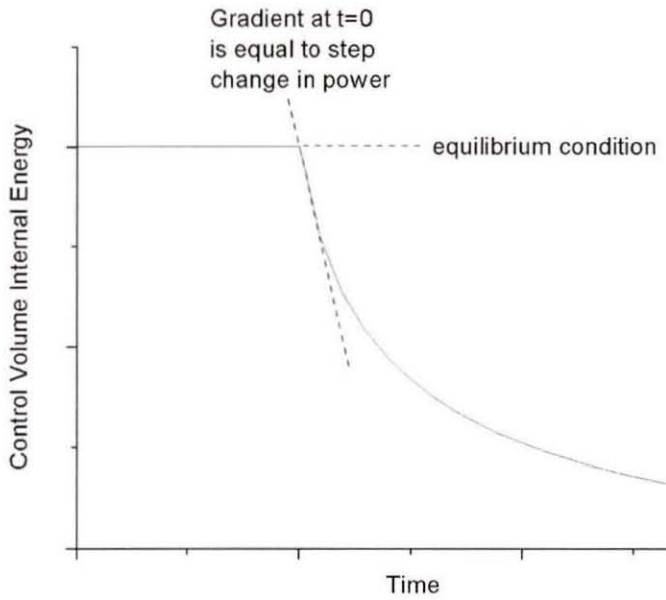

Figure 5.8. Schematic of the ideal transient behaviour of the internal energy of the control volume during a heat flux measurement.

Since this calculation requires knowledge of the internal energy of the control volume, and the internal energy is a function of temperature as in Equation 5.2, it was necessary to measure the temperature throughout the control volume. In practice a thermal imaging camera can only measure the surface temperature. The surface temperature can give a good approximation of the bulk temperature of the material if the solid is a thin structure where the heat flux is predominantly in the plane of the thin structure. This approximation is justified in Appendix B. For this reason the electrodes are produced out of sheet metal, approximating a two-dimensional (2D) structure with the control volume being defined as covering a given area of the 2D electrode. A schematic of the electrode arrangement is shown in Figure 5.9. The electrodes have a small radius at the closest point to locate the discharge which

prevented the discharge contact point moving during the test. Discharge motion during the test would result in a quasi steady state, influencing the test validity.

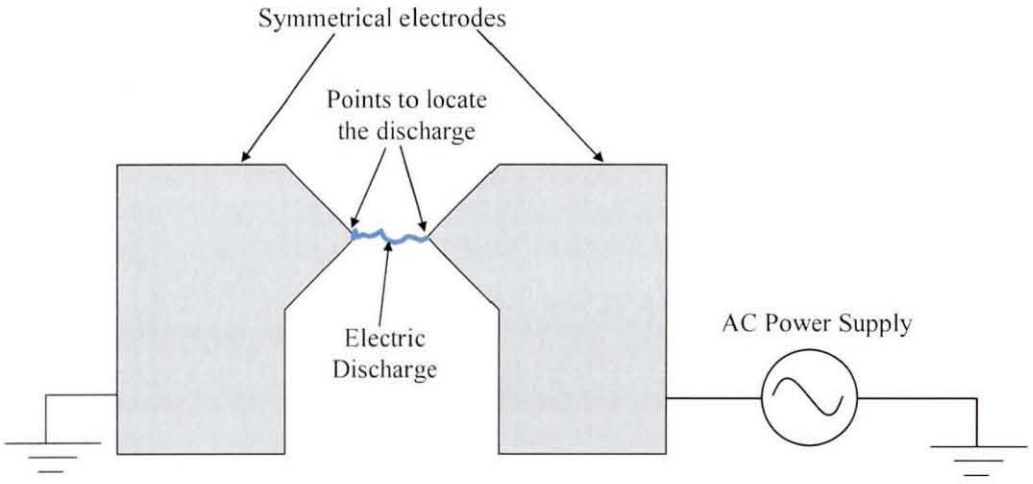

Figure 5.9. Schematic of the electrode arrangement highlighting key features required for measuring heat flux from electrical discharges.

The FLIR Thermovision A40M thermal imaging camera offered high resolution (320x240) temperature measurements across the electrode surface. For a constant thickness homogeneous material control volume, Equations 5.2 and 5.3 reduce to

$$Q = \rho c_v V \left.\frac{d\overline{T}}{dt}\right|_{t=0} \qquad (5.4)$$

where V is the size of the control volume and $\overline{T}$ is the volume averaged temperature of the control volume.

To the author's knowledge the calorimeter technique has not been applied in this way to measure discharge heat flux using thermal imaging camera. It is, therefore, necessary to validate the technique to determine its accuracy and to understand the experimental errors. To do this a layered assembly with an embedded heating element, shown in Figure 5.10, was used. The heating element was positioned between two PTFE layers which themselves were between two mild steel layers. The assembly was held together using high temperature silicone adhesive. The arrangement was thin enough that the two-dimensional approximation was still valid

and that the surface temperature was a good approximation of bulk temperature. The symmetrical nature of the setup meant that the surface temperatures should be the same regardless of the side they were viewed from.

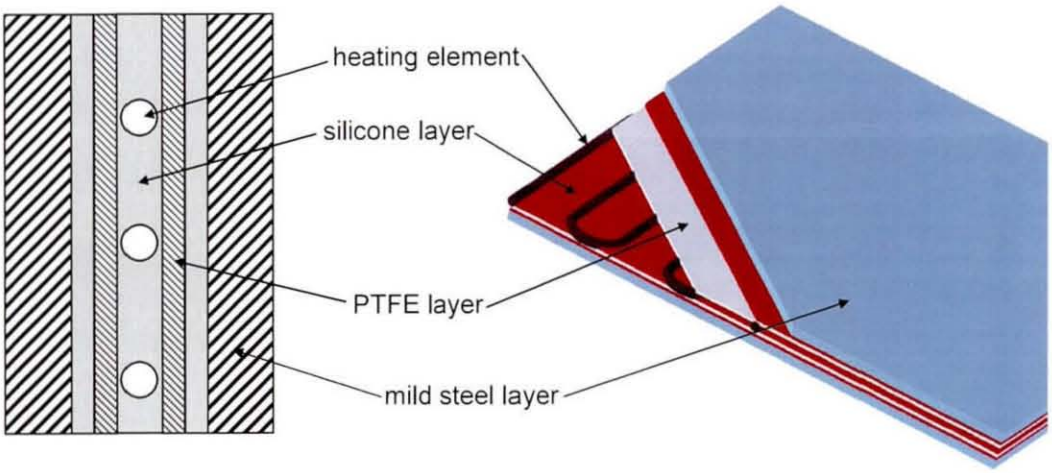

Figure 5.10. Schematic showing the cross section and sectioned pictorial view of the layered structure used for the validation.

The heating element spanned <25% of the surface area of the test sample, as shown in Figure 5.11. The element was made from 50 Ω m^{-1} resistance wire connected to low resistance copper wire at the edge of the structure. This ensured that the heat generated by current flow through the wire was nearly all within the layered structure, meaning it should be able to be measured using the calorimeter method described previously. The power input measured using the thermal imaging equipment was then compared to the power measured by calculating the product of the current and voltage applied to the heating element.

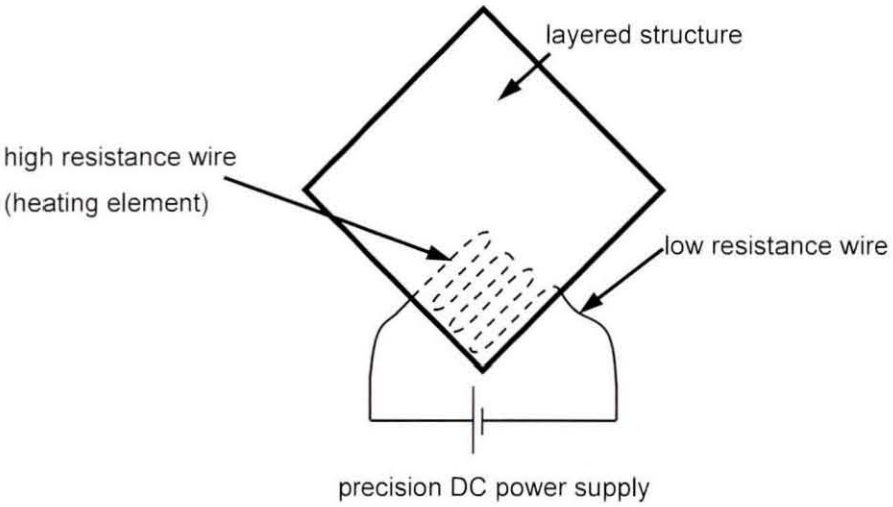

Figure 5.11. Schematic of the layered structure with the heating element used for the calorimeter validation tests.

A DC power supply was used to deliver between 2 and 10 W to the heating element. The surface emissivity was calibrated by a test point on the surface by comparison of the thermal imaging camera temperature with a K-type thermocouple reading. The power was applied until a steady state had been reached and the power supply switched off. A typical thermal image from the test is shown in Figure 5.12. The control volume boundary is highlighted, with a surface that was prepared by rubbing the oxide layer off with 150 grit emery cloth. The other regions in the image were not calibrated.

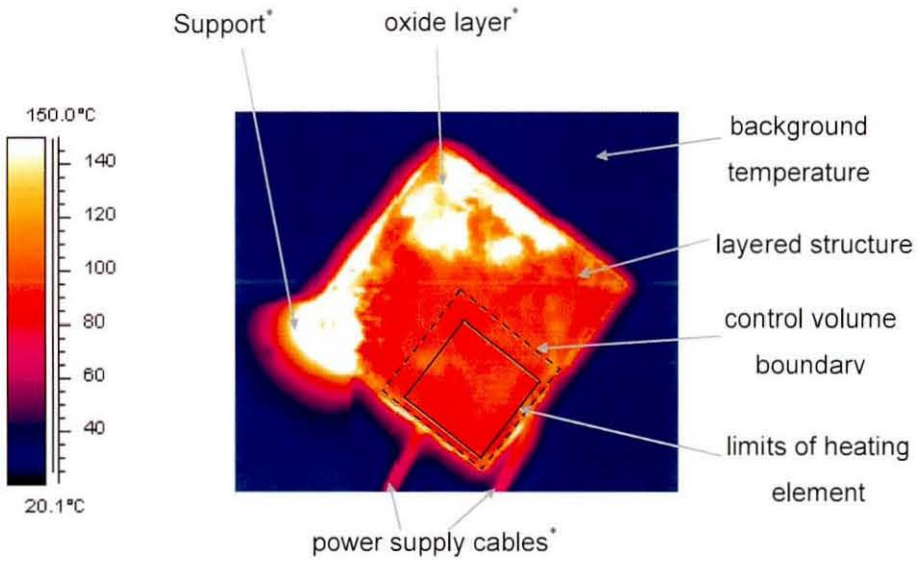

Figure 5.12. Example infrared thermal image from proof of concept tests. * denotes regions for which the emissivity was not calibrated.

An example plot of the variation in average temperature over time during the test is shown in Figure 5.13. The steady state was reached before the data was recorded so the average temperature remained constant until the power to the heater was switched off.

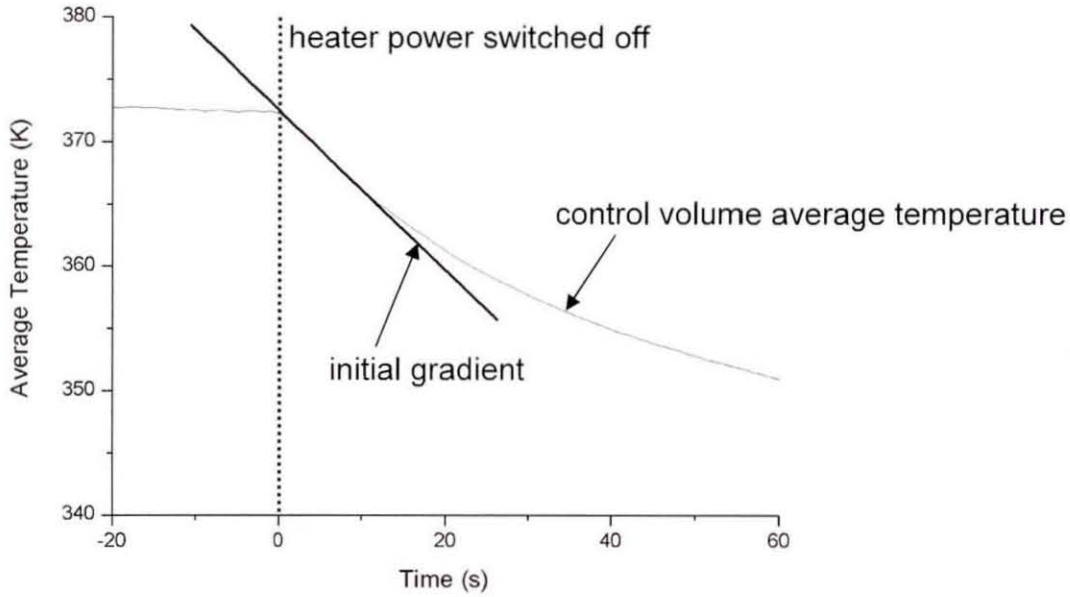

Figure 5.13. Example average temperature data as a function of time for the proof of concept tests

The rate of change of volume-averaged temperature of the control volume was calculated from the first 5 seconds of the test directly from the thermal image. In this example it was equal to -0.73 K s^{-1}. Applying relevant material data and geometric data, shown in Table 5.1, allowed the calculation of the power from Equation 5.4 to be 9.07 W. This was comparable to the electrical input power, calculated from the applied voltage and current as 9.12 W.

Table 5.1. Summary of the data used for the proof of concept calculations.

Material	Width of layer /mm	Height of layer /mm	Depth of layer /mm	Volume of layer /m^3	Density /kg m^{-3}	Specific heat capacity c_v /J kg^{-1} K^{-1}	Number of layers	Heat capacity (mc_v) /J K^{-1}
Mild Steel	35	35	1.0	12.3×10^{-7}	7870[i]	480[iii]	2	9.256
PTFE	35	35	0.25	3.06×10^{-7}	2200[i]	1050[i]	2	1.415
Silicone	35	35	0.35	4.28×10^{-7}	1020[ii]	1030[i]	4	1.801
						Overall heat capacity for use in calculation (J K^{-1})		12.472

Sources: [i] Shackelford and Alexander (2001) [ii] Dow Corning material datasheet (2002) [iii] Janna (2000)

A comparison of the electrical heating power and power measured using the thermal imaging system is shown in Figure 5.14 for varying powers of the same order of magnitude expected from the electrical discharges. If both measurements had negligible errors, the data points would coincide with the solid line. Across the range of power the two measurements are closely comparable indicating that the thermal imaging based measurement technique is a valid non-contact method for calculating heat flux.

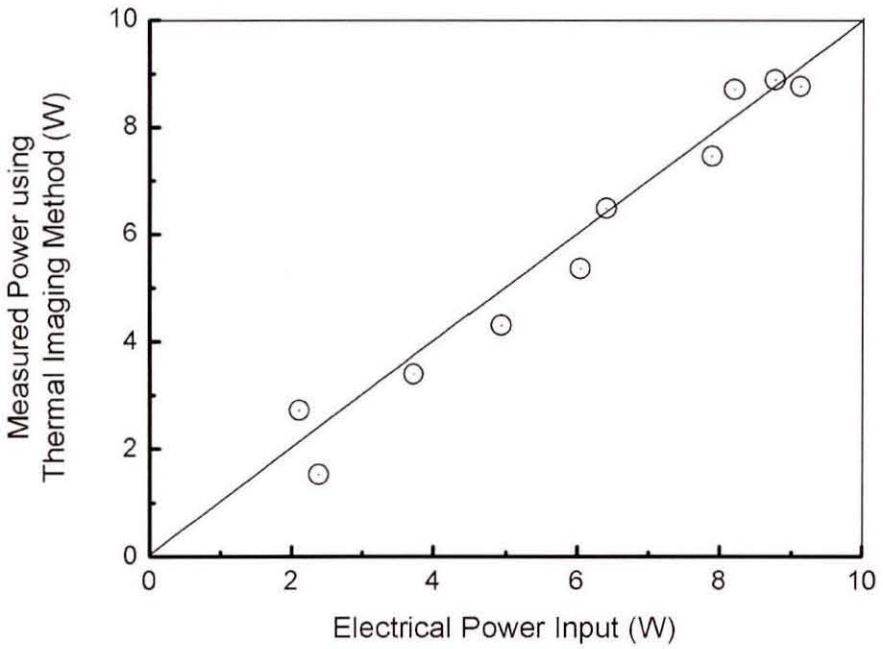

Figure 5.14. Comparison of electrical energy input and measured energy input using the thermal imaging technique.

Uncertainties in measurements of the heat flux from the electric discharge are

1. Calibration of thermal imaging equipment (i.e. emissivity).
2. Error in material properties (i.e. density and specific heat capacity)
3. Resolution of thermal imaging equipment (manifested in the definition of the control volume)
4. Signal noise on the temperature data.

Analysis of these uncertainties, shown in Appendix C, determined that the effect of signal noise and resolution of the thermal imaging equipment varied with the defined control volume size. Figure 5.15 shows the cumulative effect of these errors as a function of the control volume size. The minimum error was calculated to occur with

a control volume of between approximately 150 and 300 mm^3 for the proposed configuration. Control volumes above 350 mm^3 or below 150 mm^3 showed increasing errors mainly due to signal noise and poor definition of the control volume respectively.

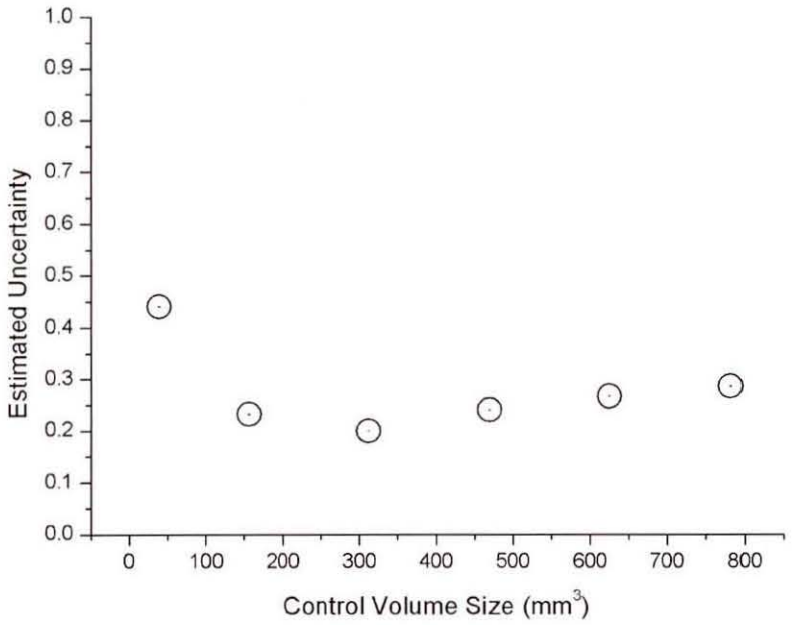

Figure 5.15. Plot of overall predicted error as a function of control volume.

For this reason, the control volume used for the study of heat transfer from electrical discharges was set at approximately 300 mm^3 encompassing the discharge electrode contact point and following the external boundary of the electrode. This is illustrated in Figure 5.16.

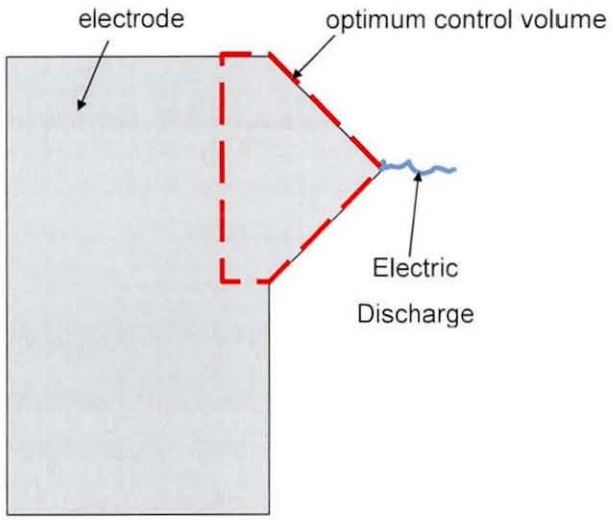

Figure 5.16. Chosen control volume boundary for heat flux measurements.

Measurements of heat flux using Equation 5.4 were taken for 24 discharges over a distance of approximately 5 mm with no forced convective flow. The results have been converted into a heating efficiency, defined as the amount of thermal flux into the electrodes divided by the electrical power consumed within the discharge,

$$\eta_h = \frac{W_{thermal}}{W_{elec}} \tag{5.5}$$

where η_h is the heating efficiency, $W_{thermal}$ is the thermal power input to the electrodes and W_{elec} is the electrical power input to the discharge. The histogram of the results is shown in Figure 5.17. The sample can be seen to approximate a normal distribution with an average value calculated as 24.8% and a standard deviation of 2.4% (i.e. plus or minus one standard deviation gives a span between 22.4% and 27.2%). This means that an electric discharge consuming approximately 40 W under the same conditions will typically have 5 W of thermal energy transferring into each electrode from the discharge.

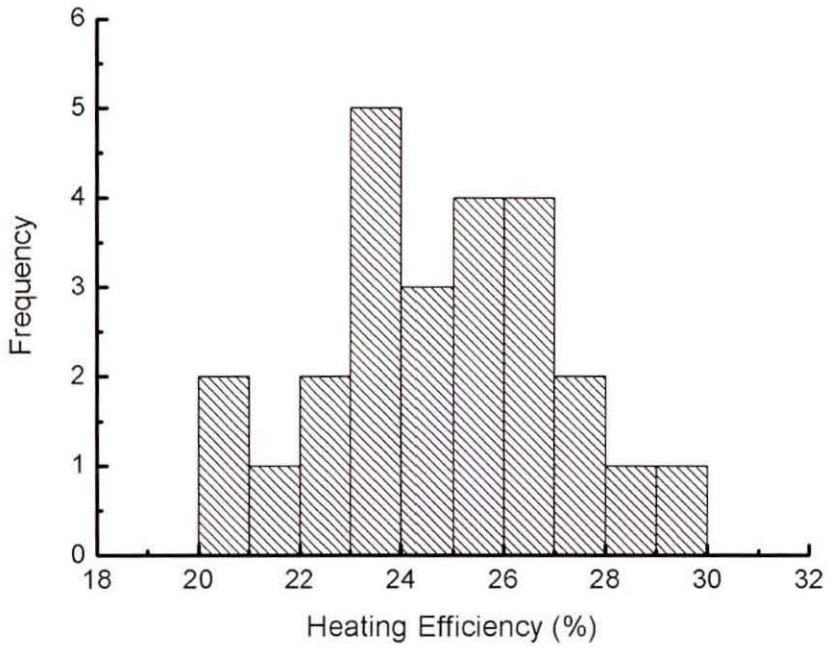

Figure 5.17. Histogram of heating efficiency measurements of a discharge over a 5 mm air gap with no airflow.

5.3.3 Thermal Heating Effect on PM Oxidation

A continuous wave low power green laser (532 nm Nd-YAG 5W) was used to apply a comparable thermal energy to an electric discharge to a carbon sample. Comparing the laser regeneration with electric discharge regeneration allowed confirmation that thermal effects are the major cause of regeneration. This testing is now described.

To simplify these experiments a single condition considering a typical stationary air discharge with a thermal heating power of 5 W was used which was comparable to the 5 W laser that was available for this testing. This corresponded to an overall discharge power of 40 W. Applying the discharge to a loaded filter for approximately half a second resulted in a relatively well defined regenerated area of 2.54 mm^2 (shown in Figure 5.18), which was taken to be an approximation of the area through which the majority of heat flux takes place. The specific power was calculated as

$$\text{Specific Power} = \frac{P}{A} = \frac{5}{2.5447} = 1.96 \text{ W mm}^{-2} \qquad (5.6)$$

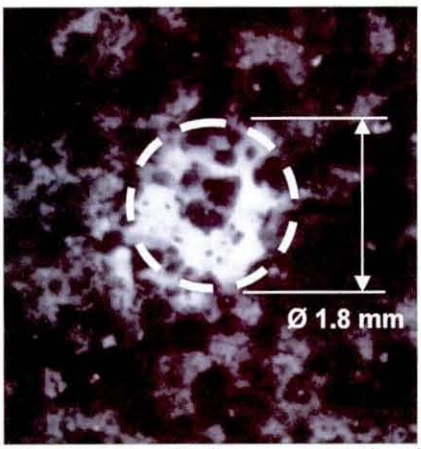

Figure 5.18. Affected area by a short duration discharge – approximating the area through which heat flux takes place.

Blocks of carbon black were prepared to allow the regeneration rate to be measured using pre- and post-weighing of the sample without the influence of the ceramic substrate. They were prepared by compressing carbon black (a soot substitute) into a mild steel holder of dimensions shown in Figure 5.19. The holder was filled with the PM compressed under a pressure of 250 kPa +/- 40 kPa to agglomerate the particles and allow the sample to be easily handled. Each sample was weighed before and after the tests to an accuracy of 1 mg using a chemical balance. Each sample had the

same environmental history and was weighed at each stage to ensure that the only mass loss was associated with regeneration.

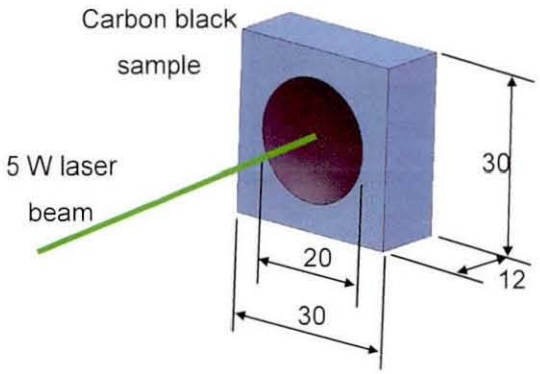

Figure 5.19. Test setup for laser regeneration tests including sample dimensions.

Figure 5.20 shows the surface of the regenerated carbon blocks from both (a) the laser regeneration and (b) the plasma regeneration. Due to the mobility of the electric discharge the plasma regenerated area is larger. The pre- and post-weighing data is shown in Table 5.3. It can be seen that during transportation there is negligible mass loss meaning that the measured change in mass is a result of applying the electric discharge or laser. Comparing the effect of the electric discharge and laser regeneration indicated that the direct thermal effects account for approximately 60% of the regeneration.

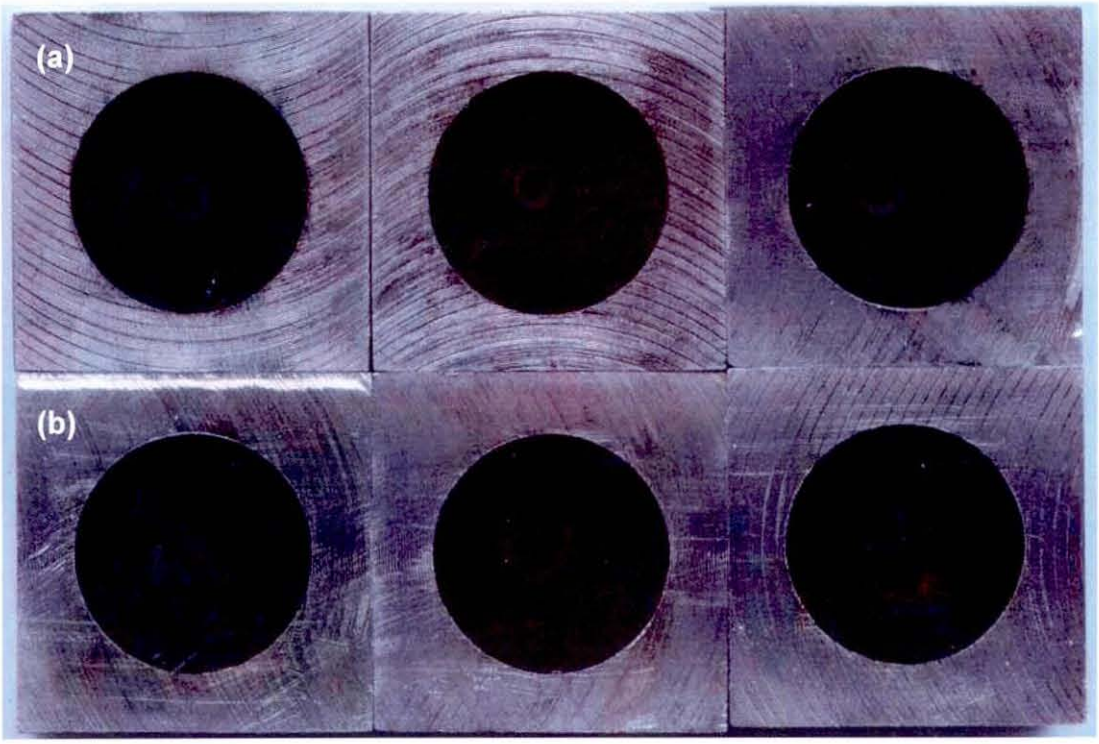

Figure 5.20. Regenerated carbon blocks using (a) 532 nm laser and (b) 40 W electrical discharge.

Table 5.2. Weight measurements of samples before and after regeneration tests.

Regeneration method	Initial mass /g	Mass after laser tests /g	Mass after discharge tests /g	Regenerated mass /g
Laser	63.174	63.166	63.166	0.008
Laser	63.179	63.171	63.170	0.009
Laser	62.763	62.755	62.755	0.008
Discharge	63.595	63.595	63.581	0.014
Discharge	62.734	62.735	62.720	0.014
Discharge	63.571	63.571	63.558	0.013

The mobility of the discharge, leading to a larger regenerated area than with the laser test, was shown to have little effect on the result. This was confirmed by repeating the laser test by dividing the two minute regeneration period into eight 15 second regeneration periods each on untested carbon (i.e. no previous regeneration). The mass loss was the same as the previous test to the degree of resolution of the scales.

The main errors associated with this comparison are related to experimental errors in matching the heat flux from the laser and discharge. This arose from variations in heat flux profiles, absorption characteristics of the carbon and errors in measuring the heat flux from the discharge. These differences manifested themselves as differences

in the distribution of regnerated PM, an estimate of which is shown in Figure 5.21. Despite these differences, these tests gave a strong indication that thermal effects were the major cause of regeneration when using the Autoselective discharge to regenerate diesel PM. This result directed the subsequent effort to optimise the regeneration rate by optimising the heating effect of the electrical discharge on the substrate, and is now discussed.

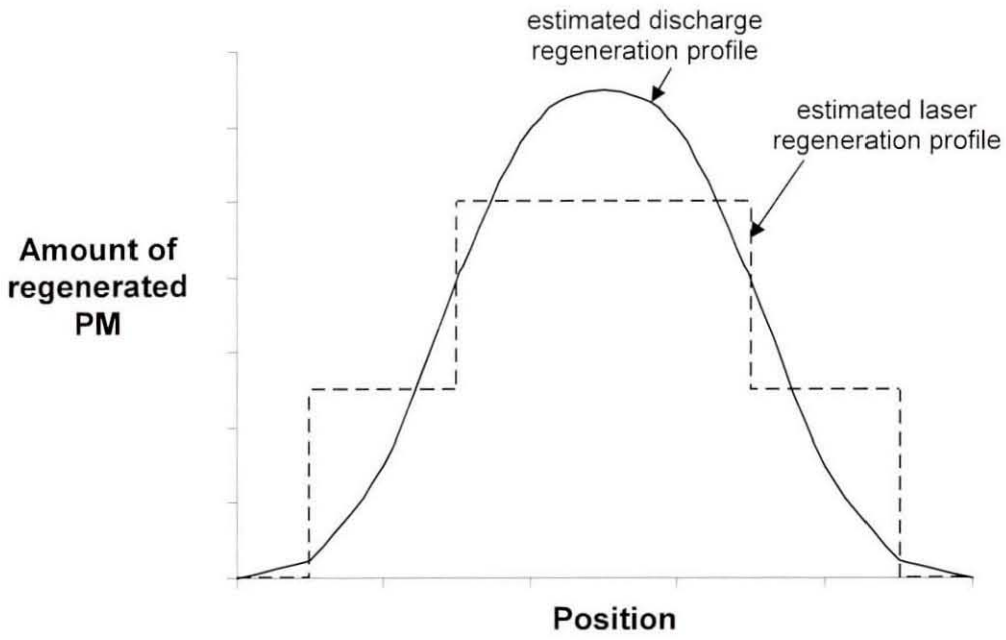

Figure 5.21. Estimated profiles of discharge and laser regeneration.

5.4 Maximising Regeneration Efficiency

The Autoselective discharge was shown by Proctor (2006) to be robust to the range of temperature, pressure and composition of diesel exhaust gases. Other environmental factors including flow direction and flow rate are known to have an effect on electrical discharges which needed understanding and relating to regeneration of PM. The study of the factors affecting the electric discharge follows.

5.4.1 Experimental Method

The influence on heating efficiency of the following factors were investigated:

1. Electrode spacing
2. Discharge current
3. Axial flow velocity
4. Perpendicular flow velocity

A typical flow rate for a gelcast ceramic foam filter discussed earlier is between 0 and 1 m s^{-1} depending on the engine speed, and load (and whether a bypass is being used). Canister design can affect the flow direction and it was therefore important to investigate the effect of the angle of the flow as well as the magnitude.

A two level full factorial experiment design was used and is summarised in Table 5.3. This test allowed the main effects and interactions between the factors to be identified.

Table 5.3. Variables and levels chosen for the heat flux experiment.

Variable	Low Value	High Value
Air gap size	5 mm	10 mm
Current	13 mA	20 mA
Axial flow velocity	0	0.6 m s^{-1}
Perpendicular flow velocity	0	0.6 m s^{-1}

An estimation of the number of replicates required to have a 95% confidence of recognising an effect of magnitude δ was found by using the statistical relationship (described in more detail by authors such as John, 1972)

$$N = 7.942\frac{\sigma^2}{\delta^2} \tag{5.7}$$

where σ is the typical standard deviation, δ is the required resolution (in the same units as σ) and N is the number of replicates required. This meant that to be confident that effects of greater than 0.05 (i.e. a resolution of 5% heating efficiency) will be recognised with a typical standard deviation on the data of 0.05 (found during preliminary tests) then approximately 8 replicates of each test point were needed.

The testing was carried out in blocks of 8 tests in a randomised run order to allow valid analysis using Stat-ease (Design of Experiments software).

The thermal imaging camera was set up to face the electrodes and the emissivity calibrated using a surface mounted thermocouple. The discharge conditions were set and the discharge operated until the electrode temperatures were close to their thermal equilibrium. This was defined by observing the temperature in real time at a point close to the discharge with the thermal imaging camera. The steady state criterion was defined in these tests as the observed temperature changing by less than 2 K in three minutes. An example image from the thermal imaging camera is shown in Figure 5.22.

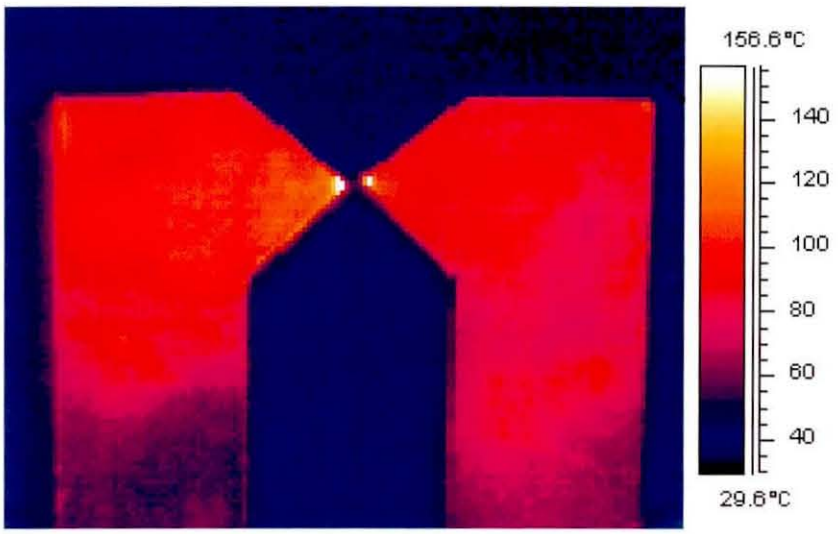

Figure 5.22. Example thermal image from discharge heating efficiency tests.

Once an equilibrium condition was reached the discharge was extinguished by switching off the power supply while recording the thermal images at a rate of 50 Hz. The control volume and subsequent calculation of the thermal flux into the electrodes was carried out based on the theory described in Section 5.3.2.

The tabulated results of the measurements are shown in Appendix D, as well as the randomised run order and the settings for the factors of each test point. A discussion of what these results mean and how it directed future work follows.

5.4.2 Data Analysis

The Design Expert software calculated the half normal plot for the factors and interactions shown in Figure 5.23. The plot shows the magnitude of the effect present in the data against the likelihood that the factor is statistically significant. The most important factors are those towards the top right hand corner of the plot. In this case the statistically significant factors have been highlighted and labelled. These are the factors that formed a model to predict the behaviour of the system. A square root transformation of the heating efficiency data was carried out to improve the model fit.

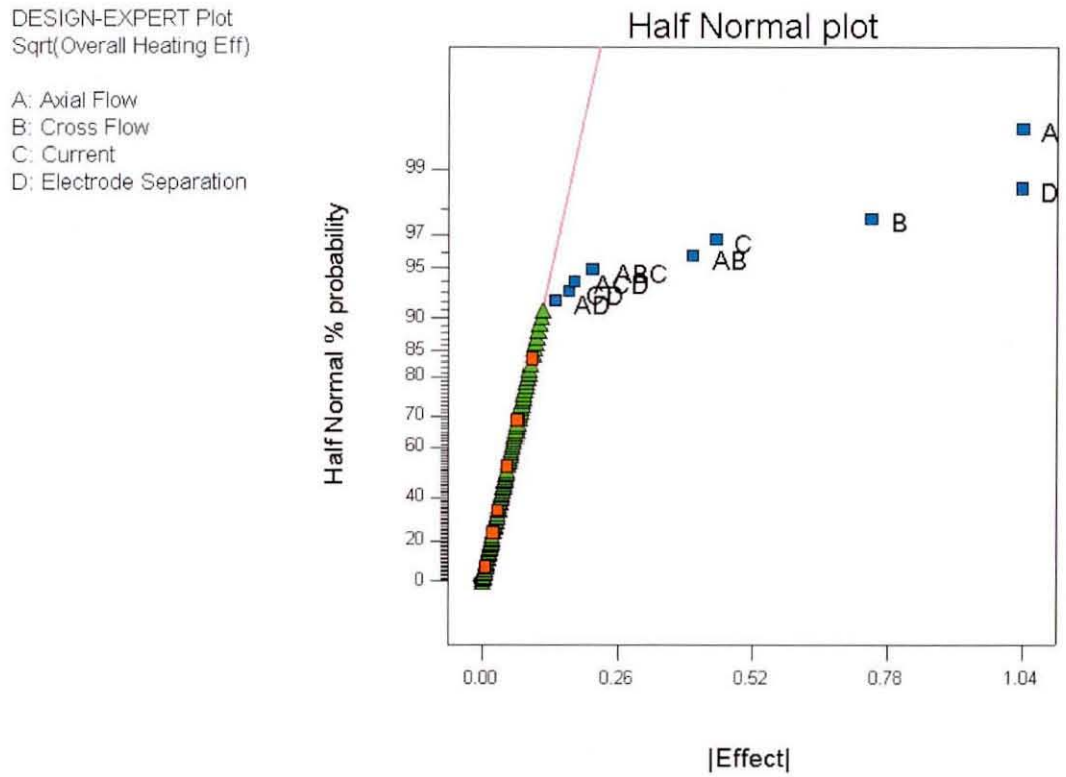

Figure 5.23. Half normal plot of the effects influencing the heating efficiency of the electrical discharge.

The final form of the factorial model representing the experiment, with the insignificant factors removed was

$$\eta_h = \left[10.28 - 7.822u_a - 3.42u_p - 0.2300I - 0.4644x + 6.333u_a u_p + 0.3198u_a I + 0.5323u_a x + 0.1145u_p I + 0.01672Ix - 0.2717u_a u_p I - 0.02690u_a Ix\right]^2 \quad (5.8)$$

where u_a is the axial flow velocity, u_p is the perpendicular flow velocity, I is the current, x is the air gap size and η_h is the predicted heating efficiency. The data shows that all the factors had an important effect on the heating efficiency of the discharge. All of the interactions identified, with the exception of that between axial flow and cross flow were small (although still present). The most significant observations were:

1. Increasing electrode spacing reduced the heating efficiency
2. Increasing current reduced the heating efficiency
3. Increasing flow rate reduced the heating efficiency

The residuals (difference between predicted and tested data) shown in Figure 5.24 for these tests appear randomly scattered implying that all major factors have been accounted for in the model and the residuals were a result of random experimental error. This supports the validity of the model within the tested range.

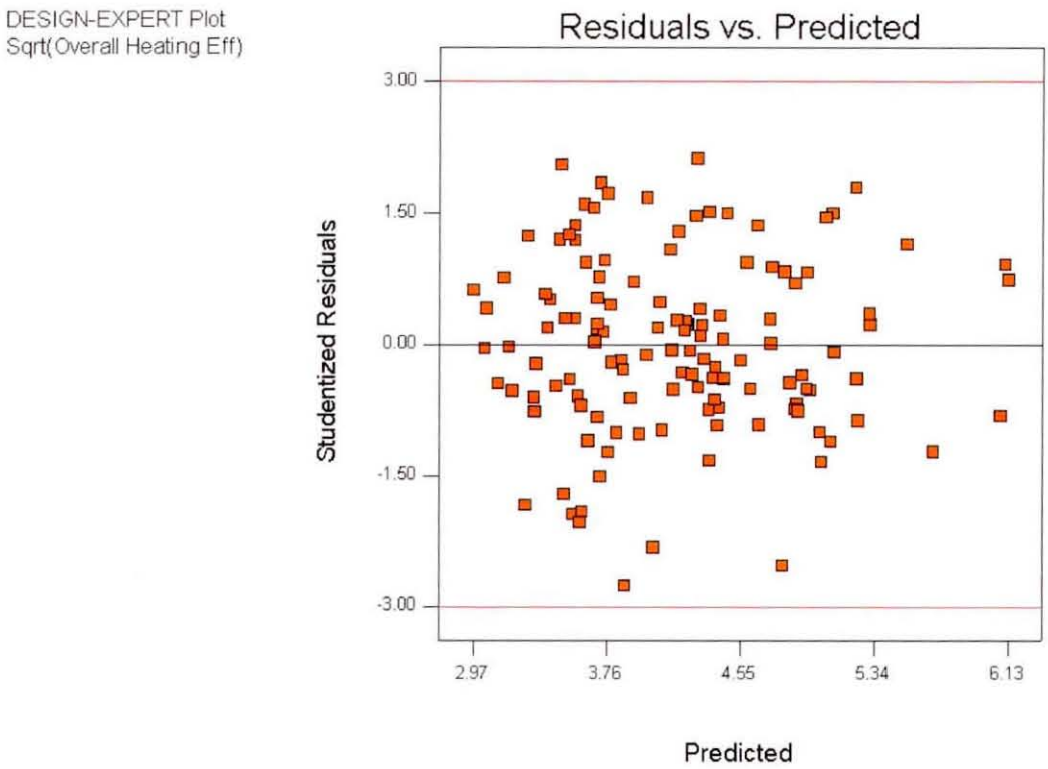

Figure 5.24. Plot of residuals versus predicted for the heat flux test data.

5.4.3 Effect of Electrode Spacing

Figure 5.25 shows the effect of electrode spacing in Equation 5.8. Increasing the electrode spacing reduces the heating efficiency under all conditions. This can be explained by considering the high temperature column of gas that forms the discharge. The heat will only flow from the discharge to the electrodes where it is in close proximity to it. As the electrode spacing increases, the fraction of the discharge in close proximity to the electrode reduces resulting in less efficient use of the electrical energy for heating. Maximising the discharge/material contact area will therefore maximise the heating efficiency and energy use.

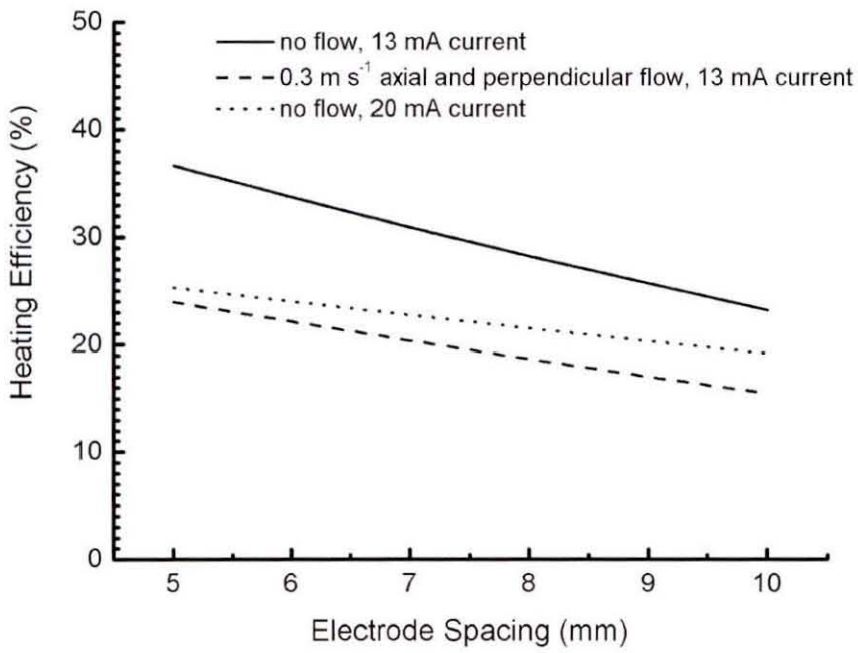

Figure 5.25. Effect of electrode spacing, based on DoE investigation.

5.4.4 Effect of Current

Increasing the current also reduces the heating efficiency under all conditions tested. This is shown in Figure 5.26. This can be explained by considering the restriction of the discharge at the electrode contacts. As the discharge current increases, the volume of the discharge increases more than the contact area at the electrodes. Therefore a larger fraction of the electrical energy will be used in the regions farther from the electrode, hence reducing the heating efficiency. The heating efficiency is more sensitive to current with no gas flow and small electrode spacing.

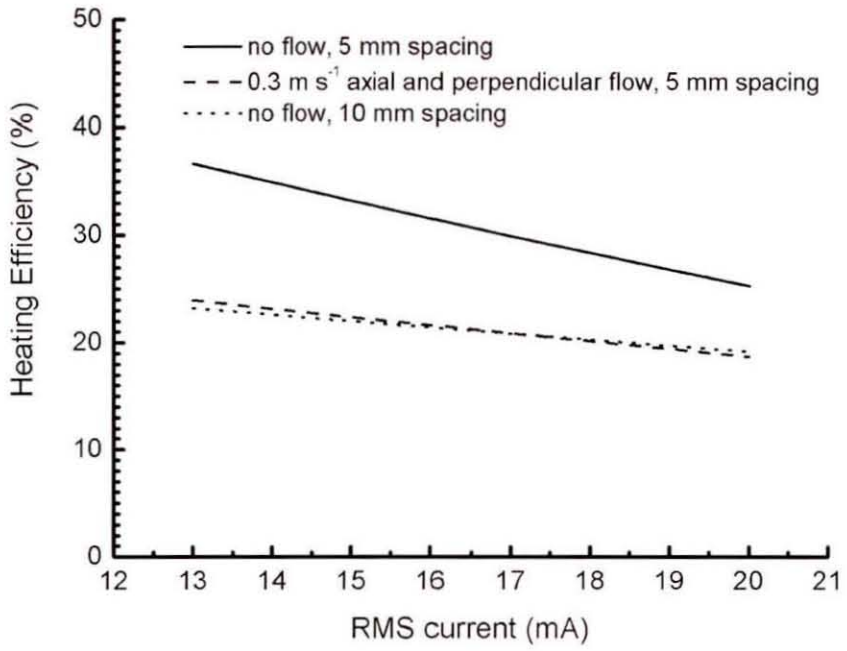

Figure 5.26. Effect of discharge current on the heating efficiency of the electric discharge.

5.4.5 Effect of Gas Flow

Axial and perpendicular flow velocity was considered separately in the DoE investigation. The effect of these parameters are shown in Figures 5.27 and 5.28. Both the axial flow and perpendicular flow act to reduce the heating efficiency. As either flow rate increases, the heating efficiency becomes less sensitive to the other flow direction. This implies the direction of the flow is not as significant as the magnitude of the flow velocity.

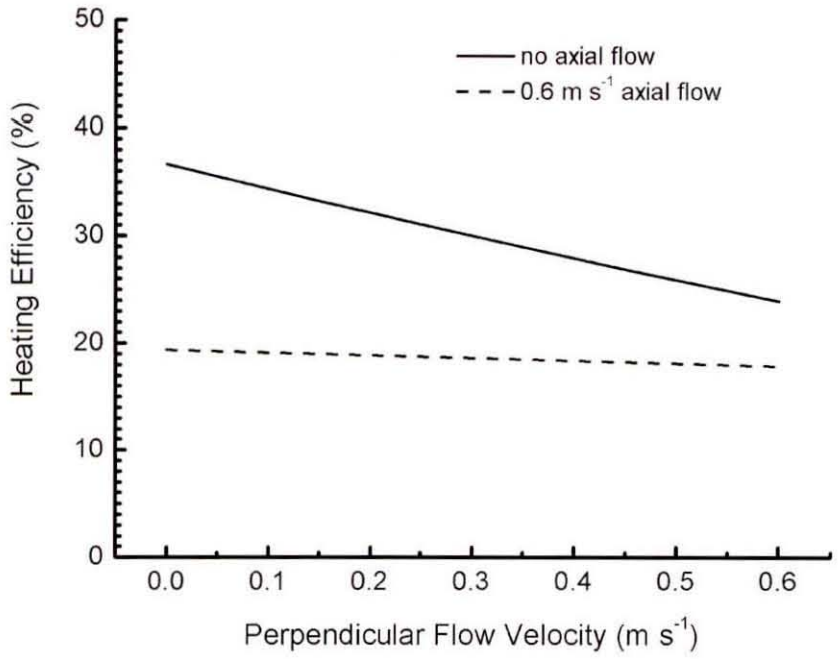

Figure 5.27. Effect of perpendicular flow velocity on the heating efficiency of the electric discharge.

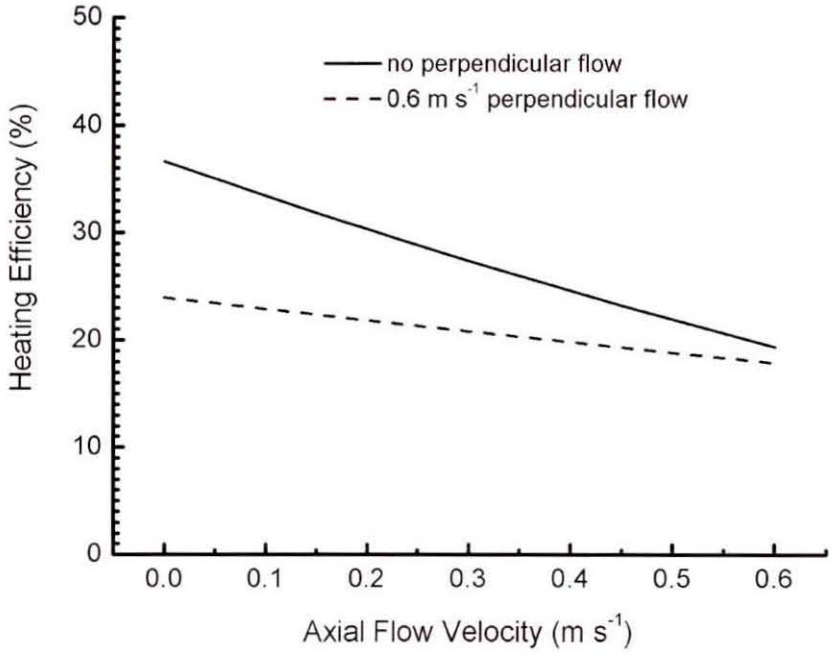

Figure 5.28. Effect of axial flow velocity on the heating efficiency of the electric discharge.

The behaviour of the heating efficiency for varying flow velocity can be explained by considering the heat flow to and from the electric discharge. Figure 5.29 shows a schematic of a hot column of gas which is constantly maintained at a fixed

temperature by energy input (electrical energy in the case of the discharge). Heat can flow away from the hot discharge either by conduction through the solid contacts, natural convection through the gas or forced convection through the gas. Radiation and conduction through the gas will also be present but is likely to be small in comparison. As the forced convective heat flux from the discharge column increases (i.e. increasing flow velocity) the fraction on electrical energy input to the electrodes reduces.

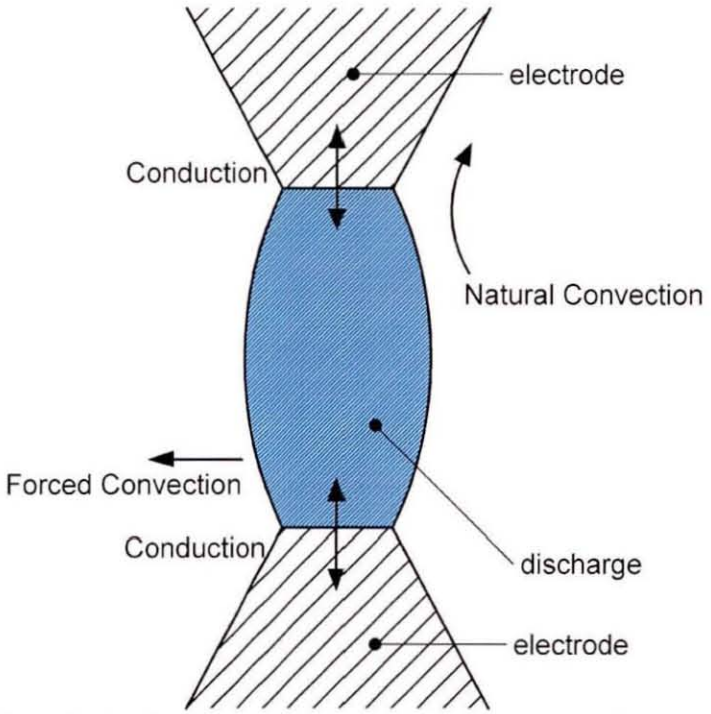

Figure 5.29. Schematic showing the model that explains the behaviour of the heating effect of the electric discharge.

5.5 Concluding Remarks

This chapter has studied the Autoselective discharge and its interactions with solid surfaces. It has identified that the heating effect of the discharge is a major effect responsible for PM oxidation. A novel method for measuring the heat flux from electric discharges has been used to study the effect of electrode spacing, discharge current and gas flow velocity on the heating efficiency of the electric discharge. A conceptual model of the discharge as a hot column of gas has been shown to explain the observed behaviour of the heating effect of the discharge. This model can be used to improve the heating efficiency by maximising the heat flux to the desired surfaces and minimising other heat losses such as forced convection.

CHAPTER 6

AUTOSELECTIVE REGENERATION OF GELCAST FOAM DPFS

Chapter 4 has discussed and developed gelcast ceramic foams as DPFs introducing new methodology to allow rapid optimisation of depth bed filtration DPFs. Chapter 5 presented analysis of the Autoselective regeneration of PM considering the behaviour of the regenerative electric discharge under a variety of conditions. This chapter now describes the research and knowledge related to integrating the two technologies to achieve a feasible filtration and regeneration technology.

6.1 General Observations

Figure 6.1 shows two examples of typical Autoselective discharges in contact with gelcast ceramic foams. The first consists of a glow discharge column in contact with

a single point on the foam. The ceramic surface reaches high enough temperatures to give off a yellow or white glow at the discharge filter contact point. These temperatures are high enough for rapid regeneration. The second type shows a series of blue discharge columns and a number of small white spots on the filter surface. The white spots are high temperature regions where particulate oxidation is taking place. In the case shown in Figure 6.1 there is unlikely to have been more than one single discharge at any one time but due to the air motion moving the discharge it strikes, extinguishes and then strikes again in another location. The effect of airflow is considered in further detail in Section 6.7.

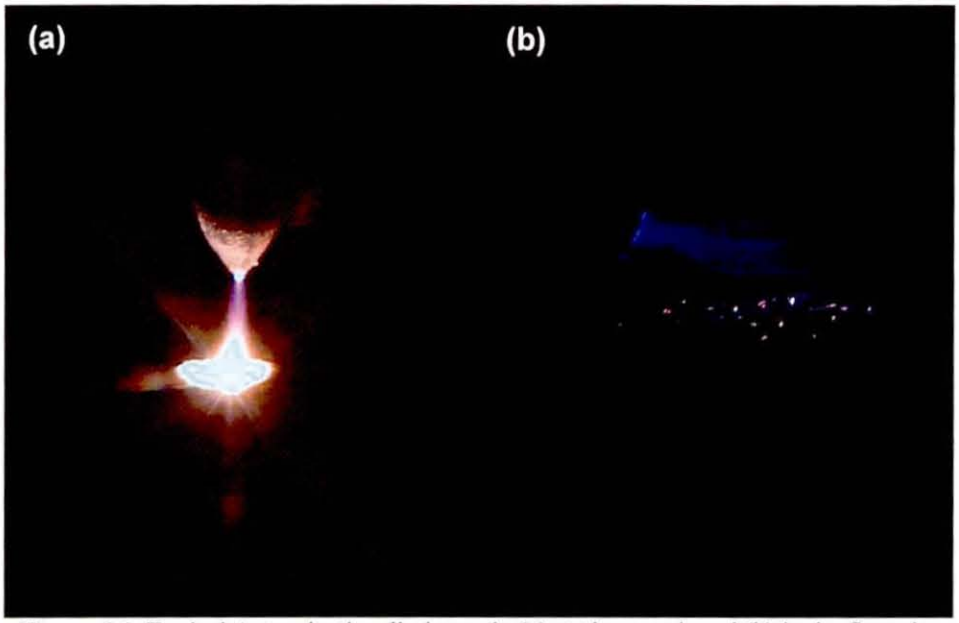

Figure 6.1. Typical Autoselective discharge in (a) stationary air and (b) in the flow rig.

Figure 6.2 shows how these two types of discharge typically affect the ceramic material. Case (a) leads to highly focused energy in one spot for an indefinite duration and can often lead to melting damage of the ceramic material. The cleaning of the surface is very rapid (<100 ms) and the filter material that is not damaged is returned to its original state. Case (b) was not found to lead to any damage to the filter surface. The regeneration occured to a lesser extent and over a much larger area resulting in a greying of the surface. The filter took longer to reach its clean state (<1 minute) but showed no signs of damage.

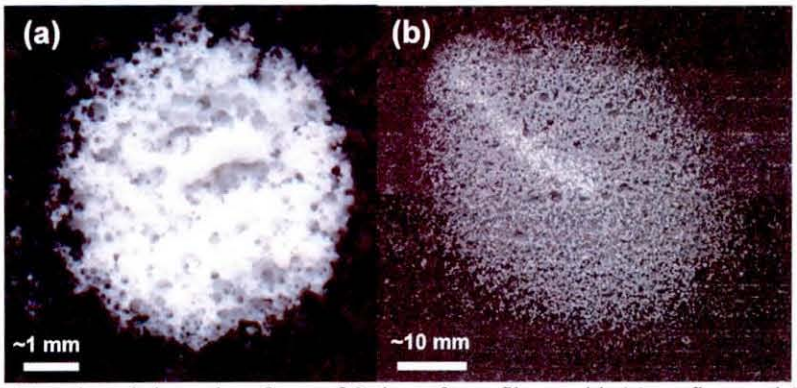

Figure 6.2. Examples of cleaned surfaces of Gelcast foam filters with (a) no flow and (b) gas flow.

The behaviour of the Autoselective regeneration of gelcast ceramic foams (e.g. where the regeneration occurs) is a strong function of a number of factors such as PM loading, power supply characteristics and system geometry. To begin to predict the behaviour of the discharge, an understanding of the electrical phenomena, and their interactions with the filter and PM was needed. This was achieved using equivalent electrical circuit modelling, described in the following sections.

6.2 Equivalent Electrical Circuit Modelling

Generating HVs with a compact power supply was achieved by resonating an inductance and capacitance (a transformer). To consider resonating and damping effects it was therefore necessary to model the transformer characteristics, as opposed to an ideal transformer. This was done using a combined resistance, capacitance and inductance shown in Figure 6.3. These equivalent circuit properties do not exist in isolation. The resistance, capacitance and inductance of the transformer exist distributed across the secondary winding of the HV transformer. The resistance, inductance and capacitance of the primary coil were negligible because of the 40:1 winding ratio of the transformer. They can be measured using a variety of techniques described in texts such as Warnes (1998). Table 6.1 shows typical values measured on the research project by other researchers. The DC resistance of the secondary coil was measured using a multimeter. The AC inductance was measured using an LCR bridge and the capactitance calculated from the open circuit resonant frequency.

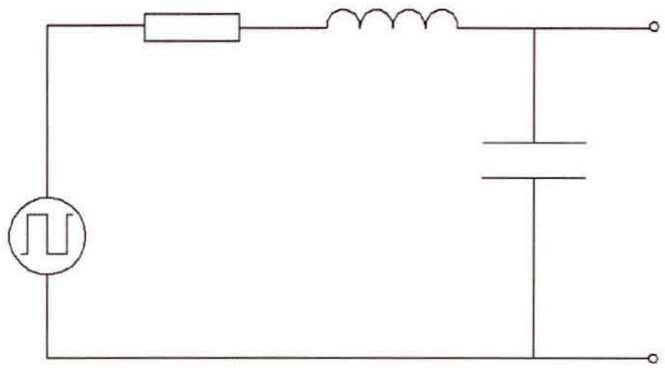

Figure 6.3. Equivalent circuit of the transformer and power supply.

Table 6.1. Typical equivalent circuit properties.

Factor	Typical Value
Resistance	900 Ω
Inductance	2 H
Capacitance	11 pF

The load connected to the power supply changed depending on the state of the discharge. This work considered the steady states during pre-break down, air gap only break down and break down within the filter. The equivalent circuits are shown in Figure 6.4.

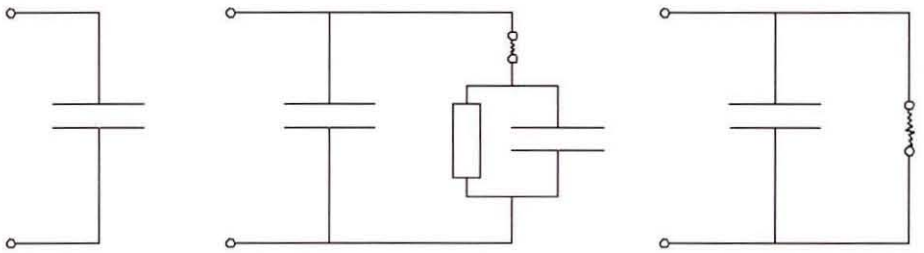

Figure 6.4. Equivalent circuit of the transformer load for states (a) no discharge, (b) a discharge within the air gap only and (c) a continuous discharge between the electrodes.

The pre-break down load represents everything connected to the HV side of the transformer in terms of equivalent capacitance, inductance and resistance. Before the break down occurs there is no direct conductive path between the electrodes meaning that there is no resistive connection. The inductance was found to be small due to the low coupling between the electrodes. The capacitance was comparable to the transformer distributed capacitance and found to be significant to the resonant properties of the circuit. This was measured using an LCR bridge.

When a steady state discharge is operating in the air gap, the current flows through the capacitance and resistance of the PM loaded filter section. The resistance was found to be negligible for typical PM loadings and the capacitance estimated from direct measurements. The equivalent circuit therefore consists of a discharge model, load capacitance and filter capacitance (including resistance when the PM loading is high).

When the discharge is active within the filter volume, there is a conductive path between the two electrodes and the effect of the filter properties become negligible. The model then consisted of the load capacitance and the discharge model. The equivalent circuit properties were measured and are discussed in the following subsection.

6.2.1 Experimental Data Collection

The open circuit load capacitance was measured for a 30x30 mm mesh electrode with a 2 mm air gap and 9 mm filter section, shown schematically in Figure 6.5.

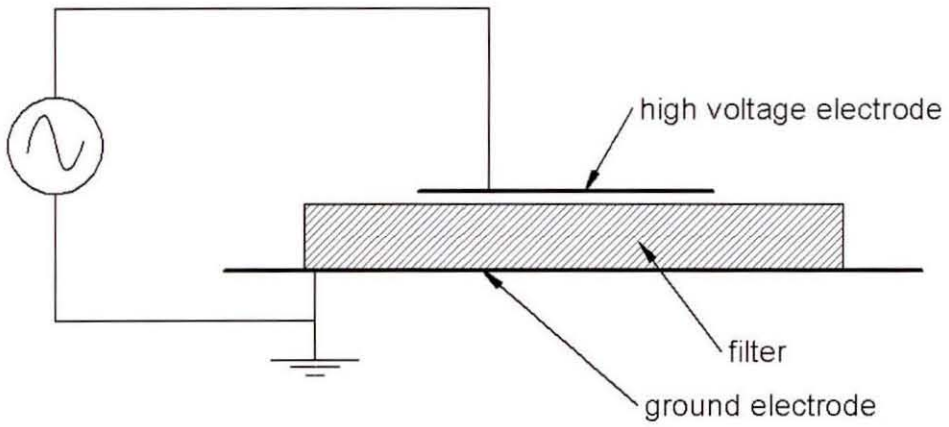

Figure 6.5. Schematic of mesh electrode experimental setup.

The capacitance of the arrangement was found by applying a sinusoidal voltage to the HV electrode. The voltage was kept low enough to avoid a discharge being initiated. The current was measured using a current probe. Considering the circuit as a parallel resistance and capacitance, the overall (measured) current was

$$I = I_C + I_R = V_{el}\left(\frac{1}{Z_C} + \frac{1}{Z_R}\right) = V_{el}\left(-\omega C_{el} j + \frac{1}{R_{el}}\right) \qquad (6.1)$$

where I is the overall current, I_C is the capacitive current, I_R is the resistive current, V_{el} is the applied voltage, Z_C is the capacitive impedence, Z_R is the resistive impedence, ω is the angular velocity, C_{el} is the capacitance, j is $(-1)^{0.5}$ and R_{el} is the resistance. The magnitude of Z was

$$|Z| = \frac{V_{el}}{I} = \frac{R_{el}}{-\omega C_{el} R_{el} j + 1} = \frac{R_{el}}{\sqrt{(\omega C_{el} R_{el})^2 + 1}} \angle \tan^{-1}(\omega C_{el} R_{el}) \qquad (6.2)$$

By measuring the peak voltage, current and phase angle it was possible to find C and R for the equivalent circuit. The peak voltage and current during the test were 6 kV and 18.4 mA respectively. The phase angle was measured as –85.15 degrees. Solving for C and R gave values of 20 pF and 3.9 MΩ respectively. The resistive current could be considered negligible.

The discharges can be described electrically by two dimensional current-voltage relationships. This is known to be a simplification of the real case in which there are hysteresis and directional discontinuities relating to cyclic break down although this will not affect the general analysis of the interactions between the discharge current and the resonating transformer circuit.

The discharge current-voltage relationships were measured by capturing current and voltage waveforms for a pin to plate or pin to pin discharge in air. The results for the pin to plate tests are shown in Figure 6.6 for the filter plasma and air gap plasma. Within the current ranges under investigation, the change in stable plasma current-voltage relationships with changing rms currents were found to be small.

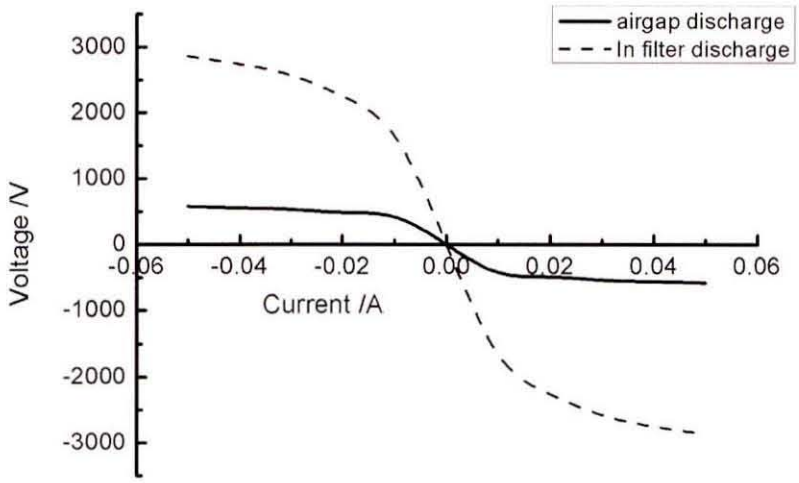

Figure 6.6. Voltage gradient – current relationship for air gap and in filter discharges under investigation.

6.2.2 Model Implementation

The transient modelling of electrical circuits has been carried out using fundamental current and voltage relationships for resistance, capacitance and inductance, implemented in Simulink (Matlab). The details of such use of Simulink is shown in Appendix E. This allows transient modelling of the equivalent circuits described in Section 6.2

6.2.3 Model Validation

The resonant behaviour of the electrical circuit model was compared to the experimental data shown in Chapter 5. A frequency sweep was carried out with a low voltage square wave input to the primary side of the transformer both on the real circuit and on the equivalent model. The gain of the resonant circuit model can be seen in Figure 6.7. The resonant frequency matched was in good agreement with the experimental case (Figure 5.6) although the model predicted higher amplitudes at resonance. This is attributed to the presence of HVs during the experimental case where corona discharges and initiation of streamers (micro discharges) further damp the electrical circuit.

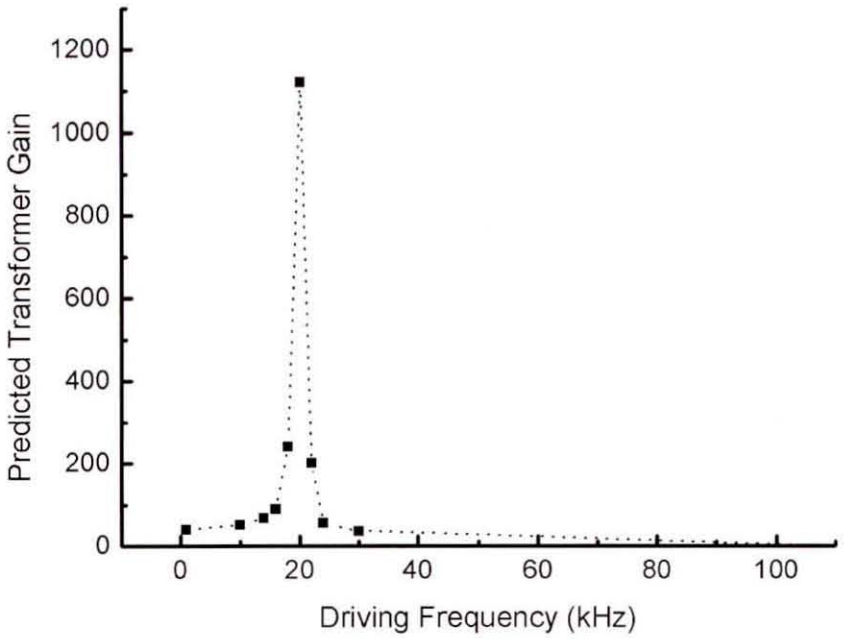

Figure 6.7. Resonant circuit gain as a function of frequency for the modelled transformer and load.

The two cases of an air gap only discharge and a spatially continuous discharge are now considered and compared to experimental data.

Figure 6.8 and Figure 6.9 show the predicted waveforms for the measured voltage and current for the case with two air gap discharges (i.e. no break down through the filter) and the actual measured current and voltage. They show reasonably good agreement with phase angle, shape and magnitude of the waveforms. It can be seen that the current is not sinusoidal and is approximately 90 degrees out of phase with the measured potential. This is because the current flow is limited by the capacitive flow through the filter section, and the capacitance is acting as a form of stabilisation allowing multiple discharges to exist simultaneously.

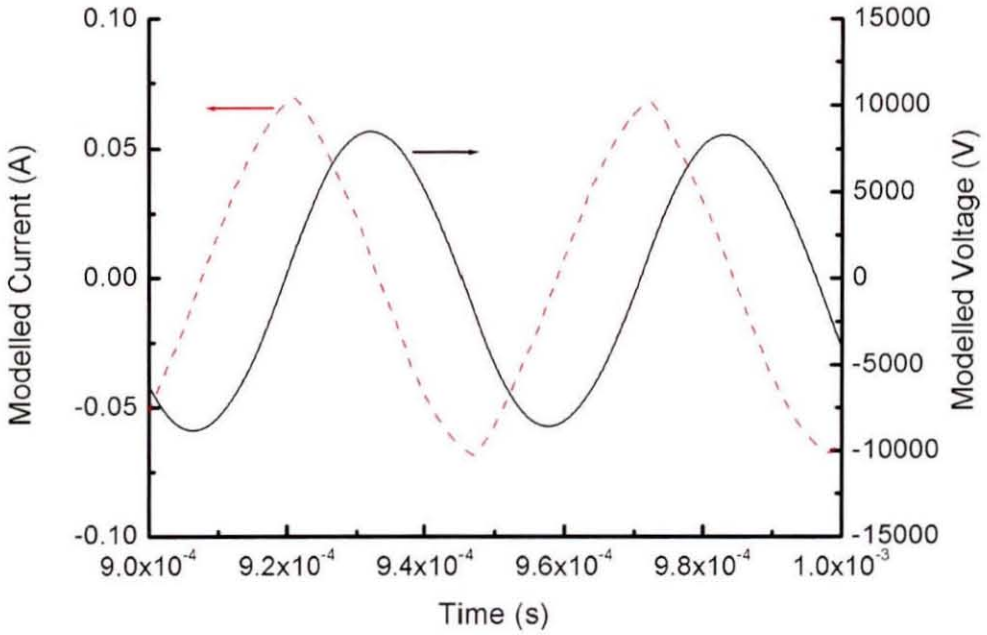

Figure 6.8. Plot of model predicted current and voltage waveforms for an air gap only discharge.

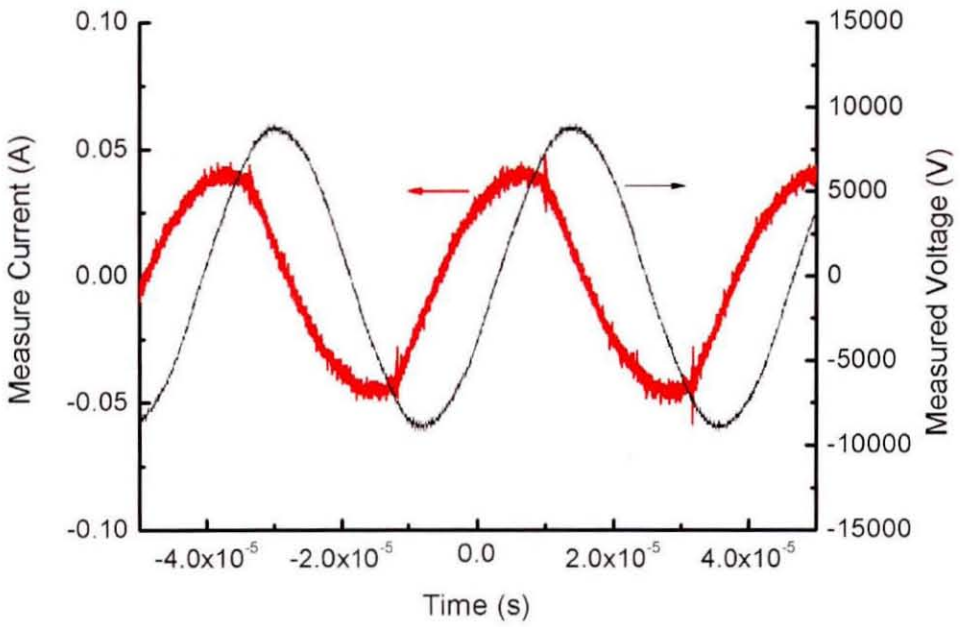

Figure 6.9. Experimental current and voltage measurements for an air gap only discharge.

Figure 6.10 and Figure 6.11 show the modelling results and measured results for a spatially continuous discharge (i.e. through the filter material as well as the air gap) respectively. The agreement of phase angle, shape and magnitude of the current and

voltage agree well with the experimental case. In case of a spatially continuous discharge the current flow through the discharge dominates. The resonant circuit is, therefore, significantly damped reducing the electrode voltages and limiting the current through the discharge.

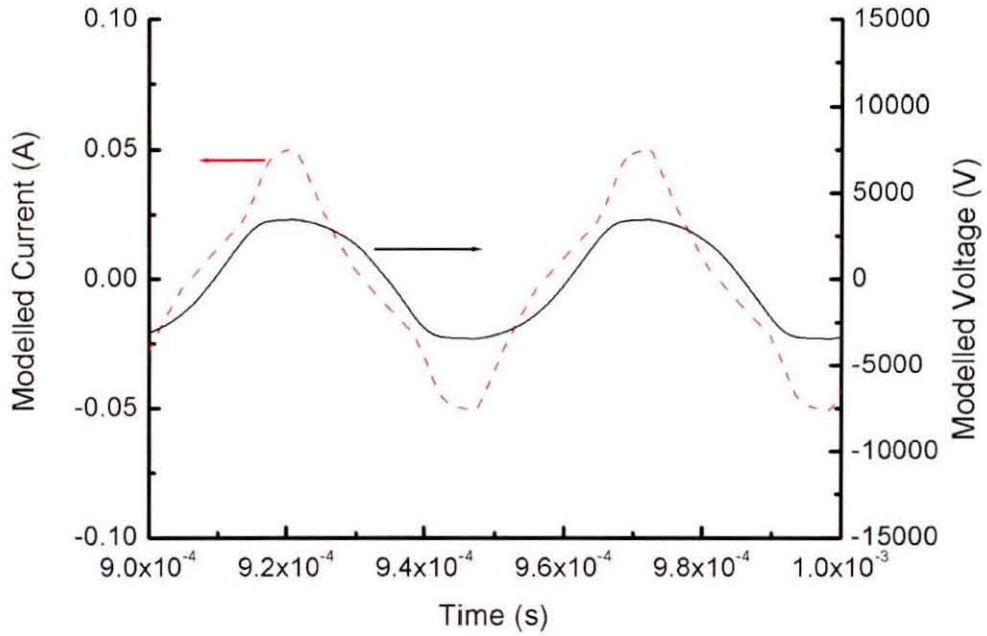

Figure 6.10. Plot of model predicted current and voltage waveforms for a spatially continuous discharge.

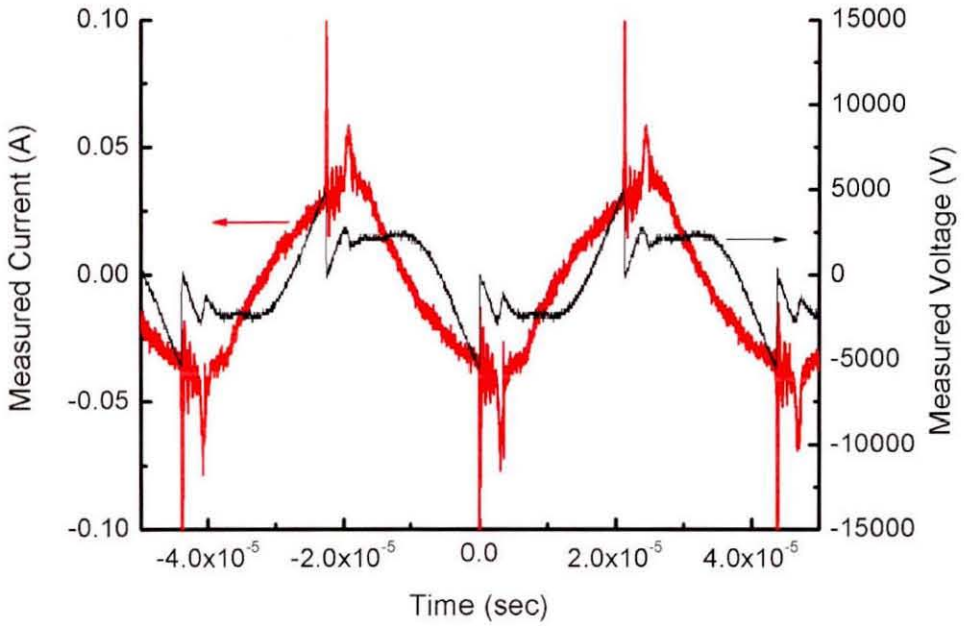

Figure 6.11. Experimental current and voltage measurements for a spatially continuous discharge.

This validation demonstrates that the equivalent circuit modelling of electric discharges for these purposes is suitable for improving the understanding of the Autoselective regeneration system and giving direction to achieve desired effects.

6.3 Break Down Processes

The discharge was observed to exist either in the air gap to the filter surface or between the electrodes, through the filter material. To understand when various gaps will break down it was necessary to understand at what voltages each part would break down.

The breakdown voltage is measured by applying an increasing AC voltage (generated from the resonating power supply) to a mesh electrode using a similar arrangement to Figure 6.5, with varying gap sizes. A Tektronix TDS5034B oscilloscope was used to monitor the applied voltage and at the point of breakdown (where the voltage significantly reduces) the peak voltage was recorded. An example of such a measurement is shown in Figure 6.12.

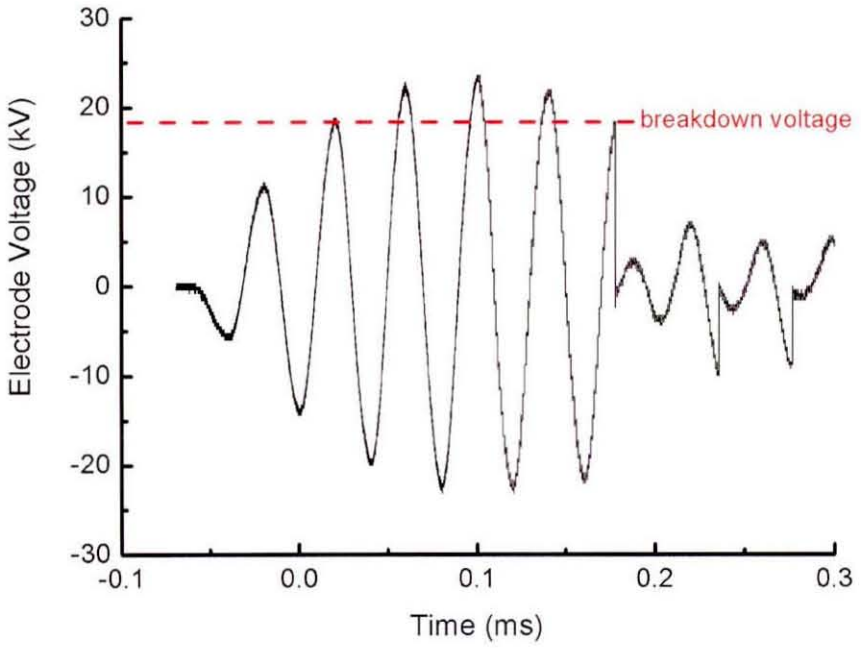

Figure 6.12. Example waveform showing measurement of breakdown voltage.

The measured break down voltage of the air gap as a function of distance for a pin to plate arrangement is shown in Figure 6.13. This can be compared to the break down voltages for the filter section which, as shown in Figure 6.14, were found to be very similar. This implies that the open highly porous structure of the foam does not interact significantly with the break down voltage of the discharge. The values for the break down voltage can be used to provide an indication of the likelihood of a break down occurring in any one part of the pre-break down transformer load of the equivalent circuit model.

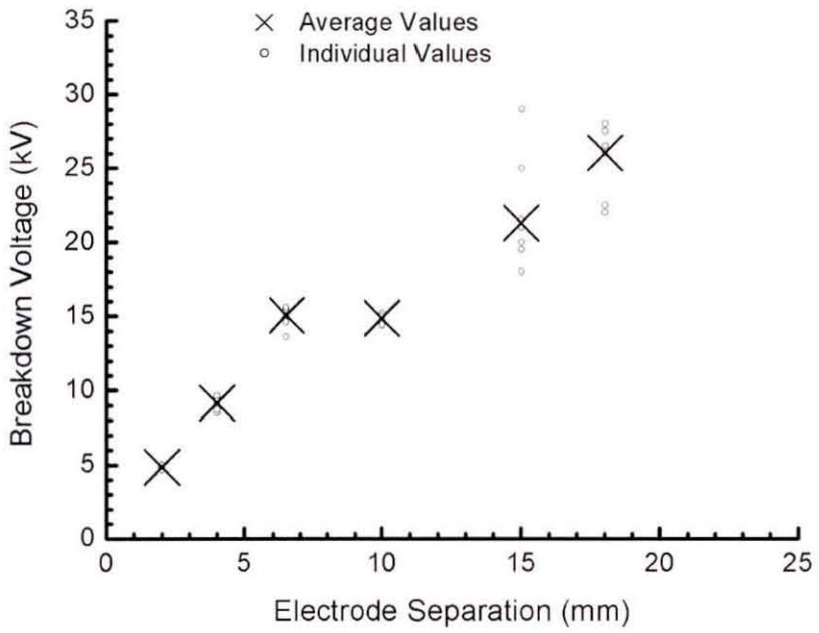

Figure 6.13. Plot of measured air gap break down voltages.

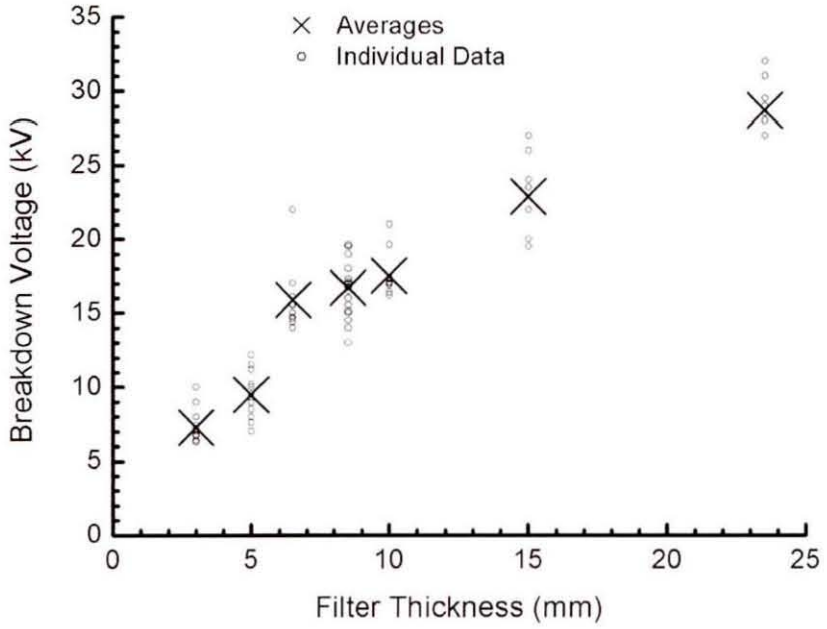

Figure 6.14. Plot of measured filter block break down voltages.

The air gap will always break down before the filter section due to its lower dielectric permittivity (~1) in comparison to a loaded filter (>2). This leads to concentration of the electric field in the air gap, explained by considering two series media in between an infinitely long plate electrode. The different materials can be considered as series capacitors where the capacitance is equal to

$$C_i = \frac{\varepsilon_0 \varepsilon_r A}{d_i} \tag{6.3}$$

where C_i is the capacitance of section i, ε_0 is the permittivity of free space, ε_r is the relative permittivity of section i, A is the area considered and d_i is the thickness of the section. The charge stored on series capacitors, Q_{el}, will be equal, therefore

$$Q_{el} = C_1 V_1 = C_2 V_2 \tag{6.4}$$

Combining these two equations leads to

$$\frac{\varepsilon_0 \varepsilon_1 A}{d_1} V_1 = \frac{\varepsilon_0 \varepsilon_2 A}{d_2} V_2 \tag{6.5}$$

Noting that

$$E_i = \frac{V_i}{d_i} \tag{6.6}$$

where E is the electric field strength, Equation 6.5 becomes

$$\varepsilon_1 E_1 = \varepsilon_2 E_2 \tag{6.7}$$

This shows that for such a series dielectric arrangement, the electric field will be highest in the material with the lowest dielectric constant and, therefore, the airgap will breakdown first.

6.4 Discussion of Air Gap Only Discharges

The discharge may break down in the air gap only (i.e. not within the filter volume). This is possible when the capacitance of the filter section is high enough to allow the current to flow capacitively without reaching break down voltages. This would happen as increased current flow acts to reduce the gain of the resonant circuit, hence reducing the output voltage. This means that the discharge will extinguish at the surface of the filter. This problem can be exacerbated by the occurrence of multiple air gap discharges resulting from the capacitive stabilisation of the discharge through the filter. This occurs, for example, when one air gap discharge is present since the voltage on the electrodes can still be high enough to break down the air gap in a different location without breaking down the filter section. When this happens, the additional resistive load further damps the resonant circuit reducing the likelihood of the discharge propagating into the filter. This would result in regenerating the surface of the filter only, as demonstrated in Figure 6.15. Since the majority of trapped PM is within the filter volume, and not at its surface, this will not noticeably reduce the back pressure of the loaded gelcast ceramic foam filters. To regenerate the filter it is necessary to generate the discharge within the filter volume.

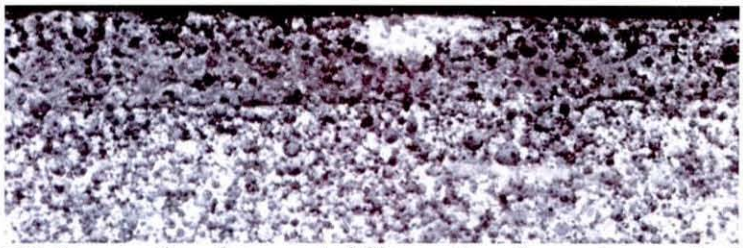

Figure 6.15. Cross section of regenerated filter section after an air gap only discharge.

6.5 Discussion of Spatially Continuous Discharges

Where the current flow through the filter section is not enough to reduce the electrode voltage below the break down voltage of the filter section then the discharge will be spatially continuous between the HV electrode and the ground electrode. When the discharge is continuous, the circuit is further damped and the voltage drops below the break down voltage of the air gap resulting in no multiple air gap discharges. The discharge current waveform becomes predominantly resistive, as shown in the example in Figure 6.11. A spatially continuous discharge enables regeneration of the filter volume. This gives the potential of complete cleaning and restoring the back pressure across the filter to the clean state. In addition, it will increase the heating efficiency of the discharge by increasing the contact area between the solid and plasma. An example of the cleaning resulting from a spatially continuous discharge is shown in Figure 6.16.

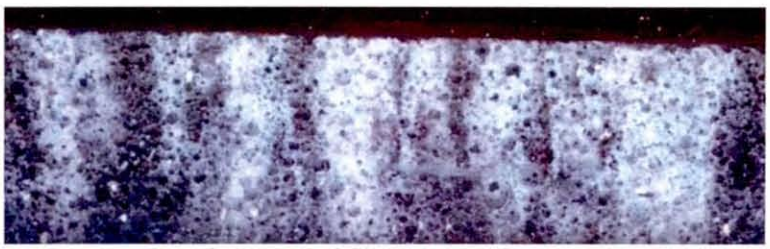

Figure 6.16. Cross section of regenerated filter section after spatially continuous discharge.

Further advantages of spatially continuous discharges include the improved transfer of thermal energy from the gas phase to the solid phase. This should result in reduced energy usage.

6.6 Promoting Spatially Continuous Discharges

The likelihood of a break down within the filter volume is a function of the electric field strength generated by the HV power supply. It follows that the voltage generated by the supply, and the peak electric field strength (for a given supply voltage) are the two main considerations. To increase the likelihood of a spatially continuous discharge, the voltage generated by the supply can be increased, or the voltage required to achieve the break down reduced.

Consideration of the variables that could easily be changed resulted in the list shown in Table 6.2. There is no clear solution as each of the variables has advantages and disadvantages associated with it. These variables were investigated using the new modelling tools to find which have the most beneficial effect. Each variable investigated is discussed in the following sections.

Table 6.2. Summary of factors under investigation with potential advantages and disadvantages of the proposed methods of increasing the likelihood of a spatially continuous discharge.

Change	Method	Potential Advantages	Potential Disadvantages
Increase the voltage drop across the filter section	Reduce the filter PM loading	1. Higher impedance of the filter section (i.e. higher voltage drop across the filter section)	1. Less efficient regeneration. 2. More frequent regeneration required. 3. Higher break down voltages.
	Increase the stabilisation current limit	1. Higher voltage drop across the filter section	1. Higher peak currents – more difficult to control damage
	Lower frequency	1. Higher impedance of the filter section	1. Higher break down voltages
Lower the break down voltage of the filter section	Increase the filter PM loading	1. Lower break down voltages. 2. Higher regeneration efficiency. 3. Less frequent regeneration.	1. Low filter section impedance (which will lower the voltage drop across the filter section).
	Alter ceramic material – e.g. electrical conductivity or dispersed metal particles	1. Lower break down voltages.	1. Lower filter section impedance. 2. Filter strength. 3. Life/ageing of conductive particles.
	Reduce the filter thickness	1. Lower break down voltages.	1. More filter layers are needed. 2. Lower filter section impedance. (3. Difficult to manufacture)
	Higher frequency	1. Lower break down voltage	1. Lower filter section impedance.

6.6.1 Effect of Filter PM Loading

The break down voltages of a 10 mm thick clean and loaded filter section were measured as 17.9 kV and 16.1 kV with standard deviations of 2.5 kV and 1.0 kV respectively. This indicates that loading only has a small effect on the break down voltage of the filter section. This can be explained by considering the air volume within the filter. The main factor affecting the break down of this gas is the electric field strength, which initiates electron avalanches. To achieve high electric field strengths, a high potential gradient is required, which is independent of PM loading. The loading gradient and conductive particles within the media appear to have a relatively small effect on the break down voltages, but a large effect on the resonant circuit characteristics.

When there is a spatial PM loading gradient present, the electric field strength with ideal plate or mesh electrodes is a function of location in the filter. In the regions with higher PM loadings, the electric field strength is lower than regions with low PM loadings, due to the variation in effective dielectric constant of the material. This variation in effective dielectric constant leads to the fraction of current flowing through the dielectric and the fraction flowing through the ionised gas to vary spatially through the filter, eventually leading to the extinguishing of the discharge once a region of too high PM loading is encountered. The current flowing through the discharge reduces as the local PM loading increases meaning that the local temperatures also reduce along with the regeneration. It is, therefore, important to consider which side of the filter the HV electrode is located. If the electrode is located on the clean side of the filter, due to the lower PM loading, the electric field strength will be higher meaning that there is more likelihood of the discharge travelling into the filter volume.

6.6.2 Effect of Changing the Transformer Core Gap

The leakage inductance (and hence the stabilisation of the transformer) was altered by varying the gap size between the two sections of transformer core, shown in Figure 6.17. The effect on the transformer equivalent circuit was used in the modelling to estimate its effect.

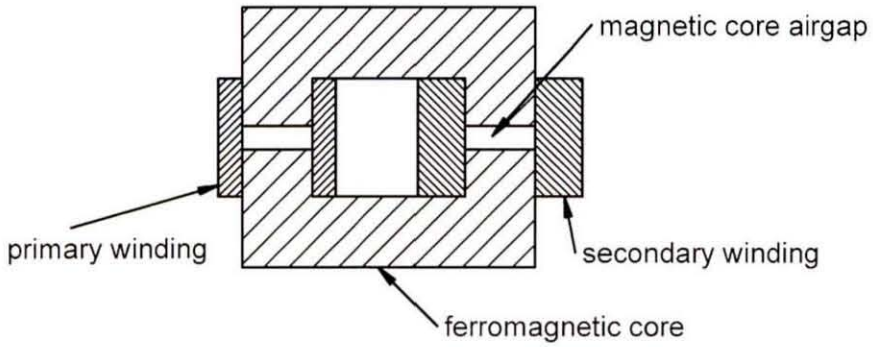

Figure 6.17 Diagram showing a cross section of the transformer core gap arrangement.

The inductance was measured at 100 Hz using a LCR bridge with the secondary of the transformer short circuited. The low frequency made the effect of the distributed capacitance small. The resistance was measured at DC across the secondary, as the primary winding has only a small effect on the overall resistance. The capacitance is calculated from the inductance and self resonant frequency (itself measured using a low frequency square wave input while minimising load capacitance).

The results are shown in Table 6.3. It can be seen that the capacitance and resistance were not affected by changing the core gap, as expected, but the inductance reduced as the core gap was increased in size.

Table 6.3. Effect of core gap size on transformer characteristics.

Core gap thickness (mm)	Inductance H	Resistance Ω	Capacitance pF
0	2.06	900	11.4
0	2.12	900	11.0
0.06	2.01	900	11.1
0.06	2.06	900	10.2
0.13	1.71	890	11.3
0.13	1.83	900	10.9

To evaluate the effect of core gap size on limiting the supply current, the following definitions were made. The input voltage was such that when the circuit is resonating (open circuit) it generated an output voltage of 1000 V. A resistive load was then applied until the output voltage had reduced to 500 V. This 500 V current limit was then used to compare the current limiting effect of the changes using the modelling.

The modelling predictions of the effect of changing the core gap size is shown in Table 6.4. Each tape layer was ~0.064 mm thick

Table 6.4. Effect of core gap size on current limiting of the supply.

Equivalent Number of Tape Layers	Inductance H	500V current limit A
0	2.09	2.625×10^{-5}
1	2.01	2.719×10^{-5}
2	1.77	3.092×10^{-5}

The variation of the effect of the core gap thickness, Figure 6.18, on the voltage across the filter section shows that the larger core gaps gave slightly increased voltages. This meant that the reduction in current limiting was more significant than the effect of increased resonant frequency on the impedance of the filter section, but the overall effect was negligible in comparison to, for example, the effect of filter thickness, discussed later.

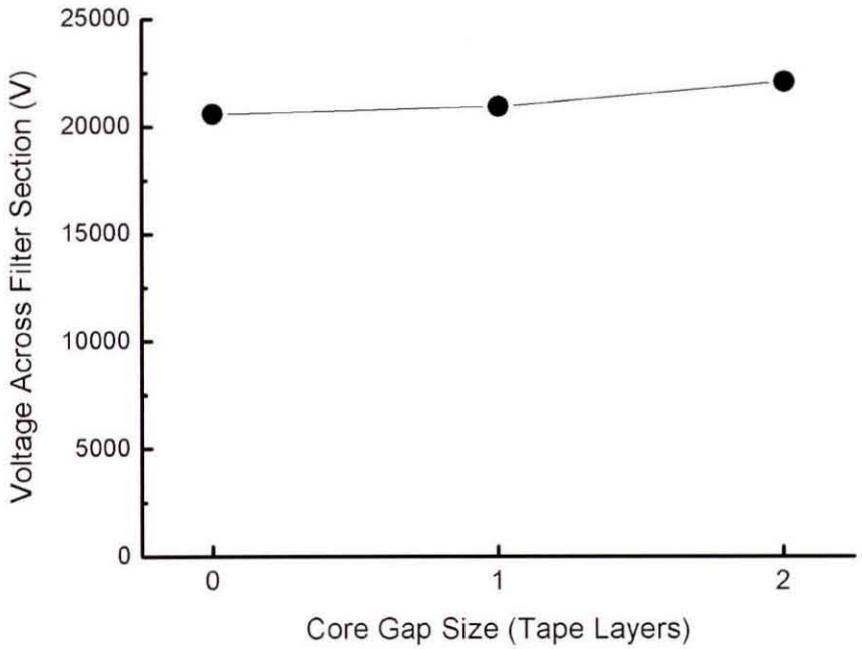

Figure 6.18. Effect of core gap thickness on the voltage generated across the filter.

6.6.3 Effect of Artificial Load Capacitance

Adding artificial load capacitance to the transformer circuit alters the resonant circuit without adding additional discharge sites which could act to further dampen the

circuit at high voltages. This was achieved in this study by attaching a HV capacitor in parallel to the filter section between the HV wire and ground electrode.

Adding additional capacitance reduces the resonant frequency of the supply, as predicted by

$$f_0 = \frac{1}{2\pi\sqrt{L_{el}C_{el}}} \tag{6.8}$$

where f_o is the resonant frequency. This means that at resonance, for a given transformer, the filter section impedance will be higher, giving higher voltage drops for a given current, increasing the likelihood of a spatially continuous discharge.

In addition to this effect, the additional capacitance reduces the impedance of the resonant circuit meaning that the current limiting of the supply is lower (i.e. higher currents can flow at a given voltage). This is demonstrated in Figure 6.19 which shows the modelled effect of the additional capacitance on the current limiting of the supply.

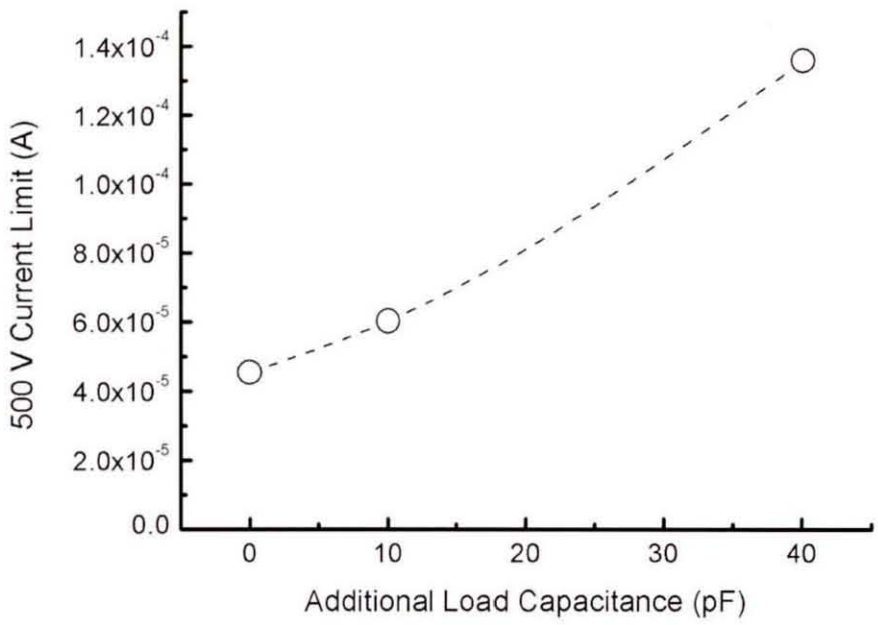

Figure 6.19. Modelling results showing the effect of additional capacitance on the current limiting of the supply.

These two effects are cumulative, both increasing the likelihood of a spatially continuous discharge.

The magnetic saturation of the transformer core sets an upper limit on the achievable current through the secondary. As the capacitance is increased, and the impedance reduced, the voltage of the secondary at saturation will decrease. Therefore, if the capacitance is too high, the core will saturate before the break down voltage is reached and no discharge will occur.

Figure 6.20 shows some measurements made of output peak voltage and current through the secondary of the transformer with a 250 pF load. This load was enough to prevent continuous break down between the HV and ground electrodes. It shows that the peak current of the secondary winding was limited to approximately 300 mA (peak to ground). This is a current limit set by the saturation of the core, and not a voltage limit on the secondary.

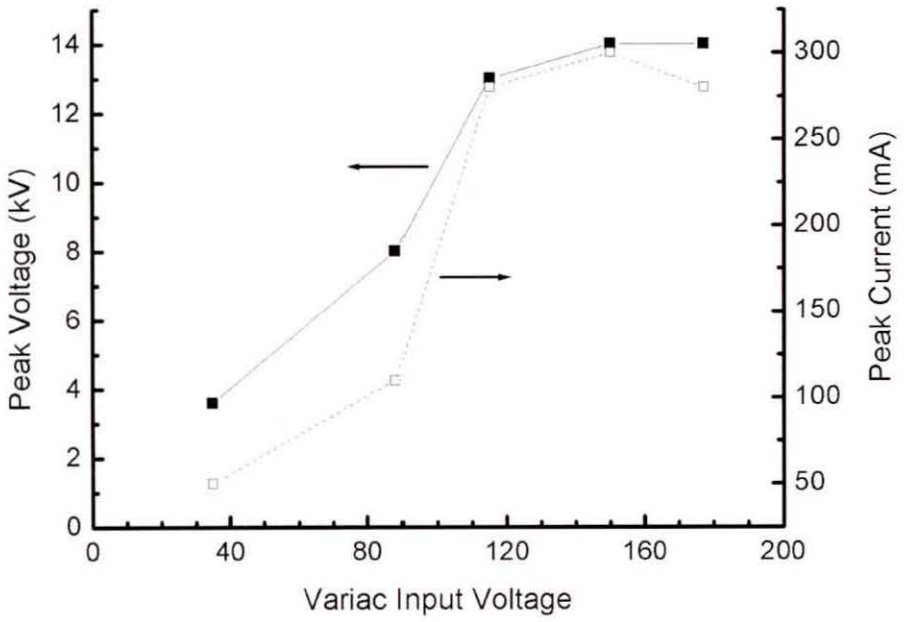

Figure 6.20. Plot of measured peak current and voltage on the secondary of the transformer as a function of supply voltage.

With this current limit known an upper limit on the load capacitance is defined by the capacitive current limit of the transformer secondary.

6.6.4 Effect of Filter Thickness

The thickness of the filter section affects the break down voltage of the filter section and the capacitance between the HV electrode and ground plane. The break down voltages were measured on 80% porous filters of different thicknesses, the data for which was shown in Figure 6.14. The break down voltage was shown to be a linear function of distance between the electrodes for short distances (< 10 mm) with the break down voltage becoming less sensitive to electrode separations at larger distances.

The effect on filter capacitance has been measured and the results are shown in Figure 6.21. As the separation increased, the capacitance decreased. The magnitude of the measured capacitance showed that the electrode capacitance contributes only a small fraction of the load capacitance. The capacitance between the HV wire and the ground plane was in the region of 20-30 pF, approximately 5 times that of the electrode. This means that the relative variation in overall load capacitance with varying filter thickness was small.

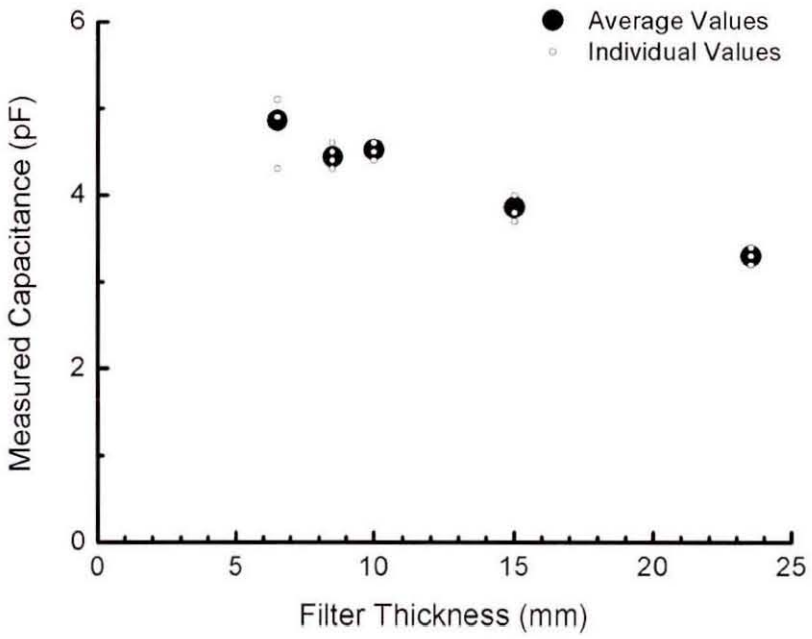

Figure 6.21. Effect of filter thickness on load capacitance.

The change in resonant frequency is therefore small due to the relatively constant electrode capacitance, but the reduction in break down voltage is significant (approximately 1.8 kV mm^{-1}). This is the dominant change when considering filter thickness and leads to an increased likelihood of spatially continuous discharges with thinner filter samples.

6.6.5 Summary of Effects

To allow a comparison of the different variables with respect to their effect on the likelihood of a break down, E (hereafter referred to as the breakdown effect) within the filter volume, an effect term has been defined as

$$E = \frac{V_{el} - V_o}{V_b} \tag{6.3}$$

where V_{el} is the modelled voltage drop prior to break down, V_o is the modelled voltage drop at the centre point conditions and V_b is the break down voltage. This means that if changing a variable leads to an increased voltage across the gap or a reduced break down voltage, the break down effect is positive, and there is a higher likelihood of achieving a spatially continuous discharge. If the voltage across the gap reduces or the break down voltage increases, the breakdown effect is negative, and there is a lower likelihood of achieving a spatially continuous discharge. The results of this analysis using the data presented earlier is shown in Figure 6.22. This shows that core gap size is expected to have only a small effect on the likelihood of a spatially continuous discharge. The filter thickness and artificial load capacitance lead to significant changes in likelihood through the changes in break down voltage and current limiting of the supply respectively.

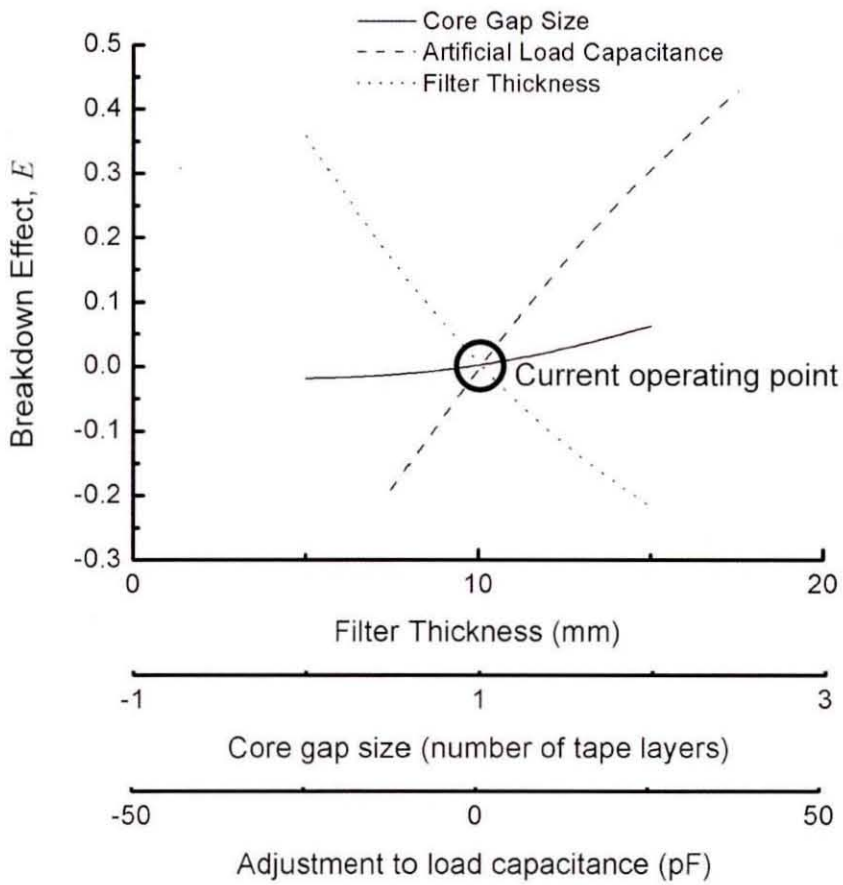

Figure 6.22. Sensitivity analysis of the three main factors investigated.

6.6.6 Test Results

The effects of adding additional load capacitance and altering the filter thickness were tested in stationary air to confirm the predicted benefits that could be achieved. A discharge was generated between a mesh HV electrode and plate ground electrode similar to the arrangement shown in Figure 6.5. The filter section was regenerated for a period of 30 minutes with intermittent discharges. This prevented filter damage and maintained discharge mobility, described in Section 6.7. Figure 6.23 shows the effect of varying the filter thickness on the penetration into the filter of the regenerative discharge. The thinner filters led to regeneration of more of the filter volume (i.e. increased penetration) confirming the modelling prediction.

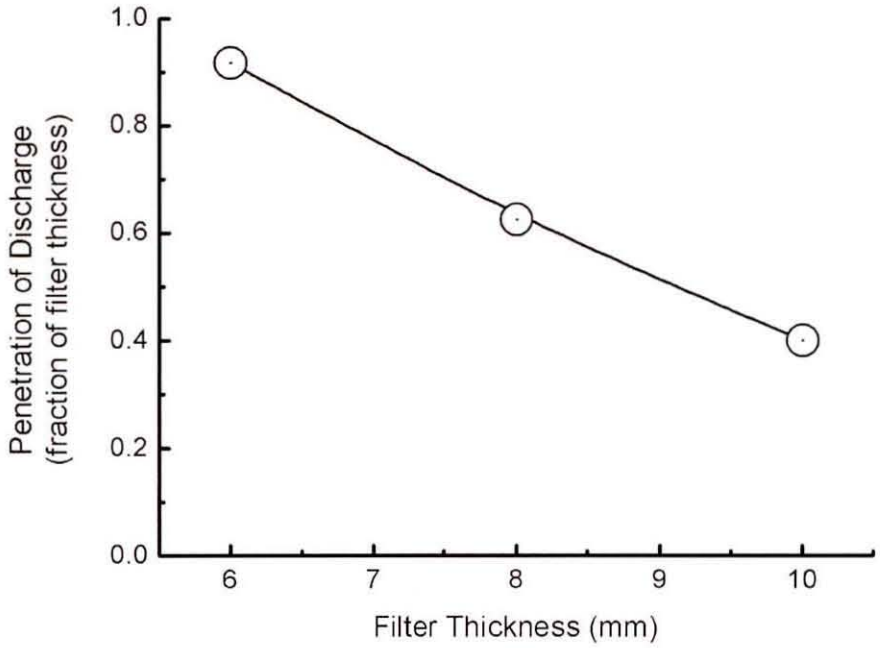

Figure 6.23. Effect of filtration thickness on discharge penetration.

The increase of the capacitive load of ~60 pF led to ~25% increase in the current flow through the discharge, with a corresponding increase in peak voltages prior to break down. It demonstrated enough effect to cause a spatially continuous discharge when it was not achieved without the additional capacitance.

6.6.7 Summary

The equivalent electric circuit modelling tool has been used to investigate the effect of varying design parameters on the interactions between the Autoselective discharge and the gelcast ceramic foam DPF. The modelling predicted that reducing the filtration thickness and increasing the additional load capacitance would increase the likelihood of the discharge penetrating into the filter volume, hence being more effective at removing PM. This has been confirmed by experimental observation highlighting that thin filter sections and control of the load capacitance are needed to optimise the Autoselective regeneration of gelcast ceramic foams.

6.7 Maintaining Discharge Mobility

The Autoselectivity of the discharge regeneration system relies on the trapped PM causing the discharge to preferentially strike in the region surrounding the PM. The

concept relies on the effect of the trapped PM on the local electric field, controlling the discharge initiation site. When considering the whole system, the likelihood of the discharge striking in a single location, when factors such as filter and electrode geometry are kept constant, is a function of:

1. the local PM Local PM distorts the electric field, tending to increase the electric field strength in the vicinity of PM (i.e. more PM leads to a more preferential location for the discharge)
2. the local ionisation fractions Presence of ionised particles and free electrons in a local region reduce the break down voltage and hence these regions become preferential for the discharge.
3. the material temperatures (and phases) Conductivity of ceramics increases with temperature (Shackelford and Alexander, 2001). Local regions of material with high temperatures and, hence, higher conductivities increase the electric field strength in that region. This resulted in higher temperature regions of the filter being preferential sites for the discharge.

The Autoselectivity of the regenerative discharge was prevented if the local ionisation or material temperatures led to a clean location of the filter being a preferential site for the discharge when compared to a PM loaded location. Experience has shown that this can regularly occur when the local ceramic temperatures are high.

Previous studies by Proctor (2006) described intermittent switching of the discharge to control ceramic damage, with the additional benefit of promoting Autoselectivity. The use of an off-period leads to dissipation of ionised particles in the region surrounding the previous discharge and reduction of local material temperature to be closer to ambient. Both of these effects lead to a reduced likelihood of the discharge striking in the same place again.

Observations have shown that gas flow also has a large effect on discharge mobility, as demonstrated in Figure 6.24. A discharge between a pin HV electrode and a loaded foam filter surface with varying perpendicular gas flow rates is shown, where the gas flow rate was measured using a hot wire anemometer.

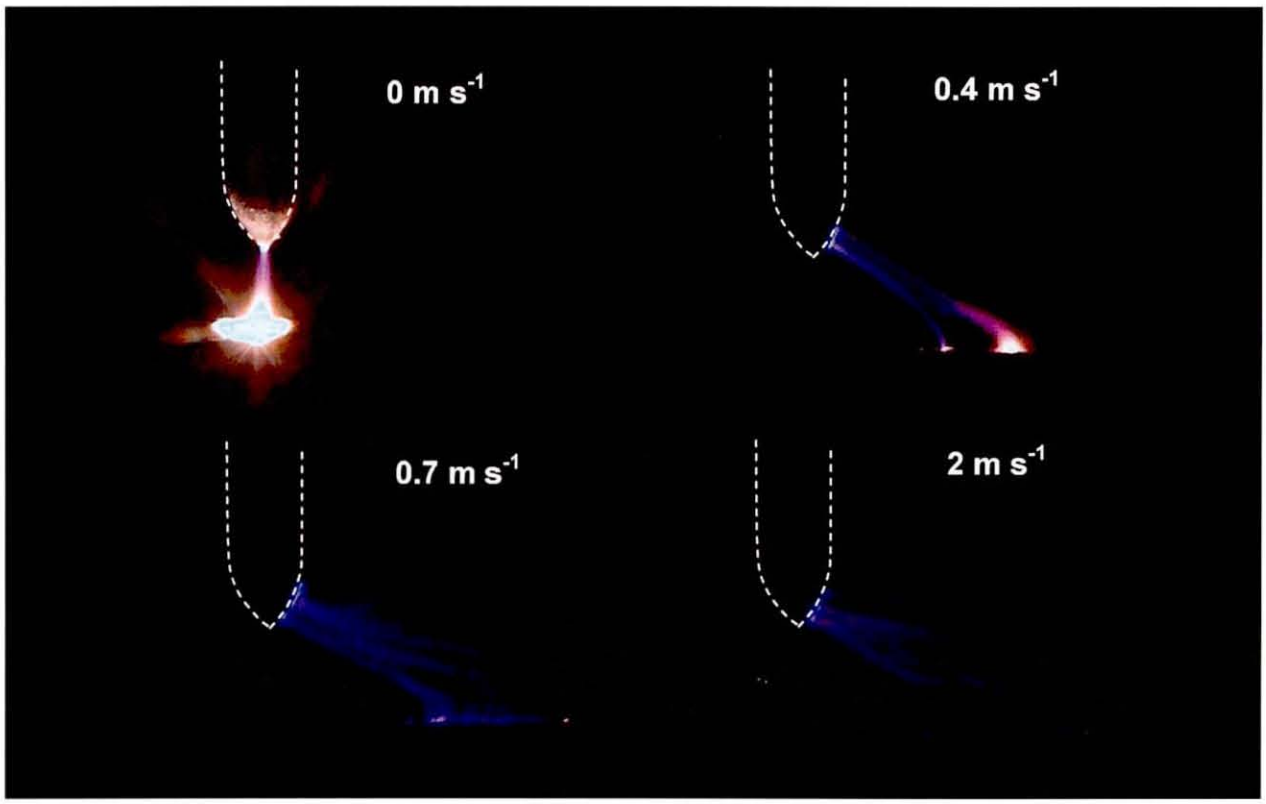

Figure 6.24. Photographs showing visual appearance of discharges experiencing different gas flow velocities.

With flow rates of 0.4 m s^{-1} the discharge was noticeably affected by the gas flow. As the flow rate increased, forced convection caused the ionised particles to be moved rapidly from the discharge column, changing the location, and potentially the filter contact point of the discharge. This demonstrated the influence of flow on the mobility of the discharge and that it can dominate the effect of loaded PM on the discharge location. There is potential to utilise flow as a control for the Autoselectivity, however, the balance between achieving Autoselectivity and dominance of flow is difficult to achieve, especially in a variable environment such as a diesel engine exhaust system with varying flow rates and flow velocities.

Other potential methods for maintaining discharge mobility and affecting the Autoselectivity of the regeneration include magnetic control and mechanical control. The former works on the theory that the current flow through the discharge column will, in a magnetic field, produce a perpendicular force on the moving charged particles giving direct control of the discharge location. In practice this is difficult to achieve due to the high frequency oscillating current and the magnitude of the

magnetic field required to affect the discharge. Tests with a 50 Hz electromagnet identified that magnetic fields of >0.14 T were needed to affect the discharge mobility for a typical setup. These tests are summarised in Appendix F. Mechanical control refers to physical movement of the electrodes to control the electric field strength again giving direct control of the initiation sites of the discharge. This was an unattractive option due to the complexity of moving parts within a PM laden exhaust system.

The use of on- and off-times was chosen for the remaining work presented as it offered a high level of control that could be optimised to suit a range of conditions whereas controls such as flow rates are unpredictable and difficult to control in the exhaust environment. Although a thorough optimisation of the on- and off-time together is beyond the scope of this work, it is possible to describe some specifications for the on- and off-time:

1. The on-time should be long enough to oxidise PM provided that it would not be long enough to damage the filter material (discussed in Chapter 7).
2. The off-time should be long enough to achieve Autoselectivity of the discharge.

6.8 Electrode Design

Generating a discharge is most simply achieved using a pin electrode arrangement to focus the electric field around a single point where the discharge initiates. This generates a single discharge column that can regenerate a cylindrical shape between itself and a flat ground electrode. This means a single pin electrode is limited in the filter volume that it can regenerate and hence the use of multiple pins connected to a single power supply is required. This increases the volume of the filter that a single power supply can regenerate. This idea can be simplified to consider a mesh electrode which will act as multiple discharge sites allowing the discharge to move across a large area and hence regenerate a large volume while still allowing gas flow through the electrode mesh. For these studies a stainless steel woven mesh electrode was used which is available in a wide range of sizes and weaves as well as at a low

cost. Examples of alternative electrodes trialled are shown in Figure 6.25 and include:

1. Pin electrode Ideal for studies of regeneration characteristics. Limited in volume of filter that can be regenerated.
2. Woven mesh electrode Behaves like multiple pin electrodes.
3. Expanded mesh electrode Also behaves like multiple pin electrodes but higher cost in small quantities.
4. Honeycomb electrodes Behaves like a mix between multiple pins and plate electrode. Can be used to straighten turbulent flow in region surrounding the filter.
5. Impregnated electrodes Behaves like plate electrode but no air gaps present. Durability of metallic layers is difficult due to either oxidation or separation from the surface.
6. Plate electrode Used for stationary air tests to achieved large area of regeneration although blocks the gas flow if applied to flow regeneration tests.

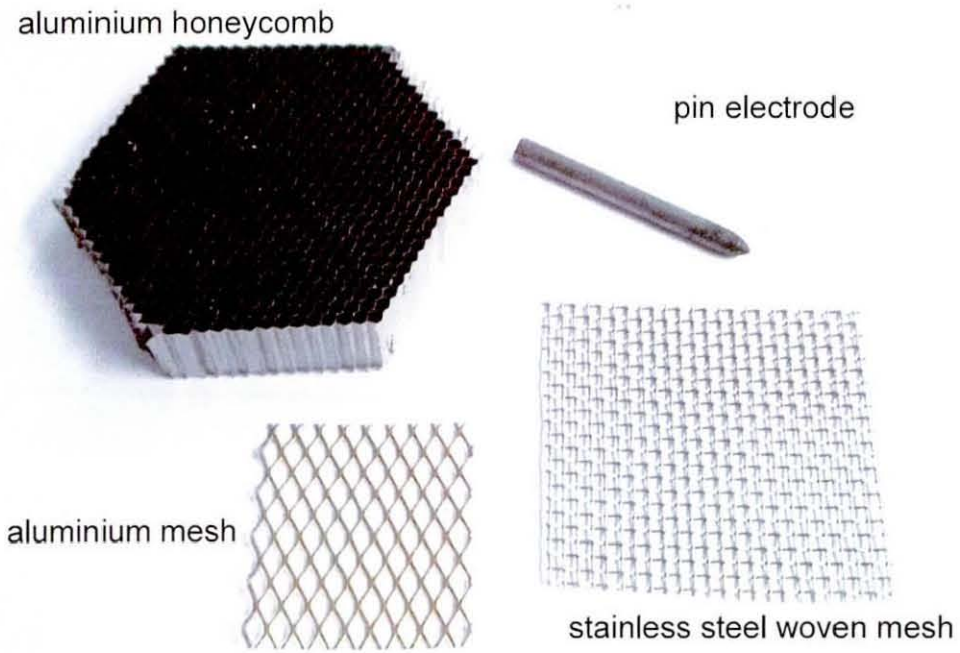

Figure 6.25. Photograph of typical electrode materials.

The conceptual case of an infinitely long plate or fine mesh electrode allows the same electric field strength to be present at each point on the mesh or plate. Although

in reality, where the mesh or plate is a finite size there is a distortion of the electric field at the edge of the electrode. This is demonstrated in the electrostatic modelling results for a plate electrode shown in Figure 6.26. The modelling assumptions for the electrostatic modelling are presented in Appendix G. The consequence of this distortion of the electric field is that it becomes a preferential location for the discharge to strike. In most cases the concentration of electric field at the edge of the electrode has a stronger influence on the location of the discharge than the PM meaning that a practical solution had to be found to maintain the discharge mobility across the entire surface area.

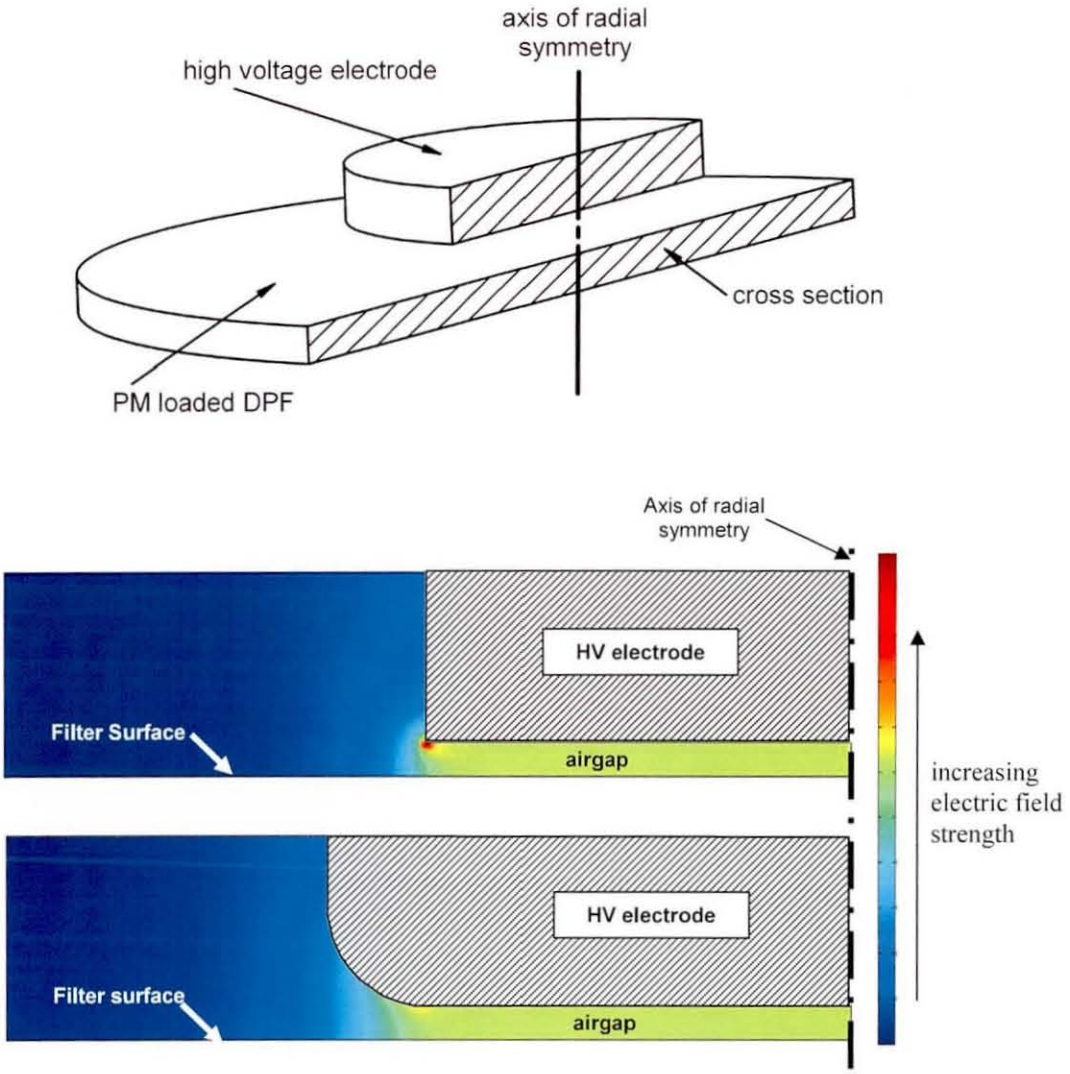

Figure 6.26. Electrostatic modelling of the concentration of electric field at the edge of the electrode.

The simplest way to control the electric field is to alter the geometry of the electrodes, typically by changing the electrode spacing. By increasing the electrode

spacing towards the edge of the electrode, the electric field strength can be reduced to match or be lower than the electric field strength over the majority of the electrode surface, also shown in Figure 6.26. This maintains the autoselectivity of the electric discharge.

The mounting of the electrodes poses its own difficulties. The electrode mounts need to:

1. Maintain the appropriate electrode spacing across their entire area.
2. Allow for variations in thermal expansion of the electrode and filter material.
3. Allow electrical connection to the power supply or ground electrode.

There are at least two possibilities that allow all of these requirements to be met, both of which are considered for the remainder of this research. The first uses the electrical connection as the electrode support. An example of such an idea is shown in Figure 6.27. The electrical feedthrough, similar to spark plug technology, is rigid enough to support the electrode. The electrode spacing will be fixed by the mounting position and the electrode is free to expand and contract without leading to potential damage of the filter or electrode. This has the disadvantage that the electrode spacing will be more prone to misalignment during manufacture and operation which will have a significant impact on discharge mobility.

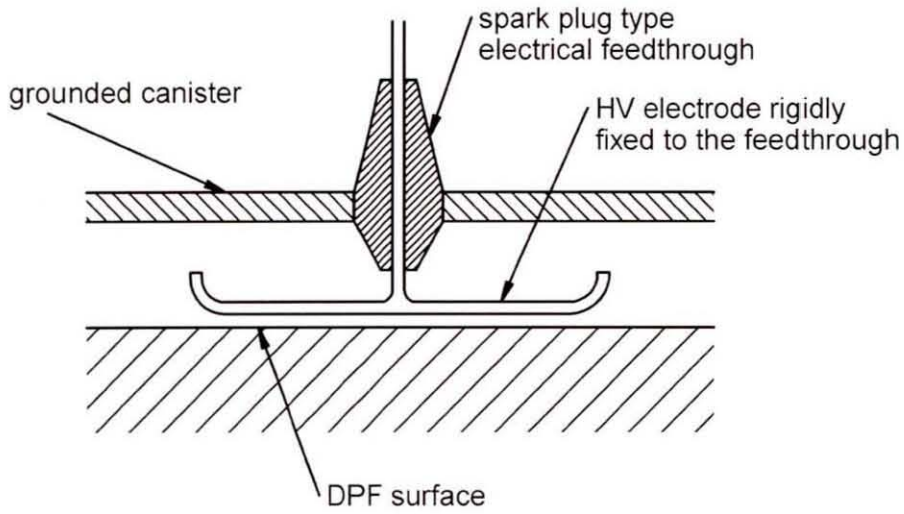

Figure 6.27. Electrode mounting design Proposal 1.

Figure 6.28 shows the second proposal which involves direct mounting of the electrodes to the filter surface with a flexible electrical connection so that minimal forces are applied to the electrode once in place. The electrodes are fixed rigidly in one direction only, perpendicular to the filter surface, to maintain the required electrode spacing. There is a limited range of movement in the two axes parallel to the filter surface to allow for variations in thermal expansion. Such electrode mounts can be moulded into the filter surface during production to reduce number of parts and manufacturing complexity.

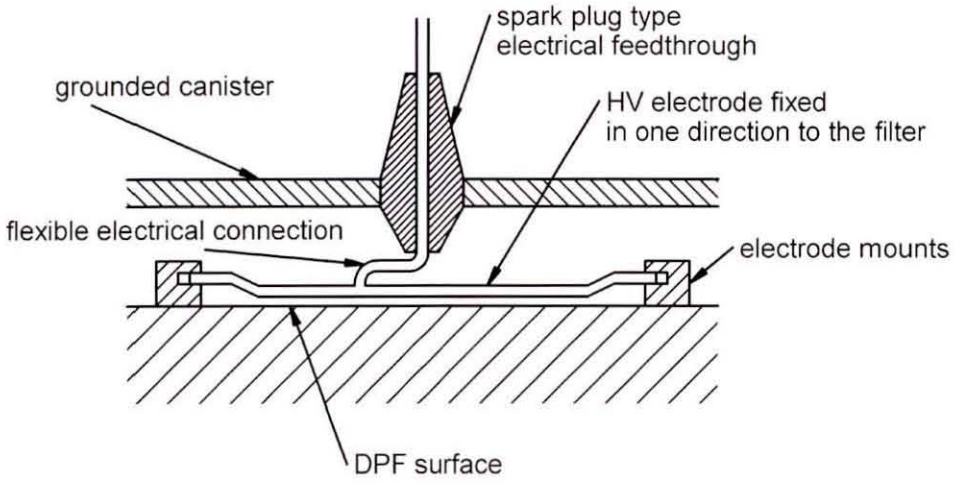

Figure 6.28. Electrode mounting design Proposal 2.

6.9 Unwanted Secondary Emissions

This section reports the work carried out to confirm that unwanted secondary emissions such as NO_X, O_3 and CN are not significant. The experimental methodology is introduced followed by the results and discussion of the measurements of secondary emissions.

6.9.1 Methodology

Transient measurements of the gas composition can be carried out using a mass spectrometer such as the Hiden Analytical HPR-20 shown in Figure 6.29. By observing changes in appropriate signal predictions can be made of the emissions from the filter regeneration. The HPR-20 spectrometer had a sensitivity of

approximately 5 parts per billion (ppb) if the ambient signal is of the same order of magnitude as the generated signal.

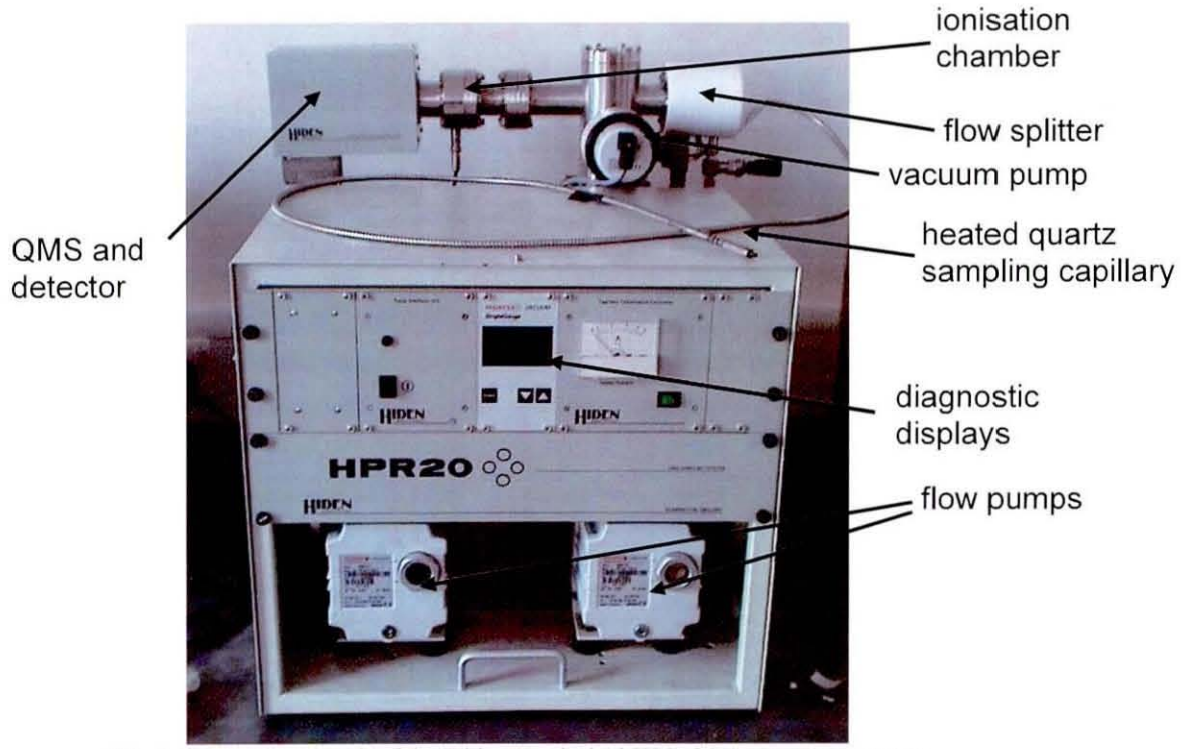

Figure 6.29. Photograph of the Hiden Analytical HPR-20 mass spectrometer.

Initial attempts to measure the generation of unwanted secondary emissions in the bulk gas downstream of the regenerating filter were unsuccessful due to the dilution of PM in the bulk gas. To overcome this issue, although achieve a less quantitative result, the probe was positioned immediately downstream of the electric discharge, shown in Figure 6.30. A single electric discharge between a high voltage pin electrode and ground mesh electrode was used to regenerate trapped PM.

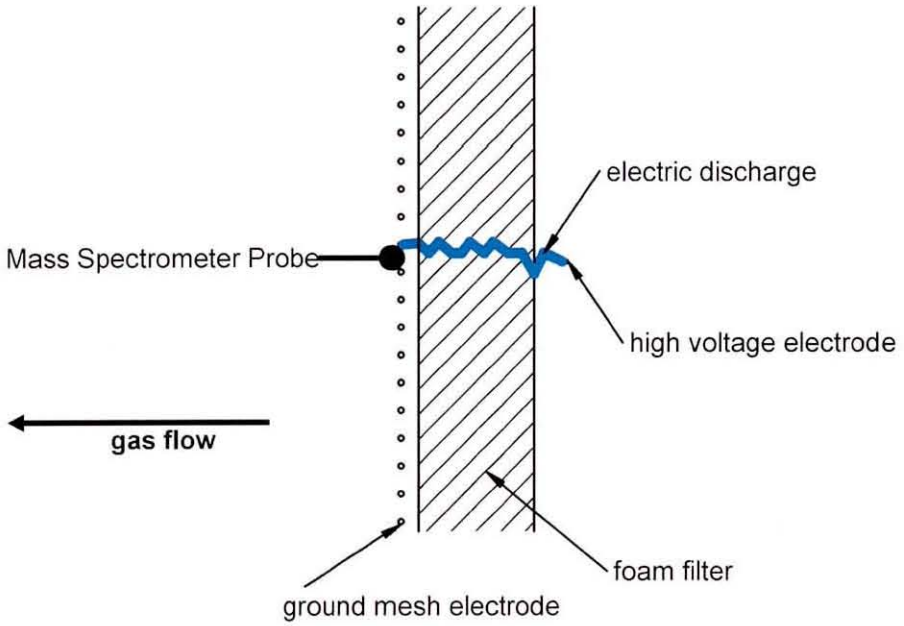

Figure 6.30. Probe and discharge arrangement for mass spectrometer measurements.

The signals of interest are generally equal to the atomic mass units (amu) of the wanted species. For CN and O_3 this is 26 amu and 48 amu respectively. The NO_x species (NO_2, NO and N_2O) generate peak signals at 30 amu (Hiden Analytical, 2005). The signal from the mass spectrometer was based on the partial pressure (of the vacuum chamber pressure) of the species being measured. The pressure in the vacuum chamber was noted to vary during the tests which directly affected the signal magnitude. Figure 6.31 demonstrates how the signal varies with the vacuum chamber pressure which was used to compensate for this variation during data analysis.

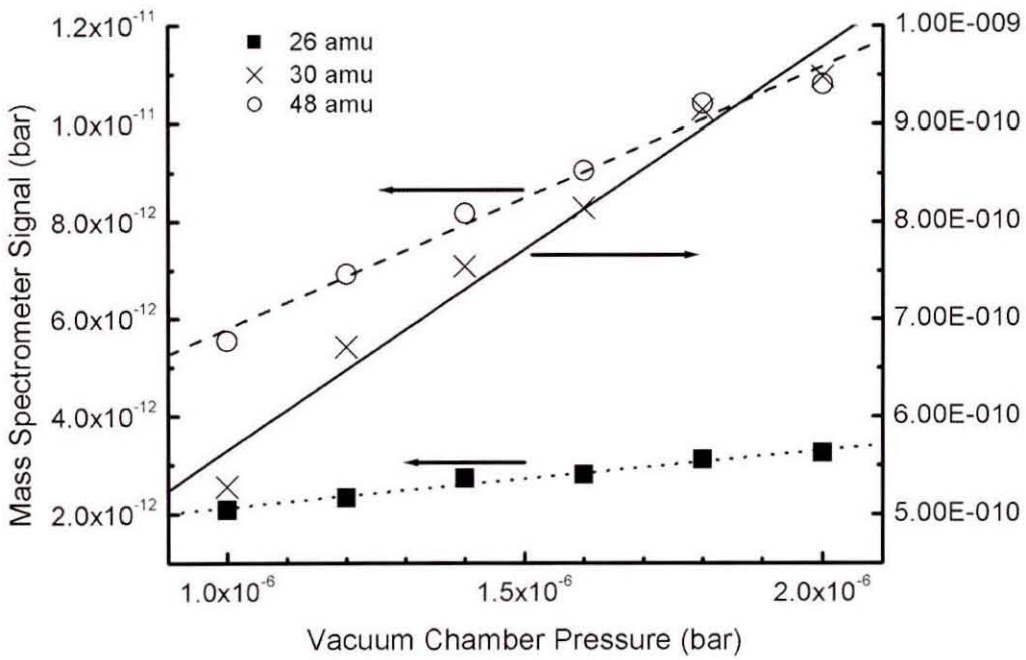

Figure 6.31. Plot of variation in mass spectrometer signal with vacuum chamber pressure

6.9.2 Results

With the correction for vacuum chamber pressure, the data was plotted as parts per million (ppm) in the gas sample during the test, and is shown here in Figure 6.32. The background signals, which can vary during the testing, were estimated using a linear fit between the initial period and final period when the discharge system was inactive. The difference between the actual reading and the background signal was taken as being a direct result of the Autoselective regeneration.

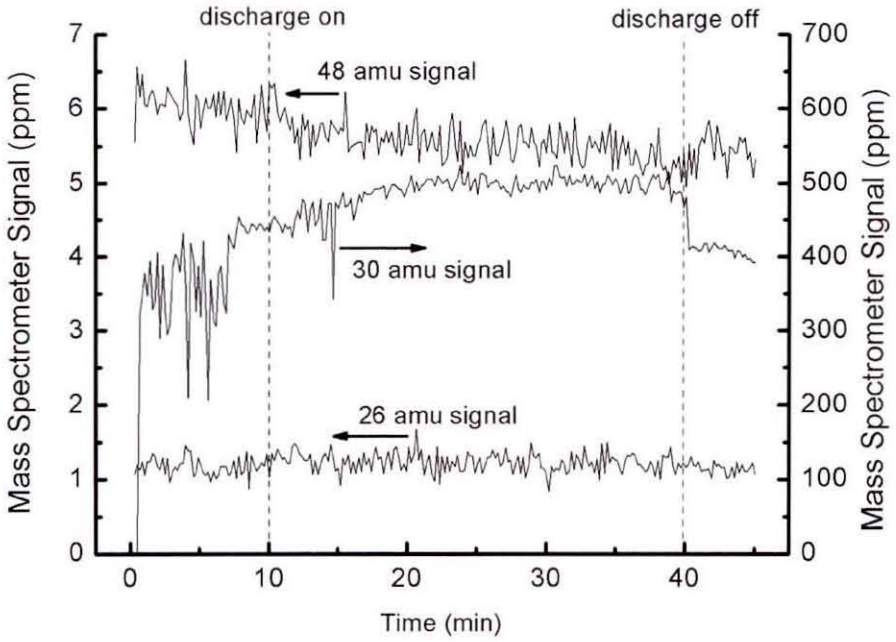

Figure 6.32. Plot of signals from the mass spectrometer for the potential by-products O_3, CN and NO_x.

The noise on the signal makes it difficult to visualise the effect directly from Figure 6.32. The large number of data points was used to calculate cumulative produced emissions throughout the test, shown in Figure 6.33. The production rate is near zero before and after the Autoselective regeneration but shows a clear production (or destruction) during the regeneration. The CN (26 amu) and NO_x (30 amu) signal show slight production rates while the Ozone (48 amu) signal shows it is being reduced by the Autoselective discharge.

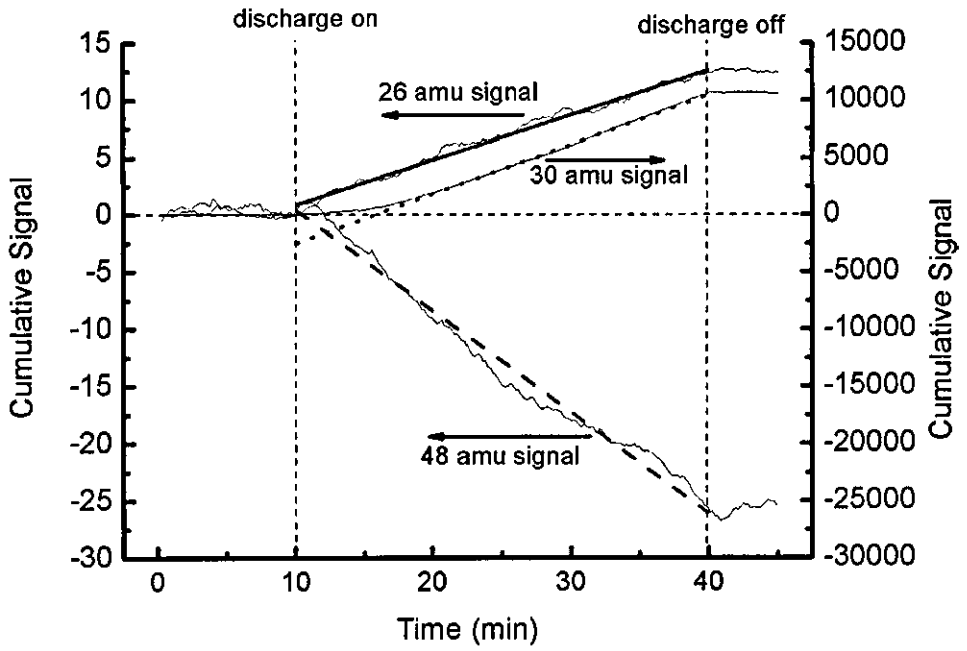

Figure 6.33. Plot of cumulative mass spectrometer signal for the potential by-products O_3, CN and NO_x.

Table 6.5 summarises the production rates of the secondary emissions at the sample point. These values indicate the production rates in the vicinity of the discharge and not in the bulk exhaust gas. An estimate is made of the production rates in the exhaust gas in the following section.

Table 6.5. Mass spectrometer secondary emission measurement results.

Signal	Cumulative Gradient (4 d.p.)	Equivalent production rate ppm (2 s.f.)
Calculated 100% gradient	7.8651×10^{9}	1.0×10^{6}
Mass 26 (CN)	5.6400×10^{2}	7.2×10^{-2}
Mass 30 (NO_x)	6.2244×10^{5}	8.0×10^{1}
Mass 48 (O_3)	-1.2753×10^{3}	-1.6×10^{-1}

6.9.3 Discussion

To broadly estimate the engine out secondary emissions, the following assumptions are needed:

1. the flow area in which the discharge generates secondary emissions is known (~10 mm diameter circle)

2. the space velocity, gas temperature and pressure is known (0.86 m s^{-1}, 320 K and $1.013x10^5$ Pa respectively)
3. the production rates are proportional to the PM oxidation rates

An example calculation of the estimated engine out secondary emissions of CN is shown to demonstrate the methodology used for all the secondary emissions. The molar density of the bulk gas is

$$\frac{n}{V} = \frac{P}{R_o T} = \frac{1.013\times10^5}{8.3144\times320} = 38.07 \text{ mol m}^{-3}$$

The molar density of the produced secondary emissions are therefore

$$\left(\frac{n}{V}\right)_{CN} = 38.07\times\frac{72}{1\times10^9} = 2.741\times10^{-6} \text{ mol}_{CN} \text{ m}^{-3}$$

The mass density of CN in the gas is then

$$2.741\times10^{-6} \text{ mol}_{CN} \text{ m}^{-3} = 7.127\times10^{-5} \text{ g}_{CN} \text{ m}^{-3}$$

The volumetric flow rate affected is given as

$$\dot{V} = \pi r^2 v = \pi\times\left(5\times10^{-3}\right)^2\times0.86 = 6.754\times10^{-5} \text{ m}^3 \text{ s}^{-1}$$

The CN production rate is estimated as

$$\dot{m}_{CN} = 6.754\times10^{-5}\times7.127\times10^{-5}\times60\times60 = 1.733\times10^{-5} \text{ g h}^{-1}$$

For regeneration rates of 0.2 g h^{-1} per discharge, the CN production rate is ~$8.7x10^{-5}$ g_{CN} g_{PM}^{-1}. Table 6.6 summarises similar calculations for O_3 and NO_x.

Table 6.6. Summary of calculations of estimated secondary emission production.

	Molar Density /mol m^{-3}	Mass Density /g m^{-3}	Production Rate /g s^{-1}	Production Quantities /g g_{PM}^{-1}
Mass 26 (CN)	$2.741x10^{-6}$	$7.127x10^{-5}$	$6.13x10^{-10}$	$8.7x10^{-5}$
Mass 30 (NO_x)	$3.046x10^{-3}$	0.1401 (max)	$1.20x10^{-6}$	$1.7x10^{-1}$
Mass 48 (O_3)	$-6.091x10^{-6}$	$-2.924x10^{-4}$	$-2.51x10^{-9}$	$-3.6x10^{-4}$

For a 56 kW engine producing ~5 g h^{-1} PM, the emissions are summarised as in Table 6.7. The estimated engine out emissions can be seen to be negligible.

Table 6.7. Estimated engine out secondary emissions

Emission	Engine out emissions g h^{-1}	Specific engine out emissions g kW^{-1} h^{-1}
CN	$4.4x10^{-4}$	$7.8x10^{-6}$
NO_x	$8.5x10^{-1}$	$1.5x10^{-2}$
O_3	$1.8x10^{-3}$	$3.2x10^{-5}$

6.10 Concluding Remarks

Chapter 6 has discussed the main issues related to integrating the Autoselective regeneration technology with gelcast ceramic foams. The discharge behaviour and interactions with the gelcast foams have been discussed and the need for spatially continuous discharges highlighted. Spatially continuous discharges allow regeneration of the filter volume as opposed to the surface and potentially offer more efficient oxidation of PM. Modelling led development of the integrated system has given a number of solutions that promote spatially continuous discharges which have subsequently been proven during rig testing. Issues relating to mobility of the electric discharge have been introduced and solutions proposed. Electrode materials and designs have been demonstrated that are low cost and effective. Secondary unwanted emissions of O_3, CN and NO_x have been shown to be negligible.

The following chapter considers the thermal flow through the integrated system, optimising the ceramic material properties and investigating the potential of filter damage.

CHAPTER 7

ANALYSIS OF THERMAL ENERGY FLOWS

Chapter 4, 5 and 6 discussed the developments of the Autoselective system including optimisation of the electric discharge for PM regeneration in the exhaust flow. This Chapter makes use of finite volume modelling techniques to study, understand and optimise the heat energy flow within the filter. The model is introduced and applied to study the effect of material choices, exhaust gas temperature and on- and off-times. The experimental and modelling investigations of the risk of damage to the filter during regeneration follow.

7.1 Thermal Effects

Observation of thermal effects within the filter volume are difficult due to the restricted depth of view into the filter. Combined with the duration needed to carry out a large number of tests to investigate a range of variables it is more time effective to develop thermal models to give an insight into the thermal behaviour of the gelcast ceramic foams with Autoselective regeneration. Commercial modelling packages are

available but those readily accessible for this project had some limitations that prevented adequate modelling of the Autoselective system (e.g. COMSOL Multiphysics general heat flux boundary condition applied a fixed heat flux to an entire boundary rather than as a function of the local temperatures). For this reason a two dimensional finite volume thermal model of the gelcast ceramic foams was developed to study the Autoselective regeneration system on porous ceramics. The model was then used to understand the effects of material choices on energy usage, the effect of ambient temperature on maximum on time and the effect of discharge power density on the required off-times.

7.1.1 Model Derivation

The thermal conduction equations for two dimensional transient problems with radial symmetry can be written as

$$\rho c_p \frac{\partial T}{\partial t} = \frac{\partial}{\partial r}\left(k\frac{\partial T}{\partial r}\right) + \frac{\partial}{\partial y}\left(k\frac{\partial T}{\partial y}\right) + S \qquad (7.1)$$

where ρ is the medium density, c_p is the specific heat capacity, k is the thermal conductivity, T is the temperature, t is the time, r is the radius, y is the height and S includes any source terms e.g. heat sources. The conceptual model that was used is shown in Figure 7.1. The cells resulting from discretisation are rings of rectangular cross section.

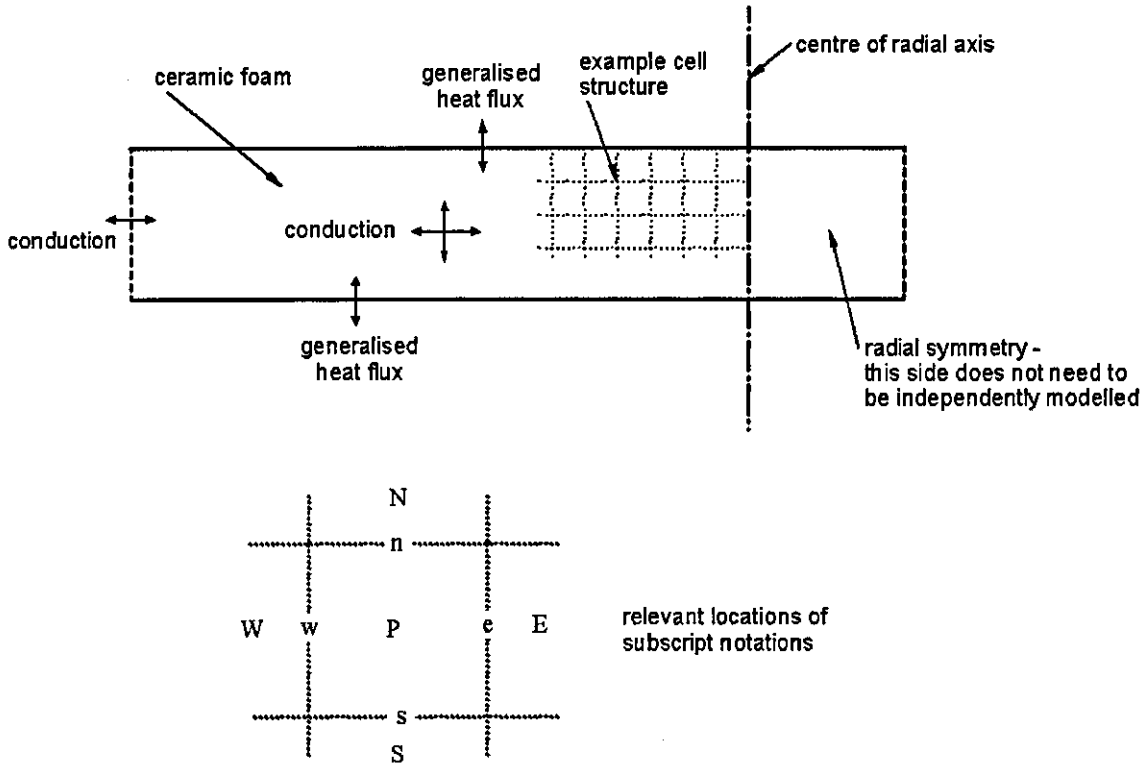

Figure 7.1. Schematic of the finite volume model discretisation.

Discretising the above equation and integrating with respect to the cell volume results in

$$\rho c_p V_P \frac{\left(T_P - T_P{}^o\right)}{\delta t} = \left(kA_e \frac{\left(T_E - T_P\right)}{\delta r} - kA_w \frac{\left(T_P - T_W\right)}{\delta r} \right) + \left(kA_n \frac{\left(T_E - T_N\right)}{\delta y} - kA_s \frac{\left(T_P - T_S\right)}{\delta y} \right) + S' \tag{7.2}$$

where the subscripts refer to the locations shown in Figure 7.1, V_P is the volume of the cell, A is the connecting area between two cells, δt is the discretisation time step, δr is the cell width, δy is the cell height and S' is the source term heat flux.

Rearranging this gives

$$a_P T_P = a_E T_E + a_W T_W + a_N T_N + a_S T_S + S' \tag{7.3}$$

where

$$a_P = \frac{\rho c_p V_P}{\delta t} + \frac{kA_e}{\delta r} + \frac{kA_w}{\delta r} + \frac{kA_n}{\delta y} + \frac{kA_s}{\delta y}$$

$$a_E = \frac{kA_e}{\delta r}$$

$$a_W = \frac{kA_w}{\delta r}$$

$$a_N = \frac{kA_n}{\delta y} \qquad (7.4)$$

$$a_S = \frac{kA_s}{\delta y}$$

$$S^{'} = q_{convection} + q_{radiation} + q_{heatsource} + \frac{\rho c_p V_P T_P^{\ o}}{\delta t}$$

These equations can be solved for either the north-south direction or east-west direction independently. Iterating the solution by alternately solving north-south and east-west directions converges on a solution for that time step. When solving in the north-south direction, the east and west terms on the right hand side of the re-arranged equation form part of the source terms. Similarly, when solving in the east-west directions, the north south terms form part of the source terms. The equations have been implemented in Matlab to allow easy solution of the equations in matrix form. Special consideration for the boundary conditions are of the form discussed by Versteeg and Malalasekera (1995). At the northern and southern boundaries there is a heat flux equal to

$$q = hA\Delta T \qquad (7.5)$$

where q is the heat flux, h is the heat transfer coefficient, A is the area through which heat flux takes place and ΔT is the difference between the bulk gas temperature and the surface temperature. At this boundary there is no conduction. The coefficients, a, then become

$$
\begin{aligned}
a_P &= \frac{\rho c_p V_P}{\delta t} + \frac{kA_e}{\delta r} + \frac{kA_w}{\delta r} + \frac{kA_s}{\delta y} \\
a_E &= \frac{kA_e}{\delta r} \\
a_W &= \frac{kA_w}{\delta r} \\
a_N &= 0 \\
a_S &= \frac{kA_s}{\delta y} \\
S^{'} &= q_{convection} + q_{radiation} + q_{heatsource} + \frac{\rho c_p V_P T_P{}^{o}}{\delta t} + hA_n\left(T_g - T_P{}^{o}\right)
\end{aligned}
\tag{7.6}
$$

and

$$
\begin{aligned}
a_P &= \frac{\rho c_p V_P}{\delta t} + \frac{kA_e}{\delta r} + \frac{kA_w}{\delta r} + \frac{kA_n}{\delta y} \\
a_E &= \frac{kA_e}{\delta r} \\
a_W &= \frac{kA_w}{\delta r} \\
a_N &= \frac{kA_n}{\delta y} \\
a_S &= 0 \\
S^{'} &= q_{convection} + q_{radiation} + q_{heatsource} + \frac{\rho c_p V_P T_P{}^{o}}{\delta t} + hA_s\left(T_g - T_P{}^{o}\right)
\end{aligned}
\tag{7.7}
$$

for the northern and southern boundaries respectively.

At the symmetry axis the area is zero meaning that conduction on the central boundary is zero. This leads to the coefficients being

$$
\begin{aligned}
a_P &= \frac{\rho c_p V_P}{\delta t} + \frac{kA_w}{\delta r} + \frac{kA_n}{\delta y} + \frac{kA_s}{\delta y} \\
a_E &= 0 \\
a_W &= \frac{kA_w}{\delta r} \\
a_N &= \frac{kA_n}{\delta y} \\
a_S &= \frac{kA_s}{\delta y} \\
S^{'} &= q_{convection} + q_{radiation} + q_{heatsource} + \frac{\rho c_p V_P T_P^{\,o}}{\delta t}
\end{aligned}
\tag{7.8}
$$

At the western boundary there is a continuous ceramic foam medium through which conduction can still take place. A known temperature boundary condition applies at the edge boundary which leads to the coefficients becoming

$$
\begin{aligned}
a_P &= \frac{\rho c_p V_P}{\delta t} + \frac{kA_e}{\delta r} + \frac{2kA_W}{\delta r} + \frac{kA_n}{\delta y} + \frac{kA_s}{\delta y} \\
a_E &= \frac{kA_e}{\delta r} \\
a_W &= \frac{2kA_W}{\delta r} \\
a_N &= \frac{kA_n}{\delta y} \\
a_S &= \frac{kA_s}{\delta y} \\
S^{'} &= q_{convection} + q_{radiation} + q_{heatsource} + \frac{\rho c_p V_P T_P^{\,o}}{\delta t}
\end{aligned}
\tag{7.9}
$$

where A_W is the known temperature at the boundary. Similar analysis for the corner cells provides boundary conditions for these locations.

To solve these equations it is necessary to define the material parameters to represent the foam structure. The following required defining:

1. Density
2. Specific heat capacity

3. Thermal conductivity
4. Surface to gas heat transfer coefficient.

The density was defined by making the approximation that the foam structure can be represented by a homogeneous medium. This defines the bulk density as

$$\rho = \rho_1(1-\varepsilon) + \rho_2\varepsilon \tag{7.10}$$

where ρ_1 is the density of the ceramic, ρ_2 is the density of the air and ε is the porosity of the ceramic foam. The specific heat capacity can be found in a similar way assuming that the trapped air is at the same temperature as the solid, giving

$$c_p = \frac{c_{p1}(1-\varepsilon)\rho_1 + c_{p2}\varepsilon\rho_2}{(1-\varepsilon)\rho_1 + \varepsilon\rho_2} \tag{7.11}$$

which when $\rho_2 << \rho_1$, and epsilon is not close to 1 or 0, can be approximated by:

$$c_p = c_{p1} \tag{7.12}$$

The thermal conductivity is based on the relationships defined by Brailsford and Major (1964) for heat flow in porous materials with spherical pores

$$k = k_s \frac{2k_s + k_a - 2(k_s - k_a)\varepsilon}{2k_s + k_a + (k_s - k_a)\varepsilon} \tag{7.13}$$

where k_s and k_a are the thermal conductivity of the solid and the air respectively. The surface to gas heat transfer coefficient is more difficult to define and is estimated as approximately 30 W m^{-2} K^{-1} based on typical values for natural convection in air (Janna, 2000).

The material properties used for the simulations are shown in Table 7.1 with the calculated bulk ceramic foam properties included.

Table 7.1. Material properties used for the modelling (based on 80% porous foams)

Material	Thermal Conductivity ($W\ m^{-1}\ K^{-1}$)	Density ($kg\ m^{-3}$)	Specific Heat Capacity ($J\ kg^{-1}\ K^{-1}$)	Melting Temperature (K)
Cordierite	1.59	2100	753.6	1650
Alumina	8, 6.3	3980	1103.4	2050
Zircon	4.2	4600	538	2400
Silicon Carbide	59.8	3210	31.4	2700
Cordierite Foam	0.25	420	754.1	1650
Alumina Foam	1.17	796	1103.3	2050
Zircon Foam	0.62	920	538.4	2400
Silicon Carbide Foam	8.57	642	32.6	2700

Sources:- CRC Handbook of Chemistry and Physics (2003), Shackelford and Alexander (2001), Ahrens (1995)

7.1.2 Model Validation

To validate the model a comparison was made with a cordierite foam test sample that was exposed to comparable thermal energy to the discharge. The model was then used to identify the time taken to cause damage with the measured thermal energy input and the results were compared. Figure 7.2 shows the results of this comparison with promising agreement. This demonstrates that the model is capable of reasonable agreement with the thermal flows in the ceramic foams.

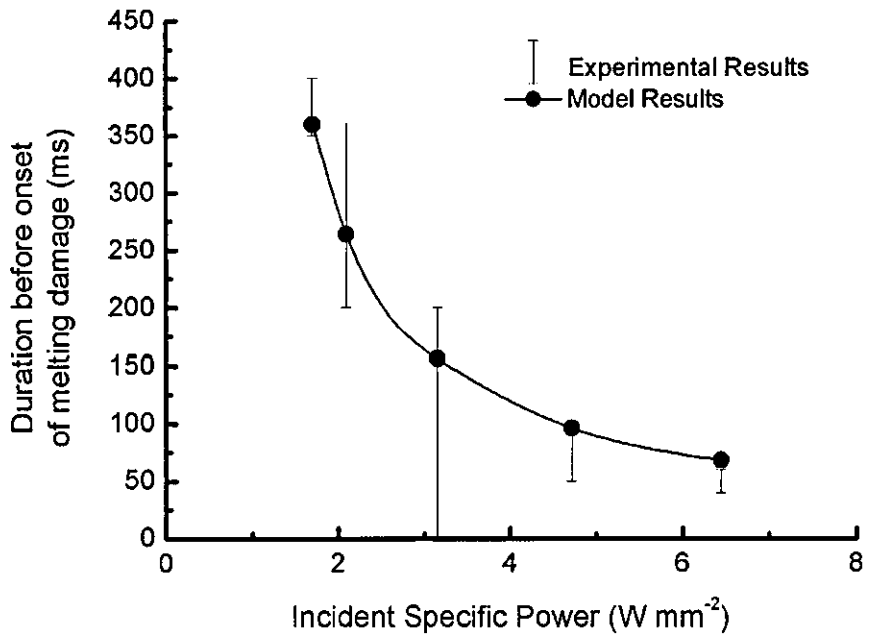

Figure 7.2. Comparison of modelling predictions and experimental measurements of exposure duration before onset of damage. Experimental results taken from Figure 7.7.

7.1.3 Effect of Material Choices on Regeneration Efficiency

If thermal damage becomes a problem it is commonly suggested to choose a material with a higher working temperature, such as changing from cordierite foams to alumina foams. Due to the increased thermal conductivity and heat capacity this has a significant influence on the flow of thermal energy through the foams. This is clearly demonstrated in Figure 7.3 which shows the predicted amount of energy required from a single discharge to raise material temperatures to 1000 K It can be seen that significantly more energy (which would be input as longer on-times) would be required to increase zircon and alumina to 1000 K than cordierite. Under the same thermal heat flux, it was predicted that silicon carbide foam would not reach 1000 K at steady state. The conclusions are that an optimum material will have a melting temperature high enough for rapid PM oxidation, low thermal conductivity and low heat capacity. Cordierite has a melting temperature higher than that required for rapid oxidation of PM and requires minimal energy to raise the local temperatures meaning this offers a good compromise allowing rapid oxidation of PM and low energy consumption.

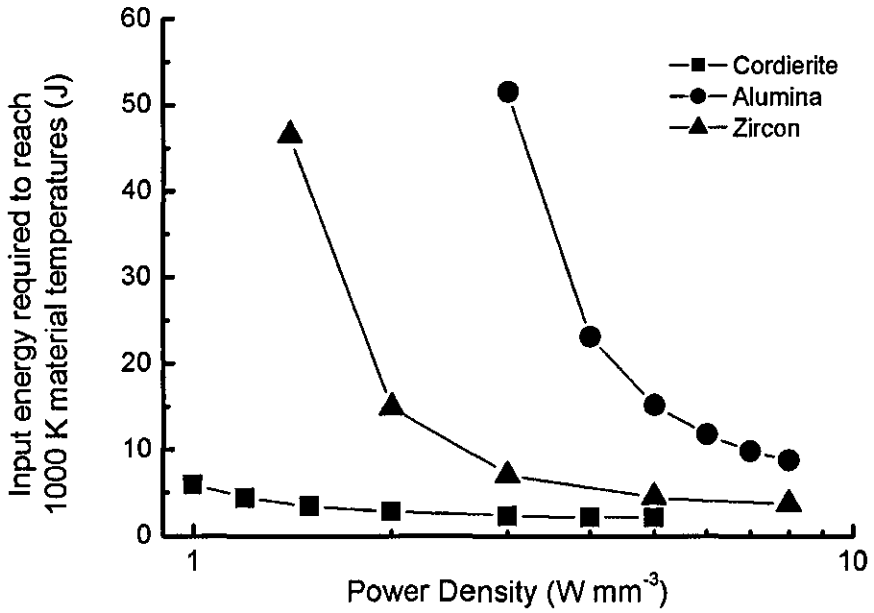

Figure 7.3. Effect of material choices on energy required to heat the local material.

7.1.4 Effect of Bulk Temperature on Maximum On-time

Figure 7.4 shows the predicted effect of bulk gas temperature on the maximum on-time before the onset of damage for a fixed energy input. It shows that over the range of ambient temperatures that will be experienced in the exhaust system a significant variation in the maximum on-times is present. The relationship is almost linear (the dashed line demonstrates a slight deviation from linearity). This implies that control of the discharge system on vehicle will need to be a function of engine operating conditions. It is important to note that this is the equivalent of the on-time required to reach a given temperature showing that at higher ambient temperatures, shorter on-times are needed to rapidly oxidise the local PM.

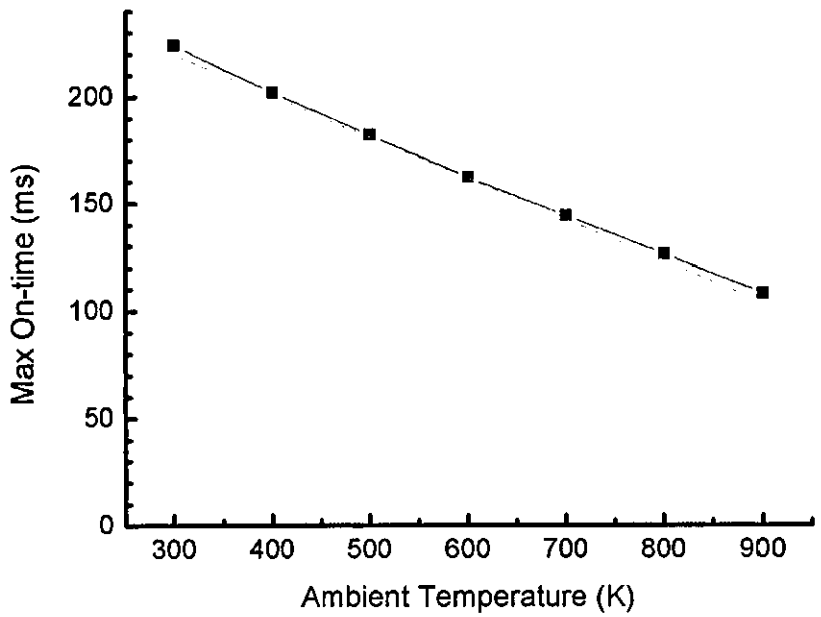

Figure 7.4. Effect of ambient temperature on maximum on time.

7.1.5 Effect of Discharge Power on Required Off-times

To highlight the complexity of optimising the off-time, an example showing the predicted effect of the discharge power on the required off-time is shown in Figure 7.5. This figure shows three different discharge powers with on times needed to reach 1100 K peak material temperatures. The discharge was then extinguished and the material temperatures noted as it cooled.

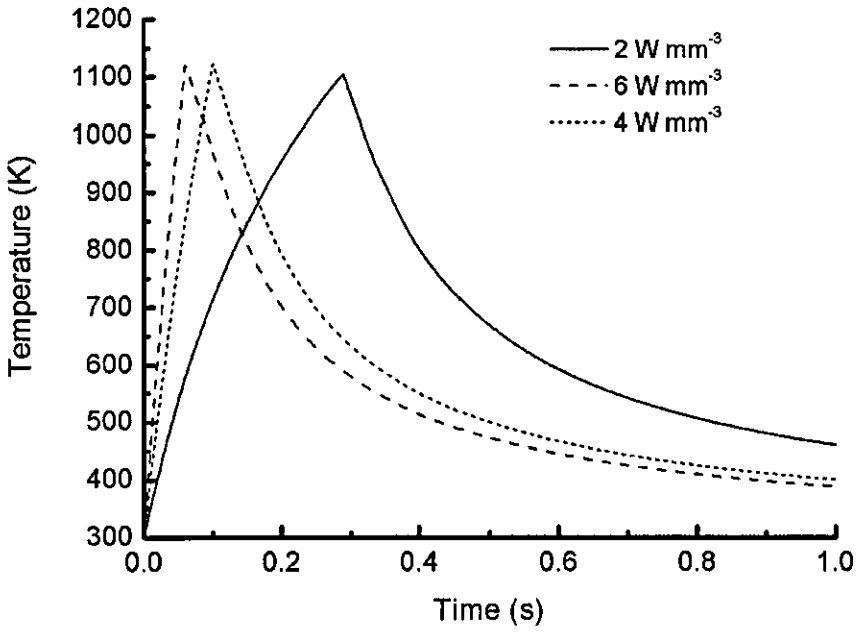

Figure 7.5. Plot showing the transient (peak) temperature for a range of power densities.

The cool down rate is summarised in Figure 7.6, giving an indication of the cool-down period as a function of the input power density showing that as the input power density reduced, the cool-down time increased due to the reduction in thermal gradients in the material at the time the discharge was extinguished.

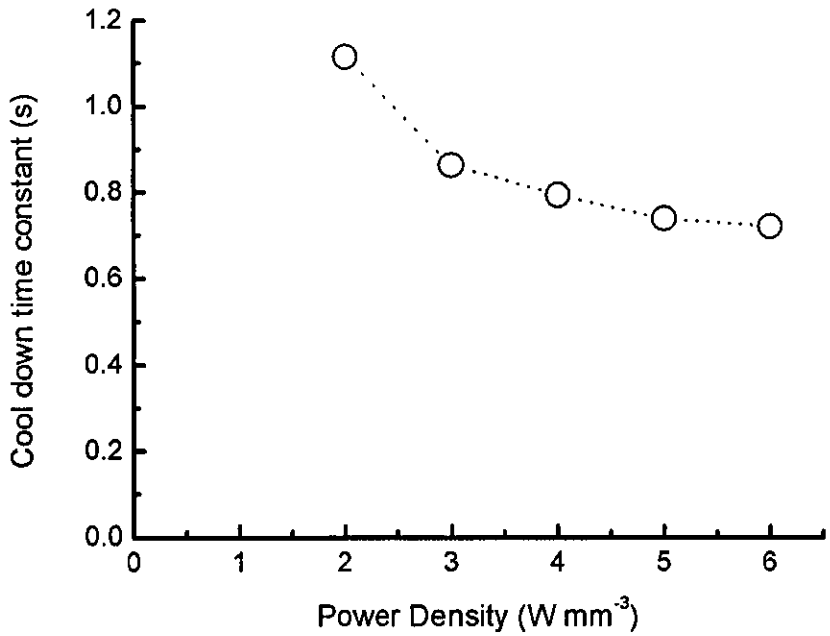

Figure 7.6. Effect of power density on the cool down time constant.

When optimising the on- and off-time considerable effort needs to be made to understand the interactions of the thermal effects being optimised. In this work appropriate on- and off-times of typically 100 ms and 800 ms respectively have been used to regenerate trapped PM, avoid thermal damage and maintain Autoselectivity. Thorough optimisation, however, has not been carried out. This modelling highlights the complexities and identifies some important considerations that must be made when optimising the discharge on- and off-times.

7.2 Filter Damage

Preliminary tests regenerating ceramic foam DPFs in stationary air showed that filter damage can be caused by either melting or thermal shock. Characteristics and factors affecting melting and thermal shock are discussed in the following text supported by modelling and experimental testing.

7.2.1 Consequences of Filter Damage

Filter damage was found to occur mainly through melting of the ceramic and thermal shock. The effect of the two types of damage can be summarised as:

1. Melting Local melting of the ceramic foam substrate on a scale smaller than the pore size alters the shape of the struts. On larger scales (~1 mm) the pore structure collapses reducing the porosity and changing the filtration properties.
2. Thermal shock Thermal shock leads to breaking of the ceramic filter into a coarse powder (~500 μm particles) which will either be lost in the exhaust gas or trapped in the remaining filter. The filtration efficiency will be slightly reduced and the back pressure increased.

For isolated cases of damage the bulk filtration and regeneration properties of the filter will not be affected. For the lifetime of an engine the cumulative effect of repetitive damage in the form of either melting or thermal shock will be unacceptable and would potentially lead to filter failure. On- and off-times must be used to control

of both thermal shock and melting damage and must be optimised before the Autoselective system is ready for production.

7.2.2 Melting

High temperatures are a pivotal requirement for effective oxidation of trapped PM. If high enough thermal flux is applied to a small enough volume (i.e. high enough power density) the material temperatures are capable of exceeding the melting temperature of the ceramic filter material. Preliminary testing showed that such an effect is typically observed to be the major cause of damage with materials that have relatively good thermal shock properties, such as cordierite.

Thermal heat flux was applied to the surface of the ceramic to allow measurements of on-times before melting for different heat flux density using a Coherent S48 continuous wave CO_2 laser (10.6 μm wavelength). The diameter of the laser beam was varied to achieve different power densities of the same order of magnitude as the heat flux density of an electric discharge. The typical heat flux from the discharge was measured as ~2 W mm^{-2} surface area. Single exposures of varying durations then allowed investigation of the effect of discharge contact duration on filter damage. The onset of damage was determined visually by observing reflections from the glass phase ceramic that results from melting damage.

The calculated power densities are summarised in Table 7.2 and the effect of exposure time on cordierite foam is shown in Figure 7.7. The top of each dataline indicates a test point where damage was observed. The bottom of the dataline indicates the closest test point where damage did not occur. It can be seen that with specific power in the region of ~2 W mm^{-2} the onset of melting occurred at approximately 350 ms. As the specific power is increased to approximately 6 W mm^{-2} the onset of damage occurred between 60 and 80 ms. This data allowed determination of the discharge mobility that is required to avoid filter damage without airflow.

Table 7.2. Determination of the specific power.

Laser Power /W	Beam Diameter /mm	Beam Area /mm^2	Power per unit area /W mm^{-2}
75	7.50	44.18	1.7
75	6.75	35.78	2.1
75	5.50	23.76	3.2
75	4.50	15.89	4.7
75	3.88	11.64	6.4

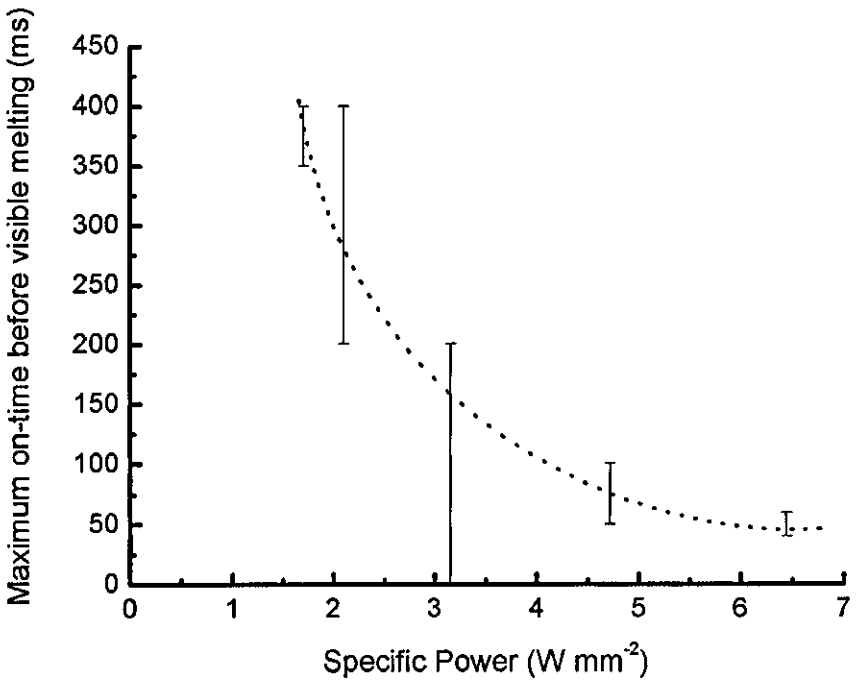

Figure 7.7. Effect of shot duration on the occurrence of melting of cordierite ceramic foam for different power densities.

Figure 7.7 shows that there is an inverse type relationship between the applied power density and the maximum exposure time before the onset of melting of the ceramic material. The constant power density asymptote corresponds to the power density at which the steady state material temperature is the melting temperature of the ceramic.

Effect of Material on Likelihood of Melting

The thermal model described earlier was used for the investigation of effects of material properties on the maximum discharge on-time for a range of available

ceramic foams. The heat source was considered to be localised in a region small compared to the overall volume of interest.

A number of ceramic materials that can be produced as ceramic foams have been investigated using this model to gain an insight into how their durability with regards melting compare. Cordierite, alumina, zircon and silicon carbide are considered with melting temperatures shown in Table 7.1. These are typical materials available in gelcast ceramic foam form. The modelling is not intended to give definitive values for maximum stationary discharge times but instead to guide material choices during design and development of this regeneration system.

Figure 7.8 shows the predicted durations for which the heat flux can occur in one position before the onset of damage using the heat transfer model for this selection of materials. The durability of the materials regarding melting varies significantly. The largest effect is due to variations in thermal conductivity which act to reduce both the rate of increase of surface temperatures and the steady-state temperatures. This also varied over a wider range than the specific heat capacity and so the effect dominates. It is worth noting that although this study focused on 80% porous ceramics, the thermal conductivity of the ceramic foam, and hence resistance to melting, can be manipulated by altering the porosity. Cordierite was shown to be the most likely to be damaged out of the four materials investigated, with Zircon and Alumina being significantly more resistant to the heat flux. This information acts not only as a guide to material durability but allows an estimate of the maximum exposure time of a filter site to the discharge. Choosing a material purely for its durability will lead to an inefficient system since, although alumina can handle significantly higher power densities before melting, the thermal energy is removed from the surface faster, leading to lower surface temperatures and less PM oxidised for higher energy inputs. This needs to be considered since regeneration effectiveness is a vital aspect of regeneration systems.

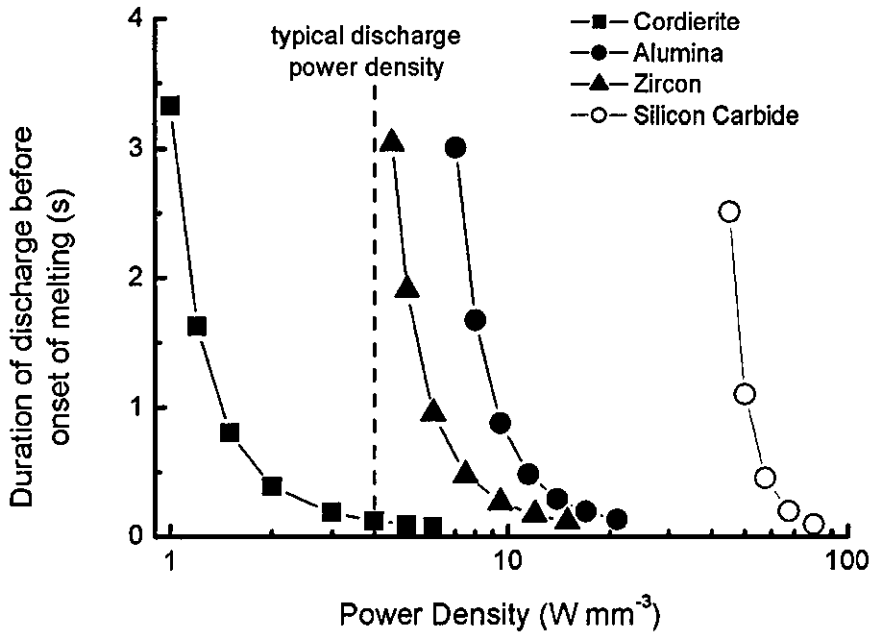

Figure 7.8. Time before melting temperatures are reached as a function of input power density.

Considering that a typical discharge power density is in the region of 4 W mm^{-3} it can be seen that on cordierite, if the discharge is left stationary for more than approximately 150 ms then the material is likely to melt. In the case of alumina and zircon the melting temperatures are never reached with power densities of this magnitude. Testing on alumina and zircon samples supported this finding as the discharge could be sustained indefinitely without melting the ceramic. This identifies materials that offer improved durability, however, cordierite was proposed due to the energy efficiency benefits, since careful control of power density can be used to avoid filter damage.

7.2.3 Thermal Shock

Another significant mode of material failure is a result of thermal shock. The highly focused heat flux from an electric discharge can lead to thermal gradients of the order of 500 K mm^{-1}. This imparts significant stresses on the ceramic due to thermal expansion of a very localised region and was observed in this research with alumina filters. Due to the complex nature of analysing localised thermal stress in the random structure of the ceramic foam the understanding of the system was achieved by experimentation.

A Coherent S48 continuous wave CO_2 (10.6 μm wavelength) laser with varying exposure time was used to investigate the effect of different power densities on thermal shock damage of alumina filters. This was identified by the breaking up of the ceramic surface into a coarse powder.

The results of the onset of damage are presented in Figure 7.9 which showed similar trends to the melting damage, shown in Figure 7.8. It highlights that as the power density increased the threshold duration for damage to be observed reduced significantly. This is a result of the thermal gradients increasing as the material temperatures increase more rapidly. If the heat flux is switched off before the temperatures become excessive, the thermal stresses can be controlled. It was necessary to test this effect on the material being used since the limit of time or power density will depend not only on the material but also the pore structure (e.g. size) of the foam. Alumina is known for poor thermal shock properties and preliminary testing demonstrated that thermal shock is a concern on alumina filters.

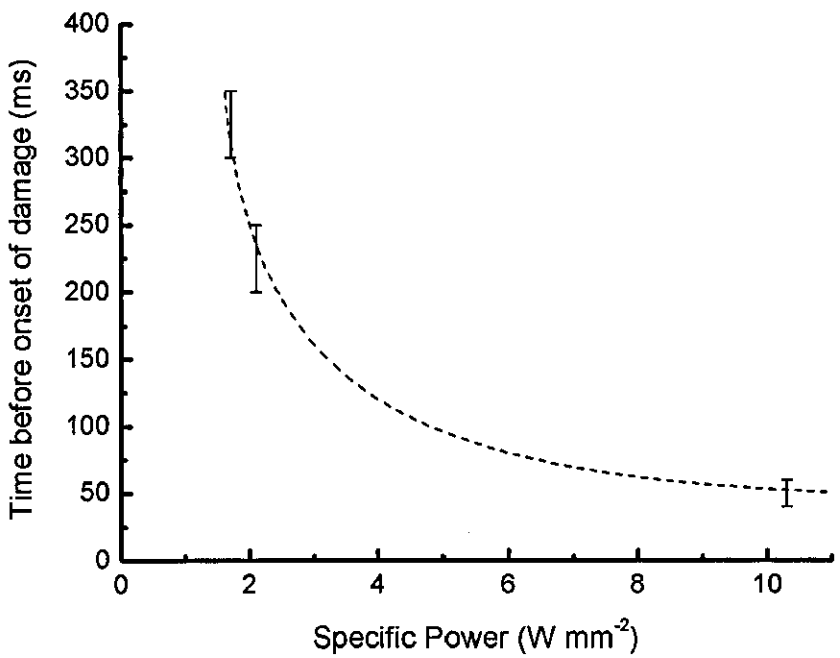

Figure 7.9 Effect of power density on the onset of damage with Alumina filters.

The thermal stress failure of ceramic foams is a complex area. Typical thermal stress resistance parameters presented by Richerson (1992) have been used to compare some available ceramic materials. These are resistance to fracture initiation:

$$R_1 = \frac{\sigma(1-\nu)}{\alpha E} \tag{7.14}$$

and resistance to fracture propagation:

$$R_2 = \frac{E}{\sigma^2(1-\nu)} \tag{7.15}$$

where σ is the tensile strength, ν is the Poisson ratio, α is the coefficient of thermal expansion and E is the Young's modulus. The material data used is shown in Table 7.3.

Table 7.3. Material data used for thermal shock analysis. Source: Shackelford and Alexander, 2002

Material	Young's Modulus /GPa	Poisson Ratio	Thermal Expansion Coefficient /K^{-1} x10^{-6}	Tensile Strength /MPa
Silicon Carbide	303	0.19	5.48	86.2
Alumina	379	0.25	9.00	241
Cordierite	138	0.17	2.70	24.1
Zircon	165	0.20	5.50	60.0

Table 7.4 shows the calculated resistance to thermal shock. All the filter materials demonstrate comparable resistance to fracture initiation although their resistance to fracture propagation varies notably. Alumina showed the least resistance with cordierite showing the most resistance to fracture propagation. This implies that when evaluating the resistance to thermal shock from the Autoselective discharge, resistance to fracture propagation is a more appropriate measure than resistance to fracture initiation. Cordierite is shown to offer an effective and durable filter material providing peak material temperatures can be controlled below the melting temperature.

Table 7.4 Resistance to thermal shock of selected ceramic materials.

Material	Parameter (for constant thermal gradient)	
	Resistance to fracture initiation (K)	Resistance to fracture propagation (Pa^{-1})
Silicon Carbide	42	$50x10^{-6}$
Alumina	53	$9x10^{-6}$
Cordierite	54	$285x10^{-6}$
Zircon	53	$57x10^{-6}$

7.3 Concluding Remarks

Chapter 7 has investigated the thermal flow through the ceramic foams when the Autoselective regeneration system is active. Modelling investigations of available materials have highlighted that cordierite has a low melting resistance to high power densities, however, requires less energy to heat the filter up to temperatures that rapidly oxidise PM. Cordierite is proposed as a promising material as the low thermal conductivity, heat capacity and reasonable working temperature allow efficient localised heating of the ceramic and trapped PM. Modelling and experimental investigations into melting and thermal shock identify design limits and further support for material decisions. The following chapter presents single electrode regeneration of a gelcast ceramic foam DPF on a 4.4 litre turbocharged heavy duty diesel engine. Effects of artifical load capacitance, applied voltage, electrode spacing and on- and off-times have been studied during the on-engine testing and are presented in Chapter 8.

CHAPTER 8

ON-ENGINE TESTING

8.1 Aims

Following successful investigation of the principles of regenerating gelcast ceramic foam filters with the Autoselective technique the concept has been investigated on an engine. This introduces a number of different factors not simulated in the hot flow rig such as continuous PM loading. The aim of the on-engine testing was to investigate the effect of a number of unknown factors on the performance of the regeneration system under real engine conditions as an initial optimisation of the design factors. Smoke measurement equipment on engine is also suitable for measuring blow-off (non-oxidised PM removed from the DPF) during regeneration. This chapter described the experimental methodology for the on-engine tests not already discussed in Chapter 3. This is followed by a description of the data analysis and presentation of the test results. There is then a discussion of the results and potential causes of the observed trends.

8.2 Experimental Method

For simplicity, a single HV electrode was mounted parallel to the surface of a 7.5 inch diameter, 10 mm thick disc filter. This avoided the complexities of electrode interactions when investigating the effect of the factors of interest. A CAD image demonstrating the electrode arrangement is shown in Figure 8.1. The high voltage electrode was smaller in diameter than the ground electrode to simulate a continuous ground across the entire filter surface. The electrode spacing increased around the edge of the electrode to maintain discharge mobility. This has been described in more detail on page 182. The electrodes were mounted by inserting a wire of the mesh through a protrusion of the ceramic foam filter. This fixed the electrode rigidly in the direction perpendicular to the filter surface, maintaining the electrode spacing, but allowed movement in the plane of the filter surface to allow for thermal expansion of the mesh and filter materials.

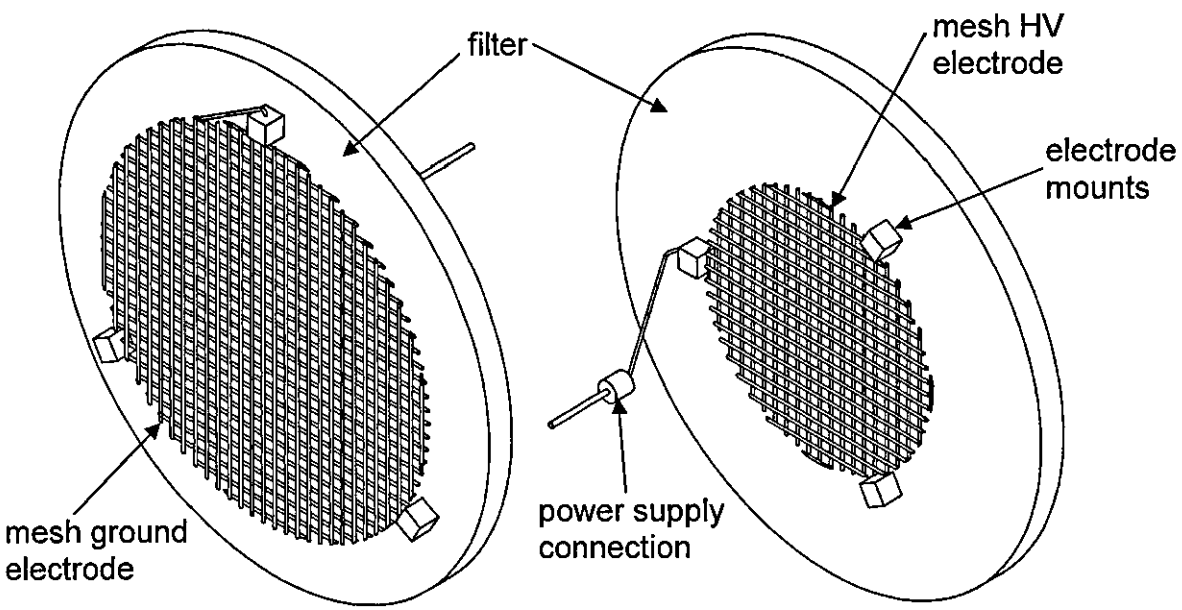

Figure 8.1. CAD image showing (a) the mesh ground electrode arrangement and (b) the high voltage electrode arrangement.

The mesh ground electrode was connected directly to the grounded exhaust canister. The HV electrode was connected to the power supply through a Macor electrical feedthrough on the downstream side of the filter.

The 4.4 litre Perkins 1100 series test engine and canister has been described in more detail in Chapter 3. The filter was mounted against the retaining ring with the high voltage electrode on the downstream side of the filter and the grounded electrode on

the upstream side of the filter. The location and key features of the experimental setup are shown in Figure 8.2. The test condition was chosen to be 1000 rpm and between 0 and 15 Nm load. This condition generated approximately 0.2 g h^{-1} PM out of the engine which was anticipated as a typical regeneration rate that could be achieved by a single electrode. The space velocity at this test condition is comparable to a cylindrical filter arrangement that forms the integrated prototype concept in Chapter 9.

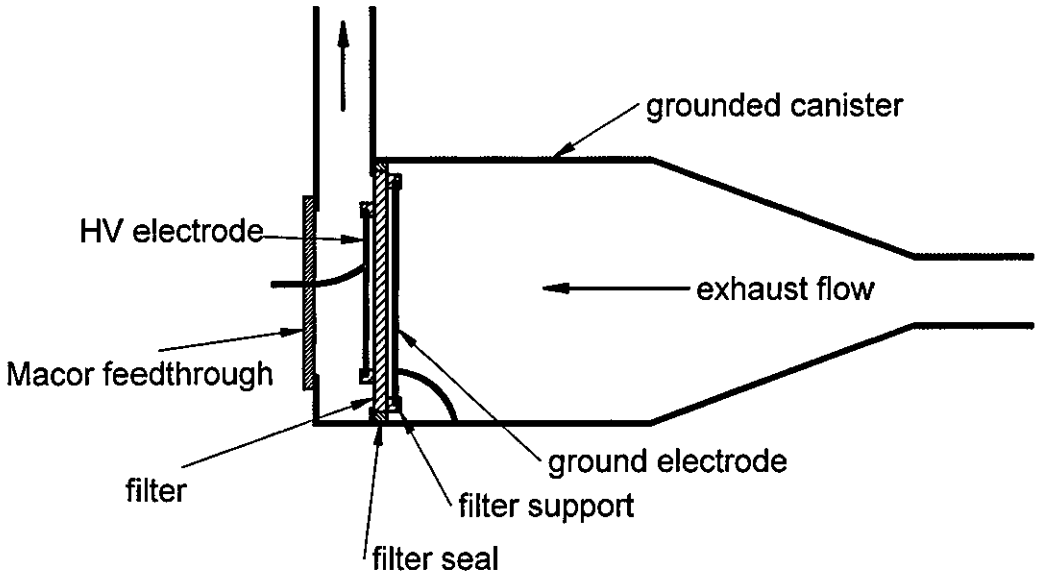

Figure 8.2. Filter setup and electrical feedthroughs for on-engine testing

Secure filter mounting and edge sealing was achieved using Interam gasket material An example of the seal is shown in Figure 8.3. The Interam provided an airtight seal that offered secure positioning of the filter sample with low risk of damage.

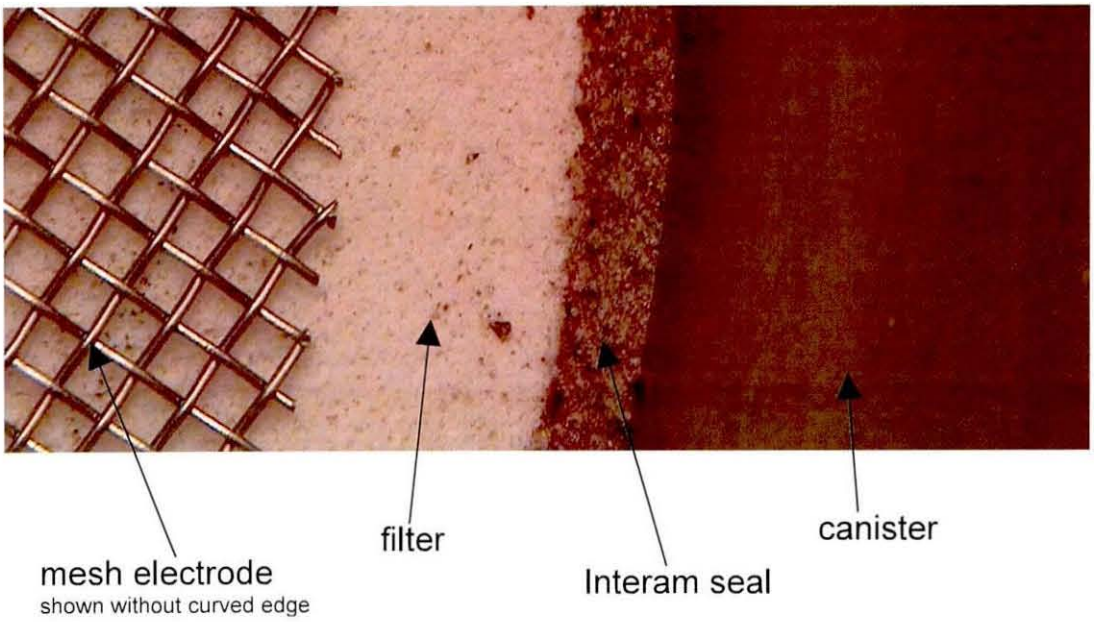

Figure 8.3. Photograph of the edge seal around filter section

Factors that have not yet been fully investigated include the on-time, off-time, input voltage (directly linked to power), electrode spacing and additional load capacitance (varying the resonant electrical circuit). These are all continuous quantitative variables. The range of factors under investigation is shown in Table 8.1. On-time was expected to have an effect on the peak temperature of the ceramic, how much PM is burnt off each time the discharge strikes and the discharge mobility. Typical on-times found to be suitable during rig testing were approximately 100-150 ms. Off time affects the discharge mobility by determining how much the local ceramic temperatures cool before the discharge strikes again. The optimum values for the off-time are unknown so a range between 500 and 800 ms was used, known to be of the order of magnitude of the cool down time constant of the ceramic. Rig testing has shown input voltage to have a significant influence on discharge behaviour, being more successful at voltages above 220 V. Electrode spacing has an affect on discharge mobility due to flow turbulence, and also heating efficiency of the discharge (Chapter 5). To increase efficiency the spacing needs to be minimised. A range of 1 to 3 mm was chosen as this can be achieved reliably in the laboratory environment and is reasonable for production implementation. Modelling has shown that adding additional electrode capacitance can increase the chance of a spatially continuous regenerative discharge through the filter (Chapter 6). A range of 55 to

100 pF was investigated here to determine if any further advantage could be achieved.

With 5 factors at 2 levels, a full factorial investigation would require 32 experiments. To quantify experimental errors, repeat runs would be needed as well as further tests (center points) to find any non-linear relationships. Using computer generated experimental designs (D-Optimal designs), it was possible to begin to quantify the effects, interactions and non-linearities of the factors listed in Table 8.1, with 5 repeat tests for quantifying experimental errors, with only 31 tests. Due to time limitations and availability of filter samples this offered the most promising experimental design for this investigation.

Table 8.1. Summary of factors and levels investigated with the on engine testing.

Factor	Low Setting	High Setting
On-Time (ms)	50	200
Off-Time (ms)	500	800
Input Voltage (V)	220	260
Electrode Spacing (mm)	1	3
Additional Load Capacitance (pF)	55	100

The performance of the regeneration system was evaluated with respect to regeneration rate, regeneration effectiveness (energy usage) and blow-off rate. The blow-off rate is defined as the difference between the downstream PM mass flow rate with the discharge active and the downstream PM mass flow rate when the discharge is inactive. The regeneration rate was estimated by considering the rate of increase in back pressure from when the system becomes active to when it is not. The test was carried out with the discharge switched off and after 45 minutes the Autoselective regeneration system was switched on. The general assumption was made that if the regeneration system is regenerating 0 g h^{-1} of PM, the rate of increase in back pressure will be equivalent to when the discharge system is not active. Likewise, if the regeneration system was regenerating at a rate equal to the trapping rate of PM, the rate of increase in back pressure would be approximately 0 kPa h^{-1}. For comparison purposes between the factors, in between these two extremes the relationship between regeneration rate and back pressure rise was considered to be linear.

As the factors were varied, the energy consumption of the system also varied. The power consumption at the electrodes can be calculated from the current and voltage waveforms measured using methods described in Chapter 3. The regeneration effectiveness was then calculated as the mass of PM regenerated per unit energy consumed.

Blow-off rate was estimated using pre- and post-filter smoke meter measurements. By comparing the downstream PM quantity with the discharge system on and off, an estimate of the amount of trapped PM leaving the filter when the regeneration system was active could be made.

Table 8.2 summarises the responses that were required and the measurements during the test that were needed to calculate the response. More details of the calculations follow in Section 8.3.

Table 8.2. Summary of responses and measures required.

Response	Units	Measures Required
Regeneration Rate	$g\ h^{-1}$	Pre- and post-smoke numbers, back pressure measurement.
Regeneration Effectiveness	$g\ kW^{-1}\ h^{-1}$	Electrode current and voltage waveforms, calculated regeneration rate
Blow-off Rate	$g\ h^{-1}$	Pre- and post-smoke numbers

8.3 Data Analysis

A typical dataset showing the differential pressure across the filter is shown in Figure 8.4. There are four main sections to this plot. Section (i) is the first period with the regeneration system off. Section (ii) and (iii) are when the regeneration system is on. Section (iv) is the final period with the regeneration system switched off. For approximately 30 seconds in between the on and off sections the engine is switched off. Period (ii) shows a significant initial drop in back pressure associated with the initial switch on of the discharge, which is done while the engine is off. The discharge loosens the PM and can redistribute it within the filter meaning that a small amount is blown off the filter when the engine is restarted. The system then settles to equilibrium (section (iii)) where the blow-off and regeneration rates have stabilised.

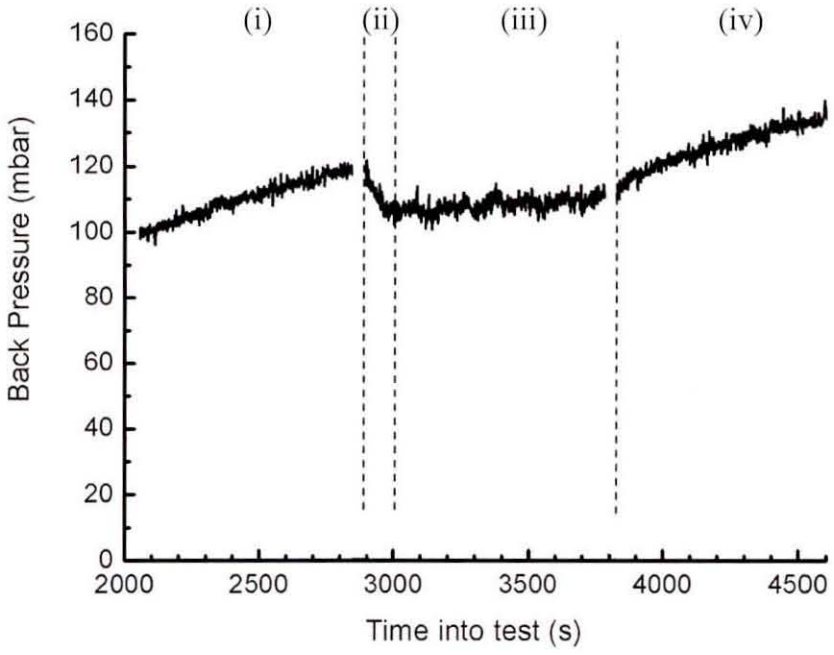

Figure 8.4. Typical back pressure dataset from the engine testing.

The PM loading rate of the filter can be estimated using the pre- and post-smoke meter measurements. The loading rate will vary during the test as the engine back pressure, filter filtration properties and blow-off conditions vary. By replotting the back pressure data against cumulative loading, the effects of varying loading rates will not affect the gradient analysis described earlier. Importantly, the reduction of PM on the filter due to any blow-off will not affect the gradient of the pressure data. The dataset shown above converted in this way is shown in Figure 8.5. The key features of Figure 8.4 are still clearly visible.

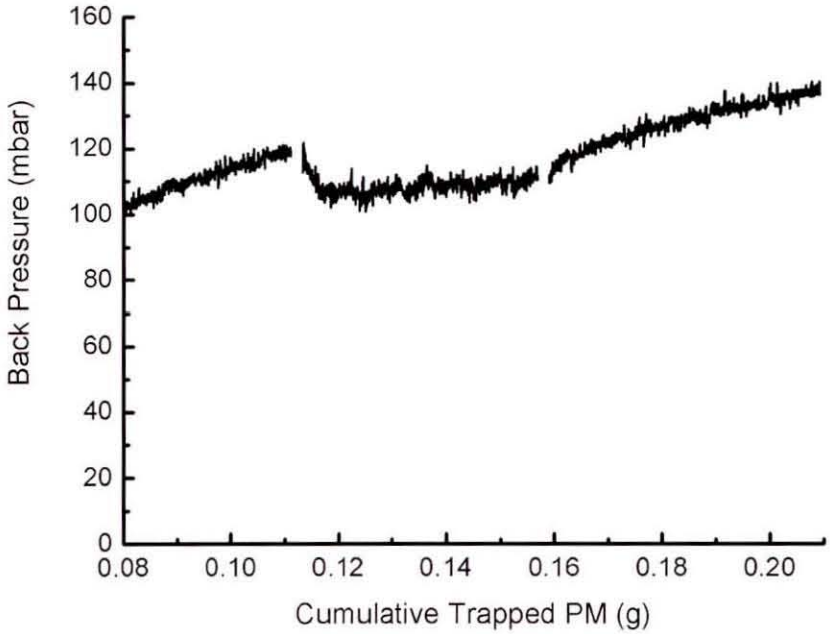

Figure 8.5. Back pressure dataset plotted against cumulative trapped PM.

With the assumptions outlined in Section 8.2, it is now possible to use a linear regression of sections (i), (iii) and (iv) on Figure 8.5 to find the gradients of the lines. The reduction in gradient, A, can be found from

$$A = \frac{\left[\frac{(m_i + m_{iv})}{2} - m_{iii}\right]}{m_i + m_{iv}} = 1 - \frac{2m_{iii}}{m_i + m_{iv}} \tag{8.1}$$

where m_i, m_{iii} and m_{iv} are the gradients of the rate of back pressure rise from Figure 8.5 for period (i), (iii) and (iv) respectively, The regeneration rate can then be found as a fraction of the PM loading rate of the filter. This means that

$$r = \dot{R}\left[1 - \frac{2m_{iii}}{m_i + m_{iv}}\right] \tag{8.2}$$

where r is the regeneration rate and $\dot{R}$ is the PM filter loading rate. To calculate the regeneration effectiveness it is necessary to first calculate the power consumption of the system. Since power supply development is being continuously carried out by

other researchers, this study focused on the power consumption at the electrode. Using the methods outlined in Chapter 3 the current and voltage flowing through the electrodes was measured, an example of which is shown in Figure 8.6. Instantaneous powers can be calculated by the product of the current and voltage, giving typical results as shown in Figure 8.7.

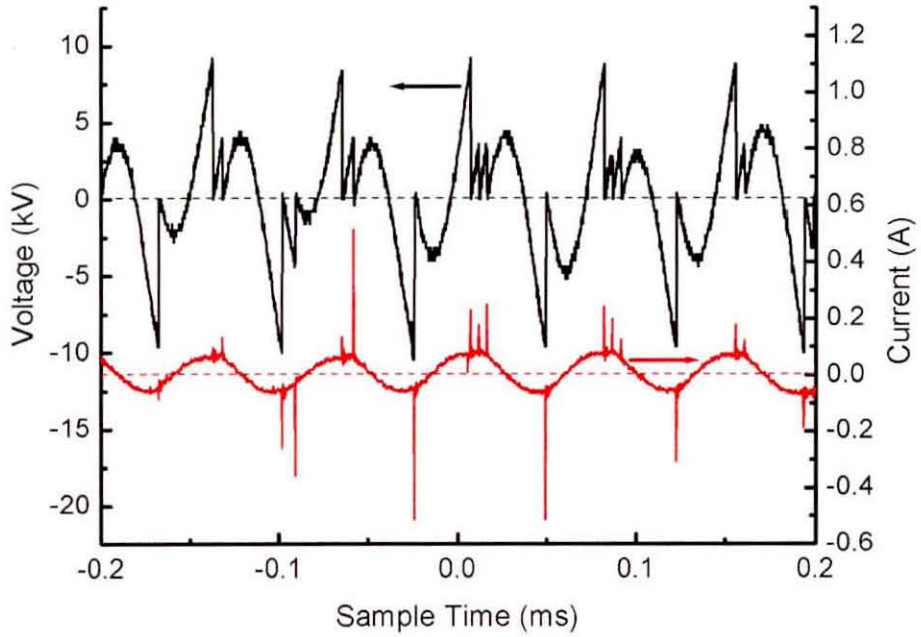

Figure 8.6. Example current and voltage waveforms

It can be seen that the instantaneous power in the discharge in this test was typically reaching 600 W. This was only for short durations (<10 μs) during the repetitive break downs of the air gap between the electrodes. There was also a cycling power flowing between the load capacitance and the transformer inductance which is visible in Figure 8.7.

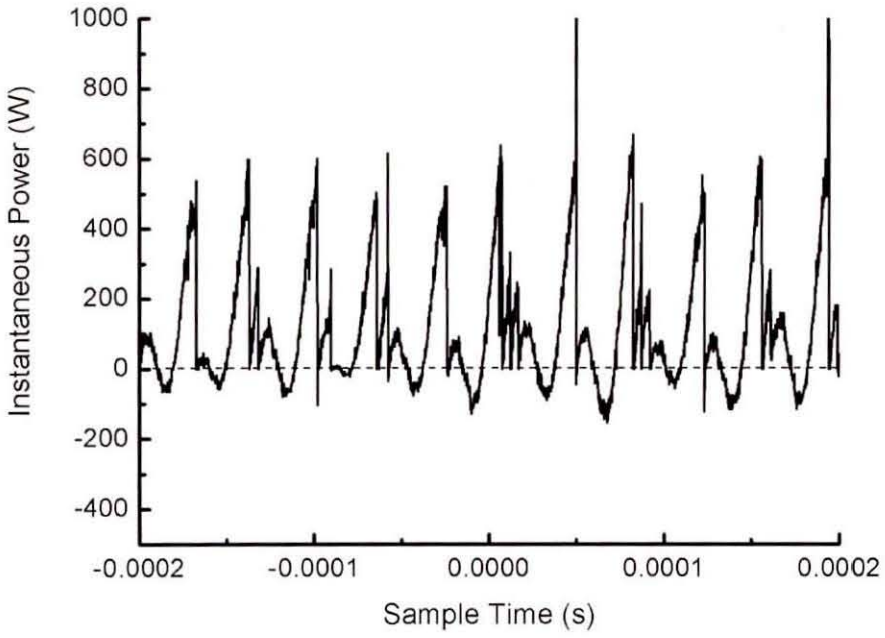

Figure 8.7. Typical instantaneous power consumption plot, at the electrodes during Autoselective regeneration.

The cyclic average of the instantaneous power provides an average power for the discharge, P, while the discharge is active. The average power while the regeneration system is on must also consider the on and off-time, giving

$$\overline{P} = \frac{t_{on}}{t_{on} + t_{off}} P = \left(\frac{t_{on}}{t_{on} + t_{off}} \right) \frac{f}{n} \int_0^{\left(\frac{n}{f}\right)} (IV) dt \tag{8.3}$$

where n is an integer, $\overline{P}$ is the average power consumption, t_{on} is the on-time of the discharge, t_{off} is the off-time of the discharge, P is the average power consumption during the on-time, f is the discharge frequency, I is the instantaneous current and V is the instantaneous voltage.

The regeneration effectiveness (with respect to energy consumption) can then be defined as

$$E_r = \frac{r}{\overline{P}} \tag{8.4}$$

where E_r is the regeneration effectiveness and r is the regeneration rate.

The filtration efficiency was calculated as

$$\eta_{filt} = 1 - \frac{\dot{m}_d}{\dot{m}_u} \tag{8.5}$$

where the downstream and upstream PM mass flow rates ($\dot{m}_d$ and $\dot{m}_u$ respectively) are calculated from the AVL 415 smokemeter readings in accordance with the manufacturer's guidelines (AVL, 2002). Figure 8.8 shows a plot of the calculated filtration efficiency as a function of time. An exponential curve fit to the filtration efficiency data during the off periods was used to predict the filters efficiency during the on period. Any difference between the actual filtration efficiency and the predicted filtration efficiency will be a result of either experimental errors or PM blow-off from the filter. Experimental errors were evaluated within the DoE software and estimated errors on the results are shown in the following section. The amount of PM that is being blown off, as a function of the incident PM rate is then given as

$$\dot{m}_{bo} = \left(\eta_{filt,pred} - \eta_{filt,actual}\right)\dot{m}_u \tag{8.6}$$

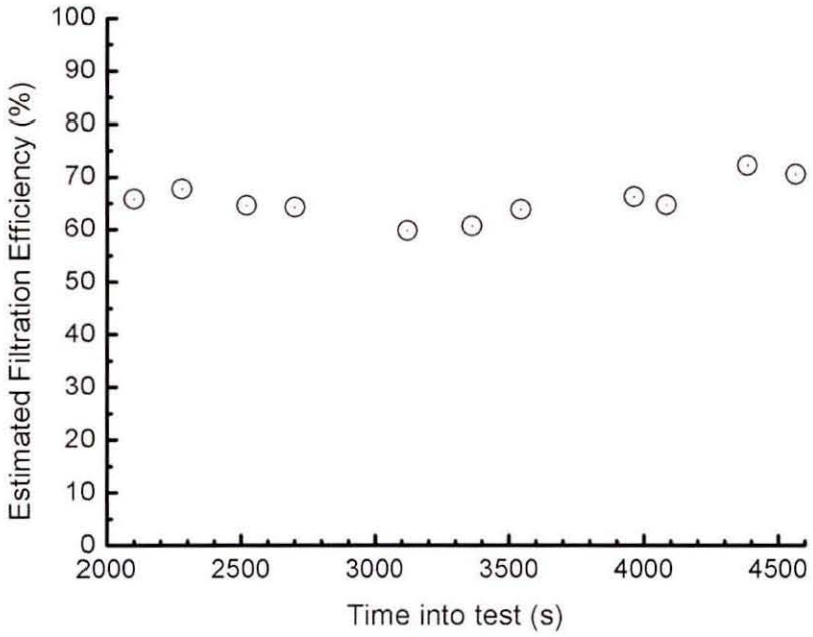

Figure 8.8. Example filtration efficiency data during the test period.

8.4 Results

The data was analysed using Stat-Ease Design Expert software. This software was designed to analyse errors and indicate the statistical significance of any proposed models. The data in Table 8.3 formed the results used in the DoE software, rounded to 3 decimal places (d.p.), 4 d.p. and 2 d.p. for the regeneration rate, blow-off rate and regeneration effectiveness respectively.

Table 8.3. DoE Software input data.

Run	On-time ms	Off-time ms	Electrode Spacing mm	Applied Voltage V	Additional Capacitance pF	Regeneration Rate g h^{-1}	Blow Off Rate g h^{-1}	Regeneration Effectiveness g kW^{-1} h^{-1}
1	125	650	2	260	77.5	0.099	0.0047	6.92
2	200	800	1	260	55	0.105	0.0182	7.26
3	50	650	2	240	77.5	0.079	0.0176	11.03
4	50	650	2	240	77.5	0.118	0.0269	26.02
5	50	500	3	220	55	0.039	0.0096	
6	50	800	3	260	55	0.054	0.0151	6.77
7	50	800	3	220	100	0.003	-0.0019	0.62
8	200	500	1	260	100	0.092	-0.0013	3.03
9	200	800	1	220	77.5	0.074	0.0046	4.29
10	50	800	2	220	55	0.045	0.0102	7.14
11	50	500	1	220	77.5	0.093	0.0146	11.77
12	125	800	1	220	100	0.077	0.0110	6.64
13	125	500	2	240	77.5	0.077	0.0149	4.13
14	50	800	1	260	100	0.101	0.0140	24.30
15	50	500	1	260	55	0.075	0.0198	6.81
16	200	500	1	260	55	0.079	0.0039	2.97
17	125	800	1	220	100	0.086	0.0016	8.24
18	200	800	2	260	100	0.067	0.0074	2.96
19	50	800	1	260	55	0.100	0.0173	14.37
20	125	650	2	260	77.5	0.110	0.0136	7.93
21	50	500	2	260	100	0.063	0.0132	3.26
22	200	500	3	260	100	0.027	0.0069	0.93
23	50	500	3	260	55	0.086	0.0210	7.68
24	50	800	3	220	100	0.041	0.0051	3.95
25	200	500	3	260	55	0.040	0.0024	1.33
26	200	500	3	220	55	0.025	0.0037	0.77
27	200	800	3	220	55	0.044	0.0136	1.40
28	200	800	3	260	55	0.074	0.0183	4.80
29	125	500	2	240	77.5	0.039	0.0254	1.20
30	200	500	2	220	100	0.036	0.0006	
31	200	500	1	220	55	0.076	0.0009	4.61

A general factorial interaction model was used initially. Anova analysis of the model fit to the experimental data indicated which factors showed the least significant fit (i.e. most likely to be a result of errors). The least significant factor was removed from the model and followed by Anova analysis of the updated model. This process was continued until all the variables had >90% confidence of a statistically significant effect. The proposed models to describe the behaviour of the regeneration system was

1. Regeneration Rate:

$$r = -0.02852 - 0.02117x + 0.000573 * V \tag{8.7}$$

2. Regeneration Effectiveness:

$$R = 73.98642 - 0.03194t_{on} - 0.06733t_{off} - 12.6823x - 0.25585V - 0.03774C + 0.000306t_{off}V + 0.043808xV \tag{8.8}$$

3. Blow-off Rates:

$$\dot{m}_{bo} = 0.020725 - 0.00025t_{on} - 0.000037t_{off} + 0.000117V - 0.0001C + 0.000000315t_{on}t_{off} \tag{8.9}$$

where the electrode spacing, x, the applied voltage, V, the on time, t_{on}, the off time, t_{off}, and the additional capacitance, C, are measured in mm, V, ms, ms and pF respectively.

8.4.1 Regeneration Rate

Graphical representation of the behaviour of the regeneration rate is shown in Figures 8.9 and 8.10. In all the figures the standard errors calculated using the statistical DoE software are shown as the error bars. Figure 8.9 shows the effect of electrode spacing on the regeneration rate. Reducing electrode spacing resulted in increasing regeneration rates if all other factors were kept constant.

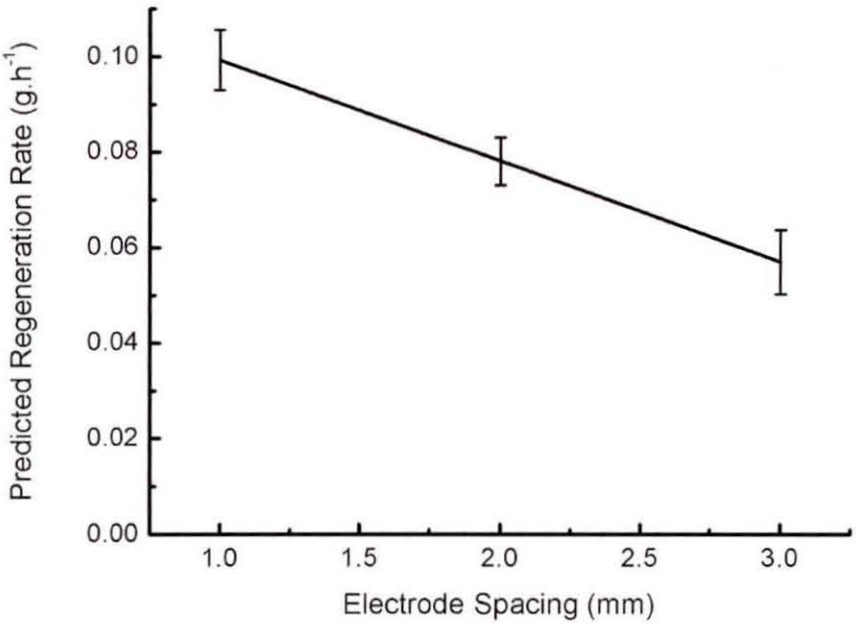

Figure 8.9. The predicted effect of electrode spacing on the regeneration rate

The effect of applied voltage, shown in Figure 8.10, shows that increasing the applied voltage led to increasing regeneration rates. The effect of the electrode spacing and applied voltage are large relative to the standard errors.

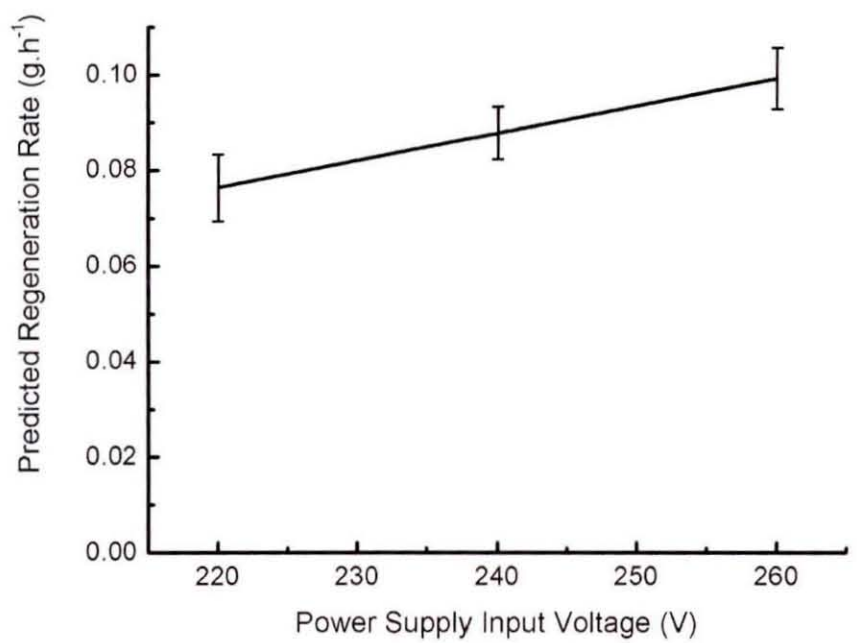

Figure 8.10. The predicted effect of power supply input voltage on the regeneration rate

The other factors had small effects relative to the errors and are consequently not discussed further here since any effect in the model could be a result of experimental error and noise.

8.4.2 Regeneration Effectiveness

Figures 8.11 to 8.13 show the effect of the factors on regeneration effectiveness. This is a more complex model and involves two interactions between the factors. Figure 8.11 shows the effect of on-time. Lower on-times offered noticeable improvements in regeneration effectiveness, increasing the regeneration effectiveness from 8 to 12 g kW^{-1} h^{-1} over the test range.

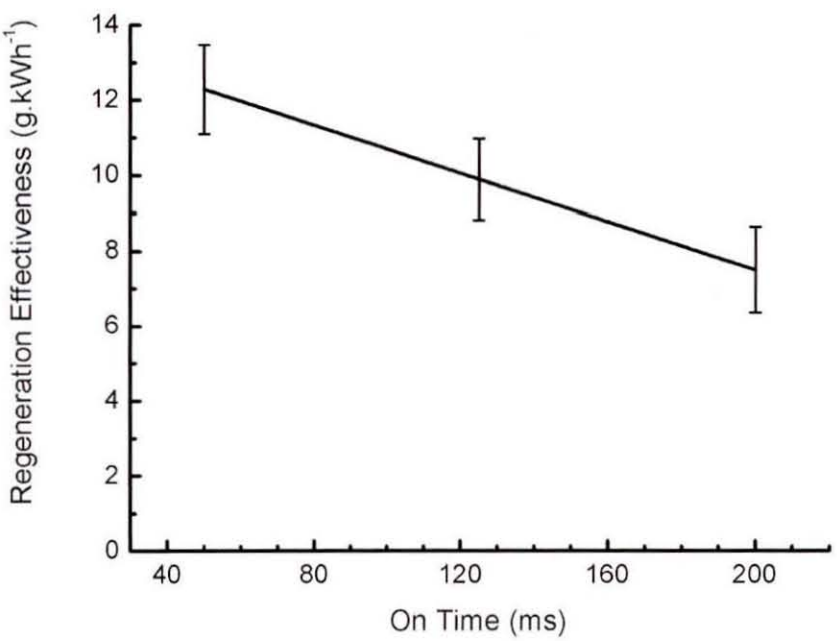

Figure 8.11. The predicted effect of on-time on the regeneration effectiveness

Figure 8.12 shows the effect of off-time. This factor had an interaction with the applied voltage meaning that the effect of the off-time depends on the applied voltage. At lower voltages the off-time had little effect. At higher voltages, increasing the off-time resulted in improvements in regeneration effectiveness.

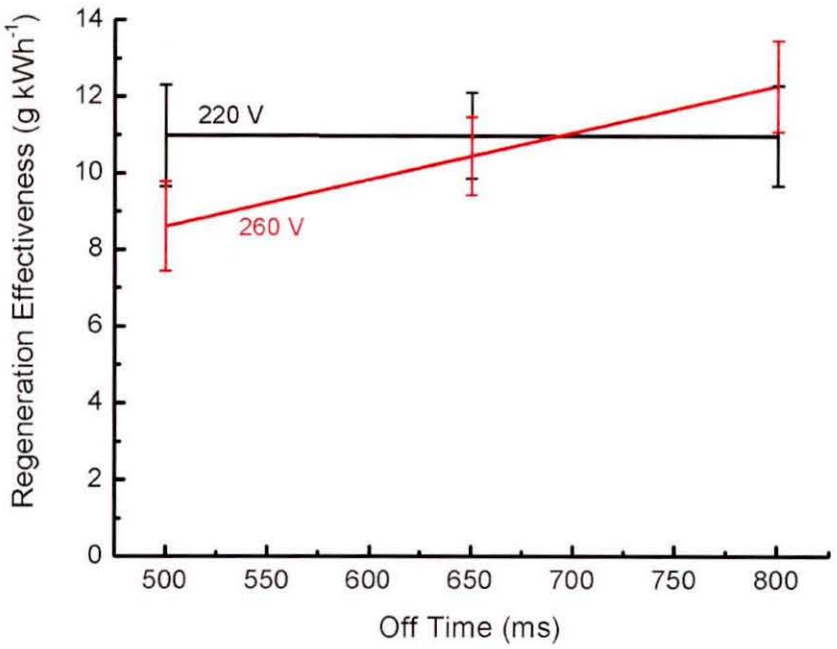

Figure 8.12. The predicted effect of off time on the regeneration effectiveness.

Electrode spacing, shown in Figure 8.13 also involved an interaction with applied voltage. At higher voltages, the regeneration effectiveness became less dependent on electrode spacing, although over the test range there was generally a trend of reducing regeneration effectiveness with increasing electrode spacing.

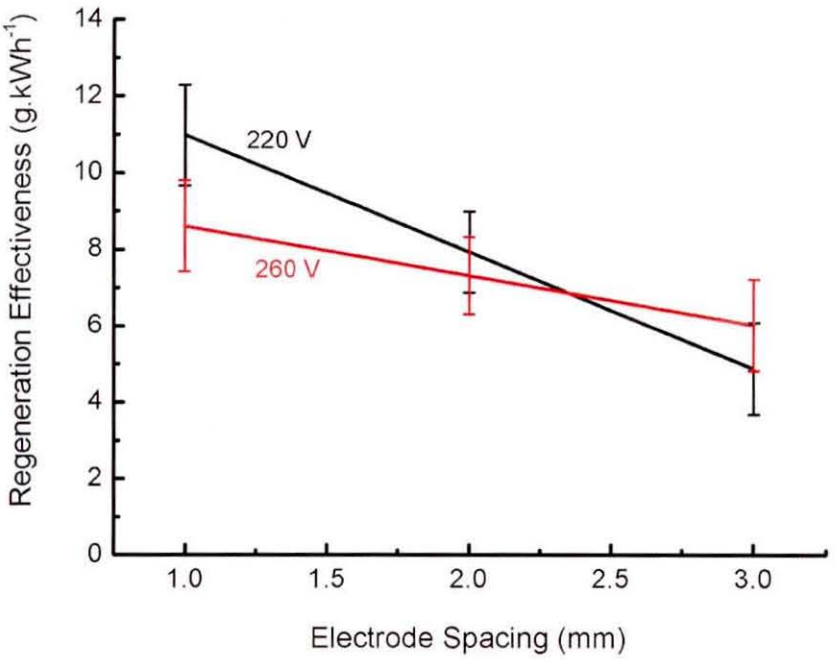

Figure 8.13. The predicted effect of electrode spacing on the regeneration effectiveness.

Other factors had a negligible effect on the regeneration effectiveness relative to the experimental error and noise.

8.4.3 Blow-off

Figures 8.14 to 8.17 show the effect of the factors on the amount of PM that is blown off the filter when the discharge system is active. The effect of on-time, shown here in Figure 8.14 included an interaction with the off-time. With short off-times, the blow off rate was highly dependent on the on-time. Under these conditions, the shorter off times led to high rates of blow-off. With long off-times, the blow-off rate became independent of the on-time.

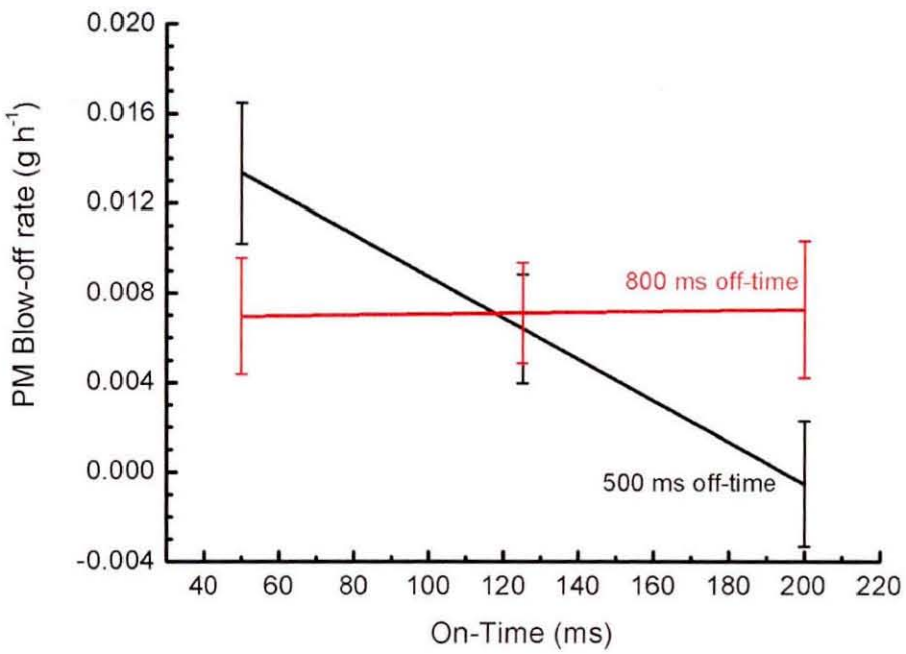

Figure 8.14. The predicted effect of on-time on the blow-off rate

Figure 8.15 shows the effect of off-time on the blow-off rate. This is a reproduction of the information shown in Figure 8.14 to aid interpretation. With short on-times, increasing off-time led to a reduction in blow-off rate. With longer on-times, increasing the off-time led to an increase in blow-off rate.

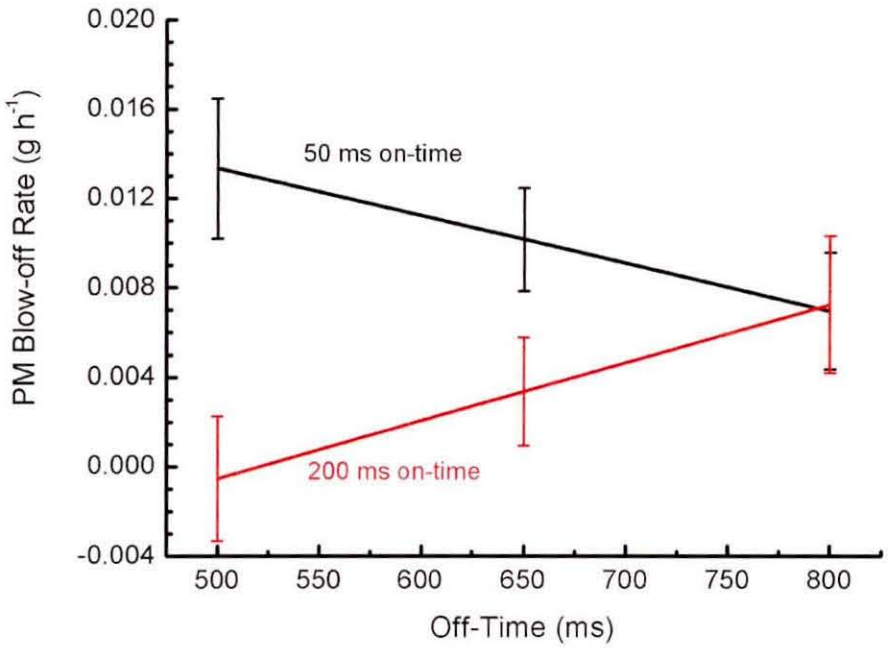

Figure 8.15. The predicted effect of off-time on the blow-off rate

The effect of applied voltage was smaller than the previous effects and was not interacting with the other variables. Increasing the applied voltage led to increased amounts of blow-off, shown in Figure 8.16.

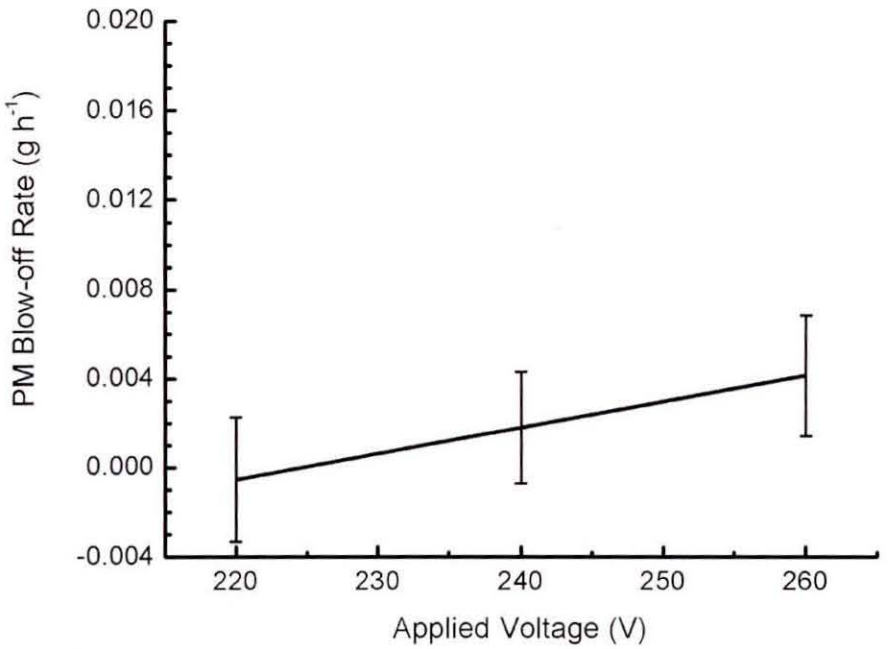

Figure 8.16. The predicted effect of applied voltage on blow-off rate.

The applied capacitance had a smaller effect again and was getting close to the confidence limits, indicated here by the standard errors in Figure 8.17. Generally, reducing the additional capacitance led to increasing blow-off.

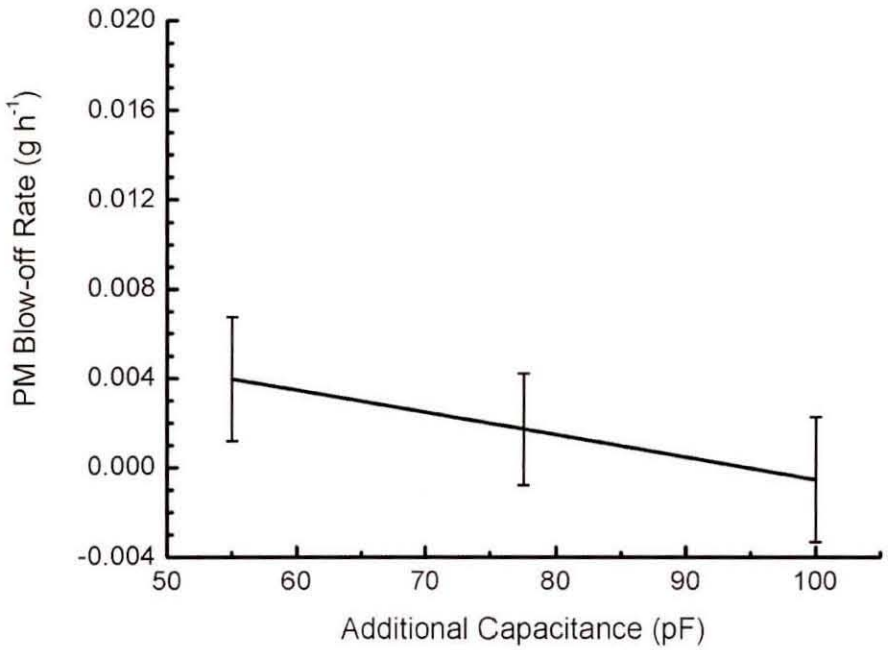

Figure 8.17. The predicted effect of additional load capacitance on the blow-off rate

8.5 Discussion

8.5.1 On Time

The negligible effect of on-time on the regeneration rate implies that the majority of the regeneration activity occured in the early stages of the on-time (within the first 50 ms). This has a significant impact on the regeneration effectiveness since when the on-time is increased, little additional benefit was gained but the amount of energy used increased almost linearly. This is a strong indication that a target on time of 50 ms or less is preferred in a prototype aimed at achieving efficient regeneration.

The effect of on-time on the blow off was a result of the break down behaviour of the system. There were two distinct periods during a single on-time, shown in Figure 8.18. The first period which can last for approximately 40 ms was a high voltage, unstable discharge period prior to a lower voltage, stable discharge. The blow-off was predicted to occur during the high voltage period when the electrostatic forces

on the trapped PM will be highest. The duration of the unstable discharge period was a function of the combined on- and off-time. This means, for example, that with short off times, the electrode gap could break down more easily and become stable in a shorter length of time. Likewise, with long on-times, the ease of break down was improved and the unstable region became shorter in duration. The effect of on-time on blow-off shown in Figure 8.14 was expected to be a manifestation of this effect where for the shorter off-times, the on-time had a significant effect on the duration of the unstable period while at longer off-times, the duration of the unstable period was determined almost purely by the off-time.

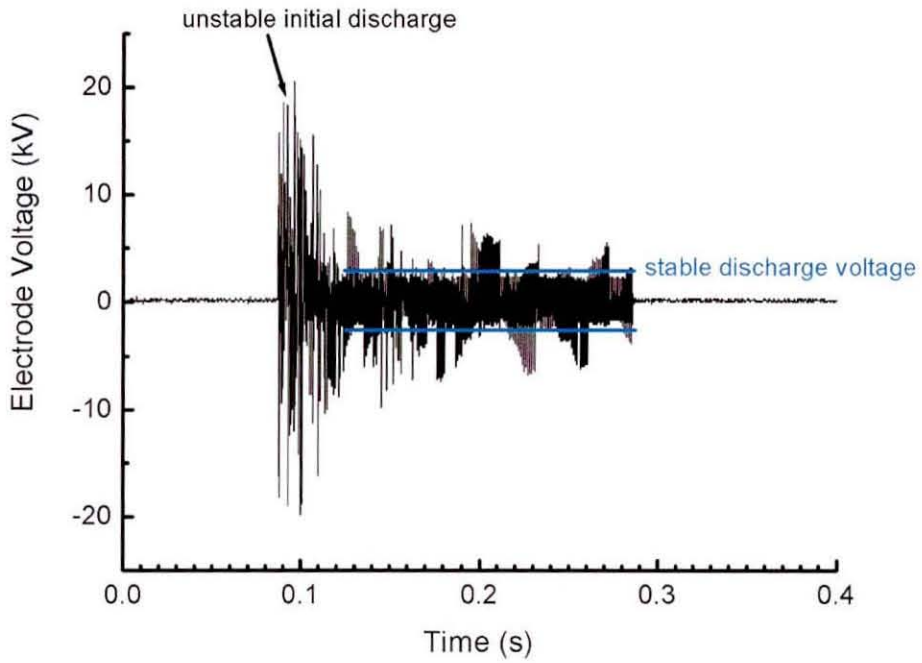

Figure 8.18. Plot of electrode voltage as a function of time showing the two distinct operating regions.

8.5.2 Off Time

The effect of off-time with low applied voltages on the regeneration rate was negligible, showing that (over the tested range) the oxidation during the on-period was more important than during the off-period. With high applied voltages, the off-time became more important. This could be explained by considering the autoselectivity of the discharge. It has already been mentioned that at long off-times, the unstable discharge period was longer since the discharge found it harder to

become stable. This effect is shown in Figure 8.15 as the easier the discharge finds it to become stable, the more likely it is to break down in the same place as the previous discharge due to presence of higher temperatures and remnant charge (both in the gas phase and dielectric charge). If longer off-times lead to increased discharge mobility then the discharge is going to focus more on regions of high PM loading, hence increasing the regeneration rate (per strike) and regeneration effectiveness.

The effect of off-time on blow-off followed the trends described in the on-time discussion. With short on-times, the unstable period duration was independent of the off-time meaning that the blow-off rate reduces as the number of unstable periods reduces. With longer on-times, the off-time had a big influence on the unstable period duration, with increasing off-times leading to increasing unstable period durations and hence blow-off rates.

If a short on-time is used for optimum regeneration effectiveness then a long off-time is proposed as this offers minimal blow-off without adversely affecting the regeneration effectiveness.

8.5.3 Effect of Electrode Spacing

The study of the effect of electrode spacing on the heating efficiency of the discharge explained the increasing regeneration rate and regeneration effectiveness with reducing electrode spacing. If the electrode spacing was small enough to begin to affect the autoselectivity the results would have shown a reducing regeneration rate with reducing electrode spacing. Since this is not observed then an electrode spacing of 1 mm is proposed for a prototype system. The electrode spacing had a negligible effect on blow-off rates which could be understood by considering the electric field strength between two plate electrodes. Although with larger electrode spacing, the electrode voltage required to achieve a break down would be higher, the electric field strength in the vicinity of the discharge will be the same meaning the electrostatic forces on the trapped PM are not going to change significantly with increasing electrode spacing.

8.5.4 Effect of Applied Voltage

The applied voltage had a direct relationship with the amount of power flowing through the discharge. This means that increasing the applied voltage increased the regeneration rate, but due to the increased power had a negligible effect on the regeneration effectiveness. It could however increase the electrode voltage during the unstable discharge period and hence increase the blow-off rates. Provided that a stable discharge can be achieved it is therefore proposed to use the lower applied voltage of the tested range.

8.5.5 Effect of Additional Load Capacitance

The range of additional load capacitance tested was found to have almost no effect on the regeneration rates and regeneration effectiveness. This implies that the minimum capacitance of 55 pF altered the resonant circuit enough to produce the required break down. The blow-off was found to reduce a small amount with increasing capacitance which can be attributed to the reduced gain of the resonant circuit with the increasing load. This will act in a similar way to reducing the applied voltage by limiting peak electrode voltages during the unstable discharge period. For a prototype system a 55 pF capacitance is proposed which can be increased further to reduce blow off provided transformer saturation is avoided.

8.6 Concluding Remarks

Successful demonstration of the effect of the Autoselective regeneration of gelcast ceramic foams on the filter back pressure on-engine has been presented. The effects of on-time, off-time, additional load capacitance, applied voltage and electrode spacing have been evaluated to give initial direction for system optimisation. Chapter 9 concludes the main discussion in the thesis by presenting a prototype design proposal for an Autoselective regenerating gelcast ceramic foam DPF.

CHAPTER 9

PROTOTYPE DESIGN

9.1 Introduction

This chapter describes the prototype design of an Autoselective regenerating gelcast ceramic foam diesel particulate filter. The prototype design follows from the developments earlier in this thesis. Its projected performance is evaluated and compared to the current state of the art.

The prototype design is based around the engine data shown in Table 9.1. The peak flow rate is calculated by the airflow through the engine with 90% volumetric efficiency and a 20:1 air fuel ratio (by mass) with the intake conditions at 1 bar, 40 ^{o}C.

Table 9.1. Engine specification used for prototype filter design.

Target engine	Perkins 1104D-44
Aspiration	NA
Engine displacement	4.4 litres
Bore and stroke	105 mm x 127 mm
Compression ratio	16.2:1
Peak engine power (at engine speed)	56 kW (at 2200 rpm)
Estimated peak engine exhaust flow rate	~305 kg h^{-1}
Estimated average PM generation rate	~5 g h^{-1}

9.2 The Prototype Design

To more easily achieve spatially continuous discharges the design has two 8 mm thick filter layers, as shown in the exploded view in Figure 9.1. The cylindrical shape of the foams allows increased flow area per unit canister volume. Between the filter layers is the ground electrode and on the inner and outer surface of the inner and outer filter respectively are HV electrodes. The HV electrodes (with profiled edges) are mounted directly to the filter surface as described in Chapter 7. The ground electrode is mounted directly to the grounded canister. The filter arrangement is such that the flow travels from the outer edge to the inner axis, shown in the cross section in Figure 9.2. This acts to generate more even PM distribution as more PM will be trapped on the upstream side of the filter.

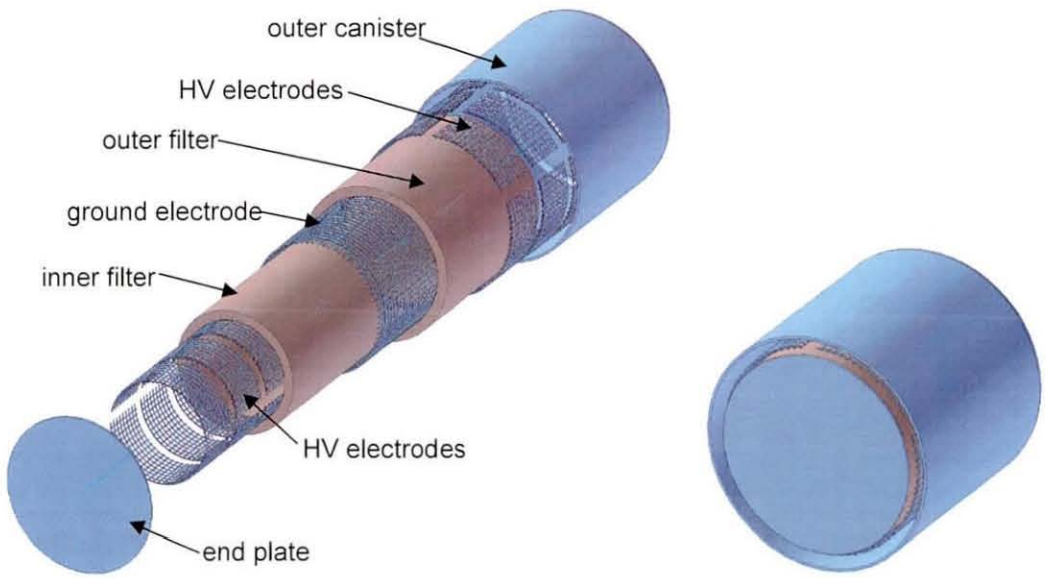

Figure 9.1. Computer generated image of the electrodes, filter and canister making the prototype design.

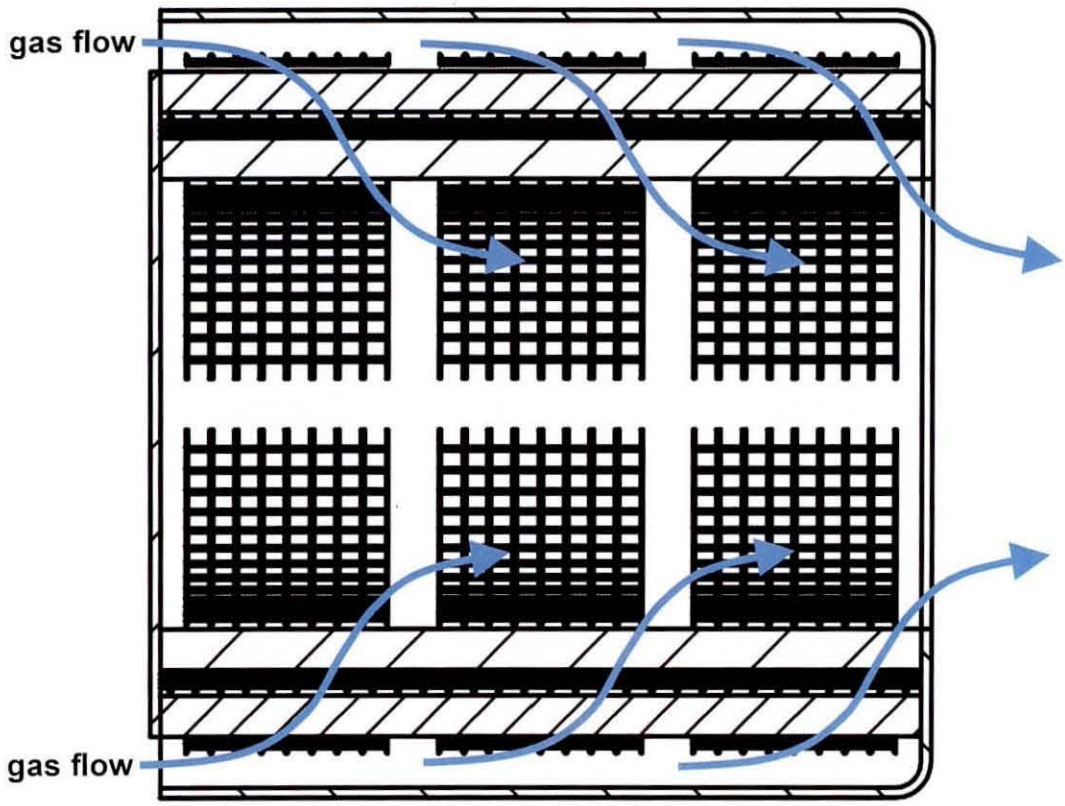

Figure 9.2. Cross section of the integrated prototype concept

The design parameters are summarised in Table 9.2. The target filtration efficiency was set at 80% to remain competitive with alternative filtration systems. Each filter section must, therefore, have 55% filtration efficiency. With 5 g h^{-1} incident PM, the outer filter will trap 2.76 g h^{-1} and the inner layer will trap 1.24 g h^{-1}. With an 8 mm thickness for each later, this corresponds to a value of η_{1mm} = 9.57% and, by curve fitting to the data in Table 4.1, a pore size of 340 μm. The estimated achievable regeneration rate is approximately 0.2 g h^{-1} per discharge. Due to the discharge and power supply characteristics, only one discharge can be generated per high voltage electrode. The outer filter therefore needs ~14 HV mesh electrodes and the inner filter ~6 HV mesh electrodes. For tessellation, 15 and 6 electrodes are proposed for the outer and inner surface respectively. This arrangement is shown in Figures 9.1 and 9.2. The electrical feedthroughs, although not yet fully investigated, are likely to be based on spark plug technology, feeding the high voltage through the grounded canister.

Table 9.2. Prototype system design parameters.

Outer section filtration area	0.0574 m^2
Inner section filtration area	0.0452 m^2
HV electrodes on outer surface	15
HV electrodes on inner surface	6
Electrode Spacing	1 mm
Pore size	340 µm

9.3 Integrated Prototype Performance

Table 9.3 shows the predicted performance of the integrated prototype concept. The predictions are based on the best results achieved during this research which may be improved upon with further study and optimisation. The filtration efficiency, as already mentioned, is 80 %. This is expected to be enough to meet 2010 legislation (Johnson, 2006). The power requirement, based on a regeneration effectiveness of ~12 g kW^{-1} h^{-1} (on-engine test results, Chapter 8) is 333 W at the electrodes. If a 70 % transformer efficiency and 60 % alternator efficiency are assumed this translates to a 794 W (or ~65 g h^{-1}) fuel consumption penalty. The PM holding capacity, to maintain back pressure below 10 kPa at rated flow is 0.162 g, calculated using methodology described in Chapter 4. This would therefore require continuous operation of the regeneration system to maintain PM loading below this value. The canister volume is comparable to a WFF, although is not limited to the cylindrical geometry.

Table 9.3. Predicted prototype performance.

Filtration Efficiency	80%
Continuous power requirement	333 W
PM holding capacity	0.162 g for 10 kPa at rated flow
Clean filter back pressure at rated flow	7.13 kPa
Canister volume	2.65 litres (as shown in Figure 9.1)

9.4 Comparison with State of the Art Regeneration Systems

The integrated prototype design offers comparable canister volumes to WFFs. The flexibility in the shape of the canister is beyond that commercially available with

WFFs. The filtration efficiency and PM holding capacity are lower and the clean back pressure is higher. These tradeoff the benefits with adaptability, robustness of the filter and filter strength. Compared to alternative foam filters, the filtration performance is comparable, the filter is more compact and mechanically stronger.

Autoselective regeneration offers average energy demands comparable to fuel burners and electrical heating, shown in Figure 9.3. Since it is continuous regeneration, Autoselective regeneration does not risk uncontrolled regeneration events with self sustained burning of the trapped PM. The instantaneous energy demand is comparable to systems that rely on bypassing the gas flow around the filter. This has significant benefits as there will be no need for a dual filter system to achieve NTE emission limits. The regeneration is more robust than any other regeneration system investigated which require a minimum temperature (in the case of catalysts), controlled airflow (in the case of electrical heating, microwave heating and fuel burning) or only operate within a small range of PM filter loading. The reliance of many systems on precious metals makes systems such as the Autoselective discharge attractive options to limit the dependence of cost on the precious metal market.

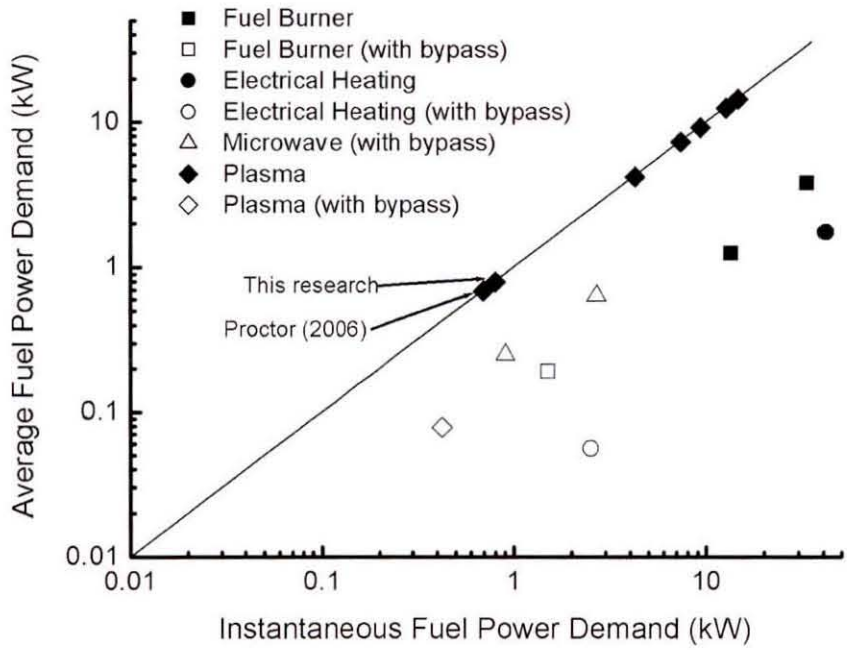

Figure 9.3. Comparison of the energy requirement of the Autoselective regeneration of gelcast ceramic foams to typical regeneration systems.

9.5 Concluding Remarks

Chapter 9 has presented an integrated prototype design using knowledge from the earlier chapters to specify design parameters. The system energy efficiency is promising which, combined with the capability of regenerating at full exhaust flow over the entire engine operating range, makes Autoselective regeneration of gelcast ceramic foams an attractive option for commercial exploitation. Chapter 10 summarises the main conclusions that have been drawn from this work and discusses potential future work related to this research.

CHAPTER 10

CONCLUSIONS AND SUGGESTIONS FOR FURTHER WORK

The research presented in this thesis has optimised gelcast ceramic foam diesel particulate filters (DPFs) and applied to them the new Autoselective electric discharge regeneration (filter cleaning) technique. This demonstrated reliable regeneration over the entire engine speed and load range, with low energy and power requirements. The Autoselective regeneration process uses the direct conversion of electrical to thermal energy in an electric glow discharge for rapid local heating of PM trapped on the gelcast ceramic foam DPFs.

This research has developed empirical models to evaluate the performance of conceptual foam DPFs and applied this model to optimise the gelcast ceramic foam geometry. Design maps were presented as a tool to understand the large number of

application dependent variables that affect the design of an optimum ceramic foam DPF. Examples of gelcast ceramic foam DPFs were presented.

The Autoselective regeneration system was developed to work effectively with the gelcast foam DPF both on dedicated exhaust flow simulation rigs and on an engine. Autoselective regeneration was shown to efficiently reduce the back pressure of gelcast ceramic foam DPFs on a heavy duty diesel engine at low exhaust temperatures making it an attractive option for future application.

This final chapter summarises the major findings and conclusions of the research to develop an Autoselective regenerating gelcast ceramic foam diesel particulate filter. This is followed by recommending some opportunities for future research resulting from this work.

10.1 Conclusions

This research has developed the novel Autoselective regeneration system to effectively and efficiently regenerate gelcast ceramic foam DPFs through generating understanding and knowledge of the physics involved. In addition, during these investigations a number of experimental techniques have been developed that supported this work and that can support similar future research and development.

The important conclusions from this research are:

1. Measuring the pore diameter of gelcast ceramic foams using planar imaging of a filter cross section requires a correction to account for the sectioning effect on the visible pore diameter. The visible pore diameter divided by 0.79 (2 s.f.) was shown to correct the average visible pore diameter to give the average pore diameter.
2. Pre- and post-weight measurements of filter samples at non-ambient temperatures led to errors in the mass measurement resulting from the buoyancy of the trapped air. Ideal gas relationships that allow the correction of the weight measurement have been presented, allowing mass measurements without needing long durations for cooling of the sample to near ambient temperatures.

3. Considering the PM density and composition, pre-loading of filter samples should be carried out with engine loads between 60 and 74% peak load for PM properties representative of real world engine cycles.
4. New methodology has been developed that allowed analysis of the effect of local PM mass loading within the filter on the generated back pressure. The relationship was derived by considering PM loading distribution with pressure drop relationships for flow through porous media. This allows predictions of filtration efficiency and back pressure characteristics of any conceptual foam filter designs that previously could not be estimated accurately.
5. The optimum microscopic and macroscopic geometry of a gelcast ceramic foam DPF is highly application dependent. To support the design of gelcast ceramic foam DPFs, an example design space was presented for a 0.06 m^2 flow area filter. Similar design maps can be readily produced from the derived relationships describing the loaded filter exhaust gas flow back pressure.
6. Filtration efficiencies >95% have been demonstrated with significantly smaller filtration volumes than current state of the art filters, although they were limited in their PM mass holding capacity. With a comparable filter size and PM holding capacity to a monolithic WFF, a filtration efficiency of ~80% is achievable.
7. Gelcast ceramic foam DPFs PM mass holding capacity can be increased by either reducing the filtration efficiency or increasing the foam pore size. This allows optimisation of the gelcast ceramic foam to suit PM loading requirements for alternative regeneration systems such as microwave heating.
8. Autoselective regeneration of diesel PM was shown to be a result of heating of the PM to temperatures at which rapid PM oxidation occurs. Generation of highly reactive species are expected to have a lesser effect.
9. New non-contact methods of measuring heat flux from atmospheric pressure electric discharges have been developed and used to investigate the effect of gas flow, electrode spacing and discharge current on the heating effect of the discharge. Increasing gas flow velocity (in any direction), increasing the electrode separation and increasing the discharge current reduces the heating

efficiency (i.e. the amount of electrical energy that is converted to thermal energy in the solid).

10. The efficiency of the conversion of electrical energy to thermal energy in the discharge-solid contacts was described by considering the discharge as a heated column of gas. Increasing heat flow from the discharge to the surrounding gas (e.g. forced convection) reduces the heating efficiency of the discharge.
11. Modelling showed that using filter materials with low thermal conductivity and low heat capacity improved significantly the effectiveness of the Autoselective regeneration of gelcast ceramic foam DPFs by reducing the energy needed to heat up the substrate and local PM. Of the materials considered, cordierite offered the best compromise between peak material working temperatures and heat flow properties.
12. Control of local material temperatures (affecting discharge autoselectivity and risk of damage) was achieved by intermittent application of the electric discharge. The optimum settings for the duty cycle and period were shown to be exhaust gas flow condition dependent.
13. For effective PM regeneration, the electric discharge must penetrate into the filter volume. With high PM loadings the resonant circuit must be capable of driving more current than with lower PM loadings, to achieve a discharge within the filter volume. This was achieved by adding additional load capacitance between the high voltage (HV) electrodes.
14. To achieve typical regeneration rates, multiple Autoselective discharges were required. This was done by using discrete high voltage mesh electrodes connected to independent power supplies.
15. Mesh electrodes on either side of a thin filter section offered regeneration of the entire filtration volume. To promote autoselectivity it was necessary to have a small air gap between the electrode and the filter surface, typically ~1 mm. The electrode spacing was required to be increased towards the perimeter of the electrode to improve the distribution of the electric field.
16. The use of atmospheric pressure glow discharges for rapid local oxidation of PM from gelcast ceramic foam DPFs has been shown to be an efficient and effective method for regenerating DPFs under full exhaust gas flow.

Regeneration effectiveness of ~12 g kW^{-1} h^{-1} was demonstrated during real engine testing.

17. An integrated prototype of an Autoselective regenerating gelcast ceramic foam DPF for a 56 kW heavy duty diesel engine has been presented. The projected filtration efficiency is 80% with a canister volume comparable to a 5.66 inch diameter monolithic wall flow filter. The predicted average electrical energy requirement was 333 W (which is ~794 W of fuel power requirement). This was shown to be comparable with current state of the art filtration and regeneration systems. The instantaneous energy requirement of 333 W is significantly lower than comparable systems such as fuel burners or electric resistance heaters.

10.2 Recommendations for Further Work

This research has successfully developed and demonstrated the Autoselective regeneration of 80% porous gelcast ceramic foam DPFs. During the process of this research a number of interesting areas worthy of further work have been identified; these are:

1. Optimisation of discharge on- and off-times. This research has identified some of the complex effects the choices of discharge on- and off-times have on the regeneration, filter damage and discharge behaviour. Initial values that proved effective have been proposed but were not optimised. Optimisation would offer further energy efficiency benefits and allow optimised regeneration under all engine conditions.
2. Extension of foam DPF optimisation. The gelcast foam DPF optimisation presented considers only 80% porous gelcast ceramic foams due to their expected strength. Expanding the gelcast ceramic foam DPF optimisation to consider a range of foam densities may offer improved filtration performance, PM holding capacity and exhaust system flow back pressure.
3. Investigation of alternative filtration substrates. The Autoselective regeneration technique has been applied here to gelcast ceramic foam DPFs and earlier to monolithic WFFs (Proctor, 2006). The availability of other

types of filtration substrate, such as fibrous filters should be investigated to determine the full potential of the Autoselective regeneration technique.

4. On engine multiple electrode prototype demonstration. An integrated prototype design has been presented which should be capable of demonstrating multiple electrode regeneration of a gelcast ceramic foam DPF on an engine. Manufacture and application of this prototype design will demonstrate the concept and for potential commercialisation of this promising technology.

REFERENCES

Adigio E.M. (2005) Modelling Gas Flow Pressure Gradients in Gelcast Ceramic Foam Diesel Particulate Filters. *PhD Thesis - Loughborough University.*

Adler J (2005) Ceramic Diesel Particulate Filters. *International Journal of Applied Ceramic Technology, Vol 2, No. 6,* pp. 429-439.

Ahrens T.J. ***(editor)*** **(1995)** Mineral Physics and Crystallography, A Handbook of Physical Constants. American Geophysical Union. ISBN 0-87590-852-7

Airtec Air Systems (2001) RT Series Datasheet for centrifugal blowers.

Ambrogio M., Saracco G. and Specchia V. (2001) Combining Catalytic Combustion in Particulate Traps for Diesel Exhaust Treatment. *Chemical Engineering Science, Vol 56* pp 1613-1621

Arai M., Miyashita S. and Sato K. (1987) Developmnt and Selection of Diesel Particulate Trap Regeneration System. *SAE Technical Paper Series* 870012

Astarita T., Cardone G. and Carlomagno G.M. (2006) Infrared thermography: An optical method in heat transfer and fluid flow visualisation *Opt Laser Eng Vol 44* pp261-281

AVL (2002) AVL 415S Smoke Meter The New Correlation Curve. Updated 15th October 2002.

Barris M.A., Monson D.R., Weik T.M. and Schaefer J.W. (1987) Material Characterisation of Diesel Particulate Trap Alternatives. *SAE Technical Paper 872246*

Bloom R. (1995). The Development of Fiber Wound Diesel Particulate Filter Cartridges. SAE Paper 950152, 1995

Boretto G., Debenedetti M., Marzorati D. and Vaglieco B.M. (1999) Diesel Particulate Filter Based on Ceramic Foams. *SAE Technical Paper 1999-24-0052*

Brailsford A.D. and Major K.G. (1964) The thermal conductivity of aggregates of several phases, including porous materials. *British Journal of Applied Physics Vol 15* pp313-319

Bull R. (2006) Experiment to determine the quantity of volatile compounds in trapped soot. LOCOFILT internal project report. 18th April 2006

Burley H.A. and Rosebrock T.L. (1979) Automotive Diesel Engines – Fuel Consumption vs Particulates. *SAE Technical Paper 790923.*

Bykowski B.B. (1987) Formulation and Evaluation of Alternative Diesel Particulate Trap Media. *Presented at the Energy-Sources Technology Conference and*

Exhibition, Dallas, Texas, February 15-20. The American Society of Mechanical Engineers

Callé S., Contal P., Thomas D., Bémer D. and Leclerc D. (2002) Evolutions of efficiency and pressure drop of filter media during clogging and cleaning cycles. *Powder Technology Vol 128* pp213-217

Cha M.S., Lee S.M., Kim K.T. and Chung S.H. (2005) Soot Suppression by nonthermal plasma in coflow jet diffusion flames using a dielectric barrier discharge. *Combustion and Flame Vol 141* pp 438-447

Ciach T. and Sosnowski T.R. (1996) Removal of Soot Particles From Diesel Exhaust. *Journal of Aerosol Science, Vol 27, Suppl 1,* pp S705-S706

Ciambelli P., Palma V., Russo P. and Vaccaro S. (2002) Deep Filtration and Catalytic Oxidation: an Effective Way for Soot Removal. *Catalysis Today Vol 73* pp 363-370

Clague A.D.H., Donnet J.B., Wang T.K., Peng J.C.M. (1999). A comparison of diesel engine soot with carbon black. *Carbon, Vol 37,* pp1553-1565

Collura S., Chaoui N., Azambre B., Finqueneisel G., Heintz O., Krzton A., Koch A., Weber J.V. (2005). Influence of the soluble organic fraction on the thermal behaviour, texture and surface chemistry of diesel exhaust soot. *Carbon, Vol 43,* pp 605-613.

Corning (2006) Corning DuraTrap ® CO filters promotional document. March 2006

Crane R.I. and Wisby P. (2000) Light-duty diesel exhaust after-treatment by a multicyclone particulate separator with an oxidation catalyst. *Proceedings of the Institute of Mechanical Engineers, Part D Vol 214,* pp 741-749

Dan Y., Dengshan G., Gang Y., Xianglin S. and Fan G. (2005) An Investigation of the Treatment of Particulate Matter from Gasoline Engine Exhaust using non-thermal plasma. *Journal of Hazardous Materials B127* pp 149-155

Dec J.E. and Kelly-Zion P.L. (2000). The Effects of Injection Timing and Diluent Addition on Late-Combustion Soot Burnout in a DI Diesel Engine Based on Simultaneous 2-D Imaging of OH and Soot. *SAE Technical Paper 2000-01-0238.*

Diesel Emissions Evaluation Program (DEEP) (1999). Project Report; Diesel Emission Control Strategies Available To The Underground Mining Industry, prepared by ESI International.

DieselNET (2007) Emission Standards Summary. Available online at www.dieselnet.com Last accessed 12th June 2007.

DUKES (2006) Digest of UK Energy Statistics. Table 5.4, Fuel used in generation, and 5.6 Electricity fuel use, generation and supply. 28th September 2006

Electrodrives (2007) Alpak II AC motor datasheet. Document 9629EI Issue 2

Energizer (2007) Engineering data for Energizer No 522. Datasheet EBC – 1108E

EPA, United States Environmental Protection Agency (1997) Emissions Standards Reference Guide for Heavy-Duty and Nonroad Engines. Document No. EPA420-F-97-014, September 1997

EPA, United Stated Environmental Protection Agency (2006) Filter stabilisation and microbalance workstation environmental conditions, microbalance specifications and particulate matter filter handling and weighing procedures. Document 86.1312-2007

Ergun S. (1952) Fluid Flow Through Packed Columns. *Chemical Engineering Progress Vol 48 No 2* pp89-94

Farnell (2007) 1100 W DC Motor Datasheet. Part number 7082782. Available online at uk.farnell.com. Last accessed 1st June 2007

Farzaneh M., Allaire M.A., Marceau K. and Lachance P. (1994) Electrostatic Capture and Agglomeration of Particles Emitted by Diesel Engines.*Industry Applications Society Annual Meeting, 1994, Conference Record of the 1994 IEEE, Vol 2* pp1534-1537

Forsythe W.E. ***[prepared by]*** **(2003)** Smithsonian Physical Tables, Ninth Revised Edition. Knovel, Norwich, New York.

Gabathuler J.P., Mizrah T., Eckert L., Fischer A., Käser P. and Maurer A. (1991) New Developments of Ceramic Foam as a Diesel Particulate Filter. *SAE Technical Paper 910325*

Garner C.P. (2006) Autoselective Regenerating Particulate Filter. International Patent WO/2007/023267 Filed 22nd August 2006.

Garner C.P. and Harry J.E. (2003) Autoselective Regenerating Particulate Filter. US Patent 6660068. Issued on 9th December 2003.

Garner C.P. (1989) The Regeneration of Monolithic Wall-flow Diesel Particulate Traps. *PhD Thesis – Loughborough University*

Garner C.P., Dent J.C. (1989). Microwave Assisted Regeneration of Diesel Particulate Traps. SAE Paper 890174, SP-775, 1989

Gautam M., Popuri S., Rankin B. and Seehra M. (1999) Development of a Microwave Assisted Regeneration System for a Ceramic Diesel Particulate System. *SAE Technical Paper Series* 1999-01-3565

Geiger H., Kleffmann J. and Wiesen P. (2002) Smog chamber studies on the influence of diesel exhaust on photosmog formation. *Atmospheric Environment, Vol 36,* pp1737-1747

Gieshoff J., Pfeifer M., Schafer-Sindlinger A., Hackbarth U., Teysset O., Colignon C., Rigaudeau C., Salvat O., Krieg H., Wenclawiak B.W. (2001). Regeneration of Catalytic Diesel Particulate Filters. *SAE Technical Paper Series* 2001-01-0907

Grill A. (1994) Cold Plasmas in Materials Fabrication. IEEE Press. ISBN 0780310551

Gross B. (1968) Plasma Technology. Iliffe. ISBN 0592050386

Harris S.J., Maricq M.M. (2001). Signature size distributions for diesel and gasoline engine exhaust particulate matter. *Aerosol Science Vol 32* pp 749-764

Harry J.E. and Garner C.P. (1998) Autoselective Regeneration of Diesel Particulate Traps Feasibility Study. *Report for Perkins Engines Ltd, Loughborough University,* 22nd October 1998.

Heaton D. (2007) Caterpillar Research, Europe. Private communication, May 2007.

Helferich R.L. and Schenck R.C. (1989) Evaluation of a Stacked Element Diesel Particulate Trap Using a Newly Developed Membrane Covered Ceramic Foam Filtering Media. *SAE Technical Paper 890787*

Heywood J.B. (1988) Internal Combustion Engine Fundamentals. McGraw-Hill Inc. ISBN 0-07-100499-8

Hiden Analytical (2005) Datatables included with HPR-20 mass spectrometer operation software.

Howitt J.S., Montierth M.R. (1981). Cellular Ceramic Diesel Particulate Filter. *SAE Technical Paper Series* 810114, Printed in the Progress in Technology Series No 25. ISBN 0-89883-113-X.

Hughes S.W. (2003) The Use of Gel Cast Ceramic Foams as Diesel Particulate Filters. *PhD Thesis – Loughborough University*

Isobe T., Kameshima Y., Nakajima A., Okada K. and Hotta Y. (2006) [a] Extrusion method using nylon 66 fibres for the preparation of porous alumina ceramics with oriented pores. *Journal of the European Ceramic Society, Vol 26,* pp 2213-2217

Isobe T., Tomita T., Kameshima Y., Nakajima A. and Okada K. (2006) [b] Preparation and Properties of Porous Alumina Ceramics with Oriented Cylindrical Pores Produced by an Extrusion Method. *Journal of the European Ceramic Society, Vol 26,* pp 957-960

Iwai K., Adachi S., Takahashi M., Moller L., Udagawa T., Mizuno S., Sugawara I. (2000) Early Oxidative DNA Damages and Late Development of Lung Cancer in Diesel Exhaust Exposed Rats. *Environmental Research, Section A, 84,* pp255-264

Jacobs T., Chatterjee S., Conway R., Walker A., Kramer J., and Mueller-Haas K. (2006) Development of Partial Filter Technology for HDD Retrofit. *SAE Technical Paper Series* 2006-01-0213.

James Walker (1997) Supergraf Laminated Jointing N7 Material Specifications. 14th January 1997, Issue 3.

Janna W.S. (2000) Engineering Heat Transfer. CRC Press, USA. ISBN 0-8493-2126-3.

Jayasinghe S.N. and Edirisinghe M.J. (2002) A Novel Method of Forming Open Cell Ceramic Foam. *Journal of Porous Materials, Vol 9,* pp 265-273

John P.W.M. (1972) Statistical Design and Analysis of Experiments. Collier-Mac. ISBN 002360820X

Johnson T.V. (2006) Diesel Emission Control in Review. *SAE Technical Paper Series* 2006-01-0030. Printed in Diesel Exhaust, SP-2022.

Kitagawa J., Toshihiko T. and Makino M. (1990) Analyses of Thermal Shock Failure on Large Volume DPF. *SAE Technical Paper 900113.*

Kitamura T., Ito T., Senda J. and Fujimoto H (2002) Mechanism of smokeless diesel combustion with oxygenated fuels based on the dependence of the equivalence ratio and temperature on soot particle formation. *International Journal of Engine Research Vol 3 No 4* pp 223-248

Kittelson D.B. (1998). Engines and Nanoparticles: A Review. *Journal of Aerosol Science, Vol 29, No 5/6,* pp575-588

Kleeman M.J., Schauer J.J., Cass G.R. (2000). Size and Composition Distribution of Fine Particulate Matter Emitted from Motor Vehicles. *Environmental Science and Technology, Vol 34, No 7,* pp1132-1142

Konno M., Chikahisa T. and Murayama T. (1992) Reduction of Smoke and NOx by Strong Turbulence Gnerated During the Combustion Process in D.I. Diesel Engines. *SAE Technical Paper 920467.*

Konstandopoulos A.G., Kladopoulou E., Skaperdas E. (2000). Transient Pressure Drop of Diesel Particulate Filters. Journal of Aerosol Science, Vol31 Suppl, ppS208-S209

Ladha K. (2007) Wall Flow Filter Auto-Selective Electrical Discharge Regeneration System. Internal LOCOFILT project presentation. 1st May 2007.

Lakkireddy V.R., Mohammed H. and Johnson J.H. (2006) The Effect of a Diesel Oxidation Catalyst and a Catalysed Particulate Filter on Particle Size Distribution from a Heavy Duty Diesel Engine. *SAE Technical Paper Series* 2006-01-0877

Law M.C. (2006) Modelling Wall-Flow Diesel Particulate Filter Regeneration Processes. *PhD Thesis – Loughborough University*

Lenz H.P. and Cozzarini C. (1999) Emissions and Air Quality. Society of Automotive Engineers, USA. ISBN 0-7680-0248-6.

Levendis Y.A., Larsen C.A. (1999). Use of Ozone-Enriched Air for Diesel Particulate Trap Regeneration. SAE Paper 1999-01-0114, 1999

Li C.G., Mao F., Swartzmiller S.B., Wallin S.A. and Ziebarth R.R. (2004) Properties and Performance of Diesel Particulate Filters of an Advanced Ceramic Material. SAE Technical Paper 2004-01-0955.

Liu Z.G, Thurow E.M., Caldow R. and Johnson T.R. (2005) Transient Performance of Diesel Particulate Filters as Measured by an Engine Exhaust Particle Size Spectrometer. *SAE Technical Paper Series* 2005-01-0185.

Löffler G., Sieber R., Harasek M., Hofbauer H., Hauss R. and Landauf J. (2006) NO_x formation in natural gas combustion – a new simplified reaction scheme for CFD calculations. *Fuel, Vol 85,* pp513-523

Ludecke O.A. and Dimick D.L. (1983) Diesel Exhaust Particulate Control System Development. *SAE Technical Paper Series* 830085

Ma J, Fang M, Li P., Zhu B., Lu Z. and Lau N.T. (1997) Microwave-assisted catalytic combustion of diesel soot. *Applied Catalysis A: General Vol 159* pp211-228

Ma J.Y.C. and Ma J.K.H. (2002) The Dual Effect of the Particulate and Organic Components of Diesel Exhaust Particles on the Alteration of Pulmonary Immune/Inflammatory Responses and Metabolic Enzymes. *Journal of Environmental Science and Health, Part C – Environmental Carcinogenesis & Ecotoxicology Reviews. Vol C20, No 2,* pp 117-147

Matschulat D., Prestel H., Haider F., Niessner R. and Knopp D. (2006) Immunization with soot from a non-combustion process provokes formation of antibodies against polycyclic aromatic hydrocarbons. *Journal of Immunological Methods Vol 310* pp 159-170

Matsui Y., Hashimoto M., Sakaguchi A., Takashima K. and Mizuno A. (2001) Oxidation of Carbon Soot Layer using Pulsed Discharge Plasma. *SAE Technical Paper Series* 2001-01-3511

Matsunuma K., Ihara T., Hanamoto Y., Nakajima S. and Okamoto S. (1996) Development of Diesel Particulate Filter Made of Porous Metal. *SAE Technical Paper 960132*

Maxwell Technologies (2007) MC Energy Series BOOSTCAP® Ultracapacitors Datasheet 1009323 Rev 5

Menchavez R.L., Fuji M., Takegami H. and Takahashi M. (2007) Electrically conductive gelcast porous alumina sintered under argon atmosphere. *Materials Letters Vol 61 (2007)* pp 754-756

Miller P.R., Scholl J., Bagley S., Leddy D. and Johnson J.H. (1983) The Effects of a Porous Ceramic Particulate Trap on the Physical, Chemical and Biological Character of Diesel Particulate Emissions. *SAE Technical Paper 830457*

Miyamoto N., Ogawa H., Nurun N.Md., Obata K. and Arima T. (1998) Smokeless, Low Nox, High Thermal Efficiency, and Low Noise Diesel

Combustion with Oxygenated Agents as Main Fuel. *SAE Technical Paper 980506*

Mizrah T., Maurer A., Gauckler L. and J.-P. Gabathuler. (1989) Open-Pore Ceramic Foam as Diesel Particulate Filter. *SAE Technical Paper 890172*

Montanaro L., Jorand Y., Fantozzi G. and Negro A. (1998) Ceramic Foams by Powder Processing. *Journal of the European Ceramic Society, Vol 18,* pp 1139-1350

NGK (2003) NGK Insulators Ltd Press Release. Business Plan for Diesel-powered Automotive Exhaust Gas Purification Ceramics. November 26th 2003.

Ning Z., He Y. (1999). Experimental Study on Microwave Regeneration Characteristics of Diesel Particulate Aftertreatment System. SAE Paper 1999-01-1470

Nixdorf R.D., Green Jr J.B.., Story J.M., Wagner R.M. (2001). Microwave-Regenerated Diesel Exhaust Particulate Filter. SAE Paper 2001-01-0903

Okubo M., Kuroki T., Miyairi Y and Yamamoto T. (2004)[a] Low-temperature Soot Incineration of Diesel Particulate Filter Using Remote Nonthermal Plasma Induced by a Pulsed Barrier Discharge. *IEEE Transactions on Industry Applications Vol 40 No 6* pp1504-1512

Okubo M., Miyashita T., Kuroki T., Miwa S. and Yamamoto T. (2004) Regeneration of Diesel Particulate Filter Using Nonthermal Plasma Without Catalyst. *IEEE Transactions on Industry Applications Vol 40 No 6* pp1451-1458

Osram Sylvania (2001) Sureheat 36000 Operating Instructions. 14th August 2001.

Palma V., D'Amore M., Russo P., D'Arco A. and Ciambelli P. (2002) Regeneration of a soot trap ceramic foam by a single mode microwave cavity. *Combustion Science and Technology Vol 174 No 11&12* pp295-308

Park K., Cao F., Kittleson D.B. and McMurry P.H. (2003) Relationship between Particle Mass and Mobility for Diesel Exhaust Particles. *Environmental Science and Technology Vol 37* pp577-583

Peng H.X., Fan Z and Evans J.R.G. (2000) Factors affecting the microstructure of a fine ceramic foam. *Ceramics International, Vol 26,* pp 887-895

Perkins Engines (2005) Perkins 1104C-44TA diesel engine datasheet. Document 1645/02/06

Pontikakis G.N., Koltsakis G.C. and Stamatelos A.M. (2001) Dynamic Filtration Modelling in Foam Filters for Diesel Exhaust. *Chemical Engineering Communications, Vol 00,* pp1-26 I108T011009.108

Proctor J.W. (2006) Investigation and Development of the Diesel Particulate Filter Autoselective Regeneration System. *PhD Thesis – Loughborough University*

Pyzik A.J. and Li C.G. (2005) New Design of a Ceramic Filter for Diesel Emission Control Applications. *International Journal of Applied Ceramic Technology, Vol 2, No 6,* pp 440-451.

Rencz M., Kollár E. and Székely V. (2004) Heat-flux sensor to support transient thermal characterisation of IC packages *Sensor Acuat A-Phys Vol 116* pp284-292

Richards P., Kalischewski W. (2004). Results from a ¼ million km, heavy duty truck trail, using FBC regenerated DPFs. SAE Paper 2004-01-0074

Richerson D.W. (1992) Modern Ceramic Engineering: Properties, Processing and Use in Design (2nd Edition). Macel Dekker Ltd. ISBN 0824786343

Robert Bosch GmbH (2004) Bosch Automotive Handbook, 6th Edition. Robert Bosch GmbH, Germany. ISBN 1-86058-474-8

Rosner D.E. and Allendorf H.D. (1965) High Temperature Oxidation of Carbon by Atomic Oxygen. *Carbon Vol 3* pp153-156.

Schnelle K.B. Jr and Brown C.A. (2002) Air Pollution Control Technology Handbook. CRC Press, USA. ISBN 0-8493-9588-7

Sepulveda P. and Binner J.G.P. (1999) Processing of Cellular Ceramics by Foaming and in situ Polymerisation of Organic Monomers. *Journal of the European Ceramic Society, Vol 19,* pp 2059-2066.

Setten B.A.A.L. van, Makkee M., Moulijn J.A (2001). Science and Technology of Catalytic Diesel Particulate Filters. *Catalysis Reviews, Vol 43 No 4,* pp 489-564

Shackelford J.F. and Alexander W. ***(editors)*** **(2001)** Material Science and Engineering Handbook. CRC Press USA, ISBN 0-8493-2696-6

Sharma M., Agarwal A.K. and Bharathi K.V.L. (2005) Characterisation of exhaust particulates from diesel engine. *Atmospheric Environment Vol 39* pp3023-3028

Shinozaki O., Shinoyama E. and Saito K. (1990) Trapping Performance of Diesel Particulate Filters. *SAE Technical Paper 900107*

Singh I., Zhong L., Lai M-C. and Henein N.A. (2003) Effect of Nozzle hole Geometry on a HSDI Diesel Engine-Out Emissions. *SAE Technical Paper 2003-01-0704*

Song J., Alam M., Wang J., Boehman A. (2004). Fuel Impacts on Soot Nanostructure and Reactivity. *2004 Diesel Emissions Reduction Conference.* The Energy Institute.

Sonnenschein (2007) Datasheet for industrial batteries Sonnenschein A500. Datasheet NXSA5TE50000402.

Schmidt-Ott A. (1988) New approaches to in situ characterisation of ultrafine agglomerates. *Journal of Aerosol Science Vol 19 No 5* pp553-563

Stone R. (1999) Introduction to Internal Combustion Engines. Third Edition. Macmillan Press Ltd, UK. ISBN 0-333-74013-0.

Tao T., Cutler W.A., Voss K., Wei Q. (2003). New Catalyzed Cordierite Diesel Particulate Filters for Heavy Duty Applications. SAE Paper 2003-01-3166

Temple-Pediani R.W. (1973) Effect of Pre-Injection Fuel Temperature Upon Diesel Engine Ignition Delay and Soot Emission. *Institute of Mechanical Engineers, Vol 187* pp 395-404

Thijs I., Luyten J. and Mullens S. (2003) Producing Ceramic Foams with Hollow Spheres. *Journal of the American Ceramic Society, Vol 87, No 1,* pp 170-172

Trethowen H. (1986) Measurement errors with surface-mounted heat flux sensors *Build Environ Vol 21 No 1* pp41-56

Tutko J.J., Lestz S.S., Brockmeyer J.W. and Dore J.E. (1984) Feasibility of Ceramic Foam as a Diesel Particulate Trap. *SAE Technical Paper 840073*

Twigg M.V. ***(Editor)*** **(1989)** Catalyst Handbook. Wolfe Publishing. ISBN 0723408572

US Department of Labor (2007) Standards – 29 CFR Table Z-1 Limits of Air Contaminants 1910.1000. Occupational Safety & Health Administration

Virtanen A.K.K., Ristimäki J.M., Vaaraslahti K.M. and Keskinen J. (2004) Effect of Engine Load on Diesel Soot Particles. *Environmental Science and Technology Vol 38* pp2551-2556

Walsh M.P. (1999) Global Trends in Diesel Emissions Control – A 1999 Update. *SAE Technical Paper Series* 1999-01-0107. Reprinted from: Diesel Exhaust Aftertreatment 1999 (SP-1414).

Warnes L. (1998) Electronic and Electrical Engineering, Principles and Practice. Palgrave, USA. ISBN 0-333-74311-3

Watabe Y., Irako K., Miyajima T., Yoshimoto T. and Murakami Y. (1983) "Trapless" Trap – A Catalytic Combustion System of Diesel Particulates Using Ceramic Foam. *SAE Technical Paper 830082*

Wikipedia (2007) LNER Class A3 'Flying Scotsman' Locamotive Data. Available online at www.wikipedia.org Last accessed 12th June 2007.

Xiao F., Liu X. (1994). Design Improvement on Diesel Particulate Bag Filters. SAE Paper 941775

Xiaoguang X., Xiyan G. and Xiancheng W. (2001) After-Treatment for Reduction of Diesel Exhaust Particulate. *SAE Technical Paper 2001-01-3204*

Yang L.C. (1981) Diesel Particulate Destruction by Electric Discharge Technique. *Final Report for State California Air Resources Board, contract AO-047-32.*

Yao S., Okumoto M., Madokoro K., Yashima T. and Suzuki E. (2004) Pulsed Dielectric Barrier Discharge Reactor for Diesel Particulate Matter Removal. *AIChE Journal Vol 50 No 8* pp1901-1907

Zelenka P., Schmidt S., Elfinger G. (2001). An Active Regeneration Aid as a Key Element for Safe Particulate Trap Use. SAE Paper 2001-01-3199

Zhang F-Z., Kato T., Fuji M. and Takahashi M. (2006) Gelcasting fabrication of porous ceramics using a continuous process. *Journal of the European Ceramic Society, Vol 26,* pp 667-671

Zikoridse G., Velji A., Heidrich E., Seguelong T., Naschke W., Kaiser F.W. (2000). Particulate Trap Technology for Light Duty Vehicles with a New Regeneration Strategy. SAE Paper 2000-01-1924, 2000

APPENDICES

APPENDIX A: OPTICAL EMISSION SPECTROSCOPY EQUIPMENT AND CALIBRATION

The Princeton Instruments PI320 Spectrometer with the PI ICCD-1024-E camera was used for this research. The equipment was loaned from the EPSRC instrument pool.

A two stage calibration was carried out. The first stage calibrated the wavelength using a Hg-Ar lamp which generated emissions at known wavelengths. The known wavelengths were used to calibrate the instrument based on linear fits between the known points. The second stage used a calibrated tungsten lamp to generate a broadband emission spectrum of known intensity at given wavelengths. This light source was used to calibrate the signal magnitude. The emission spectra from the calibration lamps is shown in Figure A.1.

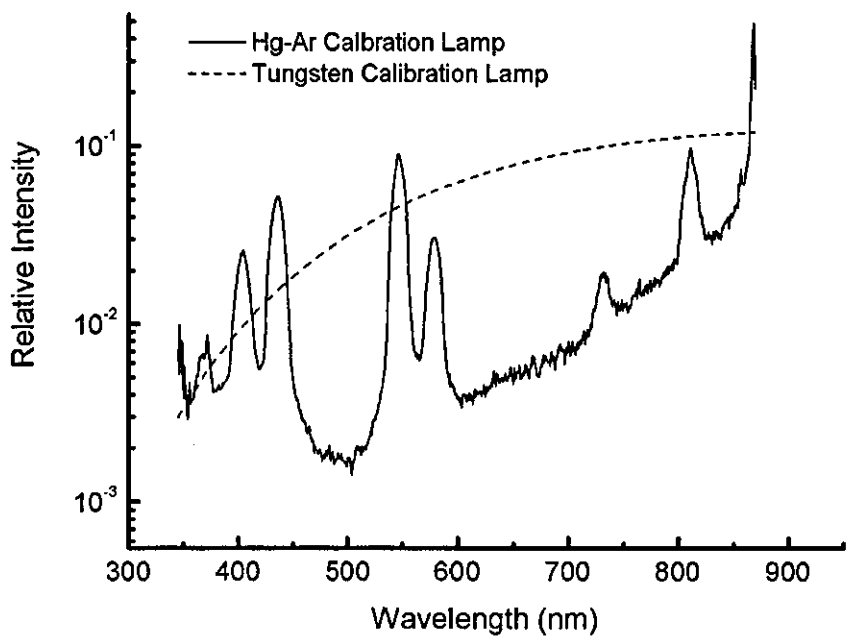

Figure A.1 Calibration lamp spectra

APPENDIX B: HEAT FLUX MEASUREMENTS – JUSTIFICATION OF 2-D APPROXIMATION

The heat flux measurement in Chapter 5 relies on the surface temperature measured with the thermal imaging camera to be representative of the bulk material temperature. The appendix shows the calculations that justify the use of 1 mm thick aluminium to approximate a two dimensional structure.

Under steady state, a one dimensional heat flux calculation can give an approximation of the difference between the average material temperature and the surface material temperature. The one dimension heat flux equation is

$$q = -kA\frac{dT}{dx} \tag{B.1}$$

where q is the heat flux, k is the thermal conductivity, A is the area, T is the temperature and x is the distance. Re-arranging and integrating gives

$$T = -\frac{qx}{kA} \tag{B.2}$$

The heat flux, q, throughout the layer will be equal to the heat flux from the surface. The heat flux from the surface is

$$q = -hA\left(T - T_g\right) \tag{B.3}$$

where h is the heat transfer coefficient, T is the surface temperature and T_g is the bulk gas temperature. The average temperature can be calculated as

$$\overline{T} = T_s + \frac{hA(T_s - T_g)t}{4kA} \qquad \text{(B.4)}$$

where $\overline{T}$ is the average material temperature and t is the material thickness. The error between the average temperature and surface temperature, E_T is therefore

$$E_{\overline{T}} = \frac{h(T_s - T_g)t}{4k} \qquad \text{(B.5)}$$

Figure B.1 shows the effect of temperature on the error associated with a given surface temperature for a 1 mm thick aluminium section. This error is less than 1% of the material temperature and is therefore negligible compared to other experimental errors. In addition, this error is not random, and the surface temperature will always underestimate the average temperature.

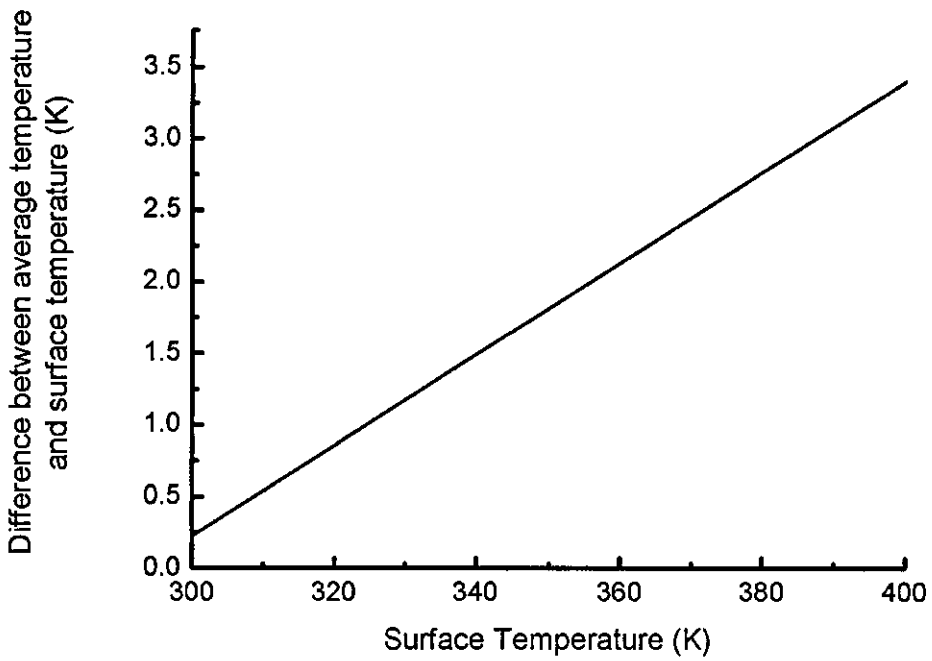

Figure B.1 Variation of error in average temperature measurement using the thermal imaging camera for a range of surface temperature.

APPENDIX C: HEAT FLUX MEASUREMENTS – UNCERTAINTY ANALYSIS

Uncertainties in the measurement of heat flux from electrical plasmas are:

1. Calibration of thermal imaging equipment (i.e. emissivity).
2. Error in material properties (i.e. density and specific heat capacity)
3. Resolution of thermal imaging equipment (manifested in the definition of the control volume)
4. Signal noise on the temperature data

The emissivity was calibrated to within 0.01 by matching the surface temperature measured using the thermal imaging equipment to the surface temperature measured with a k-type thermocouple at approximately 200 °C. The absolute value of the emissivity for the aluminium electrodes was 0.23. The material properties were taken from Shackelford and Alexander (2001) and are estimated to be accurate to within 5 %. The effect of the resolution of the thermal imaging camera resulted in errors in the defined control volume. For an arbitrary shape control volume such as that shown in Figure C.1, the maximum error in definition of the control volume size is equal to the area of the outer most pixels (the shaded region).

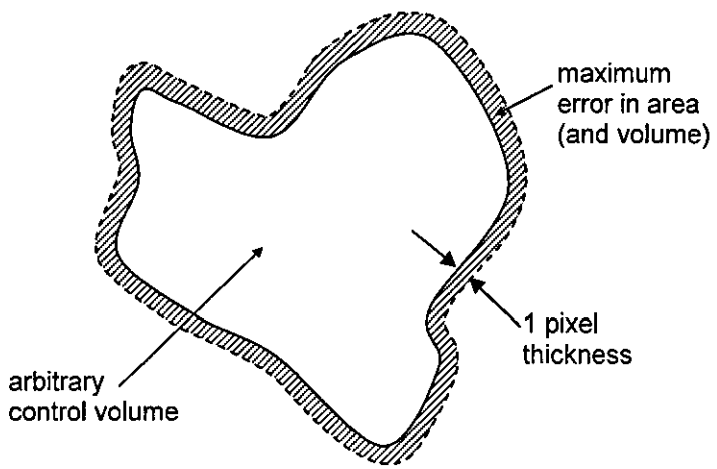

Figure C.1 Schematic showing the error in defining the control volume resulting from the resolution of the thermal imaging camera.

This means the error in volume is equal to

$$E_V = \frac{c}{p} \times p^2 \times t = cpt \qquad \text{(C.1)}$$

where c is the circumference of the control volume, t is the electrode thickness and p is the dimension of the pixel (mm per pixel). Applying this calculation to a range of control volume sizes for a sample set of data results in Figure C.2. As the control volume reduces in size to less than 50 mm^3, which corresponds to a smaller number of pixels, the associated error in the calculated thermal flux can increase to greater than 30%. Focusing the area of interest to fill the field of view of the thermal imaging equipment will maximise the resolution and minimise the resulting errors.

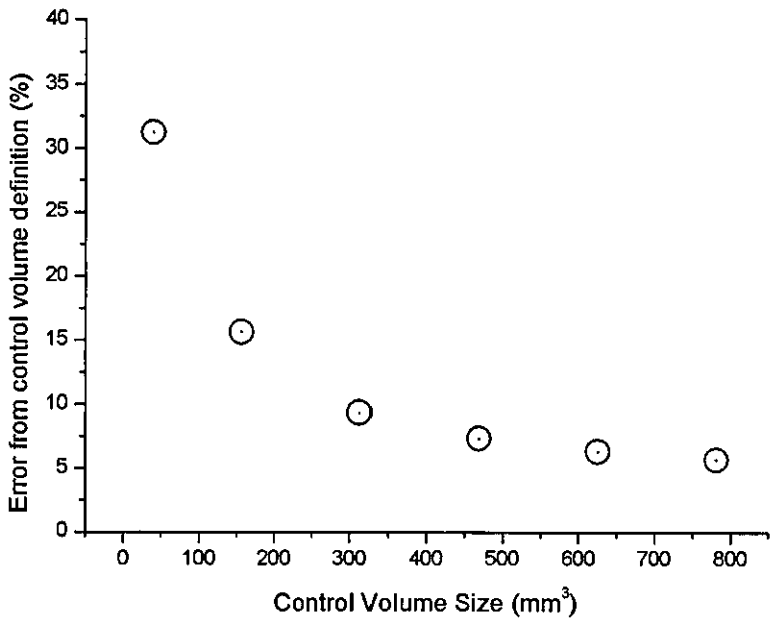

Figure C.2 Effect of control volume size on the errors from definition of the control volume.

The signal noise is magnified during the calculation of heat flux due to taking the derivative of the temperature signal with respect to time. Figure C.3 shows a sample test case of the rate of change of average temperature for a 39 mm^3 control volume.

Figure C.4 shows data calculated from the same test with a 781 mm^3 control volume. The signal noise is clearly visible on both plots.

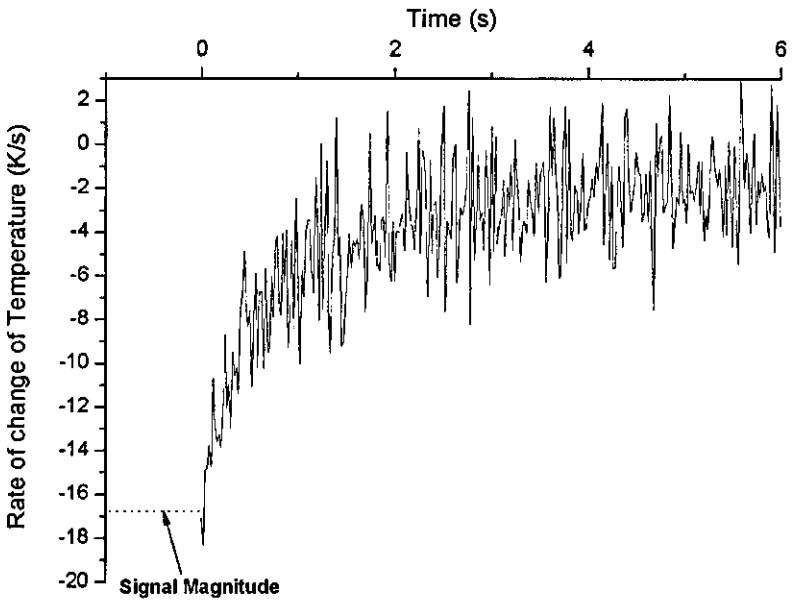

Figure C.3 Plots of typical transient data for the derivative of average temperature with respect to time for a control volume of 39 mm^3.

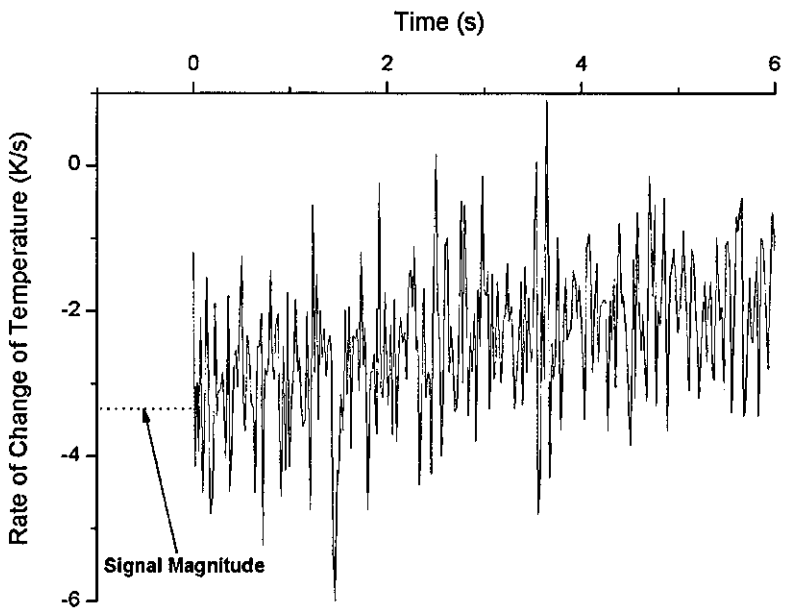

Figure C.4 Plots of typical transient data for the derivative of average temperature with respect to time for a control volume of 781 mm^3.

The absolute magnitude of the noise on the temperature measurement reduces as the control volume increases in size. The magnitude of the signal also reduces with increasing control volume size, although at a faster rate than the noise resulting in the

relative error caused by the noise to be minimised with the smallest control volume. Figure C.5 shows how the chosen control volume size affects the signal to noise ratio during these experiments taken from a single, characteristic dataset. It can be seen that for control volumes above approximately 300 mm^3 the effect of signal noise does not increase significantly. As the control volume size is reduced, the signal becomes increasingly large relative to the noise resulting in an error of approximately 5 % when control volumes of 75 mm^3 are used.

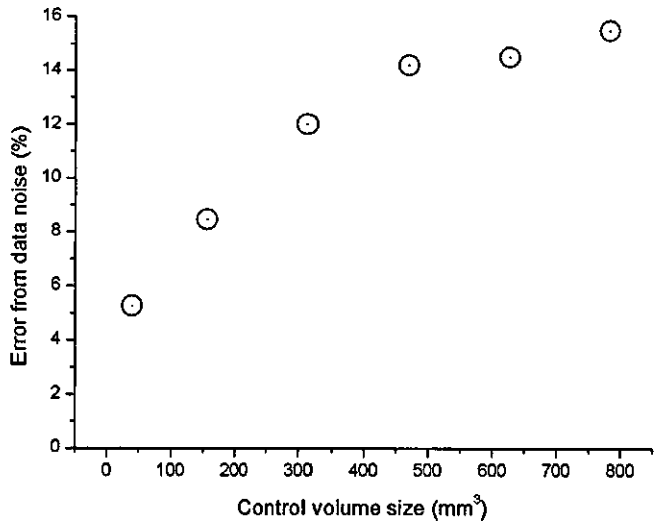

Figure C.5. Effect of control volume size on the error of the power measurement resulting from signal noise.

These two causes of error with conflicting control volume size requirements results in a compromise of control volume size that requires optimization to minimise the overall errors. To do this there is a need to understand how the errors propagate to give an overall estimated error on the measurement technique. The methodology described by Coleman and Steele (1995) for a general uncertainty analysis was therefore applied. This lead to the calculation of the overall uncertainty given by

$$U_Q^{\,2} = \sum_{i=1}^{J} (\theta_i U_i)^2 \qquad \text{(C.2)}$$

where

$$\theta_i = \frac{dr}{di} \tag{C.3}$$

and U is the uncertainty, subscript Q refers to the calculated power, and i refers to the measurement that forms part of the calculation to the result (e.g. $i = \rho$ for density).

An example of the calculation of θ_i is shown for the case of the uncertainties from the signal noise on the data for the case of 312 mm^3 control volume. It is equally applicable to the other measurements for which the values of θ and U are summarised in Table C.1. Since the relationship between the temporal temperature gradient and heat flux is given in Chapter 5, differentiation of this with respect to the temperature gradient gives

$$\theta_T = \frac{dQ}{d\left(\frac{dT}{dt}\right)} = \rho c_p V = 2700 \times 900 \times 312 \times 10^{-9} = 0.75816 \text{ W K}^{-1} \tag{C.4}$$

The effect of uncertainties in emissivity can be introduced as

$$\theta_\varepsilon = \frac{dQ}{d\left(\frac{dT}{dt}\right)} \times \frac{d\left(\frac{dT}{dt}\right)}{d\varepsilon} \tag{C.5}$$

where the $d(dT/dt)/d\varepsilon$ term is found by analysis of a typical dataset.

Table C.1. Values used for uncertainty analysis.

Control Volume	ρ /kg m^{-3}		c_p /J kg^{-1} K^{-1}	
	θ_ρ	U_ρ	θ_c	U_c
39 mm^3	5.72x10^{-4}	100	1.72x10^{-3}	50
156 mm^3	1.24x10^{-3}	100	3.73x10^{-3}	50
312 mm^3	1.65x10^{-3}	100	4.96x10^{-3}	50
468 mm^3	2.08x10^{-3}	100	6.24x10^{-3}	50
624 mm^3	2.37x10^{-3}	100	7.11x10^{-3}	50
780 mm^3	2.46x10^{-3}	100	7.38x10^{-3}	50

Control Volume	V /m^3		$\frac{d\overline{T}}{dt}$ /K s^{-1}		ε	
	θ_V	U_V	θ_T	U_T	θ_ε	U_ε
39 mm^3	3.96x10^{7}	44.4x10^{-9}	0.095	0.857	4.91	0.01
156 mm^3	2.15x10^{7}	39.5x10^{-9}	0.379	0.749	10.4	0.01
312 mm^3	1.43x10^{7}	34.5x10^{-9}	0.758	0.707	13.3	0.01
468 mm^3	1.20x10^{7}	29.2x10^{-9}	1.137	0.699	17.8	0.01
624 mm^3	1.02x10^{7}	24.4x10^{-9}	1.516	0.611	19.9	0.01
780 mm^3	8.51x10^{6}	12.2x10^{-9}	1.895	0.543	21.3	0.01

The overall uncertainty can now be evaluated from

$$U_W = \left[\left(\theta_\rho U_\rho\right)^2 + \left(\theta_c U_c\right)^2 + \left(\theta_{\dot{T}} U_{\dot{T}}\right)^2 + \left(\theta_T U_T\right)^2 + \left(\theta_\varepsilon U_\varepsilon\right)^2\right]^{0.5} \qquad \text{(C.6)}$$

Figure C.6 shows the cumulative effect of these errors as a function of the chosen control volume size. The minimum error was found to occur with a control volume of between approximately 150 and 300 mm^3. Control volumes above 350 mm^3 or below 150 mm^3 have increasing errors mainly due to signal noise and poor definition of the control volume respectively.

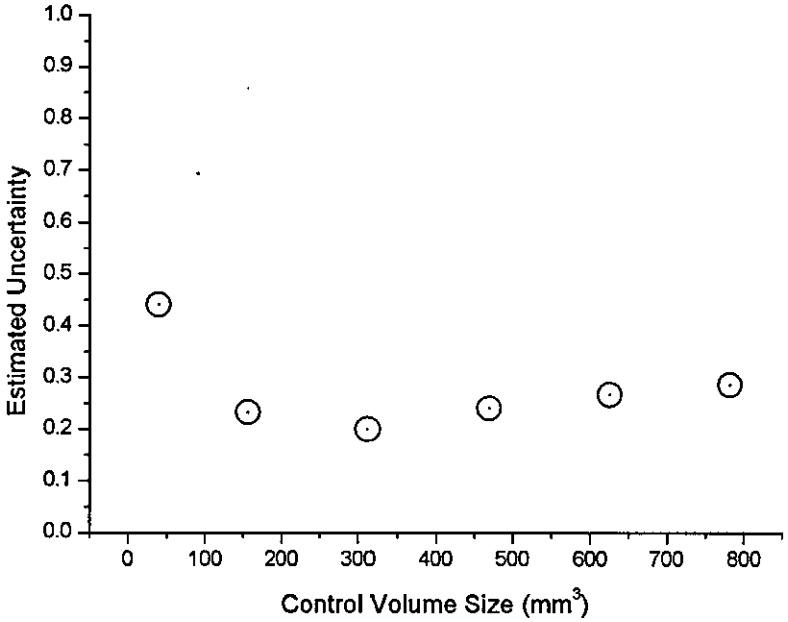

Figure C.6 Plot of overall predicted error as a function of control volume.

APPENDIX D: HEATING EFFICIENCY TESTS – TABULATED RESULTS

Table D.1 Tabulated results of discharge heating efficiency DoE investigation.

Standard Order	Run Order	Block	Axial Flow m s-1	Cross Flow m s-1	Current mA	Electrode Spacing mm	Heating Efficiency %
105	1	Block 1	0.6	0	20	10	9.387
49	2	Block 1	0	0.6	20	5	17.46
1	3	Block 1	0	0	13	5	39.825
57	4	Block 1	0.6	0.6	20	5	9.97
41	5	Block 1	0.6	0	20	5	18.475
17	6	Block 1	0	0.6	13	5	23.295
73	7	Block 1	0.6	0	13	10	13.955
89	8	Block 1	0.6	0.6	13	10	16.29
97	9	Block 1	0	0	20	10	19.965
25	10	Block 1	0.6	0.6	13	5	18.855
65	11	Block 1	0	0	13	10	22.06
9	12	Block 1	0.6	0	13	5	23.645
121	13	Block 1	0.6	0.6	20	10	9.395
113	14	Block 1	0	0.6	20	10	17.76
33	15	Block 1	0	0	20	5	25.795
81	16	Block 1	0	0.6	13	10	17.6
18	17	Block 2	0	0.6	13	5	26.565
34	18	Block 2	0	0	20	5	23.02
106	19	Block 2	0.6	0	20	10	11.845
90	20	Block 2	0.6	0.6	13	10	11.81
50	21	Block 2	0	0.6	20	5	17.96
122	22	Block 2	0.6	0.6	20	10	10.08
2	23	Block 2	0	0	13	5	40.16
82	24	Block 2	0	0.6	13	10	12.235
66	25	Block 2	0	0	13	10	25.54
98	26	Block 2	0	0	20	10	20.42
58	27	Block 2	0.6	0.6	20	5	14.47
114	28	Block 2	0	0.6	20	10	15.985
74	29	Block 2	0.6	0	13	10	11.935
10	30	Block 2	0.6	0	13	5	18.99

Standard Order	Run Order	Block	Axial Flow m s-1	Cross Flow m s-1	Current mA	Electrode Spacing mm	Heating Efficiency %
42	31	Block 2	0.6	0	20	5	17.04
26	32	Block 2	0.6	0.6	13	5	23.47
123	33	Block 3	0.6	0.6	20	10	9.85
51	34	Block 3	0	0.6	20	5	20.3
83	35	Block 3	0	0.6	13	10	14.355
75	36	Block 3	0.6	0	13	10	16.895
99	37	Block 3	0	0	20	10	23.335
11	38	Block 3	0.6	0	13	5	20.075
59	39	Block 3	0.6	0.6	20	5	19.695
3	40	Block 3	0	0	18	5	34.055
91	41	Block 3	0.6	0.6	14	10	14.18
115	42	Block 3	0	0.6	20	10	14.035
43	43	Block 3	0.6	0	20	5	17.42
107	44	Block 3	0.6	0	12	10	13.66
19	45	Block 3	0	0.6	13	5	30.025
67	46	Block 3	0	0	13	10	21.94
27	47	Block 3	0.6	0.6	13	5	18.985
35	48	Block 3	0	0	20	5	26.38
108	49	Block 4	0.6	0	20	10	14.36574
68	50	Block 4	0	0	13	10	25.24638
36	51	Block 4	0	0	20	5	22.66667
52	52	Block 4	0	0.6	20	5	18.44017
116	53	Block 4	0	0.6	20	10	16.73713
60	54	Block 4	0.6	0.6	20	5	15.23843
12	55	Block 4	0.6	0	13	5	18.45635
44	56	Block 4	0.6	0	20	5	17.06944
92	57	Block 4	0.6	0.6	15	10	12.67742
28	58	Block 4	0.6	0.6	13	5	18.44444
76	59	Block 4	0.6	0	13	10	14.09556
20	60	Block 4	0	0.6	13	5	22.16667
4	61	Block 4	0	0	18	5	28.88889
100	62	Block 4	0	0	20	10	16.24132
84	63	Block 4	0	0.6	14	10	11.33519
124	64	Block 4	0.6	0.6	20	10	9.02584
117	65	Block 5	0	0.6	20	10	9.479167
101	66	Block 5	0	0	20	10	21.81424
13	67	Block 5	0.6	0	13	5	19.52778
77	68	Block 5	0.6	0	14	10	11.83532
53	69	Block 5	0	0.6	20	5	17.9537
93	70	Block 5	0.6	0.6	15	10	10.81145
37	71	Block 5	0	0	20	5	23.12434
5	72	Block 5	0	0	18	5	32.59722
45	73	Block 5	0.6	0	20	5	16.94686
69	74	Block 5	0	0	13	10	23.08466
109	75	Block 5	0.6	0	20	10	12.59048

Standard Order	Run Order	Block	Axial Flow m s-1	Cross Flow m s-1	Current mA	Electrode Spacing mm	Heating Efficiency %
85	76	Block 5	0	0.6	15	10	15.13072
29	77	Block 5	0.6	0.6	13	5	16.19444
125	78	Block 5	0.6	0.6	20	10	9.168022
21	79	Block 5	0	0.6	13	5	17.25309
61	80	Block 5	0.6	0.6	20	5	14.75855
86	81	Block 6	0	0.6	15	10	13.67937
110	82	Block 6	0.6	0	20	10	12.89028
126	83	Block 6	0.6	0.6	20	10	11.22619
94	84	Block 6	0.6	0.6	15	10	11.13814
118	85	Block 6	0	0.6	20	10	11.09444
14	86	Block 6	0.6	0	13	5	18.01235
54	87	Block 6	0	0.6	20	5	22.67874
22	88	Block 6	0	0.6	13	5	23.26263
46	89	Block 6	0.6	0	20	5	18.08333
30	90	Block 6	0.6	0.6	15	5	19.60802
38	91	Block 6	0	0	20	5	29.49495
78	92	Block 6	0.6	0	13	10	14.27778
6	93	Block 6	0	0	13	5	34.54545
70	94	Block 6	0	0	13	10	22.39683
102	95	Block 6	0	0	20	10	18.83681
62	96	Block 6	0.6	0.6	20	5	12.68056
119	97	Block 7	0	0.6	20	10	14.92735
15	98	Block 7	0.6	0	13	5	18.53571
23	99	Block 7	0	0	17	5	29.2284
7	100	Block 7	0	0.6	13	5	22.4183
127	101	Block 7	0.6	0.6	20	10	9.808943
31	102	Block 7	0.6	0.6	13	5	14.74444
95	103	Block 7	0.6	0.6	15	10	7.838542
79	104	Block 7	0.6	0	15	10	16.30556
63	105	Block 7	0.6	0.6	20	5	15.06746
47	106	Block 7	0.6	0	20	5	15.75
71	107	Block 7	0	0	13	10	19.6087
55	108	Block 7	0	0.6	20	5	20.45726
103	109	Block 7	0	0	20	10	18.19524
39	110	Block 7	0	0	20	5	21.93478
87	111	Block 7	0	0.6	15	10	9.367284
111	112	Block 7	0.6	0	20	10	10.09383
112	113	Block 8	0.6	0	20	10	11.97721
80	114	Block 8	0.6	0	15	10	13.33681
64	115	Block 8	0.6	0.6	20	5	15.33532
72	116	Block 8	0	0	13	10	24.69949
32	117	Block 8	0.6	0.6	15	5	11.7601
128	118	Block 8	0.6	0.6	20	10	9.9677

Standard Order	Run Order	Block	Axial Flow m s-1	Cross Flow m s-1	Current mA	Electrode Spacing mm	Heating Efficiency %
48	119	Block 8	0.6	0	20	5	17.66889
8	120	Block 8	0	0	15	5	28.79012
104	121	Block 8	0	0	20	10	17.43673
56	122	Block 8	0	0.6	20	5	17.45333
40	123	Block 8	0	0	18	5	25.14251
88	124	Block 8	0	0.6	13	10	15.37593
120	125	Block 8	0	0.6	20	10	9.754522
96	126	Block 8	0.6	0.6	16	10	13.13194
16	127	Block 8	0.6	0	13	5	19.19231
24	128	Block 8	0	0.6	15	5	25.14815

APPENDIX E: ELECTRICAL MODELLING WITH SIMULINK

Modelling circuit elements

Electrical circuit modelling in simulink is achieved by considering individual electrical circuit components, typically capacitors, inductors and resistors. The method for modelling the main components of the equivalent circuit follows.

Capacitors

One equation in two forms has been used to model capacitance, depending on whether a voltage or current calculation is required.

These are:

$$i = C\frac{dv}{dt} \qquad \text{(E.1)}$$

$$v = \frac{1}{C}\int i dt \qquad \text{(E.2)}$$

The equivalent Simulink models for continuous problems are as shown in Figures E.1 and E.2.

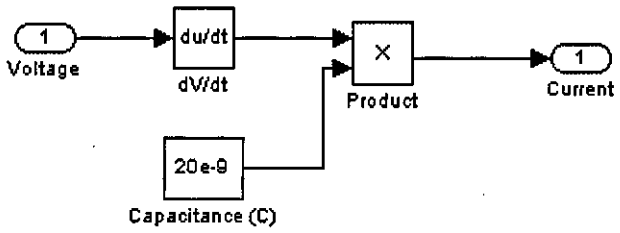

Figure E.1. Simulink model representing Equation E.1

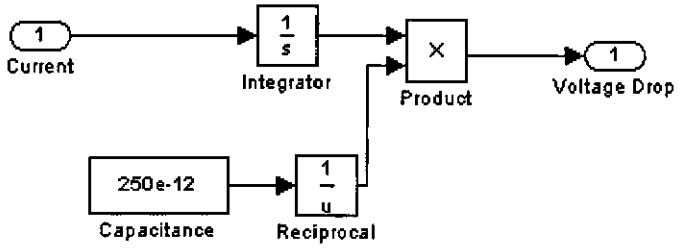

Figure E.2. Simulink model representing Equation E.2

Inductors

The equivalent equations for inductance have been used to calculate instantaneous current flows and voltage drops. These are:

$$v = L\frac{di}{dt} \tag{E.3}$$

$$i = \frac{1}{L}\int v dt \tag{E.4}$$

These equations can be represented in Simulink with the block combinations shown in Figure E.3 and E.4.

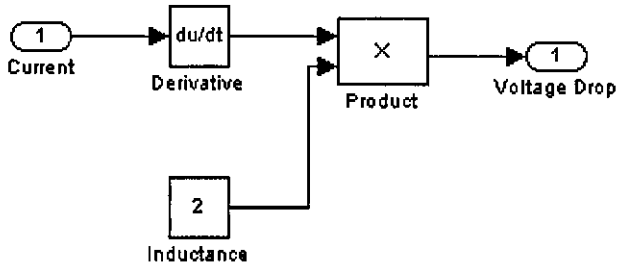

Figure E.3. Simulink model representing Equation E.3

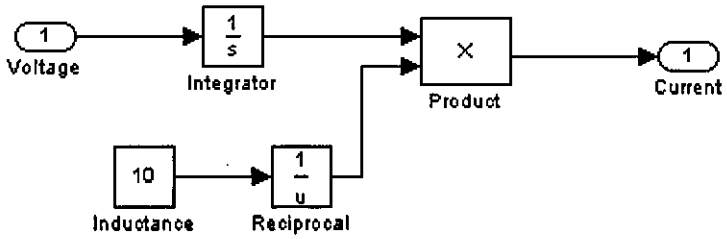

Figure E.4. Simulink model representing Equation E.4

Resistors

Following from the previous examples, equivalent relationships for resistances can be found from Ohm's law such that:

$$v = iR \tag{E.5}$$

$$i = \frac{v}{R} \tag{E.6}$$

These are represented in Simulink using the block combinations in Figure E.5 and E.6.

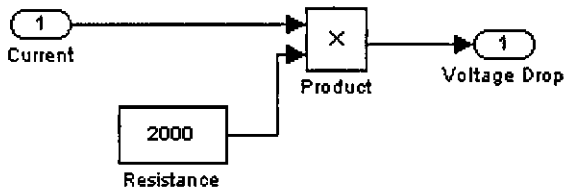

Figure E.5. Simulink model representing Equation E.5.

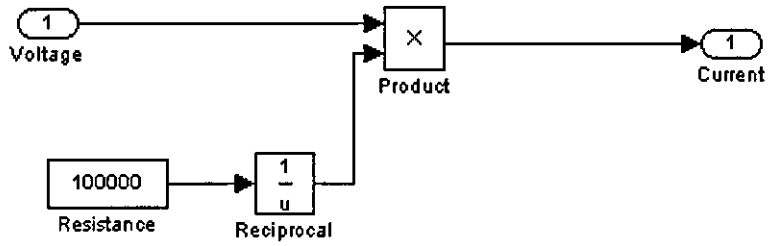

Figure E.6. Simulink model representing Equation E.6.

Electric Discharge

Modelling the discharge is somewhat more complicated than the electrical circuit elements discussed previously. Although any conceivable model should be able to be incorporated into the Simulink environment a simple resistance/voltage relationship was used for this research. Resistance/voltage relationships can be found from measurements of transient current and voltage directly from a discharge. An interpolating lookup table in Simulink is used for model calculations.

Modelling Parallel Components with Applied Potential

In all of the above mentioned circuit elements it is possible to calculated current from a known applied voltage across any given circuit element. We can therefore assemble the Simulink elements in a parallel arrangement with a known applied voltage, for example Figure E.7.

Electrical Circuit:

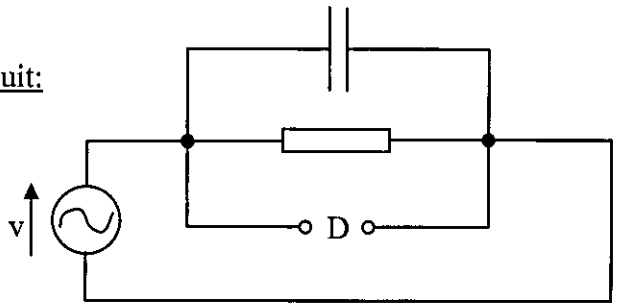

Simulink Model:

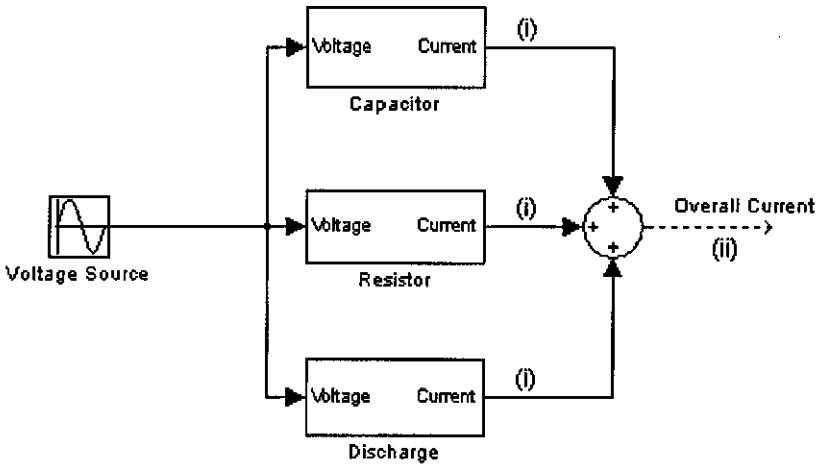

Figure E.7. Example of modelling parallel circuit components with an applied potential using each of the circuit elements discussed earlier.

The voltage across any of the circuit components is equal to the applied voltage. The current through any individual component can be found from points (i) and overall current from point (ii).

Modelling Series Components with Applied Potential

When a number of circuit elements are in series there is a potential drop across each element. There is however an overall current which must flow through each circuit element. Within Simulink, the arrangement shown in Figure E.8 can be used to model such a system.

Electrical Circuit:

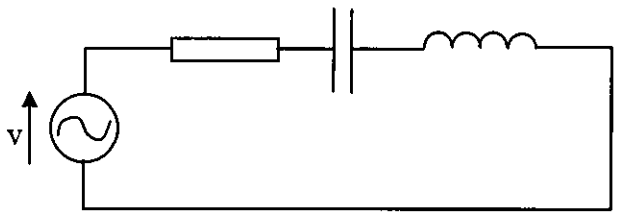

Simulink Model:

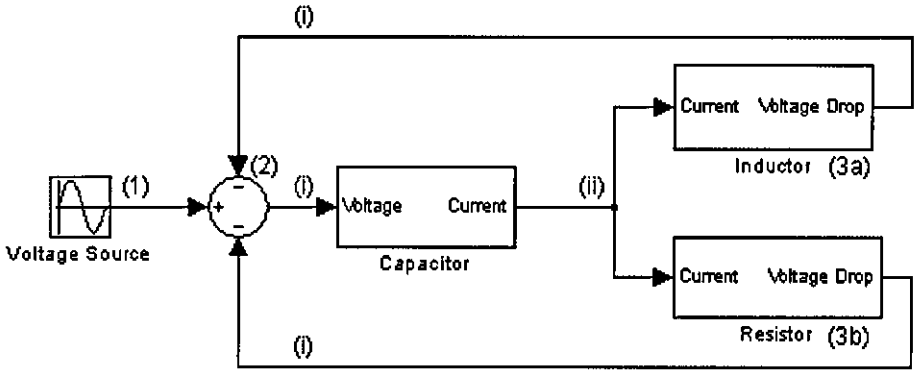

Figure E.8. Simulink example model for series circuits with applied potential. Numbering refers to points in the text.

At point (1), the potential is the applied potential. At point (2) the potential drop across all but one of the circuit elements is taken from the applied potential leaving the potential drop across the final circuit element as the output. The current through this element is then calculated using the previously described blocks giving the current flow through each series component. This current flow is then used to calculate the voltage drop through the other series components, (3a) and (3b) which feed back to the initial summation at point (2).

The voltage drop across any individual circuit element can be found from points (i) in Figure E.8. The current through the circuit can be found from point (ii).

Modelling Parallel Components with Applied Current

This case is modelled in a similar way to the series components with an applied potential. We know that the current will be different through each element but must combine to give the applied current. We also know that the potential drop across all of the circuit elements must be the same. The block arrangement in Simulink is shown in Figure E.9.

Electrical Circuit:

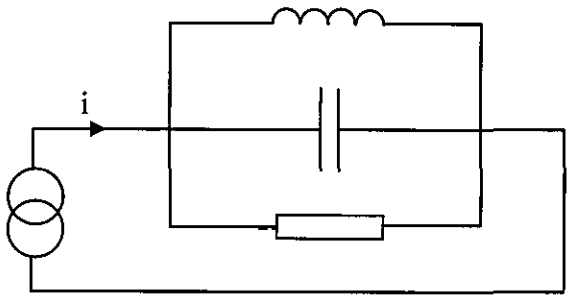

Simulink Model:

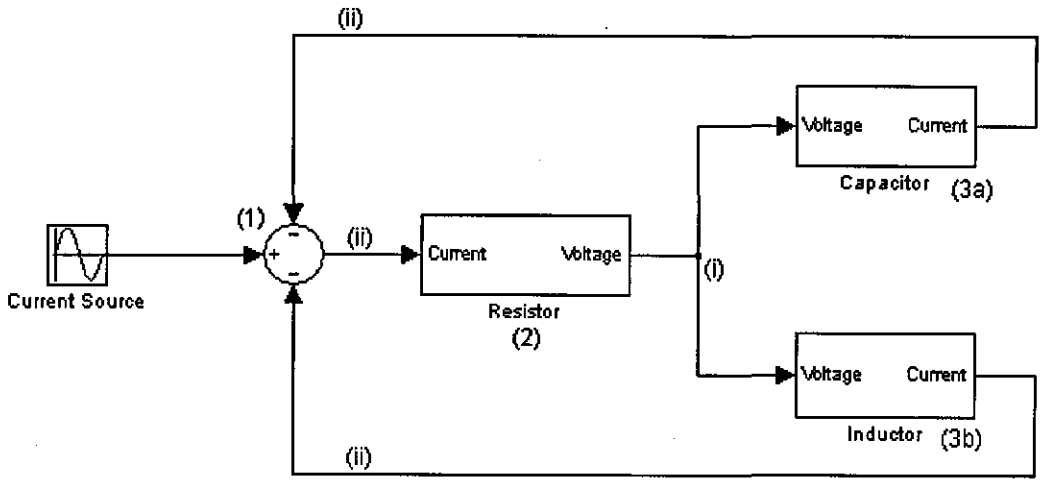

Figure E.9. Simulink example model for parallel circuits with applied current. Numbering refers to points in the text.

The current through one of the circuit components is calculated by taking the difference of the applied current and current flows through all other circuit components [at point (1)]. The resulting current flow is used to calculate the potential drop across a single circuit element at point (2). We have already said that the potential across each component must be the same so this value of voltage is used to calculate the current flow through the other circuit components at point (3a) and (3b). The current flow calculated here is then fed back to find the current flow through the circuit element at point (2).

The potential across the circuit elements can be found from point (i) in Figure E.9. The current flow through individual circuit elements can be found from points (ii).

Modelling Series Components with Applied Current

Modelling of series components with an applied current can be achieved in a similar way to modelling parallel components with an applied potential. The current flow through each circuit element will be the same, and equal to the applied current. The Simulink components can then be set up in a parallel arrangement to calculate the potential drop across each element, an example of which is shown in Figure E.10.

Electrical Circuit:

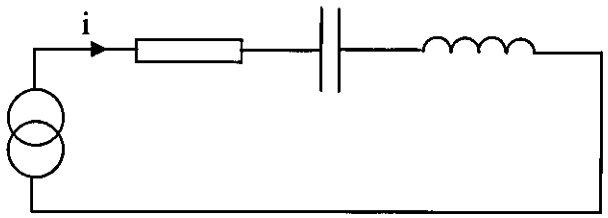

Simulink Model:

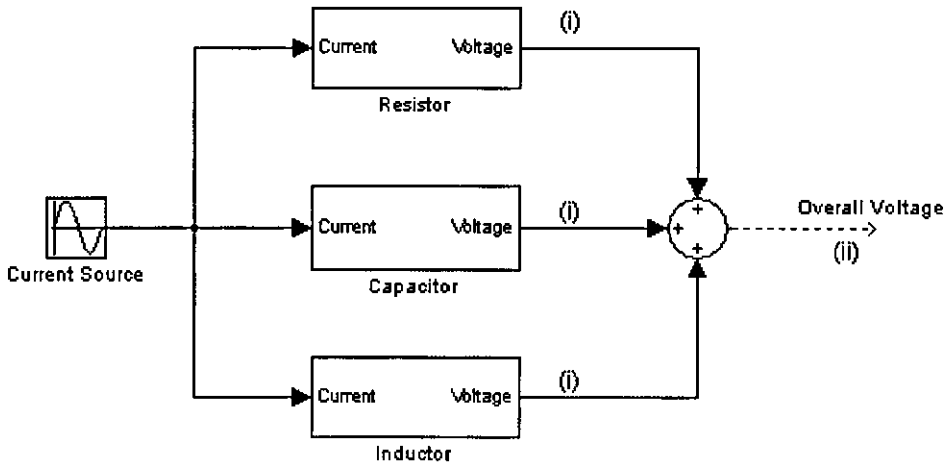

Figure E.10. Simulink example model for parallel circuits with applied current. Numbering refers to points in the text.

The current through each component is simply the applied current. The potential drop across individual components can be found from points (i) in Figure E.10. The overall applied potential can be found from point (ii).

APPENDIX F: MAGNETIC FIELDS FOR DISCHARGE MOBILITY CONTROL

This appendix summarises preliminary testing of using magnetic fields to affect the mobility of the Autoselective discharge.

Test Setup

A pre-wound coil with non-magnetic bobbin with an open core diameter of approximately 30 mm was used with a concentric electrode filter arrangement shown schematically in Figure F.1. The electrode distance was approximately 5 mm.

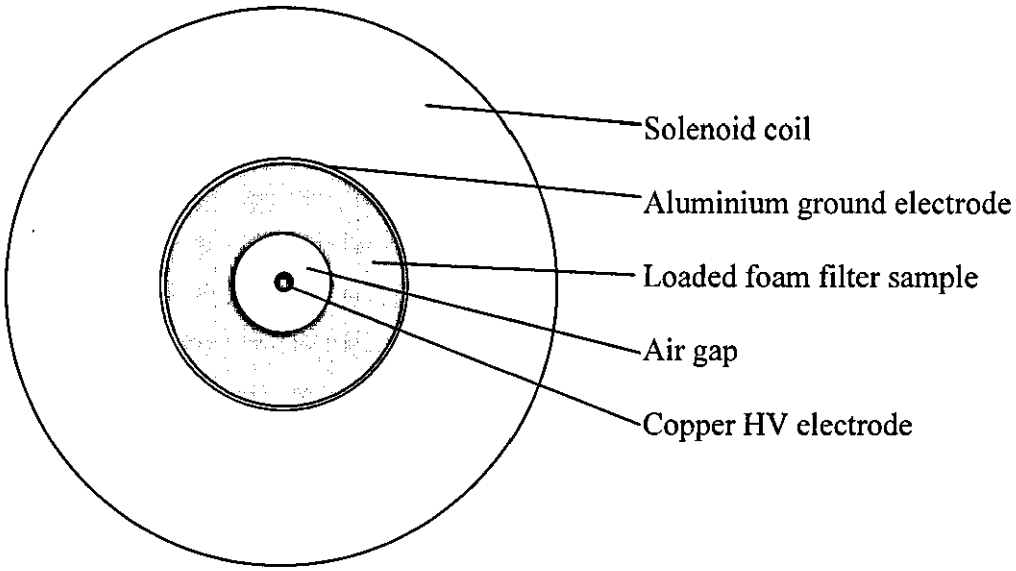

Figure F.1. Cross section of electrode arrangement when testing the effect of magnetic control.

General Observation

With rms currents less than approximately 2.8 A rms through the coil the magnetic field is not strong enough to have any visually discernable affect on the discharge. The discharge still locked onto a single point on the filter after a short period of time and subsequently remained as a single discharge column.

Above 2.8 A rms the discharge could be seen to move typically through a region with an angle of approximately 80 degrees. Inaccurate positioning of the electrode is the likely cause of it not covering 360 degrees.

Subsequent Predictions

Magnetic Field Strength:-

The applied voltage required to achieve approx 2.8 A rms is 140 V rms at 50 Hz. Assuming that the resistance is negligible in comparison to the inductive impedance the inductance of the coil can be estimated from the following relationship:

$$L = \frac{V_{rms}}{I_{rms}} \frac{1}{2\pi f} \qquad \text{(F.1)}$$

which gives us an inductance of 0.159 H.

The coil is approximately 70 mm long with an inner diameter of 38 mm and an outer diameter of 70 mm. We know an approximate relationship between physical solenoid coil properties and inductance, L, as:

$$L = n^2 l \mu A \qquad \text{(F.2)}$$

where n is the coil density, l is the coil length, μ is the permeability of the core material (air) and A is the area of the core. This allows us to estimate the coil density, n as 40000 coils m^{-1}.

The magnetic field, B, can be approximated from the relationship:

$$B = n\mu I \qquad \text{(F.3)}$$

where I is the current through the coil. This gives us an rms magnetic field strength of 0.14 T as the minimum field strength required to have a noticeable effect on moving the discharge in stationary air from a cordierite filter.

Permanent magnets are available with field strengths in the region of 0.2 T but are costly (in the region of £350-400 each) and have very localised fields.

Using 1 mm^2 solid core annealed copper wire to make a full size coil would mean a maximum current of 13 A (based on supplier recommendations). The coil density with this maximum current would be 8600 coils m^{-1}. The coil density per layer is 770 coils m^{-1}. This means that there would need to be 12 layers of coils which would lead to a thickness of less than 16 mm which is reasonable from a packaging point of view.

Power Consumption:

The resistivity of copper is known to be around $1.7x10^{-8}$ ohm m. The number of coils is the coil density multiplied by the length, 150 mm, giving 130 coils in total. The length of the wire required will be approximately 70 m with an area of 1 mm^2.

The resistance of the coil is

$$R = \frac{\rho l}{A} = \frac{1.7\times10^{-8}\times70}{1\times10^{-6}} = 1.19\ \Omega \qquad \text{(F.4)}$$

The power dissipated through this resistance is calculated as

$$P = I^2R = 13^2\times1.19 = 200\ \text{W} \qquad \text{(F.5)}$$

This is approximately half the target power consumption for the regeneration system meaning that it is less attractive option at the current time. Options using permanent magnets or alternative techniques for moving the discharge can be used.

APPENDIX G: ELECTROSTATIC MODELLING ASSUMPTIONS

Electrostatic modelling has been used to improve understanding of the effect of general design decisions regarding electrode shape. It has not bee used as a design tool for definitive and quantitive use. This Appendix summarises the assumptions and boundary conditions that have been used in the electrostatic modelling using terminology typical of that used within the COMSOL multiphysics software that was used for the modelling.

Modelling assumptions

The modelling assumptions include:

1. The electrodes are ideal conductors at a known potential.
2. The air and filter can be considered as homogeneous media with known dielectric properties.
3. The electrostatic fields give an indication of the most likely areas for the discharge to break down the air.

Boundary conditions

The boundary conditions are described, depending on the location, as:

1. Electrodes – known potential relative to ground
2. Symmetry line – axial symmetry
3. Non-conductive boundaries – zero charge/symmetry boundary (these boundaries are located where the change in electric field strength is negligible.